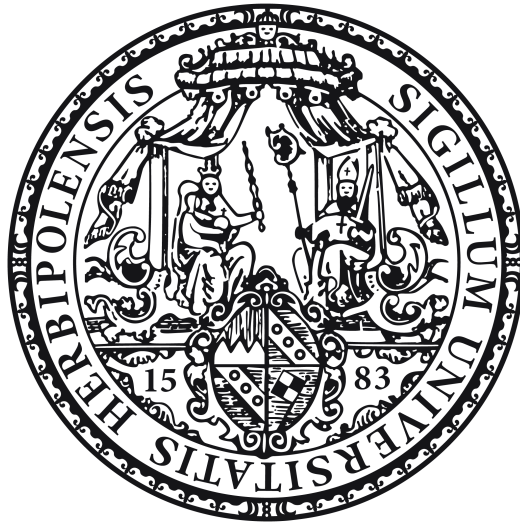**The role of megakaryocytes and platelets in vascular and osteogenic development**

• • •

Die Rolle von Megakaryozyten und Thrombozyten in vaskulärer und osteogener Entwicklung

Doctoral thesis for a doctoral degree
at the Graduate School of Life Sciences,
Julius-Maximilians-Universität Würzburg,
Section Biomedicine

submitted by

Isabelle Carlotta Becker
from Simmern, Hunsrück

Würzburg, 2020

Submitted on:

Members of the Promotionskomitee:

Chairperson: Prof. Dr. Georg Gasteiger

Primary Supervisor: Prof. Dr. Bernhard Nieswandt

Supervisor (Second):   Prof. Dr. Manfred Gessler

Supervisor (Third):   PD. Dr. Heike Hermanns

Date of Public Defense: _____

Date of Receipt of Certificates: _____

It's a crazy world out there. Be curious.

Stephen Hawking

SUMMARY

Platelets, small anucleate cell fragments in the blood stream, derive from large precursor cells, so-called megakaryocytes (MK) residing in the bone marrow (BM). In addition to their role in wound healing, platelets have been shown to play a significant role during inflammatory bleeding. Above all, the immunoreceptor tyrosine-based activation motif (ITAM) receptors GPVI as well as CLEC-2 have been identified as main regulators of vascular integrity.

In addition to ITAM-bearing receptors, our group identified GPV as another potent regulator of hemostasis and thrombosis. Surprisingly, concomitant lack of GPV and CLEC-2 deteriorated blood-lymphatic misconnections observed in $Clec2^{-/-}$ mice resulting in severe edema formation and intestinal inflammation. Analysis of lymphatic and vascular development in embryonic mesenteries revealed severely defective blood-lymph-vessel separation, which translated into thrombocytopenia and increased vascular permeability due to reduced tight junction density in mesenteric blood vessels and consequent leakage of blood into the peritoneal cavity.

Recently, platelet granule release has been proposed to ameliorate the progression of retinopathy of prematurity (ROP), a fatal disease in newborns leading to retinal degradation. The mechanisms governing platelet activation in this process remained elusive nonetheless, which prompted us to investigate a possible role of ITAM signaling. In the second part of this thesis, granule release during ROP was shown to be GPVI- and partly CLEC-2-triggered since blockade or loss of these receptors markedly deteriorated ROP progression.

Proplatelet formation from MKs is highly dependent on a functional microtubule and actin cytoskeleton, the latter of which is regulated by several actin-monomer binding proteins including Cofilin1 and Twinfilin1 that have been associated with actin-severing at pointed ends. In the present study, a redundancy between both proteins especially important for the guided release of proplatelets into the bloodstream was identified, since deficiency in both proteins markedly impaired MK functionality mainly due to altered actin-microtubule crosstalk.

Besides ITAM-triggered activation, platelets and MKs are dependent on inhibitory receptors, which prevent overshooting activation. We here identified macrothrombocytopenic mice with a mutation within $Mpig6b$ encoding the ITIM-bearing receptor G6b-B. G6b-B-mutant mice developed a severe myelofibrosis associated with sex-specific bone remodeling defects resulting in osteosclerosis and -porosis in female mice. Moreover, G6b-B was shown to be indispensable for MK maturation as verified by a significant reduction in MK-specific gene expression in G6b-B-mutant MKs due to reduced GATA-1 activity.

ZUSAMMENFASSUNG

Blutplättchen, die kleinsten Zellen des hämatopoetischen Systems, werden von großen Vorläuferzellen, den Megakaryozyten (MKs), im Knochenmark gebildet. Neben ihrer Rolle bei der Blutstillung und Wundheilung sind Thrombozyten außerdem maßgeblich daran beteiligt, Blutungen in Entzündungsprozessen zu verhindern. Insbesondere den *immunoreceptor tyrosine-based activation motif* (ITAM) Rezeptoren GPVI und CLEC-2 wird eine tragende Rolle in der Aufrechterhaltung der vaskulären Integrität zugeschrieben.

Neben den ITAM-Rezeptoren konnten wir auch für den Thrombozytenrezeptor GPV eine Funktion in Hämostase und Thrombose identifizieren. Erstaunlicherweise führte ein gleichzeitiger Verlust von GPV und CLEC-2 zu einer dramatischen Verstärkung der Blut-Lymphgefäß-Fehlbildungen, die bereits in CLEC-2-defizienten Mäusen beschrieben wurde, sodass die Tiere eine starke Ödembildung in den Extremitäten sowie Entzündungen des Dünndarms aufwiesen. Eine vertiefte Analyse der vaskulären Strukturen in Mesenterien während der Embryonalentwicklung offenbarte zusätzliche Defekte in der Blut- und Lymphgefäßtrennung in CLEC-2/GPV-defizienten Mäusen. Diese Deformationen führten zu Thrombozytopenie, Anämie und einer erhöhten vaskulären Permeabilität in adulten Mäusen, was sich auf eine reduzierte *tight-junction*-Dichte in Mesenterien und Darmgewebe zurückführen ließ, die zu einem Austritt von Blut in die Peritonealhöhle führte.

In einer kürzlich veröffentlichten Publikation wurde Plättchengranula eine Rolle in der Auflösung retinopathischer Gefäßmissbildungen zugeschrieben. Retinopathia praematurorum (ROP) ist eine Krankheit in Frühgeborenen, die aufgrund von Sauerstoffunterschieden vor und nach Geburt zu Netzhautablösung und Blindheit führen kann. Die exakten Mechanismen, die hierbei zu Thrombozytenaktivierung und nachfolgender Degranulierung beitragen, sind bisher allerdings nicht bekannt. Da eine tragende Rolle von ITAM Rezeptoren in der Aufrechterhaltung vaskulärer Integrität insbesondere in krankhaftem Gewebe zuvor bereits aufgezeigt wurde, untersuchten wir die Entwicklung von Vaso-obliteration und Neovaskularisierung in CLEC-2 und GPVI-depletierten oder defizienten Mäusen und konnten einen Beitrag beider Rezeptoren zur Progression von ROP nachweisen.

Die Produktion von Thrombozyten aus MKs ist stark von einem funktionalen Mikrotubuli- und Aktin-Zytoskelett abhängig. Aktinpolymerisation wird substanziell von unterschiedlichen Aktin-bindenden Proteinen reguliert, von denen Cofilin1 und Twinflin1 ein Abtrennen der Filamente induzieren. Wir konnten nun eine funktionale Redundanz beider Proteine in murinen MKs aufzeigen, die insbesondere für ein geregeltes Abschnüren von Thrombozyten in die Blutbahn essentiell ist und von einem Crosstalk zwischen Aktin- und Mikrotubuli-Zytoskeletts abhängig ist, der durch Twinfilin1 und Cofilin1 aufrechterhalten wird.

Neben ITAM-induzierter Thrombozytenaktivierung spielt auch die Inhibition derselbigen durch *immunoreceptor tyrosine-based inhibition motif* (ITIM)-Rezeptoren eine große Rolle in MKs und Plättchen, da diese eine überschießende Aktivierung verhindern. Wir konnten in der vorliegenden Arbeit eine Spontanmutation in *Mpig6b,* das für den ITIM-Rezeptor G6b-B codiert, in stark makrothrombozytopenen, wildtypischen Mäusen identifizieren. Außer in der stark reduzierten Thrombozytenzahl manifestierte sich die Mutation des Weiteren in einer massiven Myelofibrose, die mit einer geschlechtsspezifischen Osteosklerose und -porose in weiblichen Mäusen einherging. Überraschenderweise konnten wir zudem einen dramatischen Reifungsblock in G6b-B-mutierten MKs feststellen, der insbesondere in einer reduzierten Expression des Transkriptionsfaktors GATA-1 begründet lag.

TABLE OF CONTENTS

1   INTRODUCTION

1.1   Vascular development

1.1.1   Regulators of angiogenesis during early embryonic development

The cardiovascular system is the first functional organic system to develop in the mouse embryo in a process involving the induction of a plethora of cell types. The first cells to give rise to primitive vessels arise on *embryonic* (E) day 6.5, on which cells of the epiblast undergo epithelial-to-mesenchymal transition leading to the formation of mesoderm, which in turn develops into endothelial cell precursors, so-called angioblasts.[1] These de-novo-formed cells aggregate into a primitive vascular plexus in a process termed vasculogenesis.[2] Successively, endothelial cells arise from the plexus and form primitive vessel networks, which rapidly remodel in order to conform to the demands of the growing embryo as well as the surrounding yolk sac (Figure 1a). This angiogenesis of newly formed vessels from existing endothelial cells is highly dependent on a variety of signaling molecules, most importantly the activation of *fetal liver kinase* (Flk) 1 binding to its ligand *vascular endothelial growth factor* (VEGF). Flk-1 is the earliest differentiation marker for angioblasts and deficiency therein not only results in absent blood island development,[3,4] but further suppresses the induction of hematopoietic cells, thus implying both cell types to arise from a common progenitor.[5] VEGFA serves two purposes by propagating vascular plexus development on the one hand, while its binding to a second receptor termed *Fms-related receptor kinase* (Flt) 1, expressed on already established endothelial cells, promotes vessel growth on the other hand.[6] Stable VEGFA concentrations are indispensable for proper vascular development, since reduced concentrations as present in heterozygous mice already results in early embryonic lethality due to ineffective blood vessel development.[7] A similarly significant defect in vessel maturation is observed upon loss of the ETS transcription factor *ETS variant 2* (Etv2).[8]

Sprouting and non-sprouting angiogenesis induces the development of more elaborate vascular networks, both being tightly regulated by activation of several signaling molecules including Tie family receptor kinases.[9] Specific cells within the vessel wall, so-called tip-cells, are selected for sprouting, which is induced by VEGFA-dependent expression of *Delta-like-4* (Dll4) and inhibited in neighboring cells by upregulation of Notch1 (Figure 1b).[10,11] In addition to promoting vascular sprouting, Notch-signaling has been described to be important for arterial-venous fate decision, which is also critically regulated by Ephrins. While *ephrin* (Eph) B2 expression is restricted to arteries along with several other receptors such as *neuropilin*

(Nrp) 1, its receptor EphB4 is selectively expressed on veins on subsets of developing blood vessels, thus suggesting fate decision to occur prior to the onset of circulation, although other publications suggest that conversion of endothelial cells might also be enabled through alternating flow.[12,13] A specification of arterial and venous identities is indispensable, since it enables the recruitment of stabilizing cells, which in turn allow for the onset of blood flow. The recruitment of pericytes to the developing blood vessels is mainly initiated by the release of *platelet-derived growth factor* (PDGF) B from endothelial cells, which activates PDGFRβ on mural cells.

In addition to veins and arteries, a third subset of vessels, the lymphatic vasculature, is developing during embryogenesis, mainly through a further specification of a distinct population of venous endothelial cells (Figure 1c). Induction of *Prospero homeodomain transcription factor* (Prox1) in these cells induces the formation of primitive lymphatic structures called lymph sacs, which then, upon concomitant sprouting and migration, are transformed into primary Nrp2-expressing *lymphatic endothelial cells* (LEC).[14,15] Upregulation of Nrp2 enables the responsiveness of developing LECs towards VEGFC, which in turn induces sprouting of the developing lymph vessels.[16]

1.1.2 Vascular and lymphatic development

Binding of VEGFC to VEGFR3, an Nrp2 co-receptor, in developing lymph sacs induces LEC sprouting thus leading to the upregulation of LEC-specific proteins such as the mucin-type *glycoprotein* (GP) podoplanin and *lymphatic vessel endothelial receptor* (LYVE) 1. How the separation of venous and lymphatic cells is mediated is still controversially discussed.[17] Several mouse models with deficiencies in either podoplanin or signaling molecules downstream of its ligand, the platelet hem *immunoreceptor tyrosine-based activation motif* (ITAM) *C-type lectin-like receptor 2* (CLEC-2) display a blood-filling of lymphatic vessels, thus implying a critical role of platelets in maintaining a barrier between veins and lymph sacs during development.[18-21] Current hypotheses suggest that platelet aggregates accumulate at the junction between cardinal vein and primary lymph sacs, thus physically enforcing a separation of both vasculatures.[21] This aggregate formation is supposedly mediated by CLEC-2 interacting with podoplanin on LECs, since platelet accumulations are absent in podoplanin-deficient mice. This theory is nonetheless challenged, since no blood-lymphatic misconnections are observed in animals either lacking the platelet integrin αIIbβ3, which is indispensable for aggregate formation, or its downstream adaptors kindlin-3 or talin-1. Other studies propose CLEC-2 to induce a clustering of podoplanin on LECs, thereby enhancing LEC migration, which is supported by the notion of *in vitro* stimulation of LEC migration using a recombinant CLEC-2 ectodomain.[20] Mice lacking the cytoplasmic domain of podoplanin,

however, do not display blood-lymphatic misconnections, while mice with mutated CLEC-2 hemITAM die in utero or shortly after birth due to severe edema formation and hemorrhages in the brain.[22]
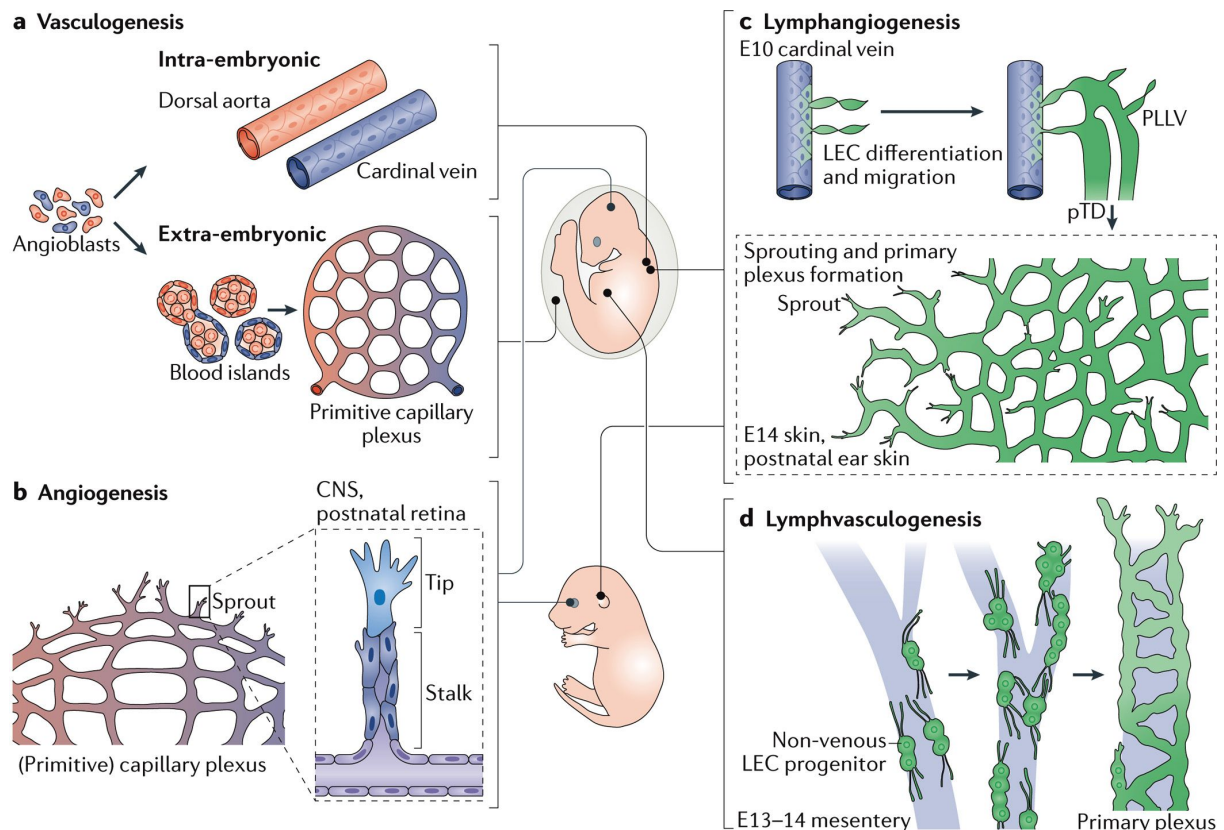
Figure 1. Vascular and lymphatic development in mice. Blood islands develop from angioblast precursors in a process termed vasculogenesis (**a**). The emerging primary capillary plexus gives rise to arteries and veins by sprouting angiogenesis (**b**) induced via the activation of a plethora of signaling pathways including VEGFA, Dll4, Etv2 and ephrins. Primary lymphatic vessels derive from the cardinal vein by angiogenic sprouting induced via upregulation of the transcription factor Prox1 (**c**). Lymphvasculogenesis in embryonic mesenteries on the other hand leads to the establishment of a primary lymphatic plexus with a non-venous origin surrounding blood vessels (**d**). Potente & Mäkinen, **Nat Rev Mol Cell Biol**, 2017.[23]

Two distinct lymphatic vessel types emerge from the sprouting primary plexus: small lymphatic capillaries and larger collecting lymphatics, which markedly differ in their appearance. While lymphatic capillaries can be distinguished by their discontinuous and highly permeable endothelium, which allows for the uptake of interstitial fluid as well as immune cells, collecting lymphatic vessels display a complete basement membrane further supported by a layer of *smooth muscle cells* (SMC).[24] Moreover, fluid backflow in collecting vessels is prevented by the frequent occurrence of valves. In contrast to this angiogenic sprouting of lymphatic vasculature, an alternative source of LECs has been described to arise in the embryonic mesenteric vasculature, where hemogenic endothelial cells contribute to the lymphvasculogenesis of lymphatic vessels (Figure 1d).[23,25]

1.1.3 Retinal angiogenesis

Due to easy visualization and accessibility, angiogenesis is nowadays mainly analyzed in the retina. Retinal vascularization is highly coordinated, organized and can be studied in both health and disease. In contrast to primary vasculogenesis during embryonic development, retinal vascularization is predominantly induced by angiogenic sprouting, beginning at the optic nerve head from which it radiates outwards.[26] Unlike human retinal vascularization, which takes place during fetal development, murine retinal angiogenesis starts post birth and is primarily oxygen-driven. Previous publications identified hypoxia-induced VEGF gradients to account for the induction and proliferation of endothelial cells. Deficiency in different VEGF isoforms is manifested by distinct and aberrant vascular patterns, thus suggesting that the expression of specific isoforms is spatially and temporally controlled.[26-28] Similar findings were made for the respective VEGFRs, which seem to mediate distinct processes of vascular patterning and endothelial migration.[29]

The adult retina as the neural system with the highest oxygen consumption per unit weight is dependent on two distinct vasculatory systems: the choroidal and the retinal vasculature. A third vasculature, the so-called hyaloid vessels, transiently develops prior to the evolvement of retinal vessels and assures the supply of the developing vitreous with oxygen and nutrients. Hyaloid arteries anastomose with anterior vessels of the choroid, which are critical for the venous drainage of the hyaloid arteries.[30] The evolution of retinal vessels coincides with the regression of the hyaloid vasculature, which is governed by apoptosis suggesting that both processes are controlled by similar signaling machineries.[31] Several diseases are associated with an incomplete degradation of the hyaloid vasculature resulting in incomplete retinal vessel formation, detachment and hemorrhage, thus highlighting the importance of a temporally controlled regression to ensure proper endothelial cell proliferation and migration in the retina.

1.1.3.1 Retinopathy of prematurity

As mentioned above, physiological retinal vascularization and patterning is highly dependent on a spatiotemporal control of oxygenation and thus VEGF levels. Hyperoxygenation during early stages of angiogenesis promotes the progression of *retinopathy of prematurity* (ROP), a possible blinding disease in premature infants. 10% of children worldwide are born before gestational week 36, which severely attenuates life expectancy. Children born before gestational week 28 are prone to develop ROP, since their neuronal and vascular development in the retina is not sufficiently concluded.[32] ROP can be divided into two distinct phases: an initial vessel regression and a subsequent aberrant vessel proliferation. The disease is thought to be initiated by a marked increase in relative oxygen levels: while in

utero, fetal blood is only saturated up to 70% with a PaO_2 of 30 mmHg. Upon exposure to room air oxygen saturation increases to 100% (60-100 mmHg PaO_2), often further elevated due to oxygen supplementation upon incomplete lung inflation.[33] VEGF transcription and release by astrocytes is supported under hypoxic conditions and induces vessel growth along a previously formed astrocyte template.[34,35] Loss of this physiologic stimulus upon sudden increase in external oxygen results in an abrupt loss of VEGF expression, thus leading to cessation of vessel growth on the one hand and degradation of already established vessels on the other hand (vasoobliteration).[36] During the second phase of ROP, relative hypoxia drives an upregulation of VEGF expression resulting in aberrant and pathological neovascularization.[37]

In order to study disease progression in more detail, ROP can be induced in young mice by exposure to hyperoxia (Figure 2). This *oxygen-induced retinopathy* (OIR) mirrors most symptoms of the disease, most importantly vasoobliteration and subsequent neovascularization, which can both be visualized in retinas isolated on *postnatal* (P) day 17. Previous publications linked thrombocytopenia to an aggravation of disease outcome in humans.[39] Moreover, a recent study suggested platelet granules to be protective during the progression of experimental OIR in mice, since granule depletion severely deteriorated disease progression.[40] How granule secretion is induced and regulated, however, is still incompletely understood.
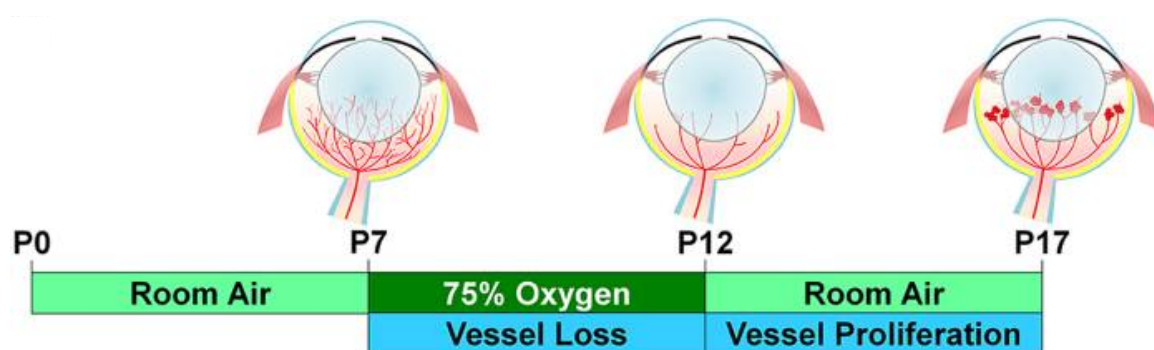
Figure 2. Experimental oxygen-induced retinopathy. Exposure of mice to 75% oxygen from P7 to P12 induces vessel regression. Subsequent transfer to room air for the following 5 days mimics the hypoxia leading to aberrant neovascularization and vascular tuft formation. Liu *et al.*, **Sci Rep**, 2016.[38]

1.2 Bone marrow homeostasis

1.2.1 Osteogenesis

A tight regulation of *bone marrow* (BM) homeostasis involving bone remodeling and adipocyte regeneration is essential not only to prevent fracture lesions, but to further assure coordinated hematopoiesis. The skeletal bone is constantly subjected to de-novo-formation

and resorption, both of which are mainly executed by two distinct cell types: osteoblasts and osteoclasts, respectively. Bone remodeling is initiated by enhanced bone resorption carried out by multinucleated osteoclasts, which derive from the hematopoietic stem cell lineage under the influence of *macrophage colony-stimulating factor* (M-CSF) and *receptor activator of NF-κB ligand* (RANKL) mainly secreted by osteoblasts, osteocytes and stromal cells.[41] Due to its myeloid descent, initial differentiation requires activity of the ETS-domain-binding factor PU.1, lack of which results in abolished osteoclast generation.[42] Binding of RANKL to its receptor is particularly important for osteoclastogenesis, since it induces transcription of a plethora of proteins among them *tartrate-resistant acid phosphatase* (TRAP), the bone collagenase cathepsin K as well as the calcitonin receptor.[43-45] RANKL signaling can be neutralized by binding of osteoprotegerin, which serves as a negative regulator of osteo-clastogenesis.[46] Activation of RANKL induces a variety of cytoskeletal rearrangements upon which a sealed compartment between the bone surface and the osteoclast membrane, mediated by αvβ3 integrins, is formed.[47] The release of hydrogen ions through activation of the *ATPase, H$^+$ transporting, [vacuolar proton pump] member I* (Atpi6) complex induces an acidification of the formed resorption pit, thus enabling dissolution of the bone-encompassing hydrogen.[48] Subsequently, degradation products such as collagen and solubilized calcium are further processed upon secretion of cathepsin K and TRAP, transported into the osteoclast and ultimately released into the circulation.[49] Impaired or enhanced osteoclast function results in severe bone remodeling defects leading to osteopetrosis or osteoporosis, respectively, which are further introduced in 1.2.4.2.

In contrast to myeloid-derived osteoclasts, osteoblasts emerge from *mesenchymal stem cells* (MSC), which are committed to the osteoprogenitor lineage upon upregulation of *Runt-related transcription factor 2* (RUNX2)- and *Distal-less homeobox 5* (Dlx5)-dependent transcription leading to the expression of type I collagen, osteocalcin and alkaline phosphatase.[50] Following a proliferation phase, final osteoblast differentiation requires osterix-induced transcription and successive secretion of osteocalcin, collagen type 1 and bone sialoprotein I/II as well as the proteoglycans biglycan and decorin.[51] Deposition of these components leads to the formation of an osteoid matrix, which is mineralized upon release of calcium- and phosphate-containing vesicles, which ultimately form hydroxyapatite crystals. Both osteoclast and osteoblast activity is highly dependent on soluble mediators, which are able to induce bone degradation or formation, respectively. Most calciotropic hormones such as *interleukin* (IL) 1β or *tumor necrosis factor* (TNF) α signal via increasing *messenger RNA* (mRNA) expression of RANKL in osteoblasts, thus enhancing osteoclast activity by interfering with osteoprotegerin-RANK interactions, which normally inhibit bone resorption.[49,52] In addition to these paracrine factors, systemic release of *parathyroid*

hormone (PTH), glucocorticoids and estrogen are markedly involved in regulating blood calcium levels and thus bone remodeling. Differences in hormonal levels are hereby often detected by a third type of bone-lining cells, namely osteocytes, which are able to respond to absence of estrogen by inducing bone remodeling through RANKL release.[53] Increasing evidence further suggests that estrogen can directly inhibit osteoclast-mediated bone degradation by binding to *estrogen receptor* (ER) α as well as by increasing osteoprotegerin production in T-cells and osteoblasts.[54-56] The exact mechanism of how bone formation and resorption are spatiotemporally linked are still incompletely understood, but several studies have identified an axis connecting PTH and *transforming growth factor* (TGF) β1 to significantly contribute to the coupling of both processes. TGFβ1 as one of the most abundant proteins in bone matrix, is released as a latent precursor molecule and activated by osteoclast-mediated cleavage, upon which it mediates MSC recruitment to the previously resorbed bone surface.[57,58] MSC differentiation into osteoblasts in turn is induced by PTH signaling, thus linking both paracrine and systemic signaling pathways in the regulation of bone remodeling. These findings suggest TGFβ1 to be markedly involved in bone remodeling as verified by elevated TGFβ1 levels in a plethora of diseases associated with bone overgrowth such as the Marfan sydrome.[59]

1.2.2 Hematopoiesis

All blood cell lineages derive from *hematopoietic stem cells* (HSC), which, due to their lifelong self-renewal potential, have the capacity to give rise to numerous progenitor cells with increasing lineage specification. Early studies identified a stem cell population expressing CD117 (c-Kit) and *stem cell antigen* (Sca)-1, while being negative for lineage-specific expression markers (Lin$^-$) termed LSK (*Lin$^-$/Sca-1$^+$/c-Kit$^+$*) that accounted for 0.05% of all BM cells.[60] Further analyses of these cells revealed additional markers, most importantly CD150 and CD34, whose expression levels are essential for the identification of HSCs within the LSK population.[61] Interestingly, murine HSCs only display a minor expression of CD34, while the molecule is highly abundant on their human counterparts suggesting differences in surface molecule expression, albeit an otherwise highly similar differentiation hierarchy.[62] The hypothesis of a tree-like hierarchy model differentiates between *short-term* (ST) and *long-term* (LT) HSCs due to their expression level of CD34. ST-HSCs are suggested to have a reconstitution ability of less than 1 month upon which they are able to differentiate into *multipotent progenitors* (MPP) with no self-renewal capacity.[63] In a first bifurcation, MPPs are able to differentiate into a *common myeloid progenitor* (CMP) on the one hand, from which in turn, depending on the transcriptional as well as paracrine activation, *granulocyte-macrophage progenitors* (GMP) as well as *megakaryocyte-erythroid*

progitors (MEP) emerge. On the other hand, MPPs can give rise to *common lymphoid progenitors* (CLP), which only display lymphoid potential and differentiate into mature B- and T-cells.[64-66]
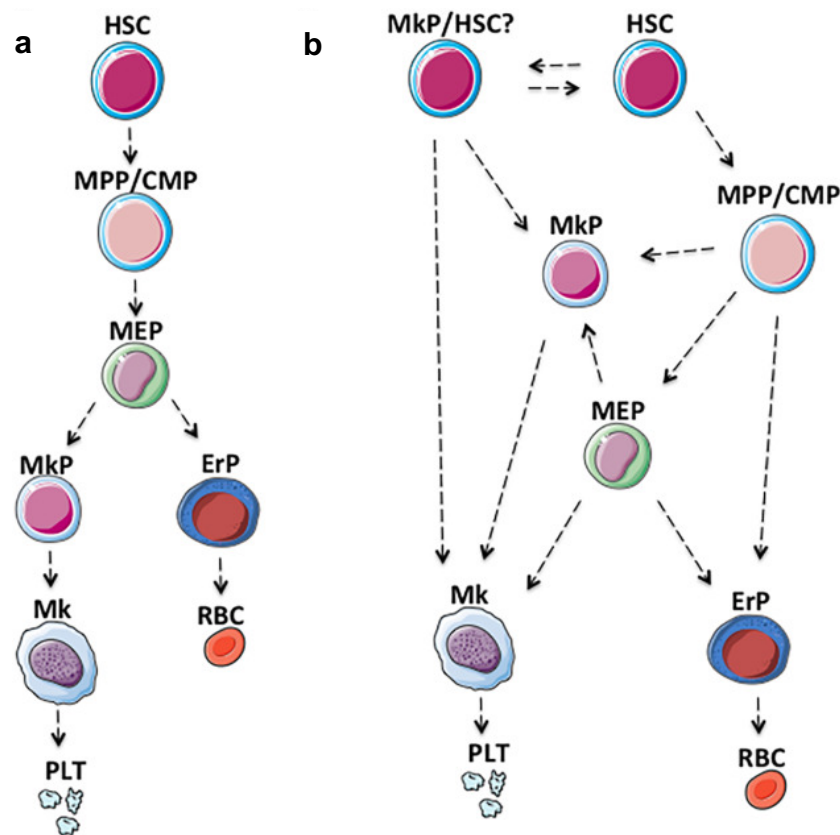
Figure 3. Models of hematopoietic differentiation. (**a**) HSCs with self-renewal potential differentiate into MPPs, from which MEPs emerge, which divide into megakaryocyte (MkP) and erythroid precursors (ErP). (**b**) New studies hypothesize MKs to be able to either emerge directly from HSCs or from earlier MkPs without undergoing the MPP stage. Xavier-Ferrucio & Krause, **Stem Cells**, 2018.[67]

Recent publications challenge the assumption of an hierarchical lineage tree based on the identification of heterogeneous HSC subpopulations with different contributions to hemato-poiesis[68] and the observation of lineage-restricted progenitors with self-renewal capacity (Figure 3b).[69] These findings are now supported by advances in single-cell omics analyses of HSCs, which are further unraveling distinguished HSC subpopulations.[70] Moreover, myeloid and more specifically *megakaryocyte* (MK) lineage commitment is still controversially discussed mainly due to the identification of *von Willebrand Factor* (vWF)[+] HSC subsets with a strong platelet-bias as well as the presence of CD41^{+} LSK cells, which might be important during inflammatory settings in order to maintain physiological platelet counts (Figure 3b).[71-73] Although several publications propose a high similarity between HSCs and MK progenitors, thus suggesting a more linear and direct link between both, the classical hypothesis of MK progeny proposes differentiation of MEPs into MKs and erythroblasts (Figure 3a).[74] Although the so far used surface marker expression to distinguish MEPs is not valid anymore, since

isolation of these CD34^{-}Lin[-]c-Kit^{+}Sca^{-}FcγR^{low}IL-7Ra^{-} cells mainly gives rise to erythroid progenitors,[75,76] it is widely accepted that both erythroid and MK progenitors are dependent on the activation of several critical *transcription factors* (TF). While the ETS family TF PU.1 is essential to maintain myeloid fate progenitors, the zinc-finger *GATA-binding factors* (GATA) 1 and 2 have been identified to be indispensable for MK and erythroid differentiation. It is established now that both proteins are dependent on their binding partner *friend of GATA-1* (FOG-1), which was first identified to selectively bind to GATA-1 by two-hybrid screenings.[77] The interaction between GATA-2 and FOG-1 precedes GATA-1/FOG-1 binding, which is in line with a proposed reversal of transcriptional output during differentiation (GATA-switch) leading to silencing of GATA-2 activity by GATA-1.[78,79] While GATA-2 has been shown to promote megakaryopoiesis, GATA-1 is primarily required for erythroid differentiation, albeit also being indispensable for the expression of a plethora of MK-specific genes in later stages suggesting a distinct spatiotemporal control of transcriptional activity.[80,81] RUNX1 directly induces the activity of the MK-specific TF *friend leukemia integration* (Fli) 1 by repressing the expression of the erythroid-inducing *Krueppel-like factor* (KLF) 1 and is further required for the induction of polyploidization in maturing MKs.[82,83] Nonetheless, although many steps of terminal MK differentiation have been elucidated so far, defining specific functional outcomes for loss of single TFs is complicated, since most serve as both transcriptional activators and repressors and can act in multiple combinations.[84]

1.2.3 Megakaryopoiesis

Due to the high specificity of MKs as platelet precursors as well as their distinct morphology, MK maturation is a strikingly organized process in order to guarantee proplatelet release and subsequent platelet maturation within the vasculature.[85] Transcriptional activation or repression necessary to drive MK-lineage differentiation is highly dependent on paracrine signaling mainly induced by a variety of cytokines. The most prominent cytokine to induce MK maturation is *thrombopoietin* (TPO), which is produced by both liver parenchymal as well as endothelial cells and signals via binding to its receptor *myeloproliferative leukemia protein* (c-Mpl) on MKs first described by several groups in 1994.[86,87] Accordingly, deficiency in either TPO or c-Mpl results in overall affected hematopoiesis, but most importantly in dramatically reduced MK counts along with severe thrombocytopenia.[88] Interestingly, *c-Mpl*^{-/-} and *Tpo*^{-/-} mice exhibited a marked reduction in progenitor cell numbers, since TPO is further able to directly stimulate HSC proliferation, thus additionally affecting the overall capacity to maintain a physiological amount of colony-forming units.[88] Of note, plasma TPO levels are inversely correlated with the respective platelet count due to an autoregulatory feedback loop involving

interaction of platelet c-Mpl with TPO thus reducing the amount of available TPO in the circulation and *vice versa*.[89,90]
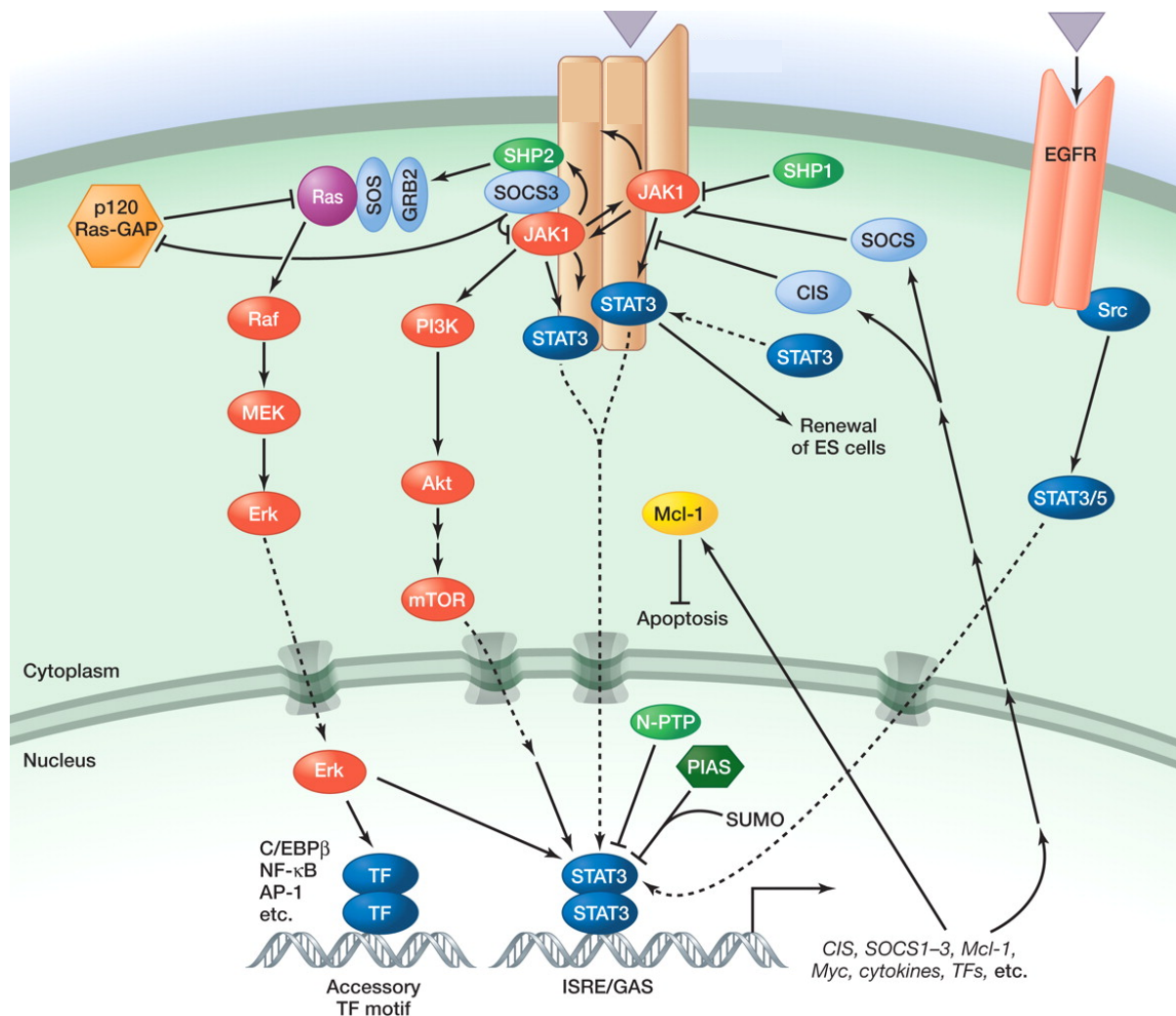
Figure 4. TPO-induced signaling cascades. Binding of TPO to its receptor c-Mpl induces JAK2 phosphorylation leading to the recruitment and subsequent activation of STAT3 and 5, which serve as TFs for the activation of MK-specific genes. C-Mpl phosphorylation further recruits the phosphatases Shp1 and 2, which in turn presumably inhibit STAT activation. Harrison, **Cold Spring Harb Perspect Biol**, 2012.[91]

TPO binding to c-Mpl induces homo-dimerization of the receptor, which in turn supports the transphosphorylation and subsequent activation of *janus kinase* (JAK) 2, which is the predominant isoform expressed in MKs. JAK2 not only phosphorylates the receptor itself, thus allowing for the binding of SH2-domain-containing proteins, but further activates the latent TFs *signal transducers and activators of transcription* (STAT) 3 and 5 (Figure 4). Moreover, TPO binding activates *protein kinase* (PK) C, *phosphoinositide 3-kinase* (PI3K) as well as *mitogen-activated protein kinases* (MAPK) such as *extracellular signal-regulated kinases* (ERK) 1 and 2, which are involved in the induction of a plethora of genes important for MK maturation.[92] While most of the phosphorylated proteins are involved in activatory

pathways, JAK2 activity also induces the phosphorylation and subsequent activation of *SH2-domain-containing protein tyrosine phosphatase* (Shp) 2, which fulfils ambivalent roles in the regulation of JAK/STAT signaling, since it has been shown to dephosphorylate both STAT3 and 5, despite also being involved in the stabilization of STAT5 phosphorylation.[93]

One important feature of mature MKs is TPO-driven polyploidization mainly induced by cycles of DNA replication without subsequent cell division - a process termed endomitosis - which culminates in polyploidy of up to 128n (Figure 6B). Several groups were now able to identify defective formation of the cleavage furrow during cytokinesis to account for the lack of cell separation.[94] It is hypothesized that the increased DNA content is mostly important for the generation of proteins and subsequently granules, which are indispensable for proper platelet function. This is supported by the notion of absent granule formation in immature 2-4n MKs, suggesting insufficient packaging therein.[95] A second feature of MK morphology is the formation of an elaborate membrane system, the so-called *invaginated* or *demarcation membrane system* (IMS/DMS), which later serves as a membrane reservoir for the generation of proplatelets. It is proposed to emerge from areas of the plasma membrane rich in the platelet-specific GPIb-V-IX complex, upon which it first locates to the middle of the cell, where it associates with the Golgi complex, which, together with the endoplasmic reticulum and the plasma membrane, delivers lipids thus allowing for the generation of a highly complex system of membrane invaginations.[96] In addition to lipid delivery, its formation further relies on *filamentous* (F-) actin rearrangements induced in response to *phosphatidylinositol-4,5-bisphosphate* (PIP$_2$) signaling.[97] A third prerequisite for platelet generation is the assembly of multiple types of granules, most importantly α-granules, dense granules and lysosomes. While dense granules mainly store calcium, adenine nucleotides and polyphosphates, α-granules contain a huge variety of (anti-)angiogenic proteins, growth factors, adhesion and activation proteins, which are essential for platelet activation. Patients with mutations in the *Neurobeachin-like 2* (*NBEAL2*) gene encoding for a protein crucially involved in membrane trafficking develop the *gray platelet syndrome* (GPS), a rare bleeding disorder characterized by defective α-granule biogenesis, which could be recapitulated in *Nbeal2$^{-/-}$* mice, thus highlighting the importance of α-granules for platelet function.[98,99]

1.2.3.1 Megakaryocyte cytoskeleton

Mature MKs have to undergo constant cytoskeletal rearrangement required for the efficient release of proplatelets into vessel sinusoids in order to maintain platelet counts of up to 1000 x 10^3 platelets per µL blood in mice.[100] MKs contain three types of cytoskeletal components: the actin cytoskeleton, microtubules and intermediate filaments, which are all interconnected by cytoskeletal integrators such as spectrins.

Double-helical F-actin filaments, which are of about 7 nm in diameter, are assembled from a pool of *globular* (G) actin monomers. Due to differences in G-actin affinity, F-actin assembly only occurs at the barbed (+)-end, while it is predominantly depolymerized at pointed (-)-ends. Three different G-actin monomer isoforms have been identified in mammals, of which only β- and γ-actin are present in MKs, while α-actin is exclusively expressed in muscle tissue.[101] At concentrations ranging between 50 and 200 μM, actin is among the most highly expressed proteins in murine MKs and platelets and accounts for up to 15% of the total protein pool.[102] Actin assembly requires both the formation of a polymerization-competent nucleus as well as polymerization, with nucleation being the rate-limiting step. G-actin monomers are able to bind *adenosine di-* (ADP) or *tri-phosphate* (ATP) in the presence of divalent cations such as calcium, but only ATP-bound G-actin is assembled into the growing barbed end. During the association of new subunits, ATP is hydrolyzed into ADP and phosphate, which happens with a significant delay after subunit addition and favors dissociation from the complex.

In order to prevent rapid polymerization at barbed ends, small actin monomer-binding proteins control guided depolymerization at pointed ends as well as assembly at barbed ends. First and foremost, barbed end polymerization is constantly prevented by the presence of *capping proteins* (CP). The actin sequestering proteins *profilin 1* (Pfn1) and *thymosin β4* (Tβ4) on the other hand compete for the binding of free G-actin leading to a shuttling of proteins due to a high dissociation constant (Figure 5a). Pfn1 is able to catalyze the nucleotide exchange from ADP to ATP, thus allowing for polymerization of the filament at the barbed end, while the main function of Tβ4 is the sequestration of free actin monomers, thus inhibiting actin polymerization.[103,104] Interestingly, *Pfn1*$^{-/-}$ MKs and platelets exhibit altered F-actin dynamics, but further display increased microtubule stability, thus emphasizing the strong link between the different cytoskeletal compartments.[105]

Actin nucleation in already formed filaments is on the one hand enabled by the activity of the formin *mammalian diaphanous* (mDia) 1 or *adenomatous polyposis coli* (APC), which are both able to prevent barbed end capping by CPs, thus, in addition to facilitating nucleation, further accelerating Pfn1-dependent actin polymerization.[106] On the other hand, actin daughter filament growth is highly dependent on the *actin-related protein* (Arp) 2/3 complex, which is only functional upon additional binding of at least two nucleation-promoting factors of the *Wiskott-Aldrich syndrome family* (WAS).[101] The intrinsic inactivity of these proteins is overcome by Rho-family GTPases and SH3 domain proteins, which, in the presence of phosphoinositides, relieve the autoinhibition of the WAS proteins.[107] In contrast to these proteins favoring actin assembly, actin depolymerization at pointed ends is mainly dependent

on the actin-severing proteins *cofilin 1* (Cof1) and *actin-depolymerizing factor* (ADF) (Figure 5a). Cof1 binds to actin-filaments upon hydrolysis of ATP to ADP-phosphate (P_i) and the subsequent release of P_i during filament growth and induces a twist in the filament, which weakens lateral and longitudinal binding, but does not directly induce dissociation of G-actin monomers.[108,109] While global deficiency in the ubiquitously expressed Cof1 is embryonic lethal, MK- and platelet-specific Cof1/ADF double-deficient mice exhibited severe macrothrombocytopenia due to virtually abolished *proplatelet formation* (PPF).[110] Activity of Cof1 is mainly regulated by *LIM kinase* (LIMK)-dependent phosphorylation, which inhibits actin severing in the resting state. Actin binding by Cof1 is enabled due to the presence of one *ADF homology domain* (ADF-H) enabling binding to both G- and F-actin.

Twinfilins (Twf) contain two ADF-H domains, which is thought to restrict their binding to monomeric G-actin. Three Twf isoforms have been identified in mammals, but only Twf1 and Twf2a are present in murine MKs and platelets. In yeast as in mammals, Twfs have been identified in areas of high actin turnover, where they interact with CPs as well as induce filament depolymerization upon association with *cyclase-associated proteins* (CAP).[111,112] Combined *in vivo* deficiency in Twf1 and either Cof1 or Pfn1 in yeast resulted in synthetic lethality suggesting that Twfs are involved in actin sequestration and severing.[113] Recent findings supported the notion of Twf1 being involved in actin severing, since treatment of yeast carrying mutations in either Cof1 or Twf1 with latrunculin A, which prevents actin polymerization, resulted in a longer maintenance of visible actin structures in both mutants thus suggesting impaired severing and subsequent depolymerization.[114] Global deficiency in Twf2a did not influence normal development in mice, which led to the conclusion that it is dispensable for embryogenesis, since its function might be compensated by the presence of Twf1.[115] Additional analyses of *Twf2a$^{-/-}$* mice revealed a mild macrothrombocytopenia caused by accelerated platelet clearance in the spleen and aberrant Cof1 and Pfn1 phosphorylation leading to increased platelet reactivity *in vitro* and *in vivo*, thus highlighting its importance for proper platelet functions.[116] The role of Twf1 nonetheless remained to be elucidated, since an MK- and platelet-specific deficiency did not impair platelet reactivity or actin dynamics *in vitro*.

All small actin-binding proteins are regulated by a variety of upstream signaling molecules, particularly those belonging to the Rho GTPase family, which cycle between an active (GTP-bound) an inactive (GDP-bound) state. Among these, *Ras homologue family member A* (RhoA) has been shown to control mDia1, *myosin light chain* (MLC) 2 as well as *Rho kinase* (ROCK) 2 phosphorylation and MK- and platelet-specific RhoA-deficient mice exhibited macrothrombocytopenia.[117] In contrast, *Ras-related C3 botulinum toxin substrate* (Rac) 1 is

an important activator of the WAVE complex, which is in turn required for Arp2/3 activation and thus regulates actin nucleation processes. Accordingly, platelets deficient for Rac1 were unable to form lamellipodia due to disabled F-actin branching.[118] A third Rho GTPase, *cell division control protein 42 homolog* (Cdc42), was shown to not only govern LIMK activity, but to further be indispensable for DMS formation as well as to share functions with Rac1.[118,119] Moreover, a RhoA/Cdc42 regulatory circuit was identified to regulate MK polarization and endothelial transmigration *in vivo*.[120]

Actin dynamics are not only essential to maintain cell shape, but are further required for a plethora of processes such as migration, motility, filopodia- and lamellipodia formation as well as penetration of the basal membrane required for the release of proplatelets from MKs. Actin polymerization upon activation increases the amount of F-actin from 40 to 50% in resting cells to up to 70% within seconds, thus highlighting the rapidity of actin treadmilling. Of significant importance for the functional generation of proplatelets *in vivo* is the formation of podosomes, actin-rich structures that have been proposed to be essential for the degradation of *extracellular matrix* (ECM) proteins, which facilitates the extension of proplatelets through the basement membrane.[121] Podosomes are organized into a core, characterized by a high actin density interconnected by WASp-activated Arp2/3, and a ring, in which vinculin and talin-1 are hypothesized to attach the cytoskeleton to the plasma membrane as well as to the adjacent ECM. Interestingly, defective podosome assembly in MKs lacking the actin regulatory protein *adhesion and degranulation-promoting adaptor protein* (ADAP) has been associated with loss of directed PPF *in vivo*, which further underlines the significance of podosomes for MK functionality.[122]

Microtubules are protofilaments consisting of heterodimers that can be assembled upon dimerization of GTP-bound α- and β-tubulin. The main isoform present in mature MKs and platelets is β1-tubulin. Thirteen of these heterodimers can laterally align into hollow tubes of 24 nm diameter with a fast polymerizing plus-end and a slow polymerizing minus-end. Microtubules are in a constant state of assembly and disassembly termed dynamic instability, which is maintained by a constant exchange of ADP- to ATP-bound heterodimers (Figure 5b). Lack of substitute ATP-tubulin results in an accumulation of ADP-bound tubulin at the plus-end leading to a rapid depolymerization termed 'catastrophe'.[123] Microtubule depolymerization is further promoted by proteins of the stathmin family, which additionally prevent heterodimer polymerization. In contrast, *end-binding proteins* (EB) stabilize heterodimers as well as protofilaments, thus preventing rapid depolymerization upon GTP hydrolysis (Figure 5b). Interestingly, several proteins primarily associated with actin rearrangements have been shown to associate with microtubules as well. *Pfn1*^{-/-} mice display

increased microtubule stability, which is manifested as a Wiskott-Aldrich-Syndrome-like phenotype. Deficiency in Rac1 and Cdc42 similarly affects microtubule stability, thus suggesting a close link of both cytoskeletal departments, which is at least partly regulated by mDia1 and APC, which have not only been shown to associate with nucleating actin fibers, but are further involved in stabilizing microtubules by interacting with EB1.[124]
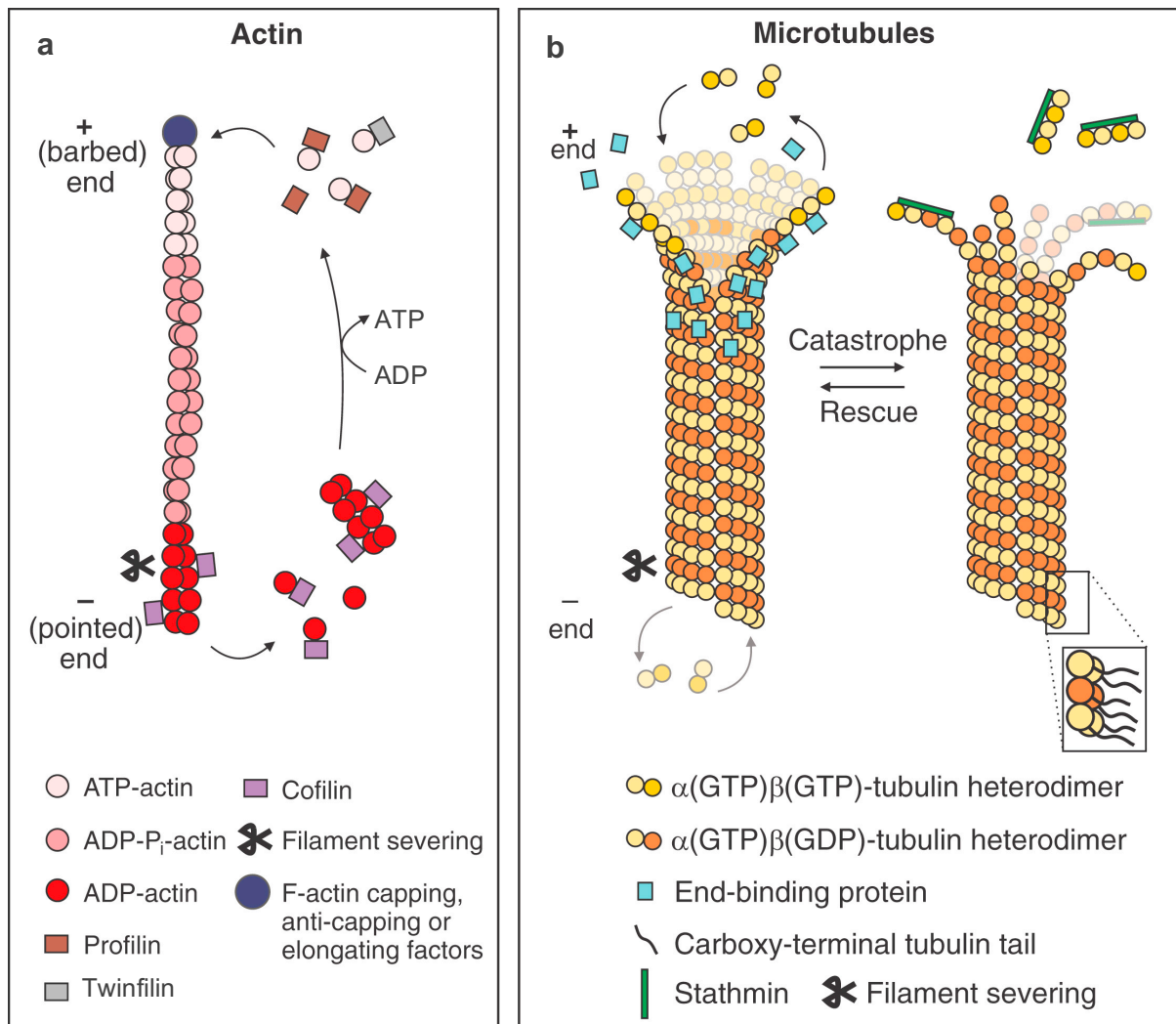
Figure 5. Simplified models of F-actin and microtubule dynamics. (**a**) G-actin monomers are sequestered by Pfn1, Tβ4 and Twf. Pfn1 enables nucleotide exchange from ADP to ATP, which allows polymerization of F-actin filaments at the barbed end. Depolymerization is inhibited by CPs. ATP is hydrolyzed in the growing filament until phosphate is released, which allows for binding of the actin-severing protein Cof1 at the pointed end. Severing and depolymerization are both thought to be regulated by Twfs. (**b**) Microtubule protofilaments consisting of αβ-tubulin heterodimers are in a state of dynamic instability, which is held upright in the presence of GTP-bound tubulin. The fast-growing plus end is stabilized by EBs, while stathmins induce heterodimer depolymerization. Modified from: Coles & Bradke, **Curr Biol**, 2015.[125]

Microtubule longevity and stability are mainly regulated by posttranslational modifications, above all by alterations at the C-terminus of α-tubulin. One important posttranslational alteration is the removal of the terminal tyrosine residue on α-tubulin, a process carried out by the carboxypeptidase complex vasohibin 1/VASH binding protein.[126] Although detyrosi-

nation of microtubules does not intrinsically alter their stability, it governs microtubule-binding proteins to the faster polymerizing plus-end, which remains tyrosinated and is therefore thought to be a site of faster microtubule turnover with an accelerated dynamic response.[127] Although EB1 binding does not require tyrosination of α-tubulin, the subsequently recruited *cytoplasmic linker protein* (CLIP) 170 only interacts with EB1 in the presence of tyrosinated tubulin.[128,129] The exact role of tubulin acetylation on Lys40 of α-tubulin, carried out by tubulin actyltransferases, still remains controversially discussed, but the identification of enhanced levels of both acetylated and detryosinated microtubules upon experimental stabilization using the toxin paclitaxel suggests increased tubulin longevity upon acetylation as well.[130]

1.2.3.2 Proplatelet formation

Proplatelets are released from a single region of mature MKs, in which a pseudopod crosses the endothelial barrier of BM sinusoids, tapers into a tubule and elongates into a 100 to 500 µm long proplatelet shaft (Figure 6D). An unperturbed maturation of the DMS is essential to guarantee PPF from mature MKs. Since the actin cytoskeleton is markedly involved in guiding DMS formation, defective actin rearrangements due to deficiency in actin-regulatory proteins have been associated with impaired PPF. This was most evident upon lack of ADF/Cof1 from murine MKs resulting in virtually abolished PPF *in vivo* due to a highly perturbed F-actin reorganization.[110] Moreover, impaired podosome formation has been associated with decreased PPF *in vivo*, since podosomes have been proposed to be essential for the degradation of ECM proteins in order to allow for proplatelet elongation into vessel sinusoids.[121] This is in line with reduced and misguided PPF from MKs lacking the actin-regulatory protein ADAP, thus suggesting podosomes to be of significant importance for PPF.[122] In addition, actin branching is suggested to be essential for proplatelet elongation by increasing the amount of available proplatelet tips, which is supported by the observation of reduced tip numbers upon treatment of MKs with the actin polymerization-blocking toxin cytochalasin.[100]

Although F-actin appears to be critical for endothelial barrier crossing and proplatelet branching, the microtubule cytoskeleton is the main driver of PPF, since drugs inducing microtubule disassembly such as colchicine or nocodazole fully block platelet generation.[131] By using fluorescently labeled EB3, studies were able to show that microtubules polymerize throughout the proplatelet shaft into both directions and drive elongation at a rate of 0.85 µm min^{-1}. Interestingly, microtubule bundles align in the proplatelet shaft, but instead of ending abruptly at the tip, they reenter the shaft, thus allowing for a sliding of neighboring protofilaments, which is essential for proplatelet elongation and is dependent on the motor protein dynein (Figure 6D). In contrast, microtubule polymerization appears to be

dispensable for shaft elongation, since treatment with microtubule assembly inhibitors such as nocodazole did not affect the rate of proplatelet elongation.[132] Furthermore, elongation does not occur continuously, but rather happens in bursts including pausing and retracting of the growing protrusion.[133]
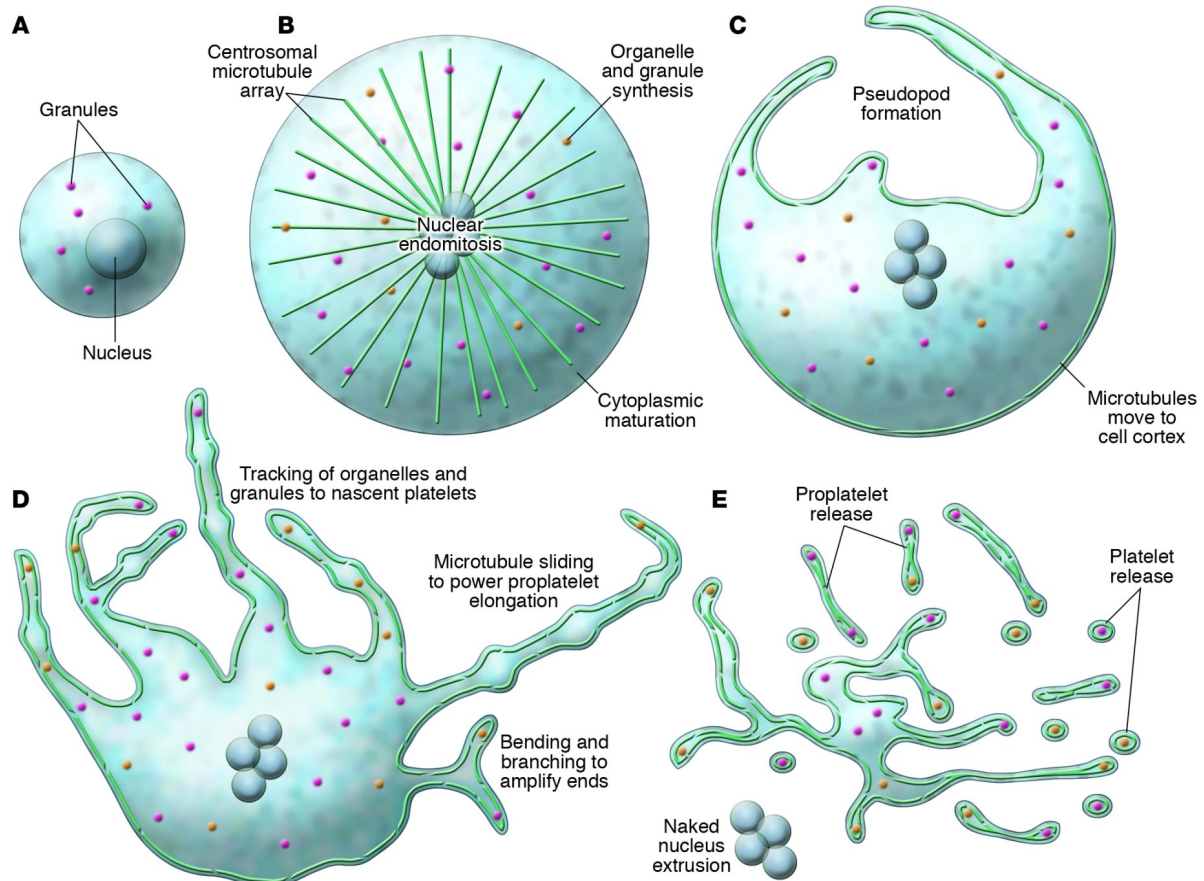
Figure 6. Mechanisms of proplatelet formation. (**A**) MKs mature from HSCs in a microtubule- and actin driven process including DMS maturation and endomitosis (**B**). (**C**) Actin-driven pseudopod formation through the endothelial lining enables guided PPF into vessel sinusoids. (**D**) Kinesin-dependent granule transport along elongating microtubule bundles is necessary for proper platelet function. Proplatelet shaft elongation is highly dependent on microtubule sliding. (**E**) Released preplatelets further mature into platelets within the sinusoids. MK nuclei are degraded. Patel *et al*., **J Clin Invest**, 2005.[134]

Platelets are exclusively released from the tip due to the aforementioned reentry of micro-tubules into the nascent shaft, thus forming a ring-like structure reminiscent of the peripheral microtubule coil observed in resting platelets. In addition to their role in shaft elongation, microtubules are further essential for the transport of granules and mitochondria into the emerging platelets, a process dependent on the motor protein kinesin.[135] The released preplatelets further mature in the vasculature in a shear-dependent process leading to the generation of mature platelets (Figure 6E).

1.2.4 Bone marrow disorders

1.2.4.1 Myelofibrosis

Fibrosis of the BM is characterized by an increased deposition of reticulin and collagen fibers in the BM and is mostly associated with clonal hematopoietic disorders. The most common myeloproliferative neoplasms causative for BM fibrosis in humans are polycythemia vera, essential thrombocytosis and *primary myelofibrosis* (PMF), all of which have been associated with activating mutations in JAK2, calreticulin or c-Mpl.[136] The high incidence JAK2[V617F] mutation induces constitutive JAK2 signaling leading to constant transcriptional activation via STAT molecules. Although the JAK2 inhibitor ruxolitinib is used in clinical trials and appears to have disease-modifying properties, progression of myelofibrosis is not fully averted, which suggests that additional signaling molecules are involved in disease onset.[137] Egress of mutated HSCs from the BM and relocation to secondary hematopoietic organs such as spleen and liver induces extramedullary hematopoiesis and splenomegaly, both of which have been associated with increased morbidity.[138] Strikingly, transgenic mice expressing mutated JAK2 under the vav-promoter, which drives expression in most hematopoietic cells, develop a PMF-like phenotype, thus undermining its importance in disease progression.[139]

PMF pathogenesis has been closely linked to aberrant activity of MKs, since they are not only involved in the maintenance of HSC quiescence by regulating BM niche homeostasis, but are further highly dependent on TPO-induced JAK2 signaling.[140] *In situ* analysis of PMF clusters revealed a markedly increased abundance of immature MKs surrounding fibrotic areas, which prompted the hypothesis of premature and aberrant granule release to promote tissue fibrosis.[141] In addition to a possible release of extracellular vesicles, which might participate in immune cell communication and activation, mature MKs further contain a plethora of proinflammatory and profibrotic cytokines that may be causative for tissue degeneration (Figure 7).[142] Besides PDGF, VEGFA and *platelet factor 4* (Pf4), increasing evidence suggests TGFβ1 to be of specific importance for PMF progression, since it is released as a latent precursor molecule and might become activated due to pathogenic changes in the BM environment and is able to induce fibrosis organ-independently.[143] Strikingly, TGFβ1 does not only increase collagen and proteoglycan synthesis, but further inhibits *matrix metalloproteinase* (MMP) activity, while actively supporting the upregulation of *tissue inhibitors of metalloproteinase* (TIMP).[144] Additional verification for an involvement of TGFβ1 on disease progression comes from several mouse models displaying myelofibrosis of the BM. Two widely used models are TPO-treated *wildtype* (*WT*) mice as well as mice lacking the distal GATA-1 promoter and the first enhancer of GATA-1 transcription being replaced with a neo-cassette, which induces a severe reduction in GATA-1 expression

(*Gata1*^{low}).[145] TPO-treatment of *WT* mice induces a myeloproliferative syndrome and enhanced reticulin fiber deposition in the BM, which could be reverted upon engraftment of *Tgfb1*^{-/-} cells, thus emphasizing the role of the cytokine during PMF progression.[146,147] In contrast to TPO-treated *WT* mice, reduced GATA-1 levels in MKs of *Gata1*^{low} mice block maturation, which leads to an accumulation of immature MKs in the BM. In contrast to *WT* mice, TPO treatment in *Gata1*^{low} mice is able to restore GATA-1 levels, thus decreasing TGFβ1 secretion, which ameliorated the onset of myelofibrosis.[146]
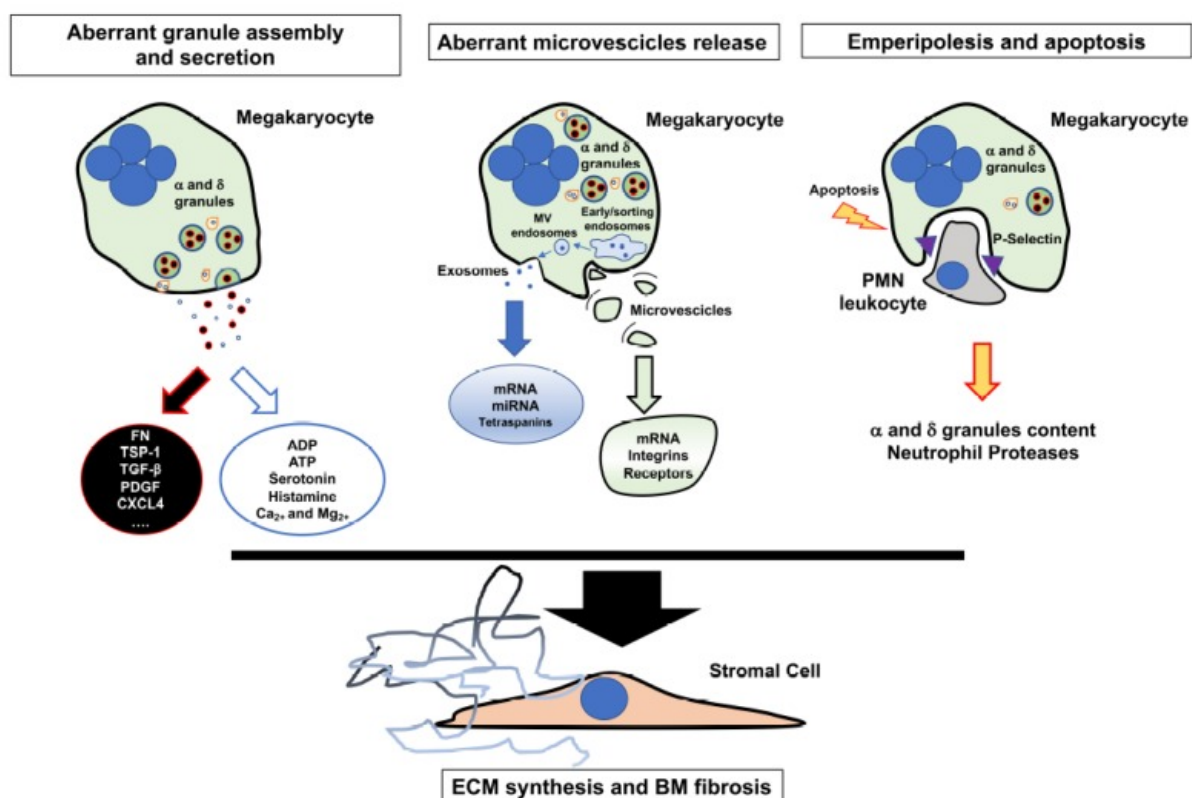
Figure 7. MK involvement in the progression of myelofibrosis. MK accumulations have been associated with anaggravation of myelofibrosis, since MKs contain a plethora of proinflammatory and profibrotic molecules (most importantly TGFβ1) that can be released upon granule secretion. Neutrophil emperipolesis induces enhanced apoptosis on the one hand and uptake of neutrophil membranes on the other hand, which in turn might further affect BM homeostasis through microvesicle release. Malara *et al.*, **Mediterr J Hematol Infect Dis**, 2018.[142]

These findings suggest TGFβ1 release to occur independently of MK maturation, but to be highly significant for the pathogenesis of BM fibrosis, which is additionally underlined by findings from PMF patients displaying increased TGFβ1 levels in platelets.[148] Of note and in addition to their myelofibrotic phenotype, *Gata1*^{low} mice also exhibit a severe thrombocytopenia due to insufficient PPF from immature MKs as well as a markedly increased engulfment of neutrophils ('emperipolesis') into immature MKs, which is a hallmark of myelofibrosis observed in the BM of PMF patients as well (Figure 7).[149,150] Several other mouse models lacking molecules essential for MK maturation or signaling have further been

shown to develop myelofibrosis, thus highlighting the significant contribution of aberrant MK function on disease progression.[151-153] Among these, deficiency or mutations in *MK and platelet inhibitory receptor G6b-B* (*Mpig6b*) have been shown to cause megakaryocytosis and myelofibrosis in mice and humans, the underlying mechanism nonetheless is so far unresolved.[154,155] Of note, G6b-B has also recently been identified as a biomarker of severe PMF in patients carrying JAK2 mutations as well as in other clonal hematopoietic disorders, suggesting it to be highly relevant during disease progression.[156]

1.2.4.2 Bone remodeling disorders

Since myelofibrosis is associated with significant changes within the whole hematopoietic BM environment, it comes as no surprise that osteoclast and osteoblast behavior is often affected in patients suffering from *chronic idiopathic myelofibrosis* (IMF) or PMF. Osteosclerosis is characterized by a dramatic increase in trabecular or cortical bone thickness resulting in loss of BM cellularity due to impaired osteoclast-mediated bone degradation or enhanced osteoblast-induced bone formation. Osteosclerosis in IMF patients has been linked to increased osteoprotegerin release by endothelial cells, thus inhibiting bone resorption by osteoclasts due to impaired sRANKL signaling.[157] Interestingly, increased bone formation has also been observed in several myelofibrotic mouse lines lacking MK-specific signaling molecules or receptors. Most prominently, mice lacking the TPO receptor c-Mpl specifically in MKs and platelets develop dramatic osteosclerotic bone alterations, in addition to a severe megakaryo- and thrombocytosis.[153,158] Of note, the progression of osteosclerosis appeared to be sex-dependent with females showing accelerated bone formation compared to male littermates, possibly due to increased estrogen levels in female BM.[159] Strikingly, similar observations of increased bone formation were also made in *Gata1^{low}* mice, which displayed a 2- to 3-fold increase in cortical as well as trabecular bone volume compared to control animals. Interestingly and in contrast to PMF patients, the observed osteosclerosis in *Gata1^{low}* mice was observed prior to the onset of myelofibrosis and was not induced by impaired osteoclast-dependent bone resorption, but rather caused by increased MK-mediated osteoblast proliferation.[160] This hypothesis was further supported by a recent study, describing enhanced osteoblast proliferation albeit unaltered differentiation upon co-incubation of osteoblasts with conditioned MK medium, thus ruling out direct cell-to-cell contacts to account for the observed increase.[161] Interestingly, the pro-proliferative effect on osteoblasts seems to be at least partly driven by TGFβ1, which is in line with increased TGFβ1 levels in the BM of myelofibrotic and osteosclerotic mice.[162] Moreover, MK-conditioned medium inhibited osteoclastogenesis, thus further implying a role of MKs in preventing bone resorption in addition to promoting bone formation.

While osteosclerotic bone lesions are rare disorders and are often secondary to myelofibrosis, osteoporosis, loss of trabecular bone and subsequent fragility fractures, is a high-incident disease affecting 25% of post-menopausal women over the age of 65. Disease progression is multicausal, but appears to be initiated by an imbalanced bone resorption to bone formation ratio mainly due to estrogen deficiency, which in turn results in reduced ERα expression levels in osteoblasts.[163,164] Interestingly, estrogen has also been shown to induce osteoclast apoptosis by increasing osteoblast-mediated release of TGFβ1 suggesting that reduced estrogen levels might impair TGFβ1-dependent osteoclast apoptosis leading to an additional increase in bone resorption.[165] In addition to age- and sex-related osteoporosis, the disease can also be caused by allelic variants of genes encoding for ERs, IL-6 or the vitamin D receptor.[166] The role of MKs in osteoporosis is still controversially discussed. Several studies identified an increased amount of MKs in the BM of estrogen-treated postmenopausal women, thus implying estrogen to be involved in MK proliferation or maturation.[159] This is in line with a recent study linking ERβ-mediated GATA-1 upregulation to increased MK polyploidization and cytoskeletal maturation.[167] Furthermore, autocrine release of estradiol from MKs has been associated with increased PPF suggesting the hormone to be relevant for MK maturation and functionality.[168] Nonetheless, many links associating aberrant MK functionality to bone remodeling disorders are still missing.

1.3 Platelets

Platelets are small anucleate cell fragments mainly responsible for the maintenance of hemostasis that are constantly produced by BM MKs. Normal platelet counts range from 150 to 400 x 10^3 platelets μL^{-1} in humans to up to 1000 x 10^3 platelets μL^{-1} in mice with an average diameter of 3-4 µm (humans) or 1-2 µm (mice), respectively. Platelets are circulating for 7-10 days in humans (5 days in mice) after which they are cleared from the circulation by the spleen and Kupffer cells in the liver, in a process dependent on activation of the Ashwell-Morell receptor and macrophage galactose lectin.[169] Most platelets are cleared without ever coming into contact with the thrombogenic ECM. However, upon vessel injury platelets become rapidly activated, change their shape and release their granules, which contain a plethora of angiogenic and proinflammatory molecules as well as coagulation factors. Uncontrolled platelet activation can lead to vessel occlusion and subsequent lack of oxygen supply and tissue damage, e.g. in the course of myocardial infarction or ischemic stroke, which still rank among the leading causes of death worldwide.[170] As mentioned earlier, platelets contain three major granule types: α- and dense granules as well as lysosomes. While dense granules contain bioactive mediators such as calcium, APD, ATP, serotonin and *thromboxane A_2* (TxA$_2$), more than 300 proteins are stored in α-granules (e.g. membrane

proteins such as P-selectin or αIIbβ3 integrins as well soluble proteins such as Pf4 or fibrinogen).[171]

1.3.1 Platelet activation

Initial platelet adhesion upon vessel damage is mediated by the GPIb-V-IX complex, which tethers to vWF bound to exposed collagen within the ECM. In addition to vWF the complex has been shown to interact with P-selectin, *macrophage antigen 1* (MAC1) as well as several coagulation factors. Mutations within either *GPIB* or *GP9* have been shown to cause Bernard-Soulier-Syndrome, a rare bleeding diathesis associated with a moderate to severe thrombocytopenia, thus highlighting the importance of the complex for PPF.[172] Similar observations were made in mice lacking either GPIb or GPIX emphasizing their necessity for complex assembly, while mutations or deficiency in *GP5* have not been associated with disease onset.[173,174] In contrast, *Gp5⁻/⁻* mice exhibit accelerated hemostasis and thrombosis *in vivo* and GPV-deficiency was able to revert bleeding phenotypes in mice deficient for the (hem)ITAM receptors GPVI or CLEC-2, thus suggesting a role of GPV as an antithrombotic molecule upon limited platelet signaling (Beck *et al*., unpublished). Interestingly, GPV contains a cleavage site for the serine protease thrombin as well as the metalloproteinases *a disintegrin and metalloproteinase* (ADAM) 10 and 17 and thus can be released as a soluble molecule upon platelet activation. Strikingly, *soluble* (s) GPV is able to prevent vessel occlusion in murine models of thrombosis, e.g. upon mechanical injury of the abdominal aorta or ferric chloride-induced injury on mesenteric arterioles as well us in ischemic stroke (Beck *et al*., unpublished). In comparison, mice carrying a mutation (R476A) in the thrombin cleavage site of (*Gp5^KIN*) thus specifically lacking thrombin-cleaved sGPV phenotypically resemble the corresponding knockout mice, thus highlighting the relevance of thrombin-mediated cleavage for GPV function. Of note, ADAM-cleaved GPV is still present in these animals.

GPIbα-vWF interactions allow for initial tethering and deceleration of platelets required to enable subsequent cellular activation and firm adhesion to the exposed ECM. Blockade of vWF-binding using Fab fragments of an antibody derivative against GPIbα (p0p/B) protected animals from occlusive thrombus formation, which could be recapitulated in transgenic mice, in which the extracellular domain of GPIbα was exchanged with the human IL4Rα (*IL4R-GPIb-tg*).[175,176] GPIb-mediated deceleration of platelets on the ECM allows for binding of the main collagen receptor GPVI to its ligand. GPVI is non-covalently associated with the ITAM-bearing *Fc receptor* (FcR) γ-chain, which is phosphorylated by the *Src family kinases* (SFK) Fyn and Lyn upon ligand binding (Figure 8). Recruitment of *spleen tyrosine kinase* (Syk) to the phosphorylated ITAM induces activation of the adapter proteins *linker of activated T-cells*

(LAT) and *SH2 domain containing leukocyte protein of 76 kDa* (SLP-76), ultimately culminating in recruitment and phosphorylation of *phospholipase* (PL) Cγ2. PLCγ2 activity in turn drives calcium release from intracellular stores resulting in granule release and integrin activation, thus driving additional platelet recruitment to the site of injury.[177] GPVI deficiency in mice mildly prolonged bleeding times, but led to a significant protection from occlusive thrombus formation, which could be reproduced upon depletion of GPVI from the platelet surface using an anti-GPVI antibody (JAQ1).[178,179] In contrast to the full *immunoglobulin G* (IgG) antibody, F(ab)$_2$ fragments thereof do not cause transient thrombocytopenia or receptor depletion, but a receptor blockade over 4 days.

Firm platelet adhesion and ultimate platelet aggregation is mediated by integrins, αβ-heterodimeric adhesion receptors on the platelet surface. Platelets express three β1 (α2β1, α5β1 and α6β1) as well as two β3 (αIIbβ3 and αvβ3) integrins with affinities towards different ECM proteins.[180] Integrin αIIbβ3, favorably binding to fibrinogen, is the most abundantly expressed integrin in platelets with a copy number of up to 100,000 per cell. Platelet activation (e.g. upon GPVI engagement) induces a conformational change within the integrin from a low- to a high-affinity-state, which enables tight ligand binding ('inside-out' signaling). Ligand binding on the other hand transduces an 'outside-in' signal involving SFK activation, thus further promoting cytoskeletal remodeling culminating in shape change and granule release.[181] Granules in turn contain a plethora of thrombogenic proteins and secondary mediators including ADP (binding to P2Y$_1$ and P2Y$_{12}$), TxA$_2$ (binding to the *thromboxane receptor* (TP)) and thrombin (binding to *protease-activated receptors* (PAR)), which further drive platelet recruitment and activation, fibrin generation and thus thrombus growth. Binding of these secondary messengers to their respective receptors, which mostly belong to the *G-protein-coupled receptor* (GPCR) family, further stimulates integrin activation and granule release. Moreover, thrombin mediates fibrinogen proteolysis, thus increasing platelet aggregation through fibrin crosslinking on the one hand, while also being responsible for the cleavage of GPV, which in contrast appears to counteract fibrin generation and additional thrombin generation. This is supported by the observation of increased fibrin generation in coagulation flow chamber assays upon lack of (s)GPV or antibody-mediated blockade of the receptor (Beck *et al.*, unpublished).

The second ITAM-bearing receptor on the platelet surface, CLEC-2, only harbors a single YxxL motif in its intracellular tail and has been identified as receptor for the snake venom rhodocytin, which induces robust platelet activation upon receptor dimerization and subsequent signaling transduction resembling GPVI-mediated platelet activation.[182] The only known endogenous ligand of CLEC-2 is the type I transmembrane sialoglycoprotein

podoplanin, which is expressed on kidney podocytes, type I lung alveolar cells, LECs as well as certain cancer cells but absent from the vasculature.[183] Nonetheless, CLEC-2 appears to participate in hemostasis, since antibody-mediated depletion using a CLEC-2-specific antibody (INU1) prolonged bleeding times and impaired thrombotic vessel occlusion *in vivo*.[184] Constitutive deficiency in CLEC-2 is embryonic lethal due to severe edema and hemorrhage formation as well as blood-filling of lymphatic vessels.[19] Strikingly, while blood-lymphatic misconnections were also visible upon lack of CLEC-2 specifically in MKs and platelets, conditional mice were viable and born at mendelian ratios. This discrepancy is supported by several studies identifying CLEC-2 to also be expressed on leukocyte subsets, most importantly neutrophils and dendritic cells.[183]
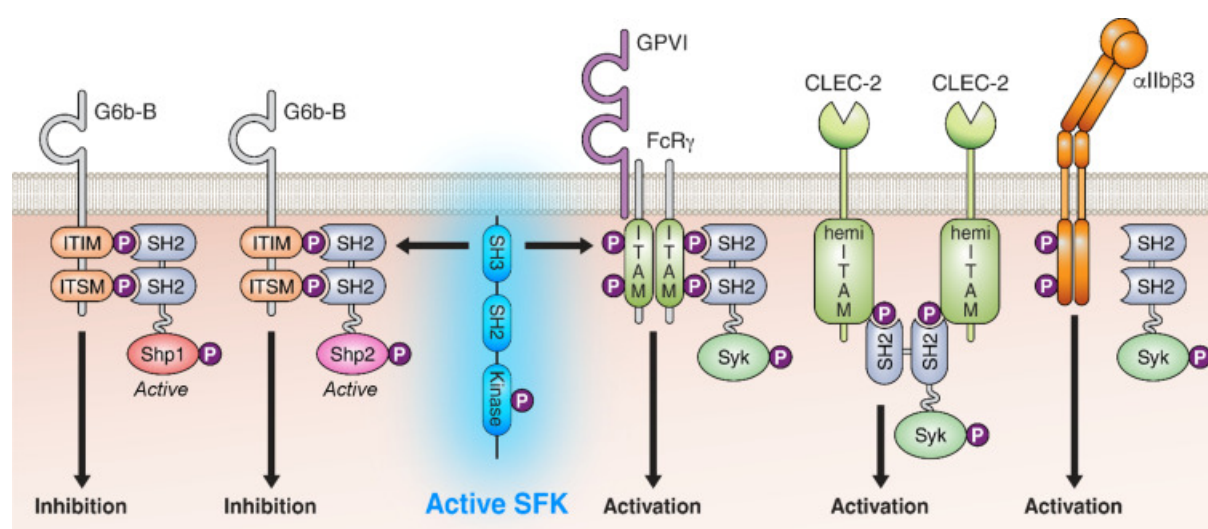
Figure 8. ITIM- and ITAM-signaling in platelets. Both platelet activation as well as inhibition are dependent of SFK-mediated phosphorylation. While G6b-B inhibits platelet activation via recruitment of the tyrosine phosphatases Shp1 and 2, GPVI and CLEC-2 propagate platelet activation via the Syk-PLCγ2 axis. Nagy & Senis, **Platelets**, 4th edition, 2019.[185]

In addition to the aforementioned receptors favoring platelet activation, overshooting aggregate formation is constantly diminished by inhibitory receptors, which either signal via increasing cytosolic *cyclic adenosine* (cAMP) or *guanosine monophosphate* (cGMP) concentrations or carry an *immunoreceptor tyrosine-based inhibition motif* (ITIM) in their intracellular tail. Six ITIM receptors have been identified on the platelet surface with *platelet endothelial cell adhesion molecule* (PECAM) 1, *trem-like transcript* (TLT) 1 and G6b-B being most highly expressed. While PECAM-1 inhibits GPVI-induced platelet activation and the α-granule-specific TLT-1 has anti-inflammatory properties, G6b-B has been shown to be indispensable for both platelet activation as well as PPF *in vitro*.[186] Surprisingly, *G6b-/-* mice exhibited a dramatic macrothrombocytopenia and increased bleeding,[155] findings that could be recapitulated in mice either lacking the G6b-B-associated phosphatases Shp1 and 2 or

carrying a mutation in both its ITIM and its *immunoreceptor tyrosine-based switch motif* (ITSM) (Figure 8).[187,188] Patients with mutations in *MPIG6B* presented with macrothrombocytopenia, bleeding diatheses as well as focal myelofibrosis, a characteristic feature in G6b-B-deficient mice as well (see 1.2.4.1).[154] Recently, perlecan, a heparan proteoglycan, was identified as a ligand of G6b-B inducing robust platelet inhibition via activation of G6b-B in *WT* platelets.[189] Although a lot of research has been focused on elucidating the role of G6b-B in platelet function, its role during MK maturation and PPF regulation still remains elusive.

1.3.2 Platelets in vascular integrity

Many studies were able to establish that platelets are not only essential for the maintenance of hemostasis, but are further crucially involved in the regulation of vascular integrity during embryonic development and under inflammatory conditions. Most focus has been laid on elucidating the role of the (hem)ITAM receptors GPVI and CLEC-2, since initial studies suggested both to be involved in the prevention of inflammatory skin bleeding.[190] Several publications proposed GPVI-depletion and the resulting impaired platelet recruitment to the endothelium to promote endothelial recovery, since atherosclerotic lesion size and neutrophil transmigration were attenuated in GPVI-depleted mice.[191,192] Moreover, a role of GPVI-blockade in inhibiting primary tumor growth by increasing intratumoral hemorrhage was recently identified.[193] These findings suggest platelets to be critically involved in monitoring vascular integrity upon an inflammatory challenge, a process involving GPVI engagement and subsequent platelet activation.

As mentioned above, conditional MK- and platelet-specific CLEC-2-deficient mice develop a severe blood-filling of lymphatic capillaries due to loss of CLEC-2-podoplanin interactions during development. The mechanisms by which CLEC-2 supports lymphatic development are controversially discussed (see 1.1.2). It is on the one hand suggested that CLEC-2 might induce thrombus formation at the cardinal vein upon development of primary lymph sacs or contribute to podoplanin clustering leading to LEC migration.[17] On the other hand, CLEC-2-podoplanin interactions have been proposed to maintain lymphatic vessel integrity throughout life by contributing to microthrombi formation at the lymphovenous junction or by supporting lymphatic valve development in adult mice.[194,195] Whether another ligand might be involved in mediating CLEC-2 functions is still elusive, although recent studies suggested CLEC-2 to be essential for venous integrity during mesenteric vessel development. A transient loss of venous vessel integrity observed in *WT* mice was dramatically impaired in *Clec2⁻ᐟ⁻* embryos leading to an accumulation of *red blood cells* (RBC) in the interstitial space even prior to lymphvasculogenesis.[196] Blood-lymphatic mixing was also observed in a plethora of other mouse models, mostly upon lack of proteins involved in the CLEC-2 signaling cascade, e.g.

SLP-76 and Syk.[197] A recent publication was able to further unravel the distinct function of CLEC-2 during embryogenesis and in adult mice by comparing lymphatic development in inducible and conditional CLEC-2-deficient mouse models.[198] While the presence of CLEC-2 was indispensable to prevent blood-filing of lymph vessels during embryogenesis, its depletion in adult mice did not affect lymphatic integrity, thus implying its negligibility therein during adulthood. Taken together, these findings not only highlight CLEC-2 to be essential for lymphatic development, but further raise the question of a possible intravascular ligand.

2 AIM OF THE STUDY

The contribution of platelet (hem)ITAM receptors in maintaining vascular integrity is widely accepted, however, how CLEC-2 regulates blood-lymphatic vessel separation during development and adulthood is still controversially discussed. In the first part of the thesis, mice lacking CLEC-2 and GPV in the MK and platelet lineage were generated and characterized concerning vascular and lymphatic development. Moreover, vessel morphology and permeability as well as blood-lymphatic separation were assessed in transgenic $Clec2^{-/-}$ mice with an additional mutation within the thrombin cleavage site of GPV to further elucidate the role of sGPV during vascular development.

In the second part of the thesis the role of platelet receptors in the development of OIR was investigated. Since it was previously suggested that platelet granule release is essential for the resolution of ROP in mice, we focused on analyzing, which platelet receptors might be involved in triggering granule release upon experimental OIR and might thus contribute to vasoobliteration and neovascularization.

Reorganization of the actin and microtubule cytoskeleton are essential for functional PPF from mature MKs. The exact mechanisms orchestrating cytoskeletal dynamics during platelet generation are still incompletely understood. In the third part of the study, we investigated how the actin-monomer binding proteins Cof1 and Twf1 regulate both actin and microtubule dynamics in proplatelet-forming MKs *in vitro* and *in vivo*.

Ultimately, we analyzed how a spontaneous mutation within *Mpig6b* encoding the inhibitory receptor G6b-B, affected platelet count, reactivity and function *in vitro* and *in vivo*. Although a role of G6b-B for PPF and the maintenance of BM homeostasis has been proposed in previous studies, the underlying mechanisms linking receptor deficiency to impaired MK functionality are still elusive. To this end, we culminated in analyzing how MK maturation and the BM compartment were affected in G6b-B-mutant mice.

3 MATERIALS AND METHODS

3.1 Materials

3.1.1 Chemicals

Adenosine diphosphate (ADP)	Sigma-Aldrich (Steinheim, Germany)
Agarose	Roth (Karlsruhe, Germany)
Ammonium persulfate (APS)	Roth (Karlsruhe, Germany)
Apyrase (grade III)	Sigma-Aldrich (Steinheim, Germany)
Adenosine triphosphate (ATP)	Fermentas (St. Leon-Rot, Germany)
β-mercaptoethanol	Roth (Karlsruhe, Germany)
Bovine serum albumin (BSA)	Sigma-Aldrich (Steinheim, Germany)
Cacodylate	AppliChem (Darmstadt, Germany)
Calcium chloride	Roth (Karlsruhe, Germany)
Collagen Horm® suspension + SKF sol.	Takeda (Linz, Austria)
Complete protease inhibitors (+EDTA)	Roche Diagnostics (Mannheim, Germany)
Convulxin (CVX)	Enzo Life Sciences (New York, USA)
4',6-diamidino-2-phenylindole (DAPI)	ThermoFisher Scientific (Waltham, USA)
Deoxynucleotide triphosphates (dNTP) mix	Fermentas (St. Leon-Rot, Germany)
Dimethyl sulfoxide (DMSO)	Sigma-Aldrich (Steinheim, Germany)
DyLight-488	Pierce (Rockford, USA)
Ethylenediaminetetraacetic acid (EDTA)	AppliChem (Darmstadt, Germany)
Eukitt® quick-hardening mounting medium	Sigma-Aldrich (Steinheim, Germany)
Enhanced chemiluminescence (ECL) detection substrate	MoBiTec (Göttingen, Germany)
Eosin	Roth (Karlsruhe, Germany)
Ethanol	Roth (Karlsruhe, Germany)
Fentanyl	Janssen-Cilag GmbH (Neuss, Germany)
Fibrinogen from human plasma (F3879)	Sigma-Aldrich (Steinheim, Germany)
Fluorescein-isothiocyanate (FITC)	Molecular Probes (Oregon, USA)
Fluoroshield™	Sigma-Aldrich (Steinheim, Germany
Fluorshield™ with DAPI	Sigma-Aldrich (Steinheim, Germany)
GeneRuler DNA Ladder Mix	Fermentas (St. Leon-Rot, Germany)
Halt protease & phosphatase inhibitor cocktail	ThermoFisher Scientific (Waltham, USA)
High molecular weight heparin	Ratiopharm (Ulm, Germany)
Igepal®CA-630	Sigma-Aldrich (Steinheim, Germany)

Immobilon-P transfer membrane, PVDF	Merck Millipore (Darmstadt, Germany)
Integrilin® (Eptifibatide)	Millennium Pharmaceuticals Inc. (Cambridge, USA)
Isofluran CP®	cp-pharma (Burgdorf, Germany)
Isolectin B4 (biotinylated)	Vector Labs, Inc. (Burlingame, USA)
Isopropanol	Roth (Karlsruhe, Germany)
iTaq Universal SYBR Green Supermix	Bio-Rad (Hercules, USA)
Loading Dye solution, 6x	Fermentas (St. Leon-Rot, Germany)
Magnesium chloride	Roth (Karlsruhe, Germany)
Magnesium sulfate	Roth (Karlsruhe, Germany)
Manganase chloride	Roth (Karlsruhe, Germany)
Medetomidine (Dormitor)	Pfizer (Karlsruhe, Germany)
Methanol	Roth (Karlsruhe, Germany)
Midazolam (Dormicum)	Roche (Grenzach-Wyhlen, Germany)
Midori Green™	Biozym Scientific (Oldenburg, Germany)
Neuraminidase (Sialidase)	Roche Diagnostics (Mannheim, Germany)
Nonidet P-40 (NP-40)	Roche Diagnostics (Mannheim, Germany)
Osmium tetroxide	Merck Millipore (Darmstadt, Germany)
PageRuler® Prestained Protein Ladder	Fermentas (St. Leon-Rot, Germany)
Paraformaldehyde (PFA)	Roth (Karlsruhe, Germany)
Phalloidin-Atto647N	Sigma-Aldrich (Steinheim, Germany)
Phalloidin-FITC	Enzo Life Sciences (New York, USA)
Piperazine-N,N'-bis(2-ethanesulfonic acid) (PIPES)	Roth (Karlsruhe, Germany)
Poly-L-lysine	Sigma-Aldrich (Steinheim, Germany)
Propidium iodide (PI)	ThermoFisher Scientific (Waltham, USA)
Prostacyclin (PGI_2)	Calbiochem (Bad Soden, Germany)
Protease Inhibitor Cocktail	Sigma-Aldrich (Steinheim, Germany)
Proteinase K	Fermentas (St. Leon-Rot, Germany)
Recombinant hirudin	Hyphen Biomed (Neuville-sur-Oise, France)
R-phycoerythrin (PE)	EUROPA (Cambridge, UK)
Rotiphorese Gel 30% (PAA)	Roth (Karlsruhe, Germany)
Sodium azide	Sigma-Aldrich (Steinheim, Germany)
Sodium chloride	AppliChem (Darmstadt, Germany)
Sodium citrate	AppliChem (Darmstadt, Germany)

Sodium dodecyl sulfate (SDS)	Sigma-Aldrich (Steinheim, Germany)
Sodium hydroxide	AppliChem (Darmstadt, Germany)
Sodium orthovanadate	Sigma-Aldrich (Steinheim, Germany)
Sucrose	Sigma-Aldrich (Steinheim, Germany)
Sulfonic acid, 2N	AppliChem (Darmstadt, Germany)
Tail lysis buffer	Viagen Biotech (Los Angeles, USA)
Tetramethylethylenediamine (TEMED)	Roth (Karlsruhe, Germany)
TissueTek O.C.T Compound	Sakura Finetec (Staufen, Germany)
Tris(hydroxymethyl)aminomethane (TRIS)	Roth (Karlsruhe, Germany)
Triton X-100	Sigma-Aldrich (Steinheim, Germany)
TRIzol®	ThermoFisher Scientific (Waltham, USA)
Trypan Blue	Sigma-Aldrich (Steinheim, Germany)
Tween 20®	Roth (Karlsruhe, Germany)
U46619	Alexis Biochemicals (San Diego, USA)
Uranyl acetate	EMS (Hatfield, USA)
Vectashield hardset mounting medium	Vector Labs, Inc. (Burlingame, USA)
Water, nuclease-free	Roth (Karlsruhe, Germany)

3.1.2 Reagents, kits and cell culture material

Cell Strainer, 70 µm	PluriSelect (Leipzig, Germany)
Cryo-tubes	Roth (Karlsruhe, Germany)
Dulbecco's phosphate-buffered saline (DPBS)	Gibco (Karlsruhe, Germany)
Dulbecco's Modified Eagle Media (DMEM)	Gibco (Karlsruhe, Germany)
Essential amino acids	Gibco (Karlsruhe, Germany)
Fetal calf serum (FCS)	Perbio (Bonn, Germany)
gentleMacs C Tubes	Miltenyi Biotec (Bergisch Gladbach, Germany)
LS columns	Miltenyi Biotec (Bergisch Gladbach, Germany)
Non-essential amino acids	Gibco (Karlsruhe, Germany)
Penicillin/streptomycin	Gibco (Karlsruhe, Germany)
Recombinant mouse stem cell factor (SCF)	BioLegend (San Diego, USA)
StemPro®-34	Gibco (Karlsruhe, Germany)
TPO	Biosource (Solingen, Germany)
Tissue culture dishes (100/20 mm)	Greiner (Frickenhausen, Germany)
Tissue culture flasks (T25/75/175)	Greiner (Frickenhausen, Germany)

| 6/12/24/48/96-well plates | Greiner (Frickenhausen, Germany) |

All remaining materials were purchased from Sigma-Aldrich (Steinheim, Germany) or Roth (Karlsruhe, Germany). *Rhodocytin* (RC) was kindly provided by Johannes Eble (University Hospital Frankfurt, Germany). *Collagen-related peptid*e (CRP) was a generous gift from Paul Bray (Baylor College, USA).

Mouse Thrombopoietin DuoSet	R&D Systems (Wiesbaden, Germany)
Mouse TGF beta1 DuoSet	R&D Systems (Wiesbaden, Germany)
Mouse VEGF Quantikine ELISA Kit	R&D Systems (Wiesbaden, Germany)
Dynal® Mouse CD4 Negative Isolation Kit	ThermoFisher Scientific (Waltham, USA)
CD61 MicroBeads	Miltenyi Biotec (Bergisch Gladbach, Germany)
iScript Select cDNA Synthesis Kit	Bio-Rad (Hercules, USA)
Pierce™ BCA Protein Assay Kit	ThermoFisher Scientific (Waltham, USA)
RNeasy Mini Extraction Kit	Qiagen (Hilden, Germany)

3.1.3 Antibodies

3.1.3.1 Commercially purchased primary antibodies

Antibody	Host organism	Manufacturer
anti-acetylated tubulin	mouse	Santa Cruz (Dallas, USA)
anti-α-tubulin (B-5-1-2)	mouse	Sigma-Aldrich (Steinheim, Germany)
anti-APC	rabbit	Abcam (Cambridge, UK)
anti-Arp2	rabbit	Abcam (Cambridge, UK)
anti-β-actin	rabbit	Sigma-Aldrich (Steinheim, Germany)
anti-β-tubulin	mouse	Sigma-Aldrich (Steinheim, Germany)
anti-Cdc42	mouse	Cytoskeleton (Denver, USA)
anti-CD105	rat	BioLegend (San Diego, USA)
anti-CD31	rabbit	BioLegend (San Diego, USA)
anti-Cofilin	rabbit	Cell Signaling (Denver, USA)
anti-P-Cofilin	rabbit	Cell Signaling (Denver, USA)
anti-Collagen I	rabbit	Abcam (Cambridge, UK)
anti-Collagen IV	goat	Merck Millipore (Darmstadt, Germany)
anti-Diaph1	rabbit	Abcam (Cambridge, UK)
anti-GAPDH	rabbit	Sigma-Aldrich (Steinheim, Germany)
anti-detyrosinated tubulin	rabbit	Merck Millipore (Darmstadt, Germany)

anti-JAK2	rabbit	Cell Signaling (Denver, USA)
anti-P-JAK2	rabbit	Cell Signaling (Denver, USA)
anti-LIM-Kinase1	rabbit	Cell Signaling (Denver, USA)
anti-P-LIM-Kinase1	rabbit	Cell Signaling (Denver, USA)
anti-Ly-6G/C (Gr1)	rat	BioLegend (San Diego, USA)
anti-LYVE-1	goat	R&D Systems (Wiesbaden, Germany)
anti-NG2	rabbit	Merck Millipore (Darmstadt, Germany)
anti-Nrp2	goat	R&D Systems (Wiesbaden, Germany)
anti-P-Profilin1	rabbit	ECM Biosciences (Versailles, USA)
anti-RhoA	mouse	Cytoskeleton (Denver, USA)
anti-TER-119	rat	BioLegend (San Diego, USA)
anti-Twf1	rabbit	Cell Signaling (Denver, USA)
anti-vinculin	rabbit	Santa Cruz (Dallas, USA)
anti-vWF	mouse	DAKO (Hamburg, Germany)
anti-ZO-1	rabbit	ThermoFisher Scientific (Waltham, USA)
Biotin anti-mouse lineage panel	rat	BioLegend (San Diego, USA)
platelet depletion antibody (R300)	rat	Emfret Analytics (Eibelstadt, Germany)

Anti-G6b-B antibodies were kindly provided by Yotis Senis (University of Strasbourg, France).

3.1.3.2 Purchased directly-coupled or secondary antibodies

Antibody conjugates	Host organism	Manufacturer
anti-α-tubulin-Alexa F488	mouse	ThermoFisher Scientific (Waltham, USA)
anti-mouse IgG-Cy3	donkey	Jackson Immuno (Suffolk, UK)
anti-mouse IgG-Alexa F488	goat	ThermoFisher Scientific (Waltham, USA)
anti-mouse IgG-HRP	rat	Sigma-Aldrich (Steinheim, Germany)
anti-mouse SMA-Cy3	mouse	Sigma-Aldrich (Steinheim, Germany)
anti-goat IgG-Cy3	donkey	BioLegend (San Diego, USA)
anti-rabbit IgG-Cy3	goat	Jackson Immuno (Suffolk, UK)

anti-rabbit IgG-Alexa F647	goat	ThermoFisher Scientific (Waltham, USA)
anti-rabbit IgG-Alexa F488	donkey	ThermoFisher Scientific (Waltham, USA)
anti-rabbit IgG-HRP	donkey	Jackson Immuno (Suffolk, UK)
anti-rat IgG-Cy3	donkey	Jackson Immuno (Suffolk, UK)
anti-rat IgG-Alexa F488	goat	ThermoFisher Scientific (Waltham, USA)
anti-rat IgG-HRP	goat	Dianova (Hamburg, Germany)

3.1.3.3 In-house generated antibodies

Antibody	Clone	Isotype	Antigen	Reference
p0p4	15E2	IgG2b	GPIbα	[199]
p0p/B	57E12	IgG2b	GPIbα	[175]
DOM2	89H11	IgG2a	GPV	[199]
p0p6	56F8	IgG2b	GPIX	[199]
JAQ1	98A3	IgG2a	GPVI	[179]
INU1	11E9	IgG1	CLEC-2	[184]
ULF1	97H1	IgG2a	CD9	unpublished
LEN1	12C6	IgG2b	α2	[200]
EDL-1	57B10	IgG2a	β3	[201]
JON/A	4H5	IgG2b	αIIbβ3	[202]
JON6	14A3	IgG2b	αIIbβ3	unpublished
WUG 1.9	5C8	IgG1	P-Selectin	[203]
HB.197	2.4G2	IgG2b	FcγR	[204]

3.1.4 Buffers, Media and Solutions

All stock solutions and buffers were prepared in deionized water (MilliQ Water Purification System, Millipore, Schwalbach, Germany) and the pH was adjusted with HCl or NaOH.

- o **_Acid-Citrate-Dextrose_ (ACD) Buffer, pH 4.5**

Trisodium citrate dehydrate	85 mM
Anhydrous citric acid	65 mM
Anhydrous glucose	110 mM

o **CATCH buffer**

PBS	
HEPES	25 mM
EDTA	3 mM
BSA	3.5%

o **CO_2-independent medium**

KCl	5.33 mM
KH_2PO_4	0.441 mM
Na_2HPO_4	0.338 mM
Glucose	5.56 mM
Sodium chloride	138 mM
$CaCl_2$	185 mg L^{-1}
$NaHCO_3$	4.17 mM
$MgSO_4$	97.6 mM
L-Glutamine	1%
Penicillin/Streptomycin	1%
Essential amino acids	2%
Non-essential amino acids	1%
HEPES pH 7	2.5%
FCS	10%

o **Decalcification buffer, pH 7.4**

PBS	
EDTA	10%

o **Endothelial cell medium**

DMEM	
FCS	10%
Heparin	50 µg mL^{-1}
L-Glutamine	1%
Penicillin/Streptomycin	1%
Non-essential amino acids	1%
Bovine Brain Extract	0.1%

o **ELISA coating buffer, pH 9.0**

	NaHCO$_3$	0.1 M

- **ELISA wash buffer**

	PBS	
	NaCl	300 mM
	Tween 20®	0.05%

- **Fixation buffer with ions (TEM)**

	Cacodylat	50 mM
	KCl	50 mM
	MgCl$_2$	2.5 mM
	Glutardialdehyde	2.5%

- **Fixation buffer (Kawamoto/MK staining)**

	PHEM	
	PFA	4%
	TritonX100	0.1%

- **Freezing medium**

	DMEM	
	FCS	50%
	DMSO	10%

- **IP buffer**

	TRIS/HCl (pH 8.0)	15 mM
	NaCl	155 mM
	EDTA	1 mM
	NaN$_3$	0.005%

- **Karnovsky fixation buffer, pH 7.2**

	Paraformaldehyde	2%
	Glutardialdehyde	2.5%
	Cacodylate	0.1 M

- **Laemmli buffer (for SDS-PAGE)**

	TRIS	40 mM

Glycine	0.95 M	
SDS	0.5%	

o **MACS buffer**

PBS		
FCS	5%	
EDTA	2 mM	

o **MK medium**

DMEM		
FCS	10%	
L-Glutamine	2 mM	
Penicillin/streptomycin	1%	

o **PBlec buffer**

PBS		
$CaCl_2$	100 mM	
$MgCl_2$	100 mM	
$MnCl_2$	100 mM	
TritonX100	1%	

o **PHEM buffer, pH 6.8**

PIPES	100 mM	
HEPES	5.25 mM	
EGTA	10 mM	
$MgCl_2$	20 mM	

o *Phosphate-buffered saline* (PBS), pH 7.14

NaCl	137 mM	
KCl	2.7 mM	
KH_2PO_4	1.5 mM	
Na_2HPO_4 x $2H_2O$	8 mM	

o **10x platelet buffer, pH 7.4**

HEPES	10 mM	
NaCl	140 mM	

KCl	3 mM
$MgCl_2$	0.5 mM
$NaHCO_3$	5 mM
Glucose	10 mM

o **Protein lysis buffer, 2x, pH 7.4**

HEPES	15 mM
NaCl	150 mM
EGTA	10 mM
Triton X-100	2%

o **RBC washing buffer, pH 7.4**

HEPES	10 mM
NaCl	140 mM

o **SDS sample buffer, 2x**

β-mercaptoethanol (for red. conditions)	10%
TRIS buffer (1.25 M), pH 6.8	10%
Glycerin	20%
SDS	4%
Bromophenolblue	0.02%

o **Separating gel buffer (Western Blot), pH 8.8**

TRIS/HCl	1.5 M

o **Stacking gel buffer (Western Blot), pH 6.8**

TRIS/HCl	0.5 M

o **Starvation medium**

DMEM	
Penicillin/streptomycin	1%
FCS	0.5%

o **StemPro MK medium:**

StemPro®-34	
L-Glutamine	2 mM

Nutrient	2.6%
Penicillin/streptomycin	1%

- **Stripping buffer (Western Blot), pH 6.8**

TRIS/HCl	62.5 mM
SDS	2%
β-mercaptoethanol	100 mM

- **50x TAE**

TRIS base	0.2 M
Acetic acid	5.7%
EDTA (0.5 M)	10%

- **Transfer buffer (semi-dry blot)**

TRIS ultra	48 mM
Glycine	39 mM
Methanol	20%

- ***TRIS-buffered saline* (TBS), pH 7.3**

NaCl	137 mM
TRIS/HCl	20 mM

- **Tyrode's buffer, pH 7.3**

NaCl	137 mM
KCl	2.7 mM
$NaHCO_3$	12 mM
NaH_2PO_4	0.43 mM
Glucose	0.1%
Hepes	5 mM
BSA	0.35%
$CaCl_2$	2 mM
$MgCl_2$	1 mM

- **Washing buffer (ELISA)**

PBS	
Tween 20®	0.05%

o **Washing buffer (Kawamoto staining)**
PHEM
TritonX100   0.1%

o **Washing buffer (Western Blot)**
TBS
Tween 20®   0.1%

3.2 Methods

3.2.1 Genetically modified mice

Conditional platelet and MK-specific CLEC-2 knockout mice were generated by intercrossing *Clec1b^{fl/fl}* mice, in which exon 1 was flanked by the *loxP* sites, with mice carrying the Cre recombinase under the Pf4 promoter, as described previously.[19,205] *Clec1b^{fl/fl,Pf4Cre}* mice are here referred to as *Clec2^{-/-}*. 8- to 12-week-old mice were used for all experiments, if not stated otherwise. For analysis of embryonic development, mice were time-mated and embryos were isolated at embryonic day 13.5 or 14.5. *Gp5^{-/-}* mice were kindly provided by Prof. François Lanza (Inserm-Université de Strasbourg, Strasbourg, France). *Clec2^{-/-}/Gp5^{-/-}* were generated by intercrossing Cre-positive *Clec1b^{fl/fl}* mice with *Gp5^{-/-}* mice. Transgenic *Gp5^{KIN}* mice, in which CGC at position 1426 was mutated to GCC resulting in an amino acid exchange from arginine to alanine (R476A), were described previously (Sarah Beck, Doctoral Thesis, 2018). *Clec2^{-/-}/Gp5^{KIN}* mice were generated by intercrossing *Clec1b^{fl/fl,Pf4Cre}* mice with *Gp5^{KIN}* mice.

Nbeal2^{+/-} mice were obtained from MMRRC (University of California, Davis, USA) and were generated as described previously.[99] *Nbeal2^{-/-}* were generated by intercrossing heterozygous animals.

(*Gp1ba-tg*) mice (C57Bl/6 background), in which the ectodomain of GPIbα was replaced by the human interleukin-4 receptor α (IL-4Rα), were described previously.[206]

Gp6^{-/-} mice were generated as previously described.[207] Briefly, exon 2 and intron 2 were targeted and the targeting vector was electroporated into Sv129-derived embryonic stem cells for homologous recombination. Successfully transformed cells were injected into C57Bl/6 blastocysts and germline transmission was achieved by intercrossing the resulting chimeric mice with C57Bl/6 mice.

For the generation of Twinfilin1/Cofilin1 double-deficient mice (*DKO*), *Twf1^{fl/fl}* mice, obtained from EUCOMM (Strain ID EM:05232), were intercrossed with previously described conditional Cof1-deficient mice.[110] *Twf1^{fl/fl,Pf4Cre}* are referred to as *Twf1^{-/-}*, while *Cof1^{fl/fl,Pf4Cre}* mice are referred to as *Cof1^{-/-}*. Constitutive Twf2a knockout mice have been described earlier and were a generous gift from Prof. Pekka Lappalainen.[115,116] Twf1/Twf2a double-deficient mice (*Twf1^{-/-}/Twf2a^{-/-}*) were generated by intercrossing *Twf1^{fl/fl,Pf4Cre}* with *Twf2a^{-/-}* mice. All animal studies were approved by the district government of Lower Franconia (Bezirksregierung Unterfranken, AZ 55.2.2-2532-2-**1021**-29).

Mice with mutated *Mpig6b* (c.404-1G>A) were identified by whole exome sequencing and are further referred to as *G6b^{mut}*. Three-, six- or twelve-week-old mice were used for all experi-

ments, if not stated differently. For the generation of BM chimeras 6-week-old male and female C57Bl/6J mice (Charles River Laboratories, Sulzfeld, Germany) were lethally irradiated with a single dose of 10 Gy. BM cells from 6-week-old male *WT* or *G6b^{mut}* mice were retrieved by centrifugation and intravenously injected into recipients at a concentration of 30 x 10^6 cells mL^{-1} (3.5 x 10^6 cells per mouse). All animal studies were approved by the district government of Lower Franconia (Bezirksregierung Unterfranken, AZ 2-351 and AZ 2-4).

3.2.2 Whole-exome sequencing

DNA from eight mutant and eight *WT* mice was purified using the GeneJET Genomic DNA Purification Kit (Thermo Scientific) after retro-orbital bleeding. DNA quality was assured by high-resolution electrophoresis on a Bioanalyzer (Agilent). Whole Exome Sequencing of mouse genomic DNA was performed according to Agilent's protocol for the SureSelect QXT reagent kit and SureSelect XT Mouse All Exon plus capture probes for Illumina paired-end sequencing (49.6 Mb capture spanning 221,784 exons and 24,306 genes). The generated paired-end sequencing with 2 × 75 bp reads were processed using FastQC[208] (v0.11.51) for assessing read quality, amount of duplicates and presence of adapter sequences. Further, the processed sequences were aligned to Mouse Build 38 patch release 5 from GENCODE[209] (Burrows–Wheeler Aligner) using default parameters. Quality score recalibration was performed to prevent false-positive SNV calls and obtain accurate scores on SNV calls at the end of sequencing reads. Finally, SnpEff (v4.3p) was used to annotate the variants and was evaluated using GQ, DP and AD parameters indicating the confidence (GQ) of total informative reads at the site (DP) and number of alternative allele at the site (AD). The intronic missense mutation c.404-1G>A in *Mpig6b* was validated by sanger sequencing on four mice.

3.2.3 Mouse genotyping

3.2.3.1 Isolation of murine DNA

Mouse DNA was obtained by incubation of a 5 mm^2 piece of the ear in 100 µL tail lysis buffer containing 5 µL proteinase K for 2h at 56°C and 1200 rpm. The reaction was stopped by incubating lysed DNA at 85°C for 30 min.

3.2.3.2 *Polymerase chain reaction* (PCR)

Different PCRs were conducted to assess the presence of the *Twf2a* locus and the Cre recombinase cassette on chromosome 9 on the one hand as well as to verify the correct targeting of the *Clec1b*, *Twf1, Cof1* and *Gp5* loci.

PCR mix for *Twf2a WT*

1.0 µL	DNA sample
2.5 µL	DreamTaq^{TM} green buffer (10x)
0.4 µL	dNTPs [10 mM]
0.1 µL	forward Primer [1 µg mL^{-1}]
0.1 µL	reverse Primer [1 µg mL^{-1}]
0.125 µL	DreamTaq DNA Polymerase [5 U µL^{-1}]
20.775 µL	H$_2$O

PCR program *Twf2a WT*:

Temperature [°C]	Time [s]	Repeats
96	180	1 cycle
94	30	35 cycles
55.5-69.0	30	35 cycles
72	60	35 cycles
72	300	1 cycle
22	∞	1 cycle

Primer *Twf2a WT* (annealing temperature 69.0°C):

Twf2a_Ex1_for: 5' CCA GGA CCA AGA GGA GAA CTC CGA C 3'

Twf2a_Int1_rev: 5' CCC AGC TAT GTA CAA CAG TCT GTT CTG CC 3'

Expected band sizes: 249 bp for the *WT Twf2a* allele

PCR mix for *Twf2a* KO (Genetrap):

1.0 µL	DNA sample
2.5 µL	DreamTaq^{TM} green buffer (10x)
0.5 µL	dNTPs [10 mM]
0.05 µL	forward Primer [1 µg mL^{-1}]
0.05 µL	reverse Primer [1 µg mL^{-1}]
0.125 µL	DreamTaq DNA Polymerase [5 U µL^{-1}]
20.65 µL	H$_2$O

PCR program:

Temperature [°C]	Time [s]	Repeats
96	180	1 cycle
94	30	35 cycles
51.4	30	35 cycles
72	60	35 cycles
72	600	1 cycle
22	∞	1 cycle

Primer *Genetrap*:

Genetrap_for: 5´ TTA TCG ATG AGC GTG GTG GTT ATG C 3´

Genetrap_rev: 5´ GCG CGT ACA TCG GGC AAA TAA TAT 3´

Expected band size: 680 bp for positive samples.

PCR mix for *Pf4-Cre*:

1.0 µL	DNA sample
2.5 µL	DreamTaq^{TM} green buffer (10x)
1.0 µL	dNTPs [10 mM]
1.0 µL	forward Primer (1/10 in H_2O; [1 µg mL^{-1}])
1.0 µL	reverse Primer (1/10 in H_2O; [1 µg mL^{-1}])
0.25 µL	DreamTaq DNA Polymerase [5 U µL^{-1}]
18.25 µL	H_2O

PCR program *Pf4-Cre*:

Temperature [°C]	Time [s]	Repeats
96	300	1 cycle
94	30	35 cycles
48.5	30	35 cycles
72	45	35 cycles
72	30	1 cycle
22	∞	1 cycle

Primer *Pf4-Cre*:

Pf4 for: 5´ CCC ATA CAG CAC ACC TTT TG 3´

Pf4 rev: 5´ TGC ACA GTC AGC AGG TT 3´

Expected band size: 450 bp for positive samples

PCR mix for floxed *Clec1b* allele:

1.0 µL	DNA sample
2.5 µL	DreamTaq^{TM} green buffer (10x)
0.5 µL	dNTPs [10 mM]
0.1 µL	forward Primer [1 µg mL^{-1}]
0.1 µL	reverse Primer [1 µg mL^{-1}]
0.125 µL	DreamTaq DNA Polymerase [5 U µL^{-1}]
20.675 µL	H_2O

PCR program floxed *Clec1b*:

Temperature [°C]	Time [s]	Repeats
95	300	1 cycle
95	30	35 cycles
60	30	35 cycles
72	60	35 cycles
72	600	1 cycle
22	∞	1 cycle

Primer floxed *Clec1b*:

Clec1b for: 5´ TTT CTG CCT CTC TGC CTT GC 3´

Clec1b rev: 5´ CGT CAT GAA CAG AAA ACT GAC G 3´

Expected band size: *WT*: 172 bp; floxed allele: 333 bp

PCR mix for *Gp5^{KIN}* allele:

1.0 µL	DNA sample
2.5 µL	DreamTaq^{TM} green buffer (10x)
0.5 µL	dNTPs [10 mM]
1.0 µL	forward Primer (1/10 in H_2O; [1 µg mL^{-1}])
1.0 µL	reverse Primer (1/10 in H_2O; [1 µg mL^{-1}])
0.5 µL	MgCl$_2$
0.25 µL	DreamTaq DNA Polymerase [5 U µL^{-1}]

18.25 µL   H$_2$O

PCR program floxed *Gp5^{KIN}*:

Temperature [°C]	Time [s]	Repeats
95	300	1 cycle
95	30	35 cycles
60	30	35 cycles
72	60	35 cycles
72	600	1 cycle
22	∞	1 cycle

Primer *Gp5^{KIN}*:

Gp5^{KIN} for: 5´ TTC ATG TGG AGA AGC CCT GT 3´

Gp5^{KIN} rev: 5´ CAC TGG AAA CCA AGC TGT CA 3´

Expected band size: *WT*: 197 bp; floxed allele: 265 bp

3.2.3.3 Agarose gel electrophoresis

The PCR product size was analyzed in 1% agarose gels, which were prepared by dilution of 1.5 g agarose in 150 mL TAE buffer (or 4 g in 400 mL for big gel chambers) followed by boiling of the solution in a microwave. Upon cooling down to 60°C, 50 µL L^{-1} Midori Green™ were added to the solution in order to visualize DNA and the gel was allowed to solidify in a tray containing a comb, which was then laid into a TAE-filled chamber. Samples were loaded together with a marker ranging from 100 to 10.000 bp and the gels were run for 30 min at 140 Volt. DNA was visualized using ultra violet light and imaged with a camera (Herolab GmbH).

3.2.3.4 Flow cytometry

The presence of the platelet glycoproteins CLEC-2, GPV and GPVI was assessed by flow cytometry in diluted whole blood. To this end, mice were bled up to 50 µL into heparin and samples were filled up to 1 mL using PBS. 50 µL of diluted blood were incubated with 10 µL of the respective *fluorescein* (FITC)-coupled antibodies (11E9, 89H11, JAQ1), incubated for 20 min at RT and diluted in 500 µL PBS. *Mean fluorescence intensity* (MFI) levels of glycoproteins were assessed by flow cytometry at a FACS Calibur (BD Biosciences). To check for the presence of G6b-B, mice were bled into ACD, 5 µL of blood were diluted in

PBS, fixed using 4% PFA and incubated with 10 µg mL^{-1} of an anti-G6b-B antibody (kindly provided by Prof. Yotis Senis). Fixed platelets were spun down at 2000 rpm for 5 min and incubated with 100 µL of a FITC-coupled anti-rat antibody for 20 min. G6b-B expression was analyzed at a FACS Celesta (BD Biosciences).

3.2.4 Analysis of platelet function *in vitro*

3.2.4.1 Preparation of washed platelets from whole blood

Mice were anaesthetized in isoflurane and retro-orbitally bled up to 1 mL into 300 µL heparin [20 U mL^{-1} in TBS]. Another 300 µL heparin were added followed by centrifugation of the blood at 800 rpm for 6 min. Afterwards, the upper phase together with the buffy coat and some RBCs was transferred into a new tube containing 300 µL heparin and centrifuged again at 800 pm for 6 min. Subsequently, the upper phase alone was transferred into a new tube, in which platelet activation was inhibited by addition of 2 µL apyrase [0.02 U mL^{-1}, f.c.] and 5 µL PGI$_2$ [0.1 µg mL^{-1}, f.c.]. Isolated *platelet-rich-plasma* (PRP) was then spun down at 2800 rpm for 5 min and platelet pellet was diluted in 1 mL of Tyrode's buffer without Ca^{2+}, containing 2 µL of apyrase [0.02 U mL^{-1}, f.c.] and 5 µL PGI$_2$ [0.1 µg mL^{-1}, f.c.]. Washing of platelets was repeated once and platelet counts were assessed in a 1/1 dilution in PBS at an automated cell analyzer (Sysmex). After an additional centrifugation, platelet counts were adjusted in Tyrode's buffer without Ca^{2+}, containing 2 µL of apyrase [0.02 U mL^{-1}, f.c.] and platelets were allowed to rest for 30 min at 37°C.

3.2.4.2 Assessment of blood parameters

General blood parameters were assessed at an automated blood cell analyzer (ScilVet, scil animal care company GmbH), as described previously.[210] Briefly, mice were bled up to 50 µL into EDTA-coated tubes, tubes were inverted 5 times and platelet count and size, white blood cell count, hematocrit and RBC count were analyzed immediately.

3.2.4.3 Platelet count and size

In addition to analysis of blood parameters at the ScilVet cell analyzer, platelet count and size were further determined by flow cytometry. To this end, mice were bled into 300 µL heparin, blood was filled up to 1 mL using Tyrode's buffer without Ca^{2+} and 50 µL of the diluted blood were incubated with fluorophore-conjugated antibodies against GPIbα (15E2-PE) as well as αIIbβ3 integrins (14A3-FITC) for 20 min at RT. The reaction was stopped using 500 µL PBS and subsequently, *forward scatter* (FSC) as well as counts per second as measures for platelet count and size were determined by flow cytometry at a FACS Calibur or Celesta (BD BioSciences).

3.2.4.4 Platelet GP expression

Surface expression of the major glycoproteins on resting platelets were assessed by determination of MFI by flow cytometry using fluorophore-conjugated antibodies. Blood was prepared as described above.

3.2.4.5 Analysis of platelet integrin activation and degranulation

Mice were anaesthetized in isoflurane, bled up to 50 µL into 300 µL heparin and washed twice in Tyrode's buffer without Ca^{2+} followed by centrifugation at 2800 rpm for 5 min. After the last washing step, washed blood was resuspended in Tyrode's buffer containing 2 mM Ca^{2+}. 50 µL of washed blood was added to fluorophore-conjugated antibodies against activated $\alpha IIb\beta 3$ integrins (JON/A-PE) as well as the α-granule specific protein P-selectin (WUG 1.9-FITC). Subsequently platelets were stimulated using agonists against GPCRs (thrombin, the thromboxane A_2 analogue U46619 and ADP) as well as against the (hem)ITAM receptors CLEC-2 (RC) and GPVI (CRP). Platelets were incubated for 6 min at 37°C, followed by 6 min at RT. The reaction was stopped by adding 500 µL PBS. MFIs were assessed by flow cytometry at a FACS Calibur or Celesta (BD Biosciences).

3.2.4.6 Aggregometry

For analysis of platelet aggregation upon stimulation, platelets were isolated as described above, adjusted to 500,0000 per µL and allowed to rest for 30 min at 37°C. 1.5×10^6 platelets were suspended in Ca^{2+}-containing Tyrode's buffer supplemented with 100 µg mL^{-1} fibrinogen and activated in aggregometer cuvettes using 100-fold concentrated agonists. GPVI-dependent activation was assessed using collagen, CRP or convulxin, while CLEC-2-associated activation was determined by stimulation with RC. GPCR-coupled activation was analyzed upon stimulation with thrombin, U46619 or ADP. Of note, thrombin stimulation was performed in the absence of fibrinogen, while ADP measurements were done in PRP. Light transmission was assessed over time (600 s) using a four-channel aggregometer (APACT, Laborgeräte und Analysensysteme).

3.2.4.7 Platelet spreading on fibrinogen and confocal microscopy

Rectangular coverslips (24 x 60 mm) were coated with 10 µg mL^{-1} human fibrinogen in a humid chamber overnight at 4°C. Platelets were washed as described above and platelet counts were adjusted to 300,000 per µL. Coverslips were blocked using 1% BSA in PBS for 1h at RT und washed using Ca^{2+}-containing Tyrode's buffer. 30 µL of the platelet suspension [3×10^5] were suspended in 70 µL Ca^{2+}-containing Tyrode's buffer, stimulated with 0.01 U mL^{-1} thrombin and immediately allowed to spread on the fibrinogen-coated surface. Spreading capacities were analyzed at different time points upon fixation of platelets using

4% PFA in PHEM for 5 min. Spreading was analyzed by *differential interference contrast* (DIC) microscopy and imaged at a Zeiss HBO 100 (Axiovert, 200M, Zeiss). Analysis was done using ImageJ Software (NIH, USA). Platelets were categorized into different phases (1: resting; 2: filopodia; 3: filo- and lamellipodia; 4: fully spread) and phase abundancy was counted manually. For analysis of platelet cytoskeleton by confocal microscopy, platelets were allowed to spread for 15 or 30 min and spreading was terminated by addition of 4% PFA in PHEM containing 0.1% TritonX100. Slides were blocked using 1% BSA in PBS and actin and microtubules were visualized using Phalloidin-Atto647N and anti-α-tubulin-Alexa F488, respectively. Platelets were stained for 1h at RT and slides were mounted using Fluoroshield. Platelet morphology were analyzed by confocal microscopy at a Leica TCS SP5 using a 100x objective.

3.2.4.8 *Transmission electron microscopy* (TEM) of platelets

For analysis of platelet morphology by TEM, platelets were isolated as described previously and platelet pellet was resuspended in TEM fixation buffer with ions. Platelets were fixed at 4°C overnight, centrifuged at 1500 rpm for 5 min and washed in cacodylate buffer three times the following day. Cells were incubated in 1% OsO_4 for 1h at RT, afterwards washed with cacodylate buffer again, followed by addition of H_2O_{bidest} and 2% uranyl acetate (in H_2O) for 1h at 4°C. Samples were then dehydrated using an ethanol series, incubated twice for 10 min in propylenoxide and then rotated in a 1:1 mixture of propylenoxide and epon for 1h. Afterwards, propyleneoxide was removed and samples were incubated overnight at RT in epon, which was then hardened for 48h. Ultrathin sections were generated and stained using 2% uranyl acetate and lead citrate. Images were acquired at a JEM-2100 (JEOL). Granule and microtubule coil abundance was determined manually using ImageJ Software.

3.2.4.9 Platelet adhesion under flow *ex vivo*

For analysis of *ex vivo* adhesion to collagen, rectangular coverslips (24 x 50 mm) were coated with 70 µg mL^{-1} Horm collagen solution at 37°C overnight. Coverslips were blocked with 1% BSA in PBS the following day. Mice were anaesthetized in isoflurane and bled up to 1 ml into 300 µL heparin [20 U mL^{-1}]. Blood was diluted 1:2 in Ca^{2+}-containing Tyrode's buffer and platelets were subsequently labeled for 5 min at 37°C using a Dylight488-coupled anti-GPIX antibody derivative [0.2 µg mL^{-1}]. The collagen-coated coverslips were placed in a metal holder and covered with a transparent flow chamber with a slit depth of 50 µm. The prepared blood was perfused over the surface for 4 min using a pulse free pump, immediately followed by perfusion with Tyrode's containing 2 mM Ca^{2+} for 4 min at the same shear rate. During washing, ten brightfield as well as ten fluorescent images were acquired at a

Leica DMI6000B and thrombus volume and surface coverage were analyzed using ImageJ Software.

3.2.4.10 Immunoblotting of platelet lysates

For analysis of whole platelet lysates, platelets were isolated as described before. The last washing step was conducted in PBS containing 2 mM EDTA and platelets were immediately lysed in IP-buffer supplemented with 2% NP-40 as well as 1x protease inhibitors. Upon lysis on ice for 20 min, samples were added with 4x reducing Laemmli buffer and boiled at 95°C for 5 min. For determination of platelet activation, platelets were activated in Tyrode's buffer without BSA or Ca^{2+} using the respective agonist and lysed on ice at different time points using 2x protein lysis buffer supplemented with 2% NP-40, 1x protease inhibitor as well as 1x Na_3VO_4. Samples were heated to 70°C for 5 min after addition of 4x reducing Laemmli buffer, proteins were afterwards separated by *sodium dodecyl sulfate-* (SDS) *polyacrylamide gel electrophoresis* (PAGE) and blotted onto *polyvinylidene difluoride* (PVDF) membranes. Membranes were probed with anti-APC [2 µg mL^{-1}], anti-Cof1 [1 µg mL^{-1}], anti-CD31 [1 µg mL^{-1}], anti-Twf1 [1 µg mL^{-1}], anti-Cdc42 [2 µg mL^{-1}], anti-RhoA [2 µg mL^{-1}], anti-ZO1 [1 µg mL^{-1}], anti-β-actin [1 µg mL^{-1}], anti-mDia1 [1 µg mL^{-1}], anti-G6b-B [1 µg mL^{-1}], anti-JAK2 [1 µg mL^{-1}], anti-P-JAK2 [1 µg mL^{-1}], anti-P-JAK2 [1 µg mL^{-1}], anti-LimK1 [1 µg mL^{-1}], anti-P-LimK1 [1 µg mL^{-1}], anti-Pfn1 [2 µg mL^{-1}], anti-P-Pfn1 [1 µg mL^{-1}], anti-α-tubulin [0.5 µg mL^{-1}], anti-acetylated tubulin [2 µg mL^{-1}], anti-detyrosinated tubulin [3 µg mL^{-1}] or anti-GAPDH [1 µg mL^{-1}].

3.2.5 Analysis of *in vivo* platelet function

3.2.5.1 Tail bleeding on filter paper

For analysis of hemostasis mice were anaesthetized using triple narcotics (Midazolam [5 µg g^{-1}], Medetomidine [0.5 µg g^{-1}], Fentanyl [0.05 µg g^{-1}]) and 2 mm of the tail tip were removed using a scalpel. Time until cessation of bleeding was monitored by gently absorbing the blood with a filter paper every 20s. Experiments were stopped if the bleeding time exceeded 20 min. Statistical analysis between definite and infinite bleeding was done using Fisher's exact test.

3.2.5.2 Analysis of platelet lifespan

For determination of platelet lifespan mice were anaesthetized in isoflurane and retro-orbitally injected with 5 µg of a Dylight488-coupled anti-GPIX antibody derivative. Of note, the amount of injected antibody was scaled down to 2 µg in macrothrombocytopenic mice.

Labeled platelets were measured over five consecutive days in diluted whole blood by flow cytometry using a FACS Calibur/Celesta (BD Biosciences).

3.2.5.3 Determination of platelet recovery upon depletion

Recovery of platelet counts was assessed upon depletion of endogenous platelets using 50 µg of an anti-GPIbα antibody derivative (R300), which was injected intra-peritoneal. Platelet counts were assessed prior and 1h after depletion by withdrawal of 50 µL blood and subsequent flow-cytometric analysis. Recovery of platelet counts was then observed by flow cytometry over 10 consecutive days beginning on day 4.

3.2.5.4 Experimental retinopathy

In order to induce ROP by hyperoxygenation, mouse pups were placed into an oxygen chamber on day 7 after birth and exposed to 75% oxygen for 5 consecutive days. Afterwards, mice were kept at normal oxygen levels for another 5 days until isolation of retinas on day 17 postnatally. To analyze the effect of platelet depletion or glycoprotein deficiency/blockade, mice were injected with 2 µg g^{-1} of an anti-GPIb antibody derivative (R300) or 50 µg of an antibody against GPIbα or GPVI on day 15 and 16 after birth or on day 5 post-birth, respectively.

3.2.6 *In vitro* function of MKs

3.2.6.1 MK culture from whole BM (Boston protocol) and retrieval of BM plasma

BM from femora and tibiae was spun out of the bone into 100 µL DMEM without supplements by centrifugation at 2.500 g for 40s. The BM plasma acquired in this process was immediately frozen and stored at -80°C until further processing. The cell suspension was passed through a 70 µm cell strainer and the cells were incubated in StemPro Medium containing 50 ng mL^{-1} *stem cell factor* (SCF). After 48h, the cells were collected and rediluted in StemPro supplemented with 50 ng mL^{-1} SCF and 50 ng mL^{-1} TPO. On day 4, the cells were resuspended in StemPro containing 50 ng mL^{-1} TPO and cultured overnight, followed by a BSA density gradient separation to enrich the culture in MKs. After another day of culture in StemPro with TPO the cells were used for further experiments.

3.2.6.2 *In vitro* differentiation of BM MKs (lineage depletion)

As described above, BM of femora and tibiae was spun out, cells were singularized and immediately subjected to a lineage depletion using an antibody mixture (Biolegend) in combination with magnetic beads. The negative fraction was then cultured in MK medium

containing 50 ng mL^{-1} TPO and, for analysis of PPF, 100 U mL^{-1} recombinant hirudin for 72h and subsequently subjected to a BSA density gradient.

3.2.6.3 *In vitro* analysis of PPF from BM MKs

For analysis of PPF, TPO- and hirudin-conditioned MKs were seeded into 96-well-plates in a dilution series in order to be able to prevent differences in cell density. Proplatelet-forming and round MKs in five visual fields per MK culture were counted manually at a Zeiss PrimoVert brightfield microscope. Brightfield images were acquired at an Evos Microscope (ThermoFisher Scientific). For visualization of the cytoskeleton round coverslips were placed into 24-well-plates and coated with 0.1% Poly-L-lysine for 20 min at RT. After washing with H$_2$O, 500 µL of 1x platelet buffer were added to the wells. Using a cut-off tip, 300 µL of the cell suspension were gently added to the wells, immediately followed by centrifugation of the plate for 4 min at 900 rpm. Cells were fixed by addition of 800 µL 4% PFA in PHEM containing 0.1% TritonX100 and blocked in 3% BSA for 1h. Cells were stained with anti-α-tubulin Alexa F488 [3.33 mg mL^{-1}], phalloidin-Atto647N [170 nM] anti-vWF, anti-acetylated tubulin [4 µg mL^{-1}] and anti-detyrosinated tubulin [2 µg mL^{-1}] and analyzed by confocal microscopy at a Leica TCS SP8.

3.2.6.4 Immunoblotting of BM MKs

Enriched MKs were washed once using 5 mM EDTA in PBS and afterwards immediately lysed using 1x RIPA supplemented with 1x Halt protease & phosphatase inhibitors, stored on ice for 30 minutes and centrifuged at 14.000 rpm for 10 min at 4°C. For analysis of TPO signaling responses, mature MKs were seeded at a density of 350.000 cells per well and starved for 4h in starvation medium and afterwards either left untreated or stimulated using 50 ng mL^{-1} TPO. 10 min afterwards, cells were collected, spun down at 2800 rpm for 1 min, and immediately lysed in 1x RIPA. Protein content was determined using a BCA protein assay by diluting 6 µL of the lysates in 54 µL 1x RIPA, followed by analysis of absorbance at 562 nm at a Tecan Spark microplate reader. Samples were added with 4x reducing sample buffer, boiled at 95°C for 5 min and proteins were separated by SDS-PAGE. Proteins were blotted onto PVDF membranes and membranes were probed with antibodies listed in 3.2.4.11. Phospho- and/or total levels of JAK2, STAT5, Shp1, Shp2, GATA-1, c-Mpl and c-Cbl were assessed at an automated capillary-based immunoassay platform (Jess, ProteinSimple) according to the manufacturers' recommendations.

3.2.6.5 Spreading and immunofluorescence of BM MKs

To analyze spreading capacities of BM MKs, round glass cover slips were placed in 24-well plates and coated with fibrinogen [100 µg mL^{-1}] or Horm collagen [50 µg mL^{-1}] for 3h at 37°C.

Slides were blocked in 1% BSA for 1h, washed with PBS and 500 µL of the cell suspension were gently added onto the slides. MKs were allowed to spread for 3h at 37°C, after which they were fixed and permeabilized in fixation buffer. Unspecific binding was blocked using 1% BSA and the cells were stained overnight using anti-α-tubulin Alexa F488 [3.33 mg mL^{-1}], phalloidin-Atto647N [170 nM], anti-Arp2 [2 µg mL^{-1}], anti-acetylated tubulin [4 µg mL^{-1}] and anti-detyrosinated tubulin [2 µg mL^{-1}]

3.2.6.6 Isolation of native BM MKs

BM was spun out as described before, cells were passed through a 70 µm cell strainer and resuspended in MACS buffer. MKs and precursors were isolated using magnetic beads coupled to an anti-CD61 antibody (Miltenyi). Immediately afterwards, cells were washed once, subjected to a BSA density gradient separation and lysed in Trizol..

3.2.6.7 RNA sequencing on native BM MKs

RNA quality was checked using a 2100 Bioanalyzer with the RNA 6000 Pico kit (Agilent Technologies). The RNA integrity number for all samples was ~8. DNA libraries suitable for sequencing were prepared from 50 ng of total RNA with oligo-dT capture beads for poly-A-mRNA enrichment using the TruSeq Stranded mRNA Library Preparation Kit (Illumina) according to manufacturer's instructions. After 15 cycles of PCR amplification, the size distribution of the barcoded DNA libraries was estimated ~300 bp by electrophoresis on Agilent DNA 1000 Bioanalyzer microfluidic chips. Sequencing of pooled libraries, spiked with 1% PhiX control library, was performed in single-end mode on the NextSeq 500 platform (Illumina) with the High Output Kit v2.5 (75 Cycles). Demultiplexed FASTQ files were generated with bcl2fastq2 v2.20.0.422.

Sequencing reads were trimmed for Illumina adapter sequence using Cutadapt version 2.5 with default parameters. Reads were subsequently mapped to the mouse genome (GRCm38.p6) using STAR v2.7.2b.[211] Clusterprofiler was used to perform gene set enrichment analysis for KEGG and GO pathways and to make an enrichment map for all of the pathways with a q-value < 0.01.[212]

3.2.6.8 Quantitative RT-PCR on native and cultured BM MKs

MKs were cultured as described above or directly isolated from the BM as described in 3.2.6.6. Cells were washed once in PBS containing 2 mM EDTA, centrifuged and immediately lysed using 500 µl Trizol reagent. RNA was extracted using the RNeasy Mini Extraction Kit (Qiagen) according to the manufacturers' protocol. Using a starting amount of 500 µg RNA, cDNA was generated by reverse transcription with the iScript Select cDNA Synthesis Kit (Bio-Rad) following the manufacturers' recommendations with random primers.

The iTaq Universal SYBR Green Supermix (Bio-Rad) was utilized for quantitative real-time PCR. *Sdha* and *Actb* served as housekeeping genes for the calculation of relative expression by the ΔΔCt method. Primer sequences are as follows:

Apc (ACCATGTACCCAGGCATTG; TACTCCTGCTTGCTGATCC)

Diaph1 (TTAACAGCGCGGCACGAG; GGTGCAACAACCACAGCAG)

Sdha (GACATCAAGACTGGCAAGGTTAC; AGTAGGAGCGGATAGCAGGAG)

Actb (ACCATGTACCCAGGCATTG; TACTCCTGCTTGCTGATCC)

Mpig6b (CTGCTGCCTTTGTTGCTCTC; TGCCCTCCAAAGAAACCTCG)

3.2.7 *In situ* and *ex vivo* analysis of BM precursors and MKs

3.2.7.1 *Hematoxylin-Eosin* (H&E) staining on paraffin sections

Mice were sacrificed and femora and spleens or livers were isolated and fixed in 4% PFA at 4°C overnight. Femoral bones were decalcified in 10% EDTA in PBS for 4 consecutive days, after which all organs were dehydrated and paraffin-embedded. 3 µm sections of the organs were obtained at a Leica microtome, rehydrated using an ethanol gradient, followed by staining with hematoxylin and eosin. The number of MKs as well as the general appearance of the organs were determined at a Leica DMI 4000B microscope.

3.2.7.2 Immunofluorescence on whole femora cryosections

Femora of mice were isolated, fixed in 4% PFA in PBS supplemented with 5 mM sucrose for 1h at RT and rotated in 10% sucrose/PBS overnight, after which a sucrose gradient was performed for 2 days. Femora were embedded in a water-soluble embedding medium, frozen at -20°C and cut into 10 µm sections at a Cryostat (Leica) using a tape-transfer system.[213] The sections were rehydrated in PHEM for 15 min, fixed in 4% PFA in PHEM, blocked in 3% goat serum and stained using antibodies against CD105 [5 µg mL^{-1}], collagen IV [10 µg mL^{-1}] and collagen I [10 µg mL^{-1}]. MKs or cytoskeleton were visualized by staining with a directly labeled antibody derivative against GPIX [10 µg mL^{-1}] or phalloidin-Atto647N [170 nM]. Nuclei were counterstained using 1x DAPI. Slides were afterwards washed and mounted using Fluoroshield. Tile scan images were acquired at a confocal microscope using a 25x objective (Leica TCS SP8), while single MKs were imaged using a 40x objective. Sections were analyzed manually using ImageJ Software.

3.2.7.3 Immunofluorescence on spleen cryosections

Spleens were processed similarly to femoral bones (3.2.7.2). Organs were embedded in glycerin-based optimal cutting temperature compound and stored at -20°C. 7 μm sections of spleens were obtained and further processed as described above.

3.2.7.4 Assessment of MK ploidy and GP expression

Determination of MK GP expression and ploidy was done in whole BM after centrifugation. BM of both tibiae and femora was spun into CATCH buffer, rinsed through a 70 μm cell strainer and resuspended in 1 mL CATCH buffer. MK size and surface expression of major glycoproteins was analyzed in 100 μL. Unspecific binding of antibodies was prevented by incubating the cells with an anti-FcγR antibody (clone 2.4G2, [0.02 mg mL^{-1}]. Subsequently, the cell suspension was washed, rediluted in CATCH buffer and GPs were stained for 20 min on ice using an MK-specific antibody panel (anti-GPIb, anti-GPIX, anti-GPV, anti-GPVI, anti-CLEC2, anti-αIIbβ3, anti-α2, anti-CD9). MKs were concomitantly stained with 10 μg mL^{-1} of an anti-GPIIb antibody (clone 5D7) to differentiate them from other BM cells. For analysis of MK ploidy, cells were fixed and permeabilized after blockade of unspecific binding and staining for GPIIb followed by labeling of DNA using 50 μg mL^{-1} propidium iodide containing 100 μg mL^{-1} RNaseA. Measurements were performed by flow cytometry at a FACS Celesta and analyzed using FlowJo Software (BD Biosciences).

3.2.7.5 Analysis of MK precursors in the BM

HSCs and MK precursors were analyzed in whole BM obtained by centrifugation of both tibiae and femora. Cells were singularized and rediluted in MACS buffer. 100 μL of whole BM cells were incubated with an anti-FcγR antibody (clone 2.4G2, [0.02 mg mL^{-1}] and afterwards stained on ice for 30 min at 4°C using an antibody panel (CD34-PE, c-Kit-Alexa F700, Sca-1-Alexa F647, CD150-Bv650, CD48-PacB, Flk2/Flt3-Cy5.5, FITC-labeled lineage mixture, CD16/32-Cy7, GPIX-Alexa F546, [1 μg mL^{-1}]) to differentiate between early and late progenitors. Subsequently, the cell suspension was washed and dead cells were stained for 30 min at 4°C using a dead cell marker. Cells were analyzed by flow cytometry using a FACS Celesta upon resuspension in 250 μL MACS buffer.

3.2.7.6 TEM on BM MKs

Mice were sacrificed, femora were isolated, cut into 4 mm pieces and immediately transferred into Karnovsky fixation buffer. Bones were fixed overnight at 4°C under rotation and afterwards decalcified in decalcification buffer over 4 days. Fatty components were fixed by incubation in 2% osmium tetroxide in 50 mM cacodylate buffer (pH 7.2). Afterwards, bones pieced were stained using 0.5% aqueous uranyl acetate, dehydrated in a graded

ethanol series and embedded in epon. Ultra-thin sections were obtained and imaged at a JEOL JEM-2100.

3.2.7.7 Intravital two-photon microscopy of the BM

Mice were anaesthetized using triple narcotics and intravenously injected with 100 µg BSA-FITC, 20 µg anti-CD105-Alexa Fluor 488 and an Alexa F546-coupled anti-GPIX antibody-derivative (clone 56F8, [0.6 mg g^{-1}]). A small incision along the midline was made to expose the frontoparietal skull and mice were immobilized on a customized metal stage equipped with a stereotactic holder. Time-lapse acquisition was performed at a fluorescence microscope equipped with a TriM Scope II multiphoton system (20x objective, LaVision BioTec), and ImSpector Pro-V380 software. Emission was captured using a tunable broadband Ti:Sa laser (780 nm) and detected with HQ535/50-nm and ET605/70-nm filters. ImageJ software was used to process and generate time-lapse videos.

3.2.8 Cytokine levels in BM and blood plasma

3.2.8.1 Multiplex cytokine analysis

BM plasma was obtained as described in 3.2.6.1 and centrifuged at 14.000 rpm at 4°C for 10 min. Blood plasma was generated by bleeding mice up to 700 µL into 70 µL citrate buffer. Blood was centrifuged once at 2.800 rpm for 5 min, plasma was retrieved and centrifuged again at 14.000 rpm for 5 min. Plasma samples were immediately frozen at -80°C until further processing. A combinable array of cytokines was designed using the ThermoFisher Scientific ProcartaPlex^{TM} panel generator. For analysis of adiponectin levels, blood plasma samples were diluted 1/2000, while BM plasma was prediluted 1/20. Assessment of TGFβ1 required activation of the samples using 1N HCl, followed by neutralization of the acidifed sampled with 1.2N NaOH. The ProcartaPlex assay was performed according to the manufacturers' protocol and data was analyzed using the Luminex xPONENT Software.

3.2.8.2 Enzyme-linked immunosorbent assays on BM and blood plasma

BM and blood plasma were obtained as described above. TPO levels were determined using the mouse thrombopoietin quantikine ELISA Kit according to the manufacturers' recommendations. A mouse VEGF quantikine ELISA Kit was used for assessment of VEGF levels, while TGFβ1 levels were analyzed using the mouse TGFβ1 DuoSet. Plates were analyzed at a Multiskan Ascent (96/384) plate reader (ThermoFisher Scientific) at 450 nm with wavelength correction (570 nm).

3.2.9 Bone analysis

3.2.9.1 Micro-computed tomography (µCT)

Micro-computed tomography scanning was done using a Skyscan 1172 µCT scanning device (Kontich) operating at 50 kV and 200 mA. Isotrophic voxel resolution was set to 8 µm. 3D analysis was conducted by CTAn and CTVol software. In the femur, three volumes of interest (VOI) were analyzed: VOI 1 (trabecular bone in the metaphyseal region) was set 360 µm proximal to the metaphyseal growth plate with a length of 280 µm. VOI 2 (cortical bone) covered the area from 80 µm proximal to 80 µm distal from the middle of the diaphysis. VOI 3 (trabecular bone in the diaphyseal area) covered the endosteal area from 80 µm proximal to 80 µm distal from the middle of the diaphysis. Bone mineral density was assessed using two phantoms with defined hydroxyapaptite contents (250 mg/cm^3 and 750 mg/cm^3). The threshold for mineralized tissue was set at 390 mg hydroxyapatite/cm^3 for trabecular bone and at 642 mg hydroxyapatite/cm^3 for cortical bone.

3.2.9.2 Histomorphometry

After µCT scans, femora were subjected to decalcified histology as described previously.[214] 7 µm sections were stained with Toluidin Blue or TRAP kits to analyze the number and surface of osteoblasts and osteoclasts as well as the mineralized bone. Analysis was done using image-analysis software from Osteomeasure systems. Region of interest for the analysis was a 200 x 400 µm area in the femur metaphysis. Osteoblasts were determined in Toluidin Blue staining as cubically shaped cells with dark blue nucleus and light blue cytoplasm residing on the bone surface. Osteoclasts were determined in TRAP staining as TRAP-positive cells with two or more nuclei residing on the bone surface.

3.2.9.3 von Kossa staining

PFA-fixed and paraffin-embedded slides were deparaffinized and hydrated. Bones were visualized with 1% silver nitrate solution under ultraviolet light for 20 minutes. Slides were washed and un-reacted silver was removed using 5% sodium thiosulfate for 5 minutes. Nuclei were counterstained using fast red and slides were rehydrated and mounted using Eukitt.

3.2.10 Analysis of endothelial development and permeability

3.2.10.1 Immunofluorescence on embryonic mesenteries

Lymphatic and endothelial development were analyzed in whole-mount embryonic mesenteries at embryonic day 13.5 or 14.15. Mice were time-mated, pregnant female mice

were sacrificed and embryos were isolated. Embryonic mesenteries were separated from the placenta, immobilized on silicon plates using insect pins and fixed in 4% PFA. Afterwards, whole-mount samples were permeabilized in 0.3 % TritonX100 in PBS and blocked in 1% BSA in PBS. Mesenteries were removed from the silicon plates, transferred into Eppendorf tubes and probed with antibodies against CD31 [1 µg mL^{-1}], Nrp2 [4 µg mL^{-1}], ZO-1 [5 µg mL^{-1}], NG2 [2 µg mL^{-1}] or α-SMA [1 µg mL^{-1}] overnight. Samples were washed in PBS the following day and stained with the respective fluorophore-coupled secondary antibodies for 2h at RT. Subsequently, mesenteries were mounted using DAPI-containing Fluoroshield. Confocal images were acquired at a Leica TCS SP8.

3.2.10.2 Evans Blue permeability assay

For analysis of endothelial permeability, mice were injected with 100 µL sterile 2% Evans Blue in PBS and anaesthetized 40 min after injection. The peritoneal cavity was flushed using 6 mL PBS and the mice were perfused with PBS afterwards. The peritoneal lavage was centrifuged at 2000 rpm for 5 min and 200 µL were immediately transferred to a 96-well-plate in triplicates. After 5 min of perfusion, one liver lobe, one lung lobe, one kidney, a 1 cm long piece of the small intestine and one ear were transferred into separate tubes, which were weighed beforehand. Organs were dried under the fume hood overnight to remove residual liquids, weighed the following day and added with 500 µL formamide to remove the remaining Evans Blue from the tissue. Tissue was incubated under shaking at 50°C for 24h. Samples were centrifuged at 2000 rpm for 5 min to remove tissue remnants, 200 µL of the formamide solution were transferred into a 96-well-plate and an Evans Blue dilution series was prepared in formamide. Evans Blue emission was analyzed at 620 nm using a Multiskan Ascent (96/384) plate reader.

3.2.10.3 Immunofluorescence on whole-mount retinas and ears

Oxygen-induced retinopathy was analyzed in murine retinas on day 17 after birth as described in 3.2.5.4. For analysis of de-novo vascularization after birth, retinas were isolated at day 6 after birth. For whole-mount analysis of retinal vascularization, mice were sacrificed and eyes were isolated. Fixation was done using 4% PFA for 30 min, followed by storage in PBS until dissection. Retinas were isolated as previously described,[215] permeabilized in 0.1% TritonX100 in PBS and blocked in 1% BSA in PBS/TritonX100. Retinas were washed in PBS and incubated overnight with 20 µg mL^{-1} biotinylated Griffonia Simplicifolia Lectin isolectin B4 in PBlec buffer under rotation at 4°C. The following day, retinal whole-mounts were washed in PBS, followed by incubation with 5 µg mL^{-1} Alexa F647-coupled streptavidin in PBlec buffer for 2h at RT. Afterwards, retinas were washed again, gently dissected using spring scissors and mounted with DAPI-containing Fluoroshield. Analysis of retinopathy scores was

performed manually using ImageJ Software.

For analysis of vascularization in the ear, mice were sacrificed, ears were cut off and ripped apart using forceps. The inner part of the ear was immobilized onto silicon plates using insect pins and subsequently fixed in 4% PFA, permeabilized using 0.1% TritonX100 and blocked in 3% BSA/PBS. Ears were stained for LYVE-1 [2 µg mL^{-1}], CD31 [1 µg mL^{-1}] and Ter119 [3 µg mL^{-1}] overnight at 4°C. On the following day, ears were washed in PBS and incubated and incubated with fluorophore-coupled secondary antibodies. Ultimately, ears were mounted using DAPI-containing Fluoroshield. Samples were visualized by confocal microscopy (Leica TCS SP8) and analyzed using AngioTool Software (NIH, USA).

3.2.11 Statistical analysis

Results are displayed as mean ± *standard deviation* (SD) from at least three independent experiments per group, if not stated otherwise. Data distribution was analyzed using the Shapiro-Wilk-test and differences were statistically analyzed using unpaired, two-tailed Student's t-test, one-way ANOVA or Fisher's exact test. Tukey or Sidak's post-hoc test was used for multiple comparisons. P-values < 0.05 were considered as statistically significant * P < 0.05; ** P < 0.01; *** P < 0.001. Results with a P-value > 0.05 were considered as not significant (ns).

4 RESULTS

4.1 Novel role of soluble GPV as a regulator of endothelial integrity in mice

The role of the (hem)ITAM receptors GPVI and CLEC-2 in maintaining vascular integrity has been extensively studied.[190,216] In particular, CLEC-2-mediated blood-lymph-vessel separation has been shown to be essential for lymphatic and venous development as well as to prevent blood-filling of lymph vessels in adult mice.[19,198,217]

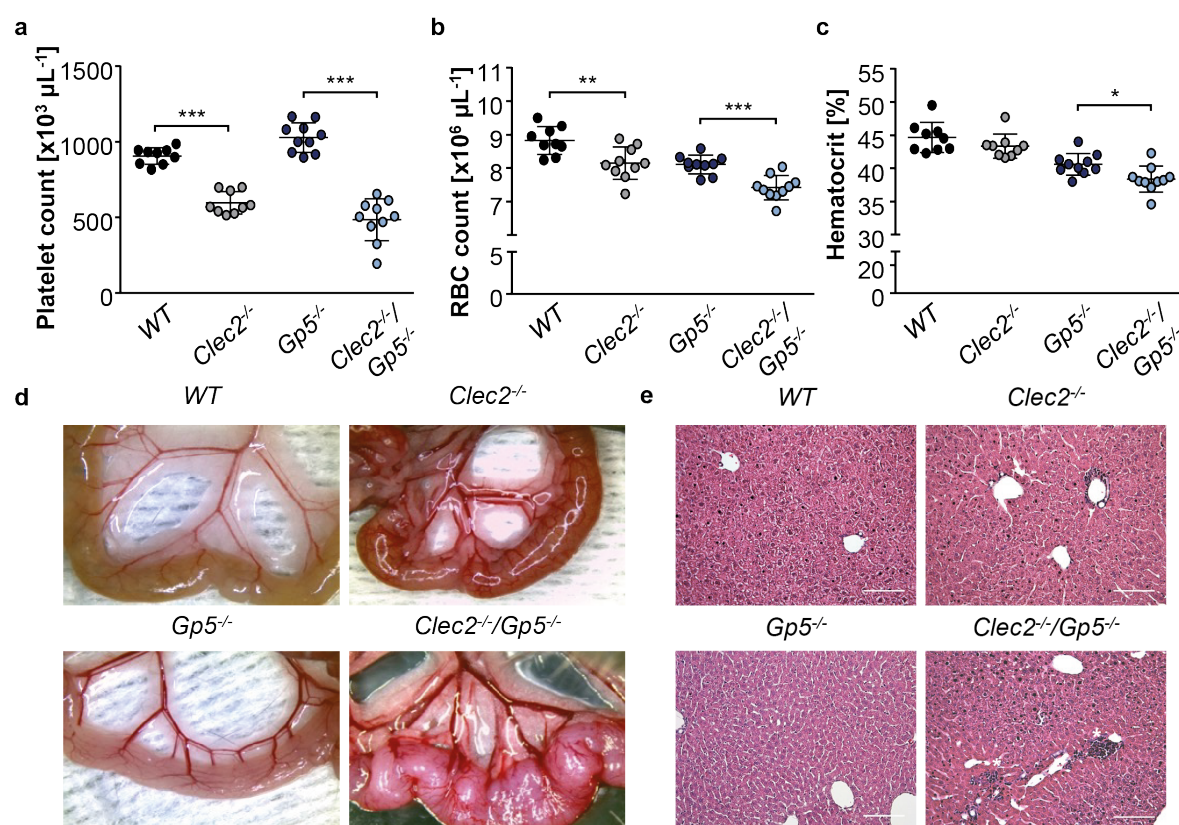### 4.1.1 CLEC-2/GPV-deficient mice exhibit anemia and thrombocytopenia

Figure 9. Thrombocytopenia, anemia and inflammation in *Clec2^-/-^/Gp5^-/-^* mice. Platelet count (**a**), RBC count (**b**) and hematocrit (**c**) in *WT, Clec2^-/-^, Gp5^-/-^* and *Clec2^-/-^/Gp5^-/-^* mice were assessed at an automated blood cell analyzer. Values are mean ± SD (n = 8). One-way ANOVA with Sidak correction for multiple comparisons. *P < 0.05; **P < 0.01; ***P < 0.001. (**d**) Representative macroscopic images of intestine and mesenteries of *WT, Clec2^-/-^, Gp5^-/-^* and *Clec2^-/-^/Gp5^-/-^* mice. (**e**) H&E-stained spleen paraffin sections. Asterisks highlight lymphocyte aggregates. Scale bars: 100 µm.

Previous results from our laboratory identified thrombin-cleaved sGPV as an important regulator of hemostasis and thrombosis in mice (Beck *et al.*, unpublished). Injection of sGPV into mice subjected to *in vivo* thrombosis models or ischemic stroke markedly reduced thrombus formation suggesting an antithrombotic function of the GPV ectodomain. Moreover, deficiency or antibody-blockade of GPV was able to revert increased bleeding induced by

loss of the (hem)ITAM receptors GPVI and/or CLEC-2. These findings prompted us to examine whether lack of GPV, in addition to normalizing bleeding, might also revert the blood-lymphatic mixing observed in the absence of the hemITAM receptor CLEC-2.[19] To this end, we crossed conditional MK- and platelet-specific CLEC-2-deficient mice with *Gp5$^{-/-}$* mice. Double-deficient *Clec2$^{-/-}$/Gp5$^{-/-}$* mice were born at the expected mendelian ratios. In contrast to our expectations, they exhibited a dramatic edema formation in their extremities and occasionally developed ascites leading to premature death. Analysis of basic blood parameters with an automated blood cell analyzer revealed a marked thrombocytopenia as well as anemia in *Clec2$^{-/-}$/Gp5$^{-/-}$* mice, which was more severe than in CLEC-2-deficient mice alone (Figure 9a, b). Moreover and in agreement with the reduced RBC count, double-deficient mice presented with a reduction in hematocrit (Figure 9c). Of note, mildly decreased hematocrit values compared to the *WT* were also detected in GPV-deficient mice. Upon macroscopic analysis, *Clec2$^{-/-}$/Gp5$^{-/-}$* mice exhibited a dramatic inflammation of the intestine and, similarly to CLEC-2-deficient mice, misconnected blood and lymph vessels in the mesenteries (Figure 9d). In addition, a high proportion of mice displayed a blood-filling of the peritoneal cavity, suggesting increased endothelial leakage in these mice. In order to assess the general inflammatory state in these mice, we analyzed H&E-stained paraffin sections of liver and lung and found focal inflammation spots in both organs (Figure 9e; asterisks), which are described to mainly consist of lymphocytes and are generally caused by increased vascular permeability leading to tissue infiltration.

4.1.2 Unaltered hemostasis in *Clec2$^{-/-}$/Gp5$^{-/-}$* mice, albeit impaired thrombus formation *ex vivo*

In order to verify whether additional lack of GPV affected hemostasis and thrombosis *in vivo* and *ex vivo*, we first performed flow adhesion assays on collagen-coated coverslips with whole blood derived from *WT, Clec2$^{-/-}$, Gp5$^{-/-}$* and *Clec2$^{-/-}$/Gp5$^{-/-}$* mice. As described before, CLEC-2-deficiency resulted in slightly reduced thrombus volume and surface coverage.[22] Surprisingly, platelets derived from double-deficient mice displayed a dramatically impaired capacity to adhere to as well as to form stable thrombi on collagen (Figure 10a, b), which might be a result of the severe thrombocytopenia. Since it has been described, that INU-1 IgG-mediated depletion of CLEC-2 results in variable bleeding times that may be reverted upon additional GPV-deficiency or antibody-mediated blockade, we next assessed hemostasis in a bleeding time assay using a filter paper. As expected, the variable bleeding times observed upon loss of CLEC-2 were reverted to *WT* levels in *Clec2$^{-/-}$/Gp5$^{-/-}$* mice (Figure 10c), thus suggesting that lack of GPV was indeed able to restore hemostasis *in vivo*

despite the pronounced thrombocytopenia. Of note, $Gp5^{-/-}$ mice exhibited an accelerated time until cessation of bleeding compared to the *WT*.
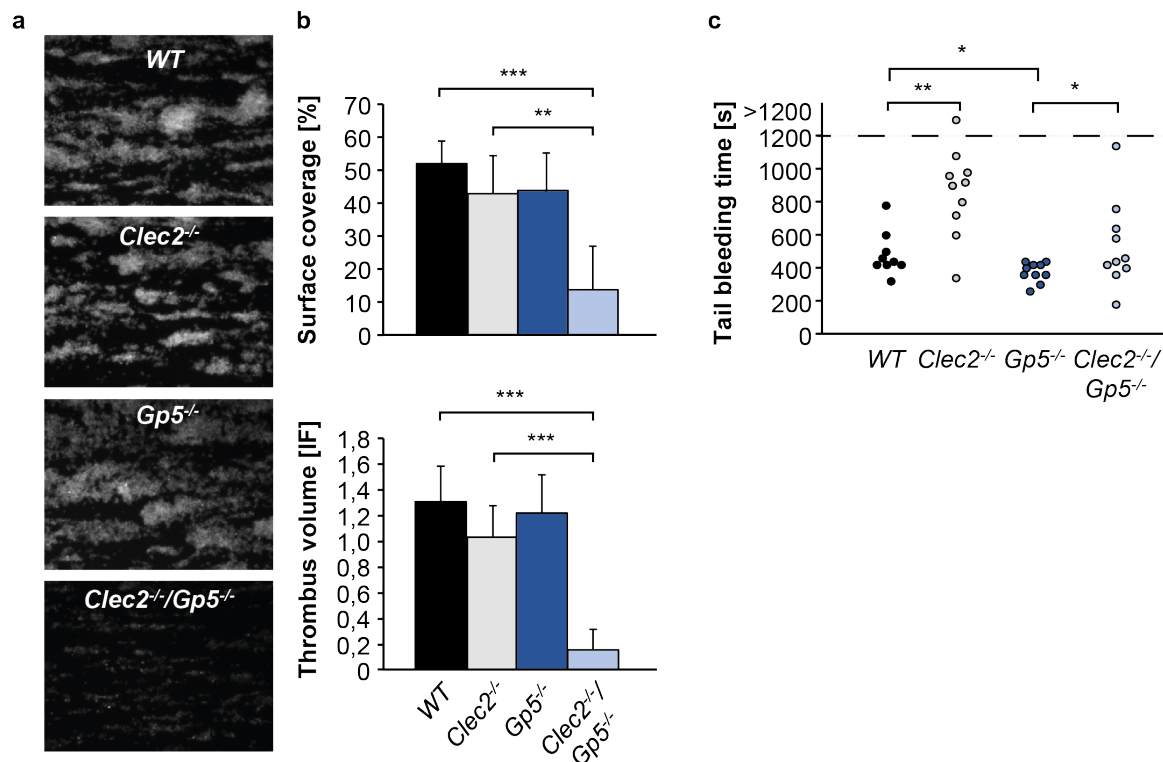

Figure 10. Unaltered hemostasis in *Clec2$^{-/-}$/Gp5$^{-/-}$* mice, but reduced thrombus formation *ex vivo*. (a, b) *Ex vivo* thrombus formation was analyzed in a flow chamber assay by perfusion of blood over a collagen-coated surface. Values are mean ± SD (n = 8). One-way ANOVA with Sidak correction for multiple comparisons. ***P < 0.001. (**c**) Hemostatic function of *WT, Clec2$^{-/-}$, Gp5$^{-/-}$* and *Clec2$^{-/-}$/Gp5$^{-/-}$* platelets was assessed in a tail bleeding time assay on filter paper. Differences between infinite and definite bleeding were analyzed using Fisher's exact test. Differences between bleeding times were determined by one-way ANOVA with Sidak correction for multiple comparisons. *P < 0.05; **P < 0.01.

4.1.3 Delayed and impaired vascularization upon loss of GPV

Due to the higher severity of blood-lymphatic misconnections leading to edema formation and blood-filling of the peritoneal cavity in *Clec2$^{-/-}$/Gp5$^{-/-}$* mice, we hypothesized a possible involvement of GPV in maintaining vascular integrity. First and foremost, we aimed to assess whether vascularization processes themselves were affected upon lack of CLEC-2, GPV or both receptors. To this end, we analyzed retinal vessels stained with Isolectin B4 at P6 by confocal microscopy. While we were unable to observe differences in the appearance of retinal vessels (Figure 11a), the degree of vascularization as assessed by vessel length and branching points was overall reduced in *Gp5$^{-/-}$* as well as *Clec2$^{-/-}$/Gp5$^{-/-}$* mice, suggesting a delay in vascularization upon lack of GPV (Figure 11b, c).
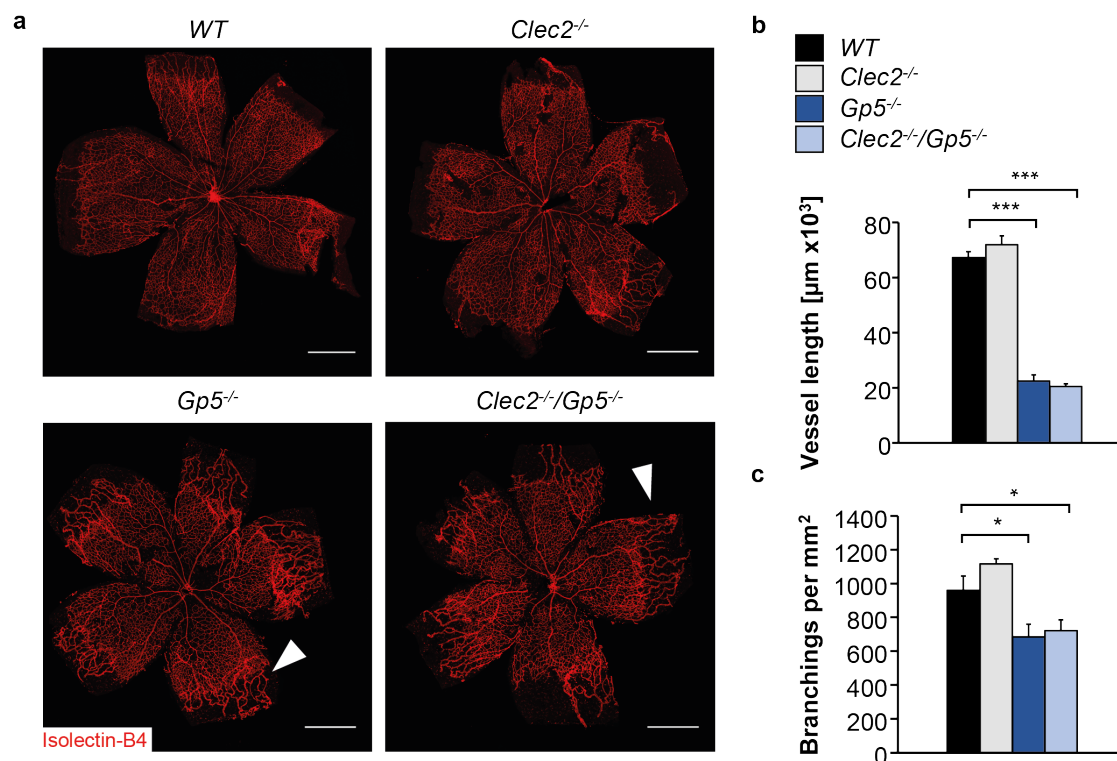
Figure 11. GPV-deficient mice exhibit delayed, but normal retinal vascularization. Retinal vascularization in *WT, Clec2*^{-/-}*, Gp5*^{-/-} and *Clec2*^{-/-}*/Gp5*^{-/-} mice at P6 was analyzed by confocal microscopy (**a**) and quantified using AngioTool Software (Leica TCS SP8, 10x objective). (**b, c**). Arrowheads point to remnants of hyaloid vasculature in GPV- and double-deficient mice. Scale bars: 750 μm. Values are mean ± SD. One-way ANOVA with Sidak correction for multiple comparisons. *P < 0.05; ***P < 0.001.

These findings were further supported by the persistence of hyaloid vessels in retinas of *Gp5*^{-/-} as well as *Clec2*^{-/-}*/Gp5*^{-/-} mice (Figure 11a, arrowheads), a vascular system that is usually rapidly regressing upon development of the retinal vasculature.[30] To analyze another vascular bed in adult mice, we next isolated ears from *WT, Clec2*^{-/-}*, Gp5*^{-/-} and *Clec2*^{-/-}*/Gp5*^{-/-} mice and visualized blood and lymphatic vessels in whole-mount samples by confocal microscopy (Figure 12a). Quantification of vessel length and branching index revealed a significant decrease in vessel area in *Gp5*^{-/-} and *Clec2*^{-/-}*/Gp5*^{-/-} mice, thus supporting the hypothesis of altered vascularization upon lack of GPV (Figure 12b). Of note, lymphatic vessels visualized by staining for the LEC cell marker LYVE-1 appeared markedly dilated exclusively in *Clec2*^{-/-}*/Gp5*^{-/-} mice, while vessel diameters in *Clec2*^{-/-} mice were comparable to the *WT*. Since vascularization processes appeared to be affected in adult mice, we next sought to investigate whether these alterations originated from defective blood and lymphatic EC development during embryogenesis. Therefore, we isolated mesenteries at E14.5, stained them for blood and lymph vessels as well as RBCs and analyzed vessel morphology by confocal microscopy (Figure 13a).
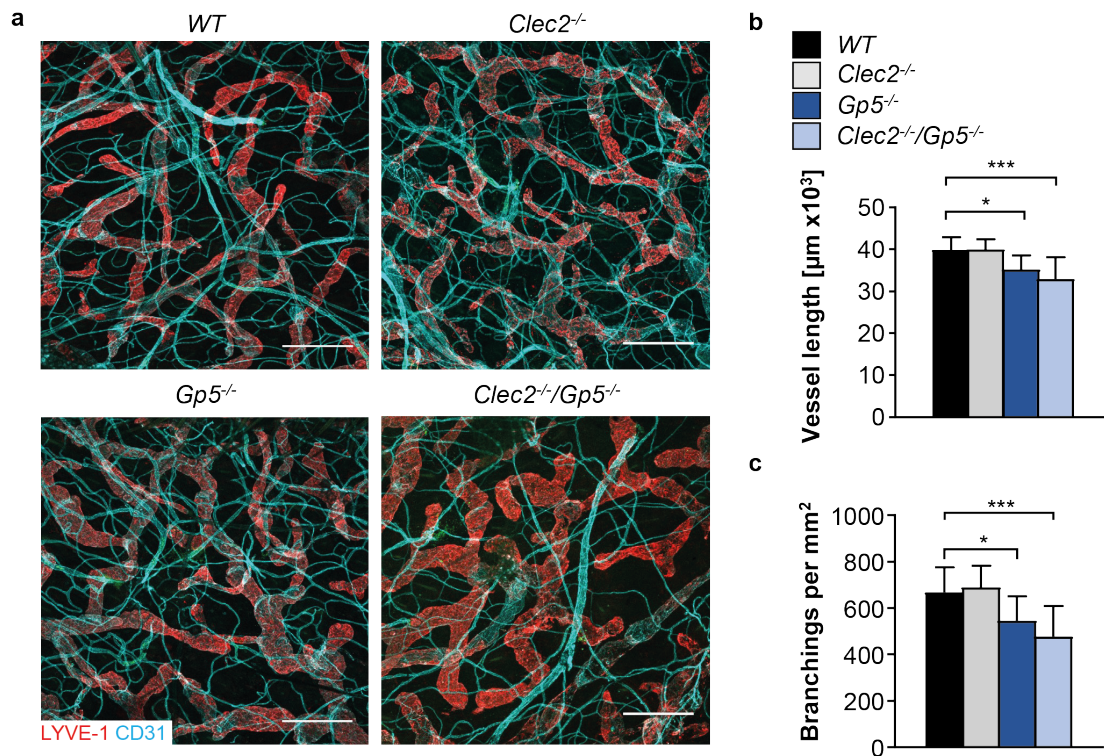
Figure 12. Reduced vessel density upon lack of GPV. Confocal microscopic analysis (**a**) and quantification of vessel length (**b**) and branching points (**c**) in Z-projections of *WT, Clec2⁻/⁻, Gp5⁻/⁻* and *Clec2⁻/⁻/Gp5⁻/⁻* ears (Leica TCS SP5, 40x objective). Blood vessels were visualized by staining for CD31. Lymphatic vessels were stained for LYVE-1. Analysis was performed using AngioTool Software. Scale bars: 250 µm. Values are mean ± SD. One-way ANOVA with Sidak correction for multiple comparisons. *P < 0.05; ***P < 0.001.

While RBCs were occasionally observed within lymph vessels in mesenteries derived from CLEC-2-deficient embryos (Figure 13, arrowheads), the lymphatic vasculature of *Clec2⁻/⁻/Gp5⁻/⁻* embryos was overloaded with RBCs leading to a dramatic dilation and disorganization of vessels that markedly exceeded the minor RBC leakage observed in *Clec2⁻/⁻* embryos (Figure 13, arrowheads).
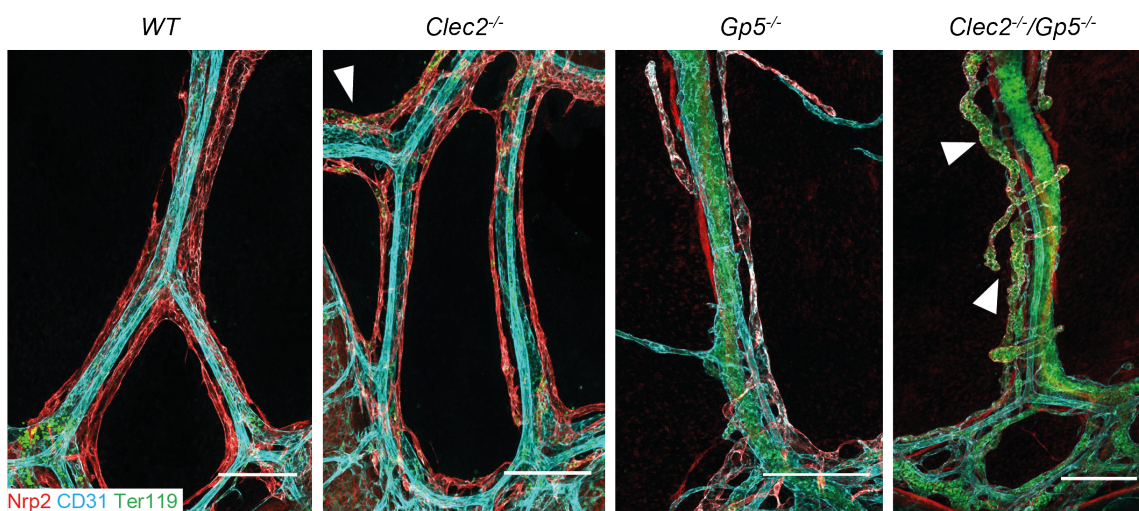
Figure 13. RBC accumulation in lymphatic vessels of embryonic mesenteries of *Clec2⁻/⁻/Gp5⁻/⁻* mice. (**a**) Embryonic mesenteries were isolated from *WT, Clec2⁻/⁻, Gp5⁻/⁻* and *Clec2⁻/⁻/Gp5⁻/⁻* mice at E14.5, stained for blood vessels (CD31), lymphatic vessels (Nrp2) and RBCs (Ter119) and analyzed by confocal microscopy at a Leica TCS SP8 (25x objective). Arrowheads point to single RBCs within lymph vessels in *Clec2⁻/⁻* mice and massive RBC accumulations in CLEC-2/GPV-deficient embryos. Scale bars: 200 µm.

Of note, we did not observed differences in LEC morphology or RBC leakage in *Gp5⁻/⁻* embryos. These results strongly suggest GPV to be involved in the maintenance of vascular integrity upon lack of CLEC-2 during development and adulthood.

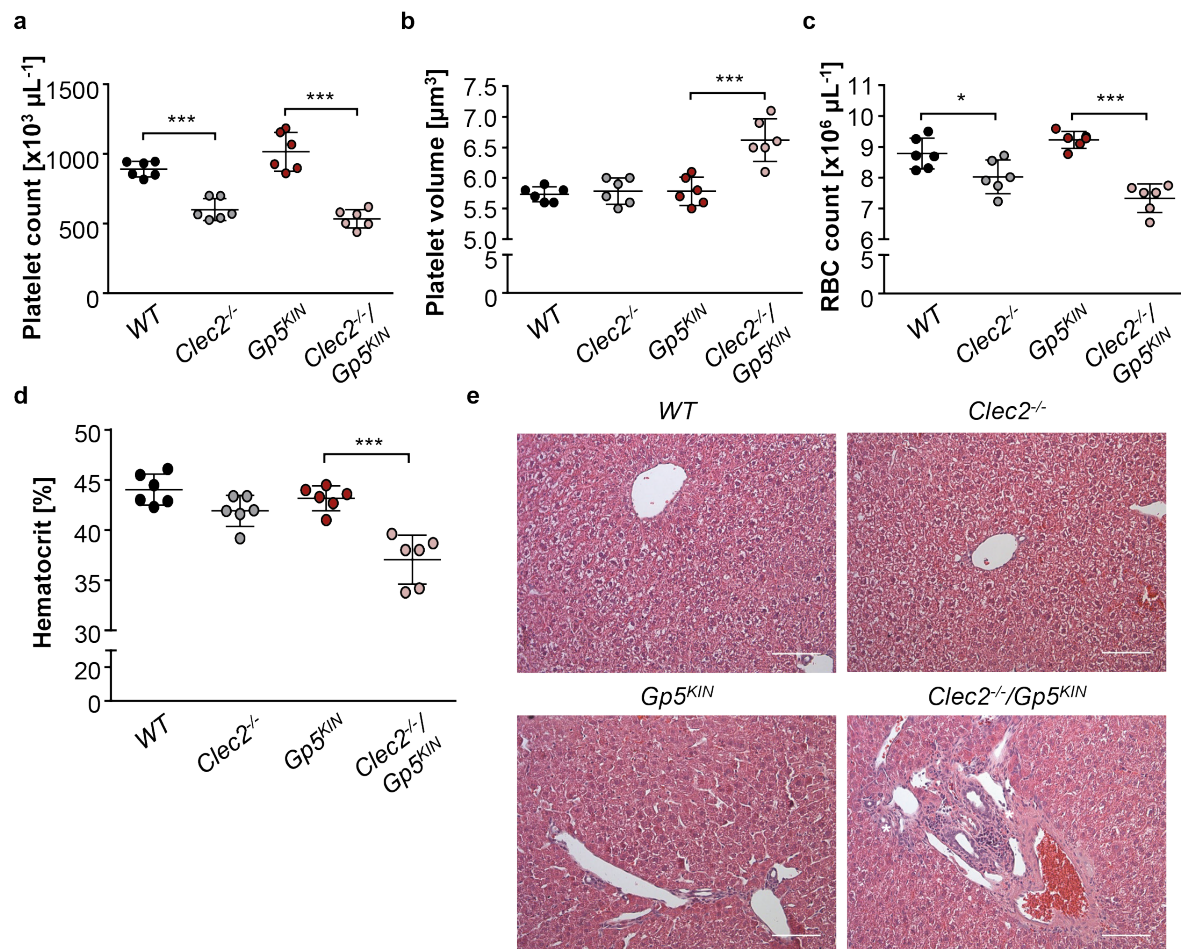### 4.1.4 *Clec2⁻/⁻/Gp5^{KIN}* mice recapitulate the phenotype of double-deficient mice

Figure 14. *Clec2⁻/⁻/Gp5^{KIN}* mice recapitulate the anemic and thrombocytopenic phenotype observed in CLEC-2/GPV-deficient mice. Platelet count (**a**), mean platelet volume (**b**), RBC count (**c**) and hematocrit (**d**) of *WT, Clec2⁻/⁻, Gp5^{KIN}* and *Clec2⁻/⁻/Gp5^{KIN}* mice were determined at an automated blood cell analyzer. Values are mean ± SD (n = 6). One-way ANOVA with Sidak correction for multiple comparisons. *P < 0.05; ***P < 0.001. (**e**) Focal inflammatory spots in H&E-stained liver sections of *Clec2⁻/⁻/Gp5^{KIN}* mice are highlighted by asterisks. Scale bars: 100 µm.

Mice lacking both CLEC-2 and GPV exhibited dramatically deteriorated lymphatic and vascular defects compared to *Clec2⁻/⁻* mice, mostly manifested by increased edema

formation and vascular leakage into the peritoneal cavity. Previous studies suggested that not the mere lack of GPV, but the absence of its cleaved form released by thrombin upon platelet activation is sufficient to revert bleeding tendencies.
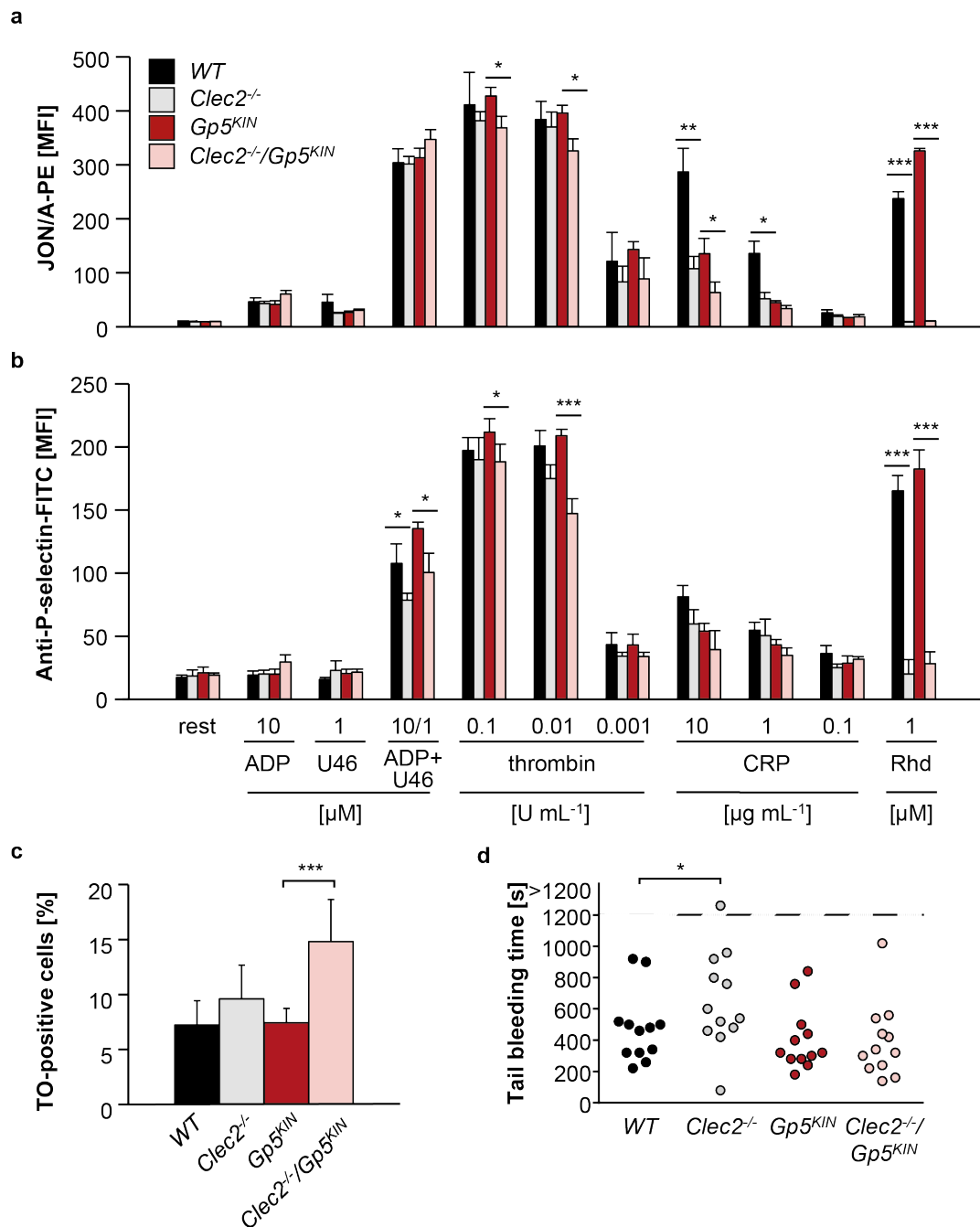

Figure 15. Slightly impaired platelet activation, but unaffected hemostasis in CLEC-2/GPV-transgenic mice. (**a, b**) JON/A-PE-binding to activated αIIbβ3 integrins (**a**) as well as P-selectin exposure as a measure of degranulation (**b**) were assessed by flow cytometry in washed blood from *WT, Clec2$^{-/-}$, Gp5^{KIN}* and *Clec2$^{-/-}$/Gp5^{KIN}* mice. (**c**) The amount of reticulated platelets was assessed by flow cytometry. Analysis was done using ImageJ Software. Values are mean ± SD (n = 4). Unpaired, two-tailed Student's t-test. *P < 0.05; **P < 0.01; ***P < 0.001. (**d**) Hemostasis was assessed in a tail bleeding assay on filter paper. Differences were assessed using Fisher's exact test and unpaired, two-tailed Student's t-test. *P < 0.05.

Therefore, we generated mice lacking CLEC-2 and further carrying a mutation within the thrombin cleavage site of GPV ($Gp5^{KIN}$) making it impossible to be removed from the platelet surface by thrombin. Similar to double-deficient mice, $Clec2^{-/-}/Gp5^{KIN}$ mice presented with marked edema in the feet and also displayed focal inflammation in lung and liver (Figure 14e). Surprisingly and in line with our findings from double-deficient mice, $Clec2^{-/-}/Gp5^{KIN}$ mice exhibited a marked thrombocytopenia together with a significant increase in platelet size (Figure 14a, b) as well as a dramatic anemia resulting in a distinct decline in hematocrit (Figure 14c, d). Analysis of platelet αIIbβ3 integrin activation and degranulation by flow cytometry revealed mild activation defects in double-transgenic platelets upon stimulation with high doses of the GPCR agonists ADP or thrombin and the GPVI-agonist CRP, while activation of CLEC-2-deficient platelets was only attenuated upon GPVI-dependent activation (Figure 15a, b).
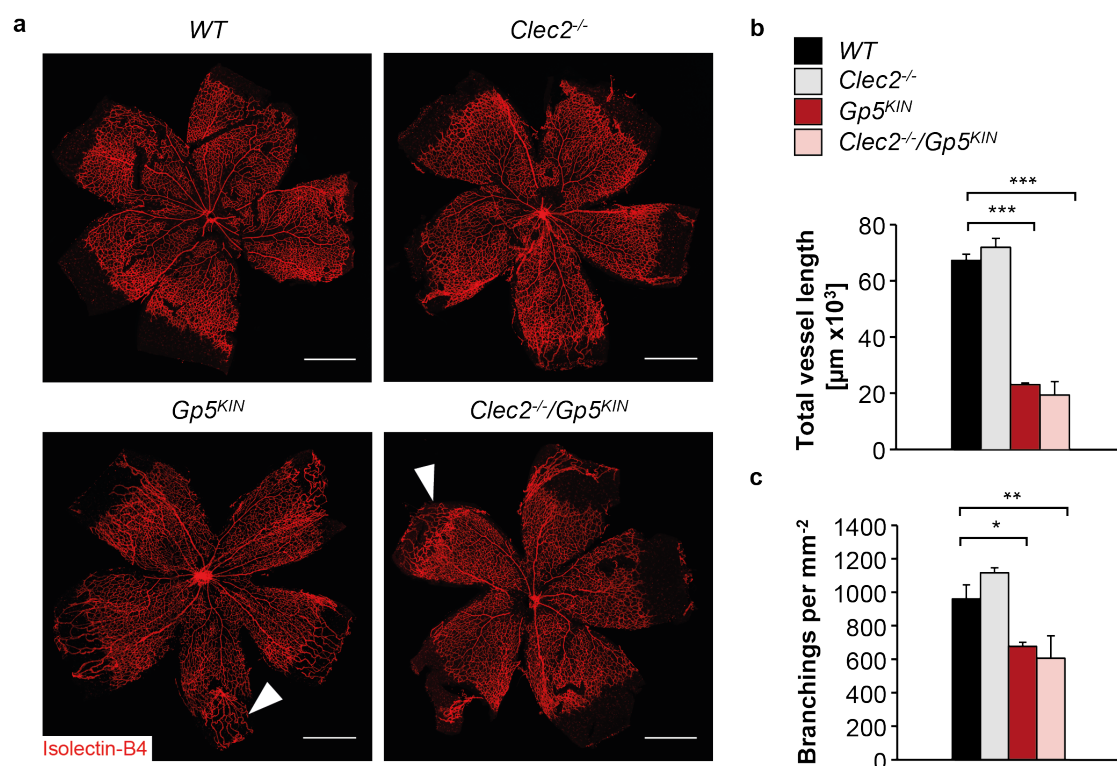

Figure 16. Vascularization phenotype in *Clec2^{-/-}/Gp5^{KIN}* mice phenocopies observations from *Clec2^{-/-}/Gp5^{-/-}* mice. Confocal microscopic visualization (**a**) and quantification (**b, c**) of retinal vasculature in *WT, Clec2^{-/-}, Gp5^{KIN}* and *Clec2^{-/-}/Gp5^{KIN}* mice at P6 (Leica TCS SP8, 10x objective). Vessel length and branching index were determined using AngioTool Software. Scale bars: 750 µm. Values are mean ± SD (n = 3). One-way ANOVA with Sidak correction for multiple comparisons. *P < 0.05; **P < 0.01; ***P < 0.001.

Of note, $Gp5^{KIN}$ platelets exhibited a marked activation defect upon GPVI stimulation possibly due to an unidentified genetic cosegregation. As expected, stimulation of CLEC-2 using the snake venom rhodocytin was fully abolished in $Clec2^{-/-}$ as well as $Clec2^{-/-}/Gp5^{KIN}$ platelets, thus verifying the absence of the receptor. Due to the dramatic macrothrombocytopenia, we

further assessed the amount of newly generated, highly reticulated platelets by flow cytometry and found it to be significantly increased only in double-transgenic mice, while it was unaltered in CLEC-2-deficient and *Gp5^{KIN}* animals (Figure 15c). In order to verify whether lack of soluble GPV was still able to prevent prolonged bleeding in these animals, we determined tail bleeding times using the filter paper method. Indeed, the highly variable bleeding times observed in *Clec2$^{-/-}$* mice were reverted to *WT* levels in double-mutant mice (Figure 15d). In line with our findings from the double-deficient mice, *Clec2$^{-/-}$/Gp5^{KIN}* as well as *Gp5^{KIN}* mice exhibited a comparable delay in retinal vascularization (Figure 16a, b). Moreover, hyaloid vasculature persisted longer in these animals than in the *WT* or *Clec2$^{-/-}$* mice, thus also recapitulating our findings from *Clec2$^{-/-}$/Gp5$^{-/-}$* mice (Figure 16a, arrowheads). Taken together, these findings strongly imply sGPV to contribute to vessel development and to be indispensable for the maintenance of vascular integrity in the absence of other regulators, such as CLEC-2.

4.1.5 Thrombocytopenia in double-transgenic mice is caused by blood leakage into the peritoneal cavity

In order to identify the cause of the thrombocytopenia in *Clec2$^{-/-}$/Gp5^{KIN}* mice, we analyzed platelet lifespan by measuring the proportion of fluorescently labeled platelets over 5 consecutive days upon injection of a Dylight488-labeled anti-GPIX antibody derivative. Interestingly, we could not detect differences in platelet clearance between *WT* and *Clec2$^{-/-}$* mice, while platelet lifespan was dramatically reduced in *Clec2$^{-/-}$/Gp5^{KIN}* mice suggesting loss of platelets due to altered clearance mechanisms or vascular leakage (Figure 17a, b).
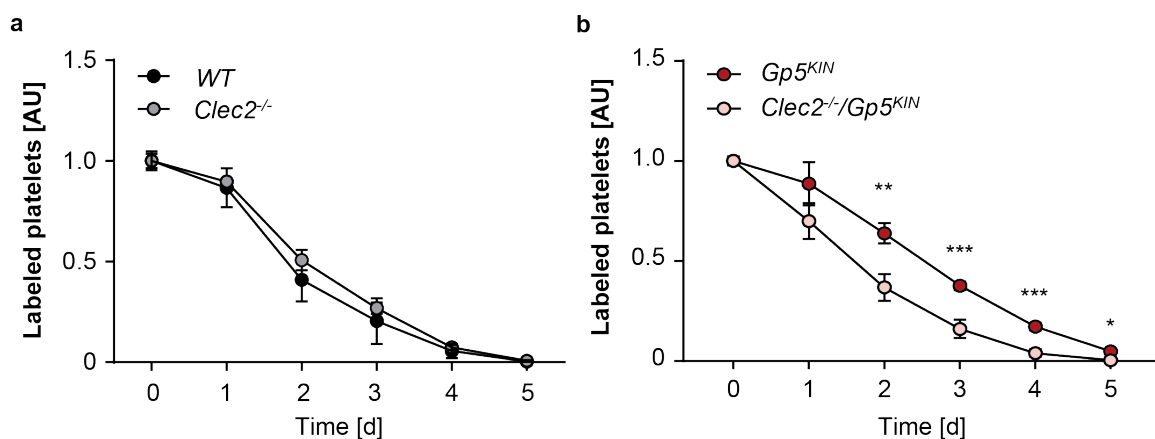
Figure 17. Decreased platelet lifespan in *Clec2$^{-/-}$/Gp5^{KIN}* mice. (a, b) *WT, Clec2$^{-/-}$, Gp5^{KIN}* and *Clec2$^{-/-}$/Gp5^{KIN}* mice were injected with a Dylight488-coupled anti-GPIX antibody derivative and the proportion of fluorescently labeled platelets was followed over time by flow cytometry. Values are mean ± SD (n = 5). Unpaired, two-tailed Student's t-test. *P < 0.05; **P < 0.01; ***P < 0.001.

To identify possible defects in vascular integrity, we performed a permeability assay by injecting the azo dye Evans Blue and subsequently determining leakage of the dye into the peritoneal cavity of different organs, respectively. Notably, we detected an increased leakage of Evans Blue into the peritoneal lavage of *Clec2^-/-/Gp5^KIN* mice, whereas permeability was unaffected in *Clec2^-/-* mice (Figure 18a, b).
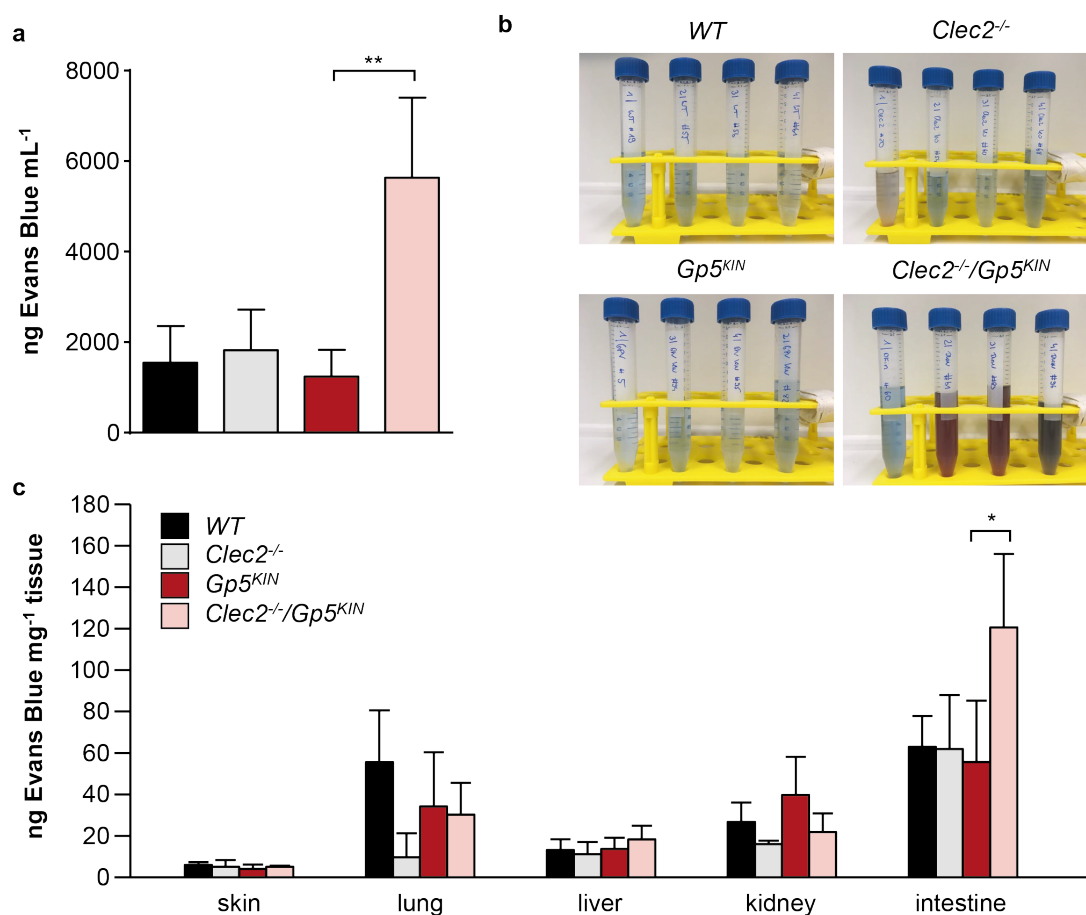

Figure 18. Increased endothelial permeability in mesenteries and intestine of *Clec2^-/-/Gp5^KIN* mice. (**a, b**) Mice were injected with 100 µL 2% Evans Blue, anaesthetized after 1h and a peritoneal lavage was performed. Quantification (**a**) and representative images (**b**) of Evans Blue leakage into the lavage are shown. (**c**) Evans Blue leakage into different organs of *WT, Clec2^-/-, Gp5^KIN* and *Clec2^-/-/Gp5^KIN* mice was determined by incubation in formamide for 24h. Concentration was determined at a Multiscan ELISA reader. Values are mean ± SD (n = 6). One-way ANOVA with Sidak correction for multiple comparisons. *P < 0.05; **P < 0.01.

Moreover, analysis of Evans Blue extravasation into various organs revealed a significantly increased vascular permeability specifically in the intestine of double-transgenic mice, but not in other organs such as spleen, kidney or skin (Figure 18c), thus implying that blood leakage from mesenteric and intestinal vessels into the peritoneum promotes thrombocytopenia and anemia in *Clec2^-/-/Gp5^KIN* mice. In order to investigate whether these defects in adult mice were manifested during development, we next analyzed vessel morphology in embryonic mesenteries of *WT, Clec2^-/-, Gp5^KIN* and *Clec2^-/-/Gp5^KIN* mice.
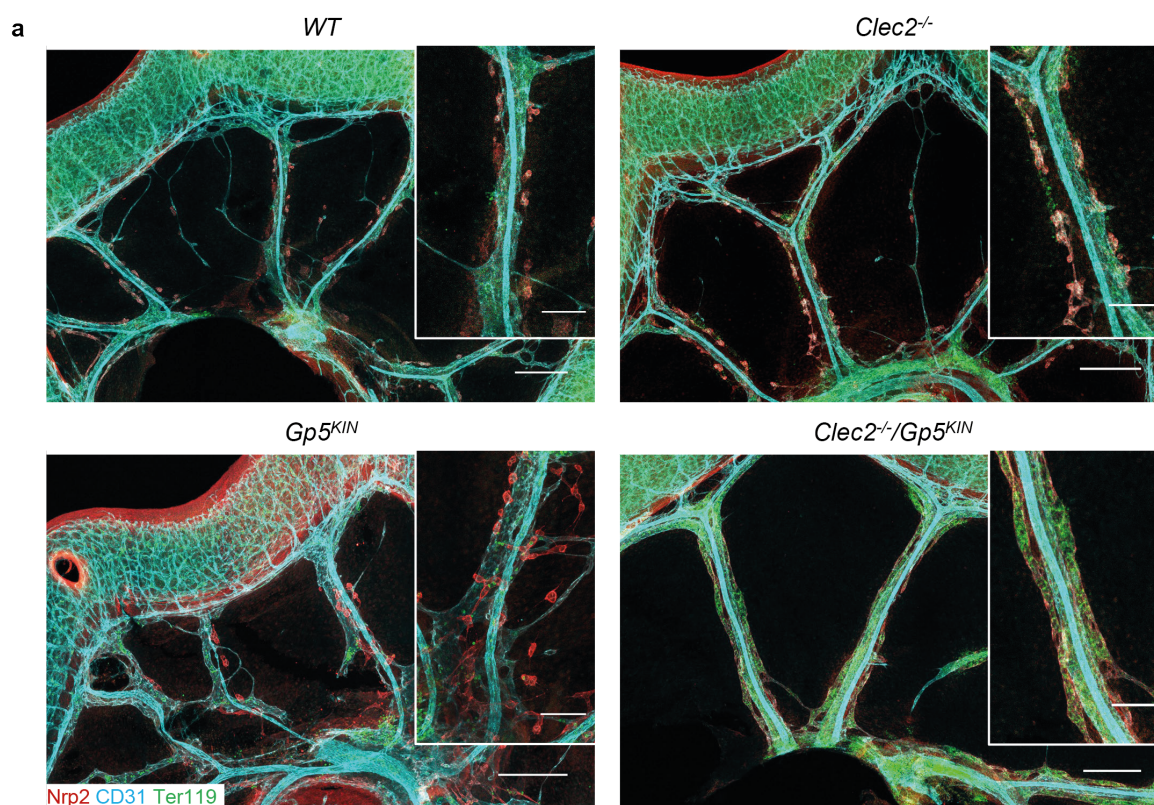
Figure 19. Dramatic RBC leakage into lymphatic vessels of embryos lacking CLEC-2 and thrombin-cleavable GPV. (a) Embryonic mesenteries of *WT, Clec2^-/-, Gp5^KIN* and *Clec2^-/-/Gp5^KIN* mice were stained for CD31, Nrp2 and Ter119 and analyzed by confocal microscopy (Leica TCS SP8, 25x objective). Scale bars: 300 µm; insets: 100 µm.

Similar to CLEC-2/GPV double-deficient mice, *Clec2^-/-/Gp5^KIN* embryos exhibited a severe blood-filling of lymphatic vessels, while only marginal RBC leakage into lymph vessels was observed in embryonic mesenteries of *Clec2^-/-* mice and no differences between *WT* and *Gp5^KIN* embryos were identified (Figure 19a). Moreover, lymphatic vessels of double-transgenic mice appeared dramatically dilated due to improper drainage of blood, which further led to leakage of blood into the interstitial space similarly to adult mice. In order to identify the cause of blood leakage, we ultimately sought to investigate, whether endothelial coverage or junction density was affected upon concomitant loss of CLEC-2 and sGPV. While we did not observe differences in smooth muscle cell or pericyte coverage (Figure 20a, b), tight junction density as assessed by confocal microscopy and immunoblotting of intestinal lysates revealed a significantly decreased expression of *zonula occludens* (ZO) 1 in *Clec2^-/-/Gp5^KIN* embryos and adults, while CD31 as another endothelial cell marker appeared to be expressed normally (Figure 20c, d). In summary, our findings support that sGPV not only plays a key role in hemostasis and thrombosis, but is further critically involved in maintaining endothelial barrier function.
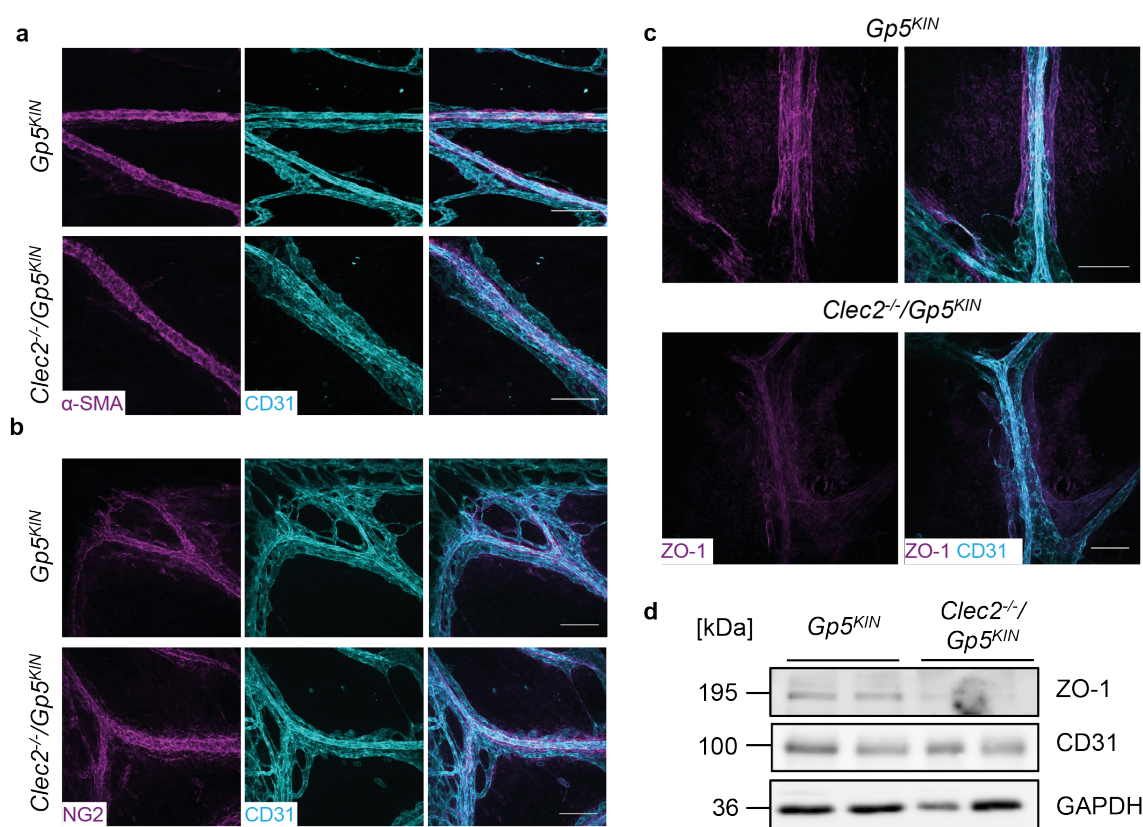
Figure 20. Defective tight junction assembly, but unaltered pericyte coverage in mesenteries of *Clec2⁻⁻/Gp5ᴷᴵᴺ* embryos. SMC (**a**) and pericyte (**b**) coverage was analyzed by confocal microscopy by staining for α-smooth muscle actin and NG2, respectively (Leica TCS SP8, 40x objective). Scale bars: 100 μm. Tight junction density was assessed by immunofluorescence staining for ZO-1 (**c**) as well as by immunoblotting (**d**). GAPDH served as a loading control.

4.2 GPVI-triggered platelet α-granule release limits the progression of ROP

ROP is a possibly blinding disease occurring in preterm infants born before gestational week 28, which induces retinal degradation due to aberrant vessel growth.[32] The formation of neovascular tufts is primarily induced by altered VEGFA secretion induced upon sudden changes in the exterior oxygen levels.[27]

4.2.1 Platelet depletion impedes resolution of retinopathy in mice

Recent studies suggested an impact of platelets during the resolution of experimentally induced ROP in mice.[40] In order to verify this data, we assessed retinal vascular development at P17 in healthy mice as well as mice with OIR, being left untreated or upon anti-GPIbα-antibody (R300)-mediated platelet depletion at P15 and 16, by confocal microscopy. As shown in Figure 21a, platelet depletion itself did not affect retinal vascularization as visualized by immunofluorescence labeling using Isolectin-B4.
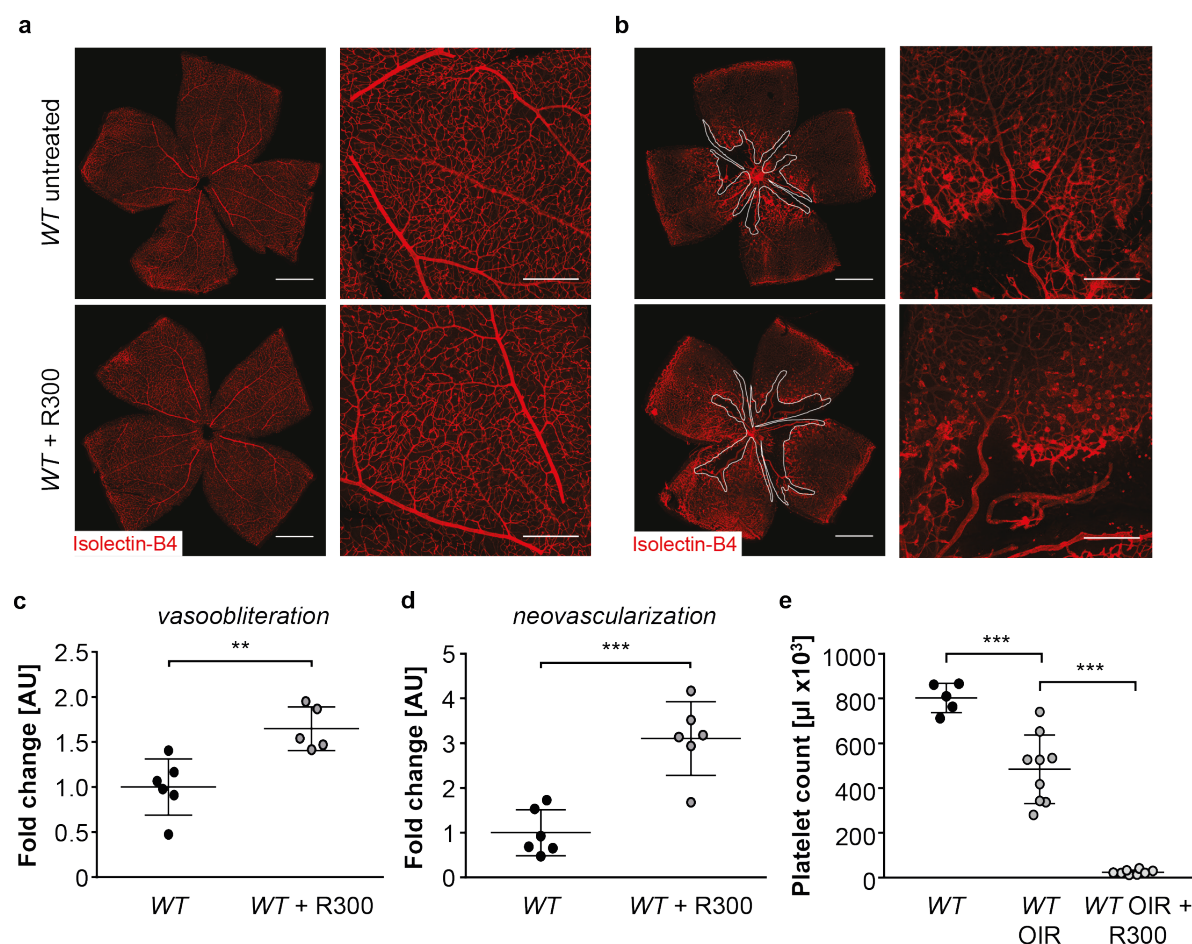
Figure 21. Platelet depletion aggravates the progression of OIR in mice. Retinal vascularization in native (**a**) and mice with induced retinopathy (**b**) was analyzed by confocal microscopy upon staining with Isolectin-B4 at a Leica TCS SP8 (10x objective). Scale bars: 800 µm; insets: 300 µm. Avascular area is encircled in white. Vasoobliteration (**c**) and neovascularization (**d**) upon induction of retinopathy in untreated and platelet-depleted mice were quantified manually using ImageJ Software. Values were normalized to the respective untreated OIR *WT* mice. Values are mean ± SD (n = 6). Unpaired, two-tailed Student's t-test. **P < 0.01; ***P < 0.001. (**e**) Platelet counts in native, OIR and platelet-depleted mice were analyzed at an automated blood cell analyzer. Values are mean ± SD (n = 8). One-way ANOVA with Sidak correction for multiple comparisons. ***P < 0.001.

In contrast, induction of retinopathy in platelet-depleted mice severely deteriorated the resolution of OIR, most evident by an increased abundance of neovascular tufts (Figure 21b, insets). Analysis of the avascular area revealed a significant increase in vessel ablation upon platelet depletion (Figure 21c). Even more strikingly, the degree of neovascularization as a measure for ROP severity revealed a drastically enhanced de-novo vessel growth upon platelet depletion (Figure 21d), thus suggesting platelets to be highly relevant for the resolution of ROP. Interestingly, we observed bleeding into the eye in platelet-depleted mice, suggesting loss of vascular integrity upon severe thrombocytopenia. Of note and in line with previous publications,[40] OIR mice exhibited variable levels of thrombocytopenia compared to control mice (Figure 21e). Taken together, we could confirm that platelet depletion deteriorates the progression of experimental ROP in mice.

4.2.2 Platelet α-granule release is critically involved in the resolution of OIR
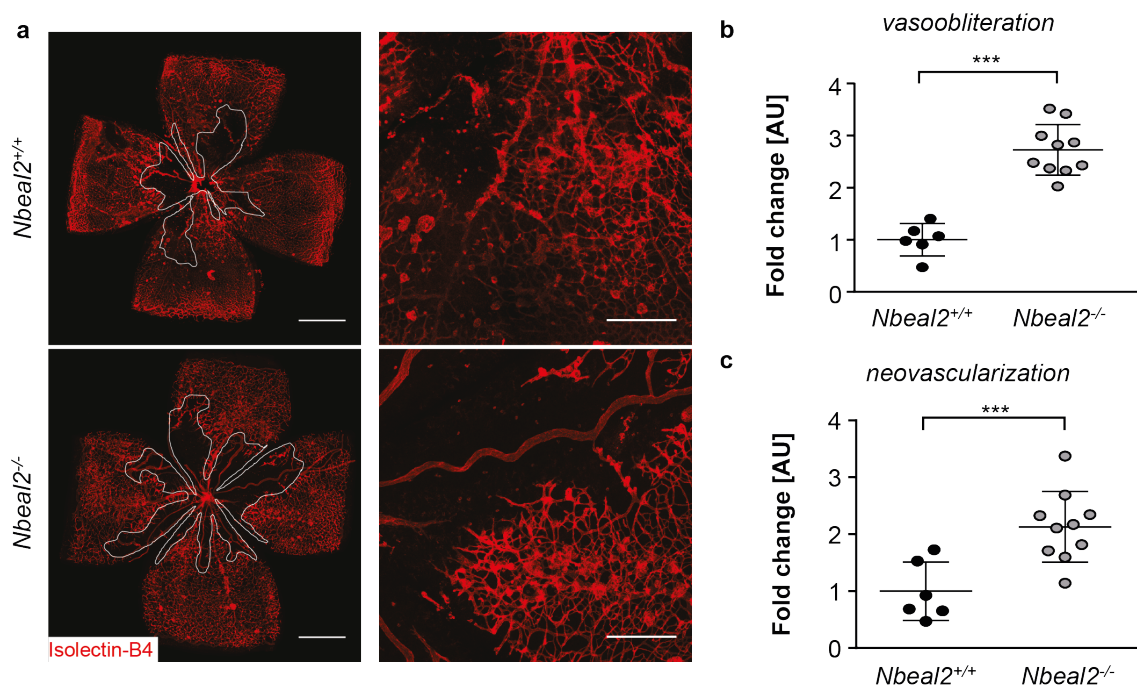

Figure 22. Platelet α-granule content prevents deterioration of OIR. Visualization (**a**) and quantification (**b, c**) of vasoobliteration and neovascularization in *Nbeal2⁻/⁻* and control animals with OIR. Avascular area is encircled in white. Analysis was done using ImageJ Software. Values were normalized to the respective *WT* mice. Values are mean ± SD (n = 6). Unpaired, two-tailed Student's t-test. **P < 0.01; ***P < 0.001.

Since it was suggested that antiangiogenic factors released by platelets upon activation are essential for the amelioration of ROP,[40] we next analyzed how lack of platelet α-granules affected the outcome upon OIR.[99] To this end, we induced experimental retinopathy in *Nbeal2⁻/⁻* mice and the respective controls and assessed the progression of OIR by analyzing the degree of vasoobliteration and neovascularization by confocal microscopy (Figure 22a). Similar to the deterioration of ROP upon platelet depletion, lack of α-granules impeded the resolution of retinopathy resulting in increased avascularization (Figure 22b) and neovascularization (Figure 22c), suggesting that the release of α-granules is indeed critical for limiting the prevalence of aberrant vessels formation during experimental retinopathy.

4.2.3 Blockade or lack of GPIbα does not influence the progression of OIR

Several studies previously implied the platelet receptor GPIbα, the major ligand-binding subunit of the GPIb-V-IX complex, to be critically involved in the maintenance of vascular integrity under inflammatory conditions.[218] To identify a possible role of GPIb-mediated platelet adhesion for the acceleration of ROP resolution, we induced OIR in mice, in which the extracellular domain of GPIbα is exchanged by the human IL4Rα (*IL4Rα-GPIbα-tg*).
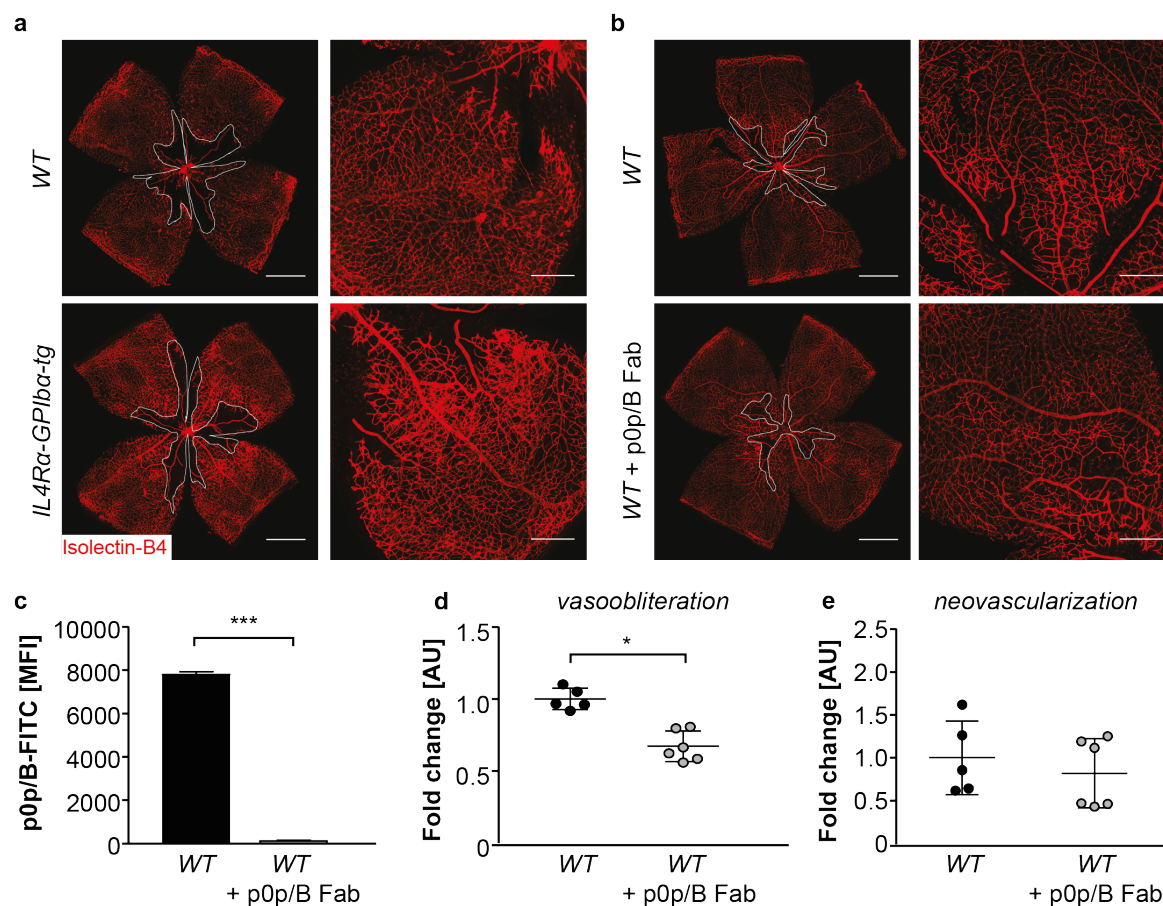
Figure 23. OIR is not affected by lack or blockade of GPIbα. (**a, b**) ROP in *WT* and *IL4Rα-GPIbα-tg* mice (**a**) as well as p0p/B-Fab-injected and control mice (**b**) was visualized by confocal microscopy (Leica TCS SP8, 10x objective). Scale bars: 800 µm; insets: 300 µm. Avascular area is encircled in white. (**c**) Blockade of GPIbα upon injection of p0p/B-Fab was verified by flow cytometry. Values are mean ± SD (n = 6). Unpaired, two-tailed Student's t-test. ***P < 0.001. Analysis of vasoobliteration (**c**) and neovascularization (**d**) in control and p0p/B-Fab-injected animals was performed using ImageJ Software. Values were normalized to the respective untreated OIR *WT* mice. Values are mean ± SD (n = 3). Unpaired, two-tailed Student's t-test. *P < 0.05.

As depicted in Figure 23a, the degree of retinopathy was comparable between *WT* and *IL4Rα-GPIbα-tg* mice (neovascularization score of 1 ± 0.51 in the *WT* vs. 0.80 ±0.43 in the *IL4Rα-GPIbα-tg*). To further support these findings, we next injected mice with a Fab fragment of the GPIbα-blocking antibody p0p/B on day 15 and 16 post birth. Blockade of the receptor was verified by flow cytometry using p0p/B-FITC (Figure 23c). Surprisingly, the degree of vasoobliteration in p0p/B-injected mice was even less severe than in *WT* mice injected with a control antibody (Figure 23d), while no differences in the neovascularization score could be identified (Figure 23e). These findings indicate that GPIbα-mediated platelet deceleration and activation are not involved in the progression of OIR.

4.2.4 Depletion or lack of (hem)ITAM signaling aggravates OIR progression

In addition to GPIbα, several publications implicated the (hem)ITAM receptors CLEC-2 and GPVI as main regulators of vascular integrity during inflammation.[190,193,218] To address whether these receptors might also be involved in the resolution of experimental retinopathy in mice, we first analyzed the progression of OIR in conditional *Clec2⁻/⁻* mice. Interestingly, deficiency in CLEC-2 indeed delayed the resolution of retinopathy as revealed by increased vasoobliteration in CLEC-2-deficient mice (Figure 24a, b). In contrast, neovascularization appeared unaffected by lack of CLEC-2 (Figure 24c), thus suggesting that avascularization and aberrant vessel growth are regulated differentially.
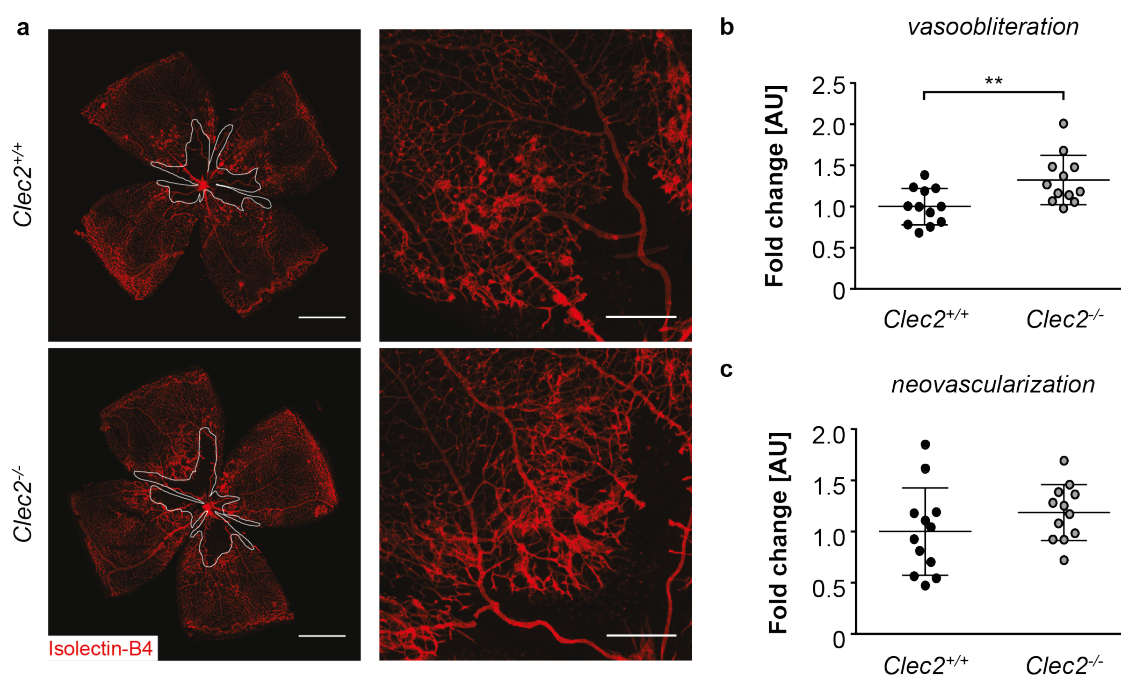
Figure 24. CLEC-2 deficiency delays revascularization upon OIR in mice. OIR in conditional CLEC2-deficient mice and littermate controls at P17 was visualized by confocal microscopy (Leica TCS SP8, 10x objective) (**a**) and analyzed manually using ImageJ Software (**b, c**). Scale bars: 800 μm; insets: 300 μm. Avascular area is encircled in white. Values were normalized to the respective controls. Values are mean ± SD (n = 6). Unpaired, two-tailed Student's t-test. **P < 0.01.

GPVI is the main platelet collagen receptor and critical for platelet activation and consequent firm adhesion to the ECM. In order to identify possible mechanisms leading to α-granule release during OIR, we induced retinopathy in *Gp6⁻/⁻* mice and controls and analyzed the progression of OIR by confocal microscopy. Of note, physiological vascularization at P17 was not affected by the lack of GPVI (Figure 25a). Strikingly, the resolution of vaso-obliteration as well as neovascularization was significantly impaired in the absence of GPVI (Figure 25b-d), which was accompanied by inflammatory bleeding into the eye similar to what was observed upon platelet depletion.

Figure 25. Severely impaired resolution of ROP upon lack of GPVI in mice. Vascularization in *Gp6*^{-/-} and control mice was analyzed under control conditions (**a**) and upon induction of ROP (**b**) at P17 by confocal microscopy (Leica TCS SP8, 10x objective). Scale bars: 800 μm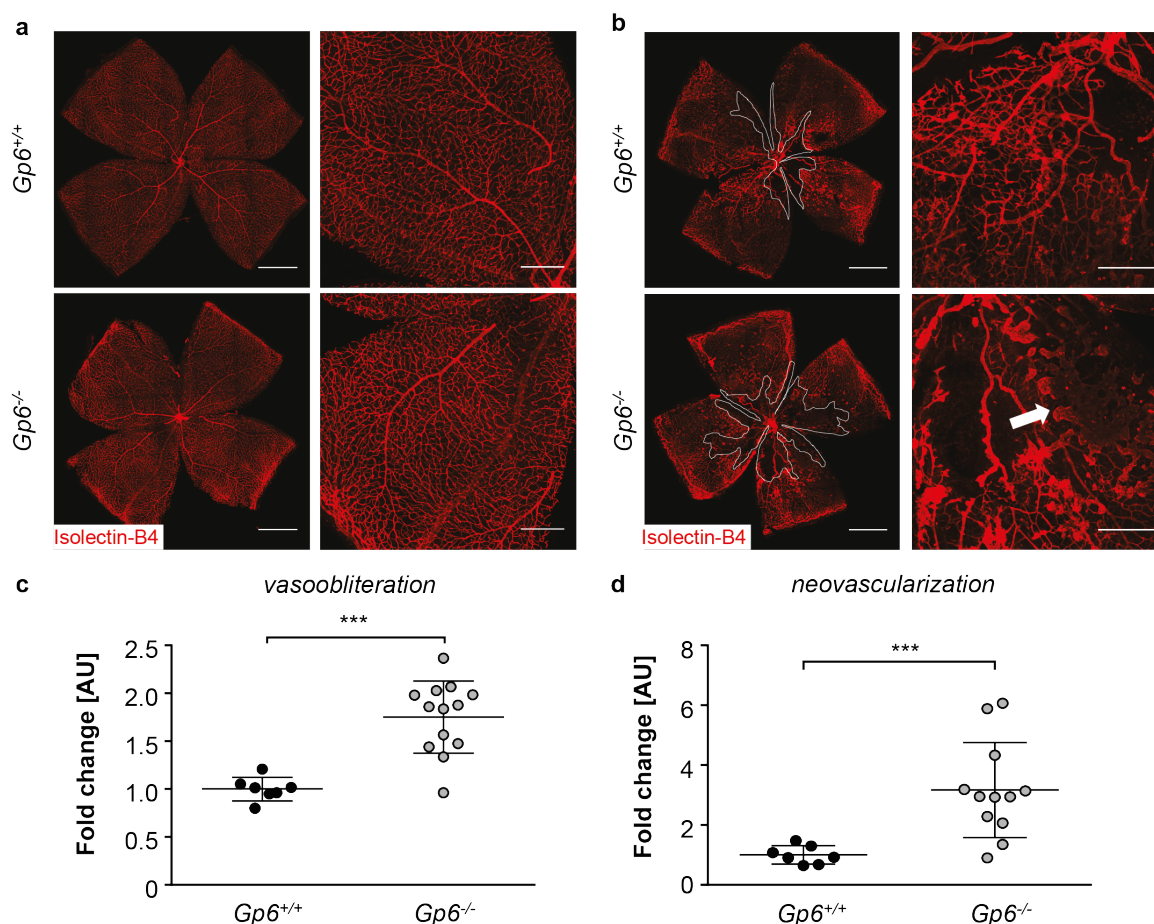; insets: 300 μm. Avascular area is encircled in white. Arrows point to neovascular tufts. (**c, d**) Quantification of vasoobliteration and neovascularization in *WT* and GPVI-deficient mice with ROP. Values were normalized to the respective controls. Values are mean ± SD (n = 4). Unpaired, two-tailed Student's t-test. **P < 0.01.

To further address, whether blockade of the collagen-binding site would be sufficient to prevent GPVI-mediated platelet activation under OIR, we injected mice with JAQ1 F(ab)$_2$ at P15 and 16 and analyzed retinal vascularization as before. Surprisingly, GPVI-blockade, which was verified by flow cytometry (Figure 26c) did not deteriorate ROP under these conditions (Figure 26a, d, e) suggesting that the function of GPVI is either important during an earlier stage or that the collagen-binding site is not involved in the regulation of GPVI-mediated platelet activation under OIR. To address the latter, we therefore injected mice with JAQ1 IgG leading to GPVI-depletion on P7, prior to inducing experimental retinopathy. Loss of GPVI from the platelet surface was verified by flow cytometry (Figure 26f). Interestingly, depletion of GPVI deteriorated OIR progression similarly to platelet depletion manifested by enhanced avascularization (Figure 26g) and an increased abundance of neovascular tufts (Figure 26h).
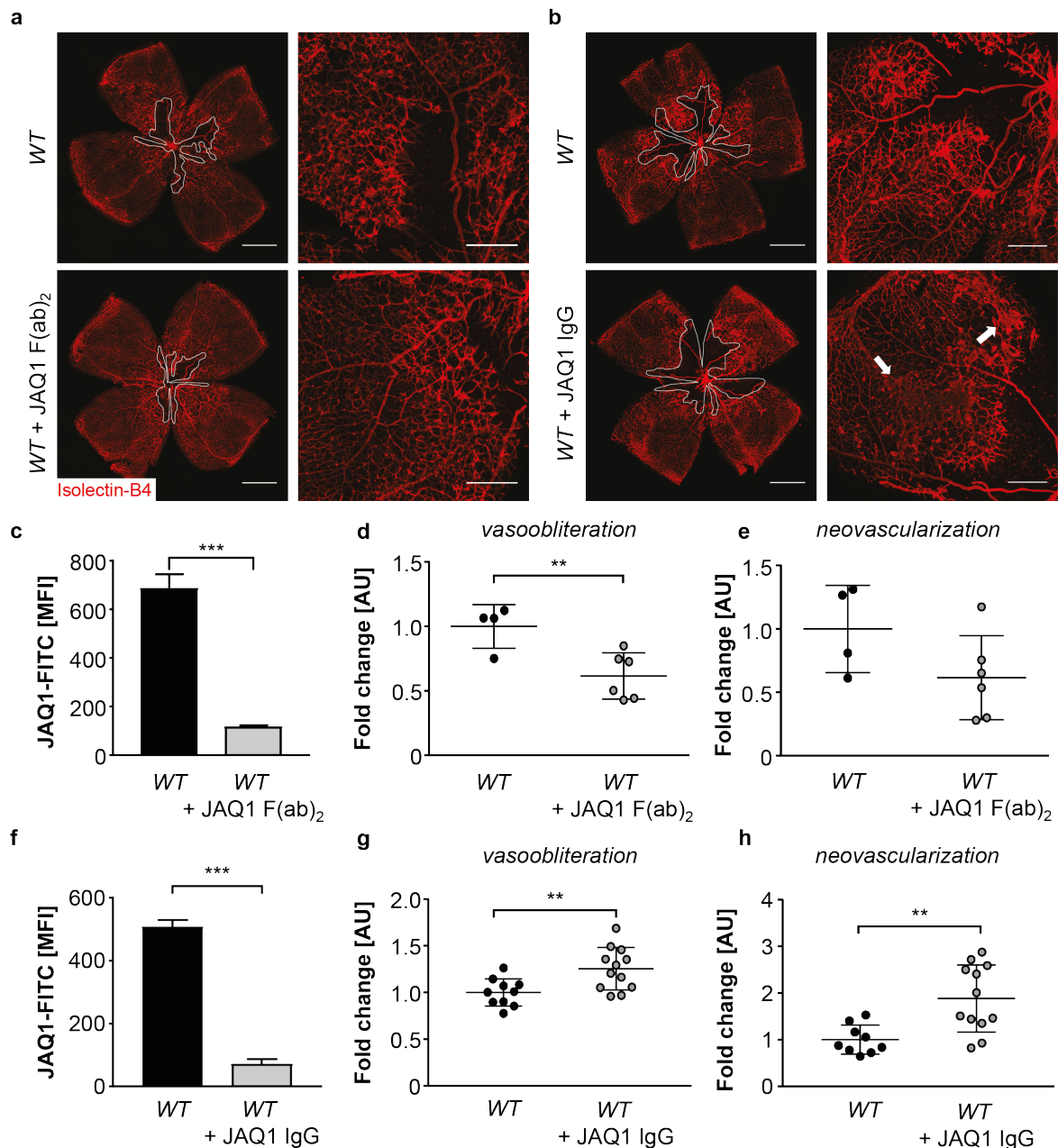
Figure 26. Depletion, but not blockade of GPVI impairs the resolution of OIR in mice. OIR was visualized in mice upon antibody-mediated blockade (**a**) or depletion (**b**) of GPVI by confocal microscopy (Leica TCS SP8, 10x objective). Scale bars: 800 µm; insets: 300 µm. Avascular area is encircled in white. Arrows point to neovascular tufts. GPVI blockade (**c**) or depletion (**f**) was verified by flow cytometry. Values are mean ± SD (n = 3). Unpaired, two-tailed Student's t-test. ***P < 0.001. Vasoobliteration and neovascularization scores in GPVI-blocked (**d, e**) and GPVI-depleted mice (**g, h**) were assessed manually using ImageJ Software. Values were normalized to the respective untreated OIR mice. Values are mean ± SD (n = 6). Unpaired, two-tailed Student's t-test. **P < 0.01.

In summary, these findings point towards a GPVI-mediated platelet activation and subsequent α-granule release to narrow ROP progression. Interestingly, the collagen binding site in GPVI appears not to be required for this to occur.

4.3 Twf1 and Cof1 are critically involved in the regulation of PPF

Previous studies implicated Twf1 to share functions with Cof1, since disruption of both proteins resulted in synthetic lethality in yeast.[113,114] In addition, it was shown to actively induce actin severing and depolymerization in addition to its actin sequestering capacities. Although Twf1 expression was shown to be dispensable for platelet function,[116] a functional overlap with Twf2a or Cof1 in murine MKs was not investigated so far.

4.3.1 Twf1 and 2a have non-redundant functions in MKs and platelets
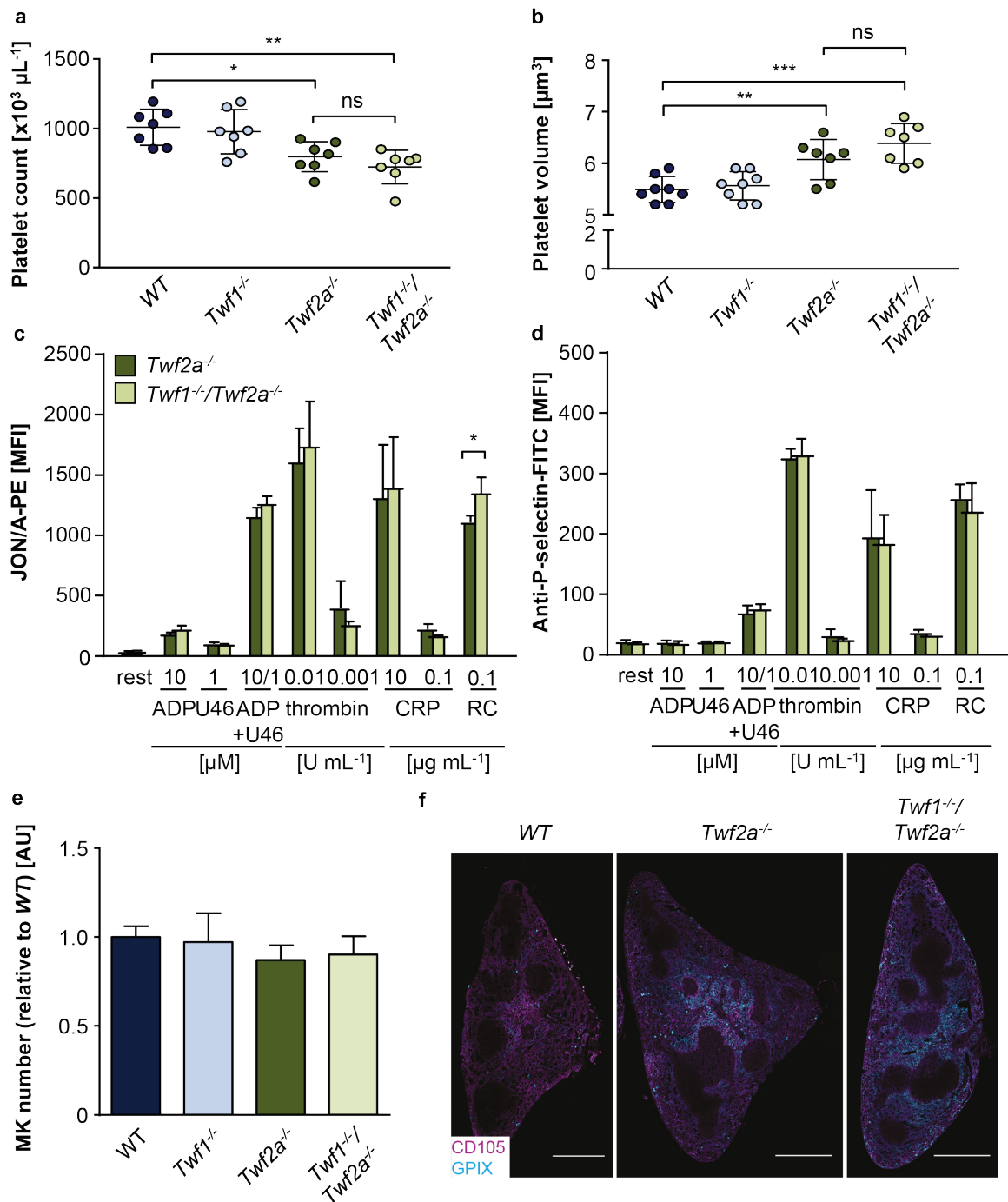
Figure 27. Isoform-specific functions of Twf1 and Twf2a. Platelet counts (**a**) and size (**b**) of *WT, Twf1^{-/-}, Twf2a^{-/-}* and *Twf1^{-/-}/Twf2a^{-/-}* mice were determined with an automated blood cell analyzer. Values are mean ± SD (n = 7). One-way ANOVA with Sidak correction for multiple comparisons. *$P < 0.05$; **$P < 0.01$; ***$P < 0.001$. (**c, d**) Integrin αIIbβ3 activation (**c**) and P-selectin exposure (**d**) of *Twf2a^{-/-}* and *Twf1/2a[-/-]* platelets was assessed by flow cytometry. Values are mean ± SD (n = 4). Unpaired, two-tailed Student's t-test. *$P < 0.05$. Femora and spleen cryosections (**f**) were stained for CD105 and GPIX and analyzed by confocal microscopy (Leica TCS SP8, 25x objective). (**e**) MKs were counted in whole femora using ImageJ software. Values were normalized to *WT* levels. Mean ± SD (n = 3). Scale bars: 750 μm. Becker, Scheller *et al.*, **Blood Adv**, 2020.[219]

Although the role of Twf2a in murine platelets and MKs has been investigated before,[116] a possible redundancy between Twf1 and Twf2a has not been addressed so far. To answer this question, we generated mice lacking both proteins in MKs and platelets and were surprised to find platelet count and size to be unaffected in double-deficient animals when compared to *Twf2a^{-/-}* mice (Figure 27a, b), which have been described to exhibit a mild macrothrombocytopenia and platelet hyperreactivity. Similarly, platelet integrin activation and P-selectin exposure in response to different agonists was not additionally affected (Figure 27c, d).

Figure 28. Conditional deletion of Twf1 and Cof1 results in macrothrombocytopenia. (**a**) Conditional deletion of Twf1 and Cof1 in *WT*, *Twf1⁻ᐟ⁻*, *Cof1⁻ᐟ⁻* and *DKO* platelets was verified by immunoblot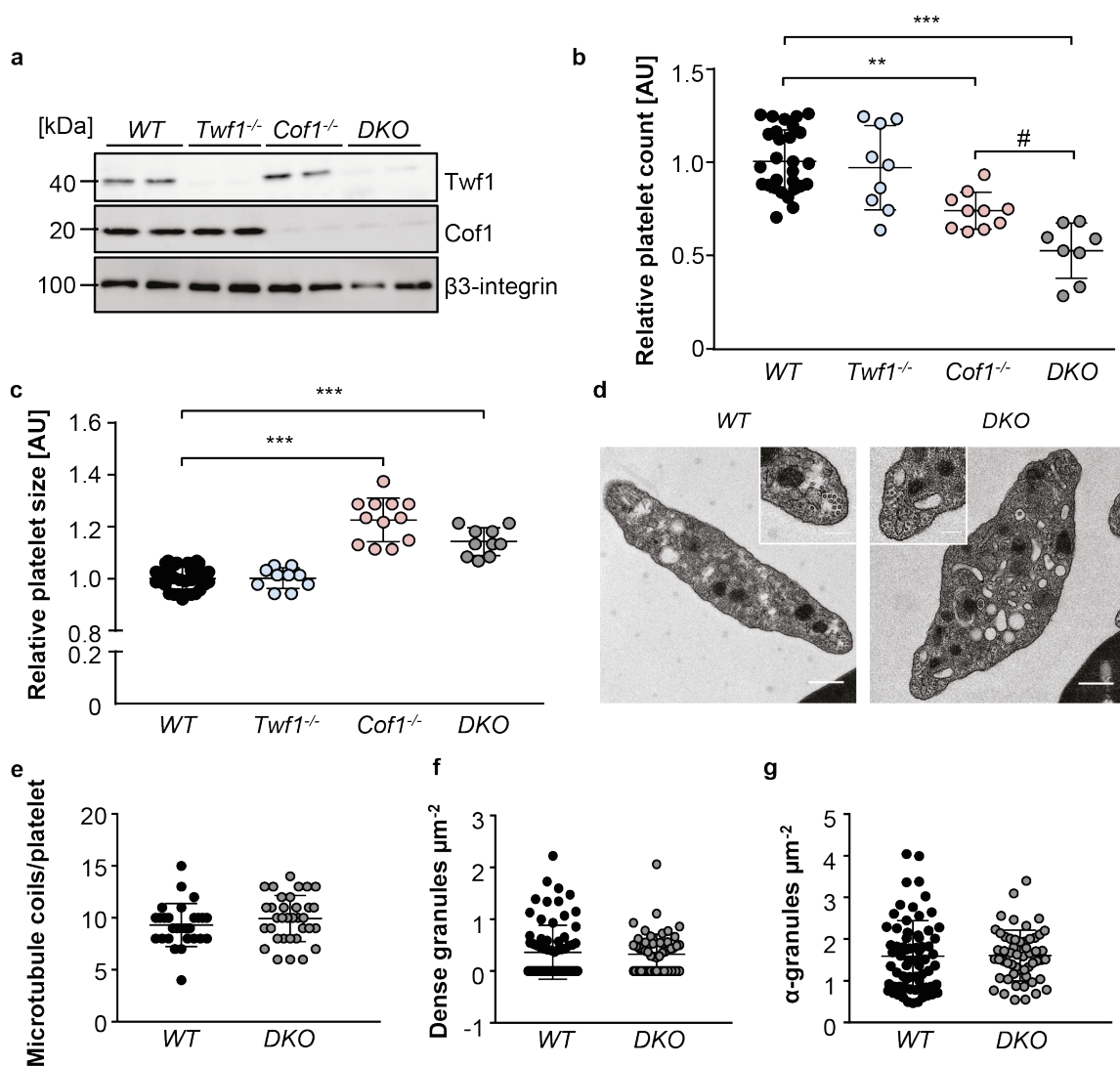ting. Platelet count (**b**) and size (**c**) were analyzed using an automated blood cell analyzer. Values of *Twf1⁻ᐟ⁻*, *Cof1⁻ᐟ⁻* and *DKO* mice were normalized to the respective *WT* control. Values for all *WT* controls are shown. Mean ± SD (n = 9). One-way ANOVA with Sidak correction for multiple comparisons. #P < 0.05; **p < 0.01; ***p < 0.001. (**d**) Platelet microtubule (**e**), dense granule (**f**) and α-granule (**g**) numbers in *WT* and *DKO* platelets were analyzed in transmission electron micrographs and counted manually using ImageJ software. Scale bars: 0.5 µm. Insets display microtubule coils. Scale bars: 0.2 µm. Values are mean ± SD (n = 3). Becker, Scheller *et al.*, **Blood Adv**, 2020.[219]

MK numbers in the BM of *Twf1⁻ᐟ⁻/Twf2a⁻ᐟ⁻* mice as analyzed by immunofluorescent stainings of whole femora cryosections were comparable not only to the *Twf2a⁻ᐟ⁻* littermates, but also to the respective *WT* control (Figure 27e). Moreover, and in agreement with previous observations from *Twf2a⁻ᐟ⁻* mice,[116] Twf1/Twf2a double-deficient mice exhibited an accumulation of GPIX-positive particles in the spleen suggesting enhanced platelet clearance as cause for the observed thrombocytopenia (Figure 27f). In summary, these results exclude a possible redundancy between Twf1 and Twf2a in MKs and platelets.

4.3.2 Persistent macrothrombocytopenia but higher MK numbers in Twf1/Cof1-deficient mice
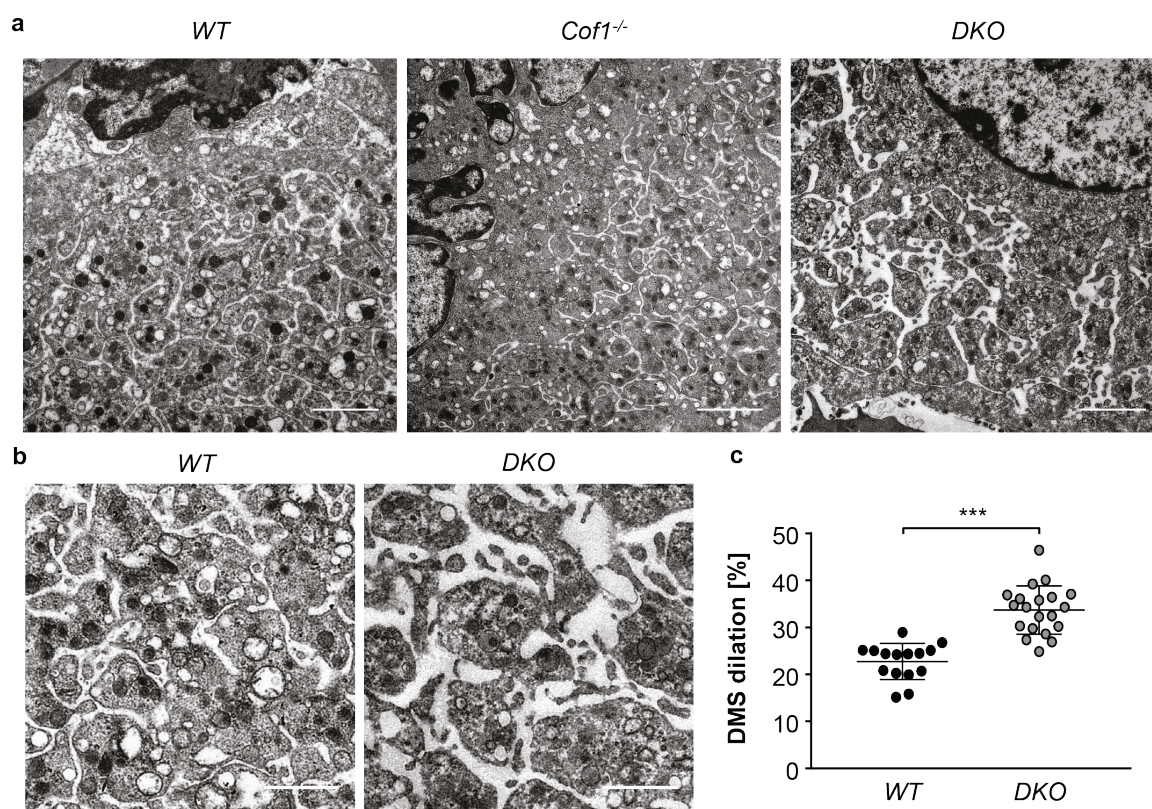
Figure 29. Altered morphology of *DKO* MKs *in situ*. (**a**) BM MKs of *WT*, *Cof1⁻ᐟ⁻* and *DKO* mice were analyzed *in situ* by TEM. Scale bars: 2 µm. (**b**) In-depth analysis of the DMS in *WT* and *DKO* MKs in transmission electron micrographs *in situ*. Scale bars: 1 µm. (**c**) Dilation of the DMS as a measure of impaired DMS maturation was quantified using ImageJ software. At least 5 MKs of each mouse were analyzed. Values are mean ± SD (n = 3). Unpaired, two-tailed Student's t-test. ***P < 0.001. Becker, Scheller *et al.*, **Blood Adv**, 2020.[219]

Since studies from yeast pointed towards a possible functional overlap between Twf1 and Cof1,[114] we next decided to generate conditional Twf1/Cof1 double-deficient mice (*DKO*) lacking both proteins in MKs and platelets. Absence of both proteins was verified by immunoblotting of platelet lysates (Figure 28a). Using an automated blood cell analyzer, we detected a thrombocytopenia in double-deficient mice that was slightly more severe than in the Cof1-deficient controls (Figure 28b). Platelet size on the other hand was not additionally affected (Figure 28c), which is in line with previous descriptions of Cof1 as a regulator of platelet sizing.[110] The increase in platelet size was further verified by TEM (Figure 28d). Interestingly, no differences in α- or dense granule numbers or marginal microtubule coils were detected by analysis of platelet TEM images, suggesting unaffected granule trafficking into platelets (Figure 28e-g). Due to the severe macrothrombocytopenia observed in double-deficient mice, we next sought to investigate possible defects in platelet generation by MKs in the BM. *In situ* analysis of MK morphology and DMS maturation by TEM revealed fewer and irregularly distributed invaginations in Twf1/Cof1-deficient MKs, which was in contrast to the grossly normal DMS maturation in *Cof1*^{-/-} MKs (Figure 29a).
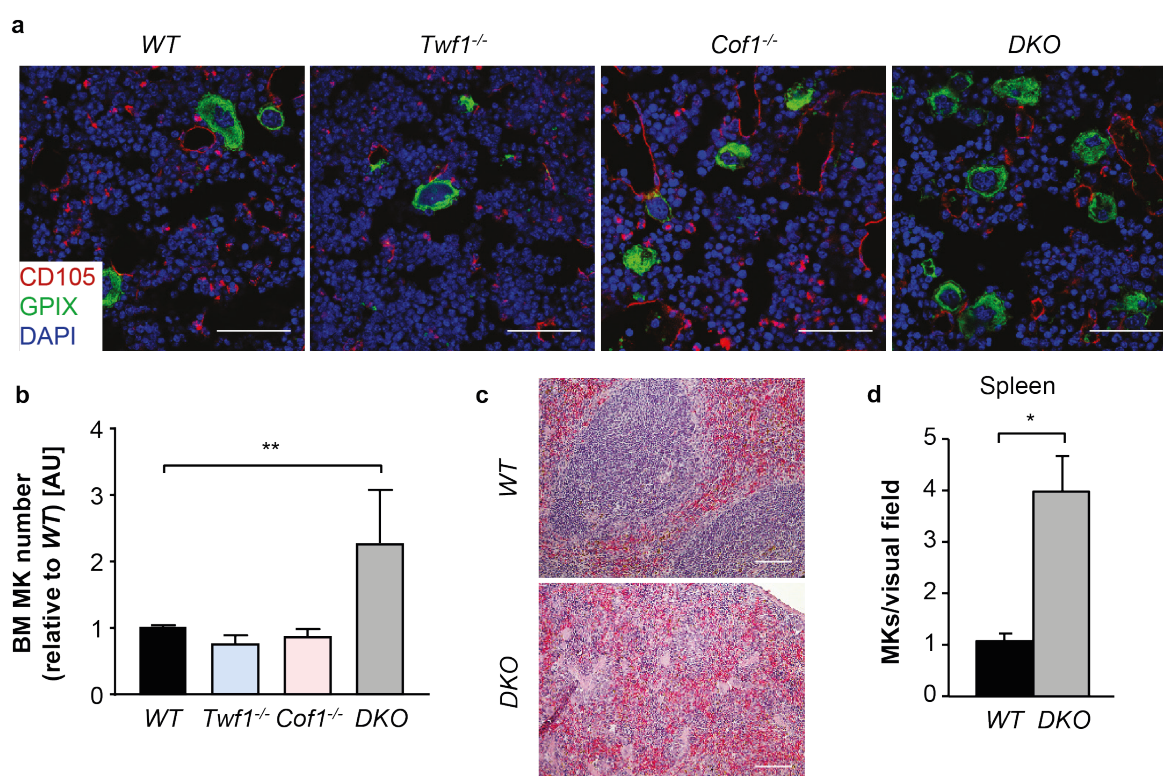
Figure 30. Increased MK numbers in BM and spleen of *DKO* mice. Confocal microscopic visualization (**a**) and quantification (**b**) of MKs and platelets (GPIX; green) as well as endothelial cells (CD105; red) in femora cryosections of *WT*, *Twf1*^{-/-}, *Cof1*^{-/-} and *DKO* mice (Leica TCS SP5, 40x objective). Nuclei were counterstained using DAPI (blue). Scale bars: 50 μm. Values were normalized to the respective WT control. Values are mean ± SD (n = 3). One-way ANOVA with Sidak correction for multiple comparisons. **$P < 0.01$. (**c, d**) MK numbers were counted in H&E-stained paraffin sections of spleens derived from *WT* and *DKO* mice. Values are mean ± SD (n = 3). Unpaired, two-tailed Student's t-test. *$P < 0.05$. Becker, Scheller *et al*., **Blood Adv**, 2020.[219]
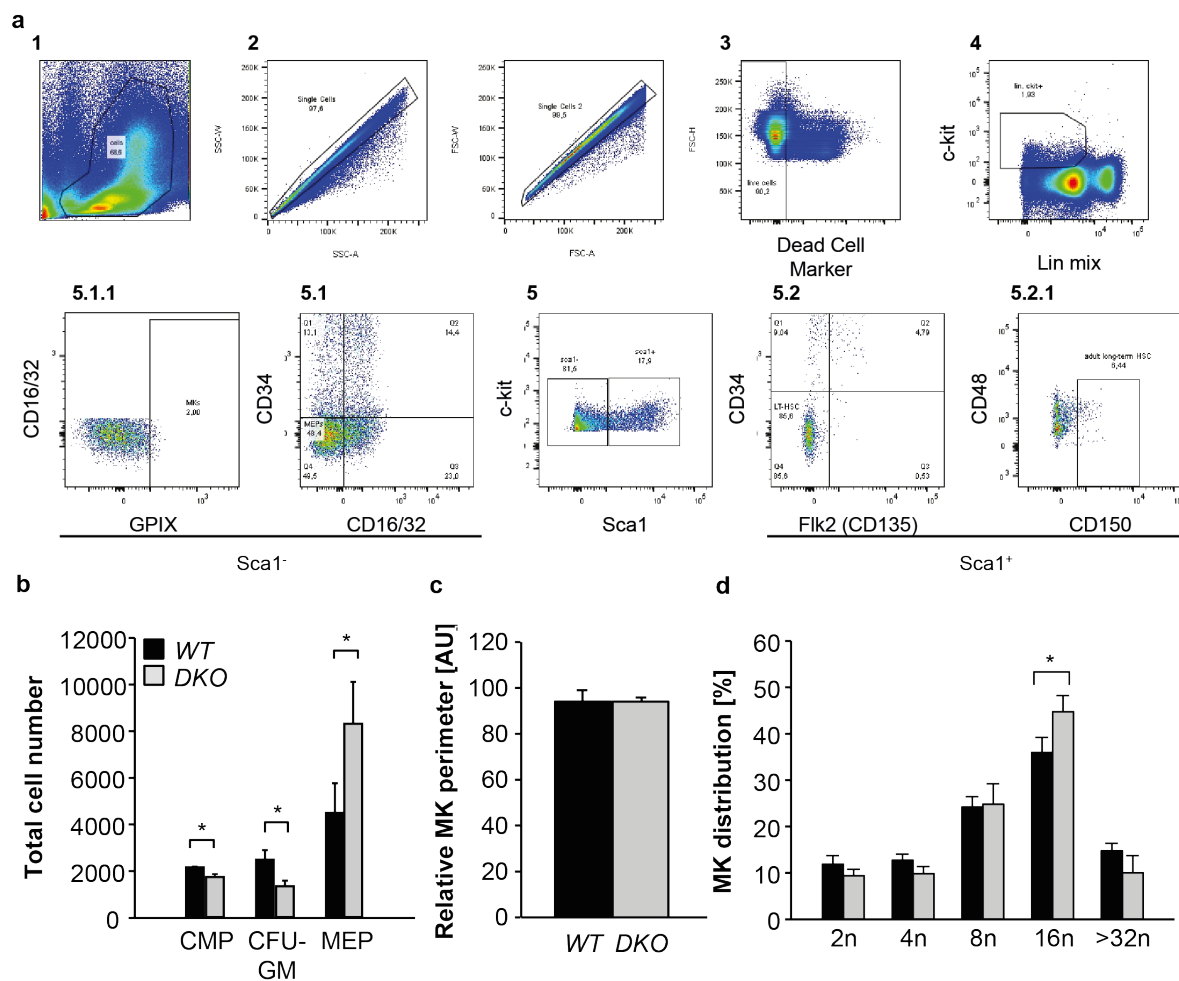
Figure 31. Increased megakaryopoiesis, but unaffected polyploidization and maturation of *DKO* MKs. (**a, b**) Myeloid precursors in flushed BM with adjusted cell count were analyzed by flow-cytometry. Experiment was performed by Carina Gross. Values are mean ± SD (n = 6). Unpaired, two-tailed Student's t-test. *P < 0.05. (**c**) *WT*- and *DKO*-derived, TPO-conditioned BM MKs were analyzed by brightfield microscopy and the relative size was determined using ImageJ Software. At least 50 MKs per animal were analyzed. Values are mean ± SD (n = 3). (**d**) Whole BM was stained for MKs using a FITC-labeled anti-αIIbβ3 antibody (clone 5D7) and DNA distribution was determined by flow cytometry upon labeling of DNA using propidium iodide. Values are mean ± SD (n = 3). Unpaired, two-tailed Student's t-test. *P < 0.05. Becker, Scheller *et al.*, **Blood Adv**, 2020.[219]

DMS dilation as a measure of defective maturation of the DMS and analyzed by thresholding of the invagination diameter was markedly increased in double-deficient MKs (Figure 29b, c) suggesting impaired cytoplasmic maturation upon loss of Twf1 and Cof1. In addition, the number of MKs in the BM of double-deficient mice was significantly increased as assessed by manual quantification of MKs in whole femora cryosections (Figure 30a, b). A similar increase in MK numbers was detected in H&E-stained paraffin sections of the spleen (Figure 30c, d) pointing towards extramedullary hematopoiesis in *Twf1⁻ᐟ⁻/Cof1⁻ᐟ⁻* mice. In line with the dramatically increased MK numbers, we identified an elevated amount of MEPs in the BM of double-deficient mice as assessed by flow cytometry, while the number of CMPs was simultaneously reduced (Figure 31a, b). Although MK cytoplasmic maturation appeared to be

defective *in situ*, MK size of Twf1/Cof1-deficient MKs upon *in vitro* maturation using TPO was unaltered compared to the *WT* control (Figure 31c) as was MK ploidy determined by flow cytometry in primary BM MKs (Figure 31d). Conforming to the enhanced MK mass, we found TPO levels to be significantly decreased in double-deficient mice (Figure 32a). Since previous studies identified constant TPO signaling to account for increased MK numbers,[220] we next assessed TPO signaling in platelets (Figure 32b, c) and MKs (Figure 32d, e) and found it to be unaltered in comparison to the *WT*, which was in line with the normal maturation of double-deficient MKs upon stimulation with TPO *in vitro* (Figure 31c). Taken together, these findings identify Twf1 and Cof1 to be critically involved in cytoplasmic MK maturation and subsequent platelet generation *in situ*, while they appear to be dispensable for endomitosis.
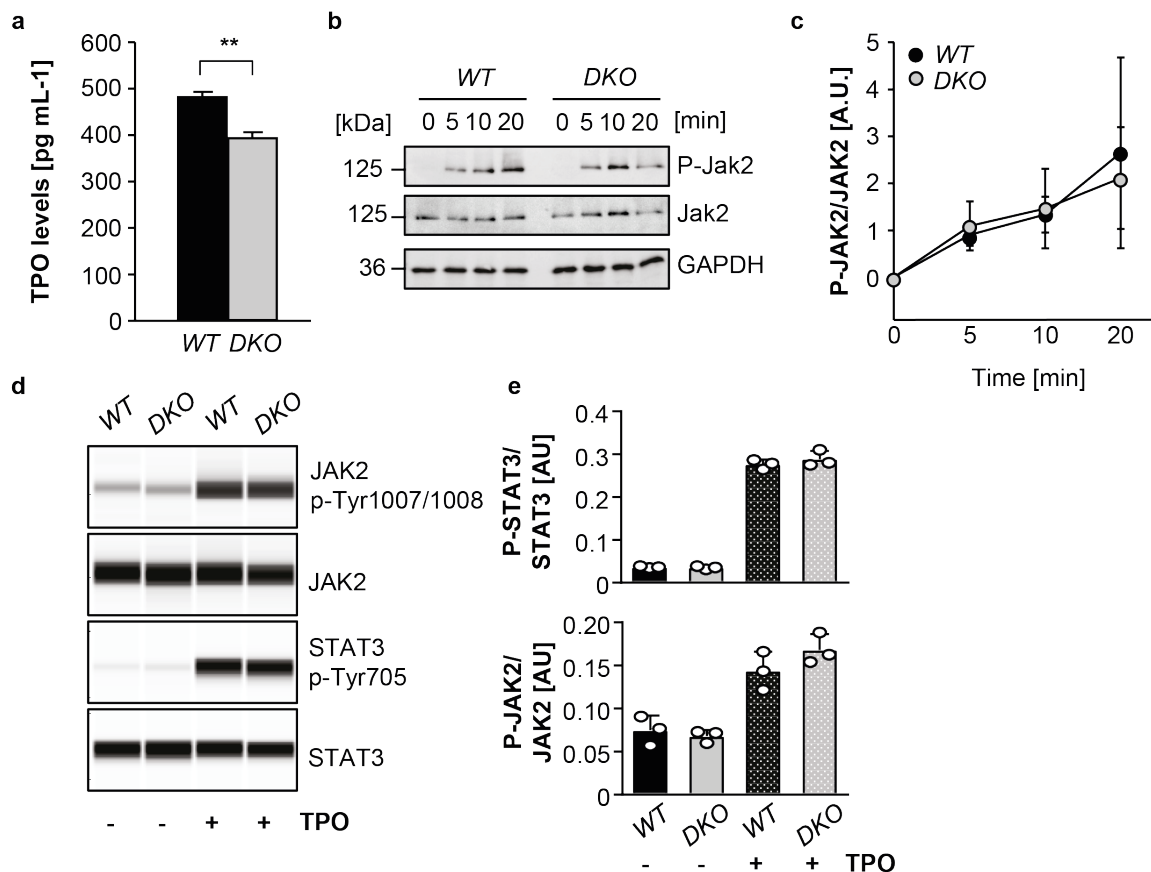
Figure 32. Unaltered TPO signaling in *DKO* platelets and MKs. (**a**) TPO levels in citrated plasma of *WT* and *DKO* mice were assessed using an immunosorbent assay. Values are mean ± SD (n = 3). Unpaired, two-tailed Student's t-test. **P < 0.01. (**b, c**) JAK2 phosphorylation (Tyr1007/1008) was assessed by immunoblotting upon stimulation of *WT* and *DKO* platelets with 50 ng mL^{-1} TPO for 20 min. (**b**) Images were acquired at an Amersham Image 680. (**c**) Densitometric analysis was performed using ImageJ Software. Values are mean ± SD (n = 3). (**d, e**) STAT3 and JAK2 phosphorylation following starvation and subsequent stimulation of MKs with TPO for 10 min were analyzed (**d**) and densitometrically quantified (**e**) by automated immunoblotting. Immunoblotting was performed by Dr. Zoltan Nagy. Values are mean ± SD (n = 3). Becker, Scheller *et al.*, **Blood Adv**, 2020.[219]

4.3.3 Defective PPF of double-deficient MKs *in vitro* and *in vivo*

Despite the marked increase in the number of BM MKs in *DKO* mice compared to *Cof1*^{−/−} mice, platelet counts were still significantly reduced suggesting ineffective proplatelet generation *in vivo*. To further verify this hypothesis, we analyzed platelet lifespan and recovery upon depletion. While the half-life of fluorescently labeled platelets was unaltered in double-deficient mice (Figure 33a), recovery of platelet counts upon GPIbα-mediated platelet depletion was notably delayed in *Twf1*^{−/−}/*Cof1*^{−/−} mice (Figure 33b). This apparent decrease in platelet generation was in line with a slightly impaired PPF from double-deficient MKs *in vitro* (Figure 33c). To test this notion, PPF was further visualized by two-photon intravital microscopy in the BM of the skull.
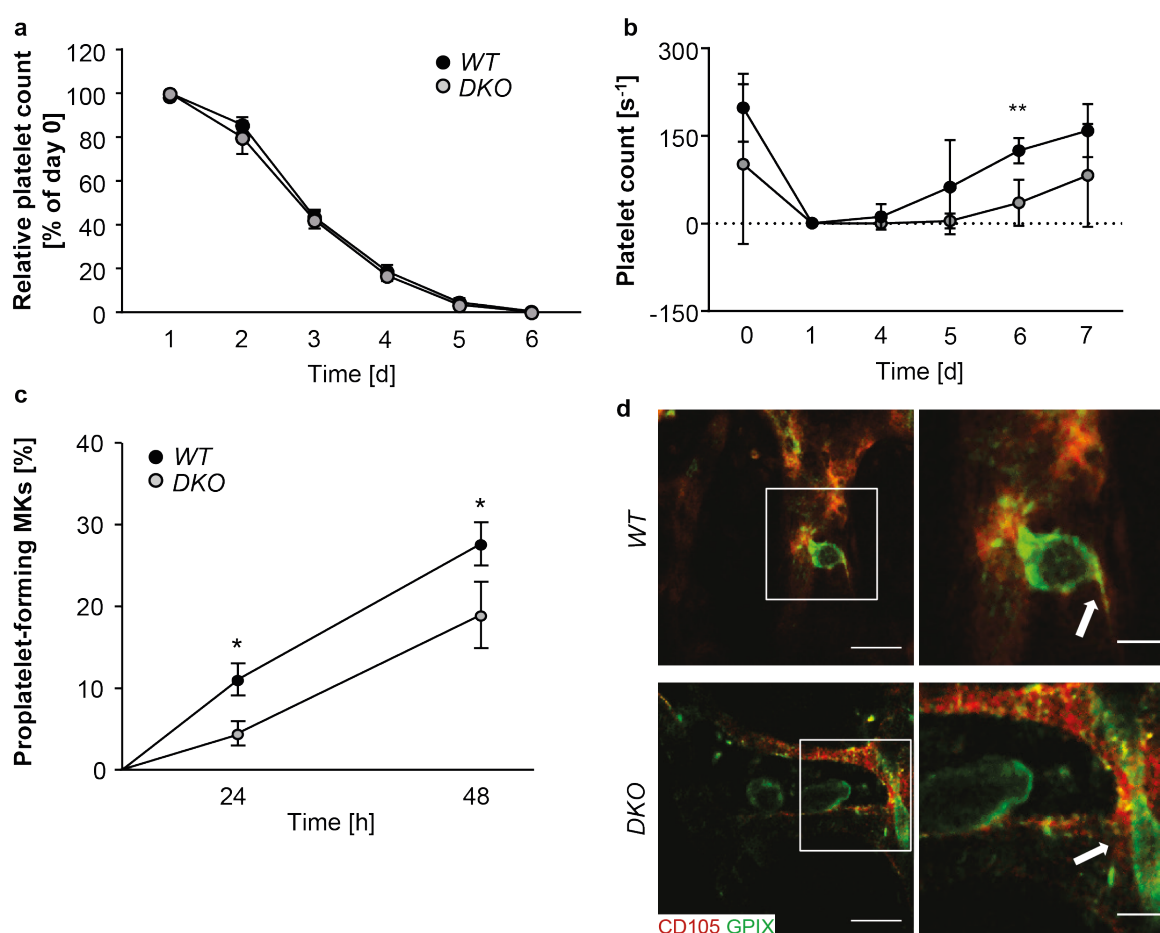
Figure 33. Reduced PPF in the absence of both Cof1 and Twf1. (**a**) Platelet clearance was analyzed upon injection of a Dylight488-conjugated anti-GPIX antibody derivative and subsequent assessment of the fluorescence-positive platelet population at the indicated time points by flow cytometry. (**b**) Platelets in *WT* and *DKO* mice were depleted by i.p. injection of R300. Platelet size and count were determined by flow cytometry over 7 consecutive days. Values are mean ± SD (n = 5). Unpaired, two-tailed Student's t-test. **P < 0.01. (**c**) PPF of *DKO* MKs was assessed by brightfield microscopy. Values are mean ± SD (n = 3). Unpaired, two-tailed Student's t-test. *P < 0.05. (**d**) Intravital two-photon microscopy of BM MKs (GPIX; green) in the skull. Blood vessels were visualized with BSA-FITC and CD105 AlexaF488. Arrows point to proplatelet shafts reaching into sinusoidal vessels. Scale bars: 50 μm; Insets: 20 μm. Becker, Scheller *et al.*, **Blood Adv**, 2020.[219]

While platelet generation from *WT* MKs was evident as a rapid release of preplatelets from elongated proplatelet shafts into vessel sinusoids, proplatelet protrusions in double-deficient mice appeared thickened and shortened in size (Figure 33d). Moreover, the aberrantly stable shafts were not shed off by shear forces as rapidly as in the *WT* or the *Cof1*^{-/-} controls, but rather stayed attached to the respective MK during the observation period of up to 20 minutes. These findings prompted us to investigate the cytoskeleton of proplatelet-forming MKs by confocal fluorescence microscopy.
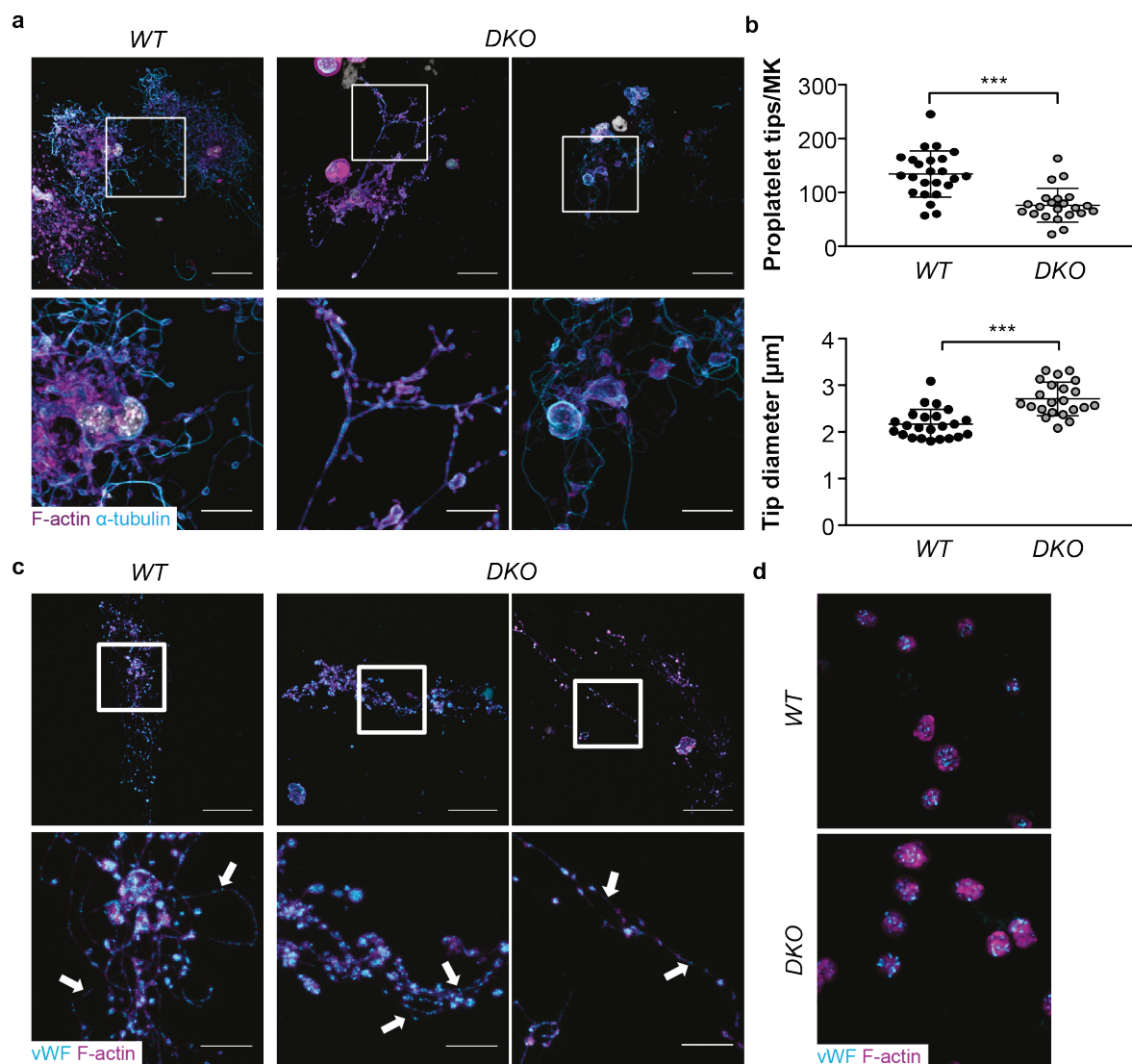
Figure 34. Defective proplatelet generation, but unaltered granule distribution into *DKO* MKs. (**a**) Proplatelets were stained for α-tubulin and F-actin and analyzed by confocal microscopy (Leica TCS SP8, 40x objective). Scale bars: upper panels: 50 µm; lower panels: 20 µm. (**b**) Number of proplatelet tips per MK and tip size of *in vitro*-matured *WT* and *DKO* MKs was analyzed using ImageJ Software. Values are mean ± SD (n = 3). Unpaired, two-tailed Student's t-test. ***P < 0.001. Granule distribution into proplatelets (**c**) and resting platelets (**d**) was visualized using a FITC-labeled vWF antibody and phalloidin-Atto647N and analyzed by confocal microscopy (40x objective, Leica TCS SP8). Scale bars: upper panels: 50 µm; lower panels: 20 µm. Becker, Scheller *et al.*, **Blood Adv**, 2020.[219]

Visualization of F-actin and microtubules by immunofluorescence revealed markedly thickened proplatelet shafts in the absence of Twf1 and Cof1 (Figure 34a). Moreover, the number of proplatelets formed by each individual MK was significantly lower in double-deficient MKs with a notable increase in proplatelet diameter, which was in line with the elevated platelet size *in vivo* (Figure 34b). Granule trafficking on the other hand as visualized by staining for vWF appeared to be unaffected in *DKO* MKs (Figure 34c), which was reminiscent of unaltered granule numbers (Figure 28e-g) and distribution (Figure 34d) into double-deficient platelets. In contrast to *Twf1$^{-/-}$/Cof1$^{-/-}$* MKs, PPF in the absence of either Twf1 (Figure 35a) or Cof1 (Figure 35b) was unaltered compared to the respective control in line with a normal morphology of the cytoskeleton in proplatelet-forming MKs spread on fibrinogen and analyzed by confocal microscopy (Figure 35c). These findings thus highlight the important roles of both Twf1 and Cof1 during PPF from BM MKs *in vitro* and *in vivo*.
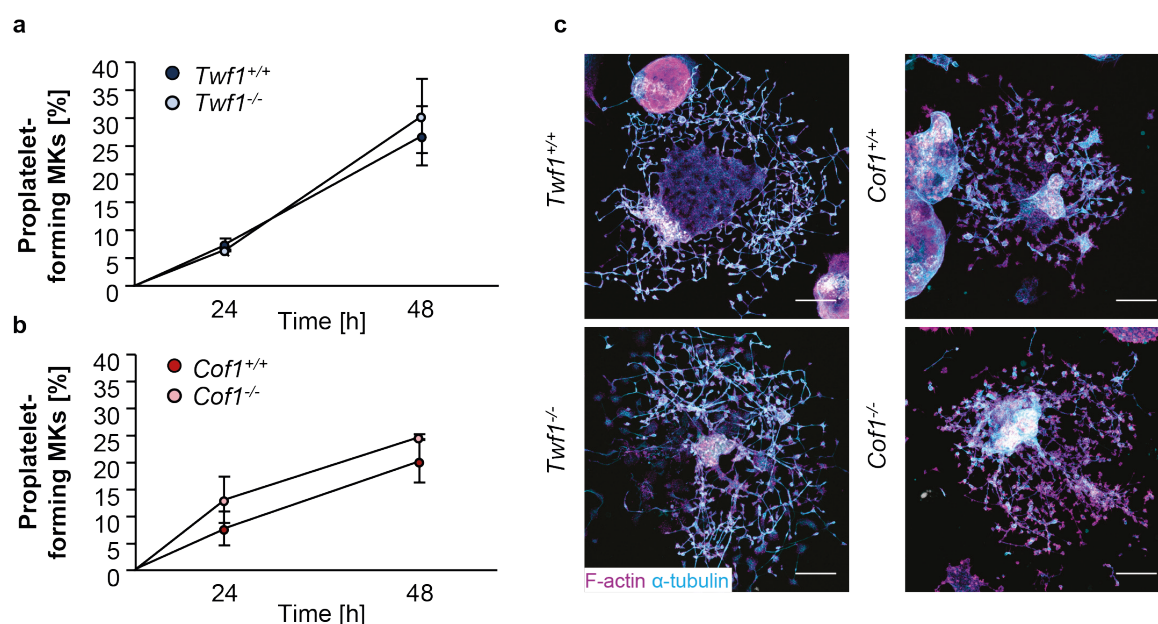
Figure 35. Loss of Twf1 or Cof1 does not affect PPF *in vitro*. (**a, b**) Proplatelet-forming MKs derived from *Twf1$^{-/-}$* or *Cof1$^{-/-}$* mice were counted using a light microscope (40x objective). Average of 5 analyzed visual fields. Values are mean ± SD (n = 3). (**c**) Visualization of actin and microtubule cytoskeleton of *Twf1$^{-/-}$* or *Cof1$^{-/-}$* MKs spread on fibrinogen by confocal fluorescence microscopy (Leica TCS SP8; 40x objective). Scale bars: 50 μm. Becker, Scheller *et al*., **Blood Adv**, 2020.[219]

4.3.4 Defective actin distribution in spread *Twf1$^{-/-}$/Cof1$^{-/-}$* MKs

We next sought to investigate whether the defective proplatelet elongation and release was caused by altered cytoskeletal dynamics in double-deficient MKs. To this end, we allowed spreading of *Twf1$^{-/-}$/Cof1$^{-/-}$* MKs and the respective *WT* control on Horm collagen and analyzed spreading area and F-actin distribution by confocal microscopy (Figure 36a). As apparent upon visualization of F-actin and α-tubulin by immunofluorescence, double-deficient

MKs displayed a marked reduction in spreading area (Figure 36c) with a concomitant increase in the amount of F-actin as assessed by quantification of fluorescence intensity of phalloidin in relation to α-tubulin (Figure 36b, d). Additionally, the formation of actin-rich podosome-like structures, which have been implied to be important for the degradation of basement membrane proteins during PPF from BM MKs *in vivo*, was dramatically decreased in double-deficient MKs (Figure 36e, f). Podosome density on the other hand, which was normalized to the respective spreading area, was only affected upon analysis of the F-actin channel, while Arp2, expressed in the podosome core, appeared to be distributed normally (Figure 36e).
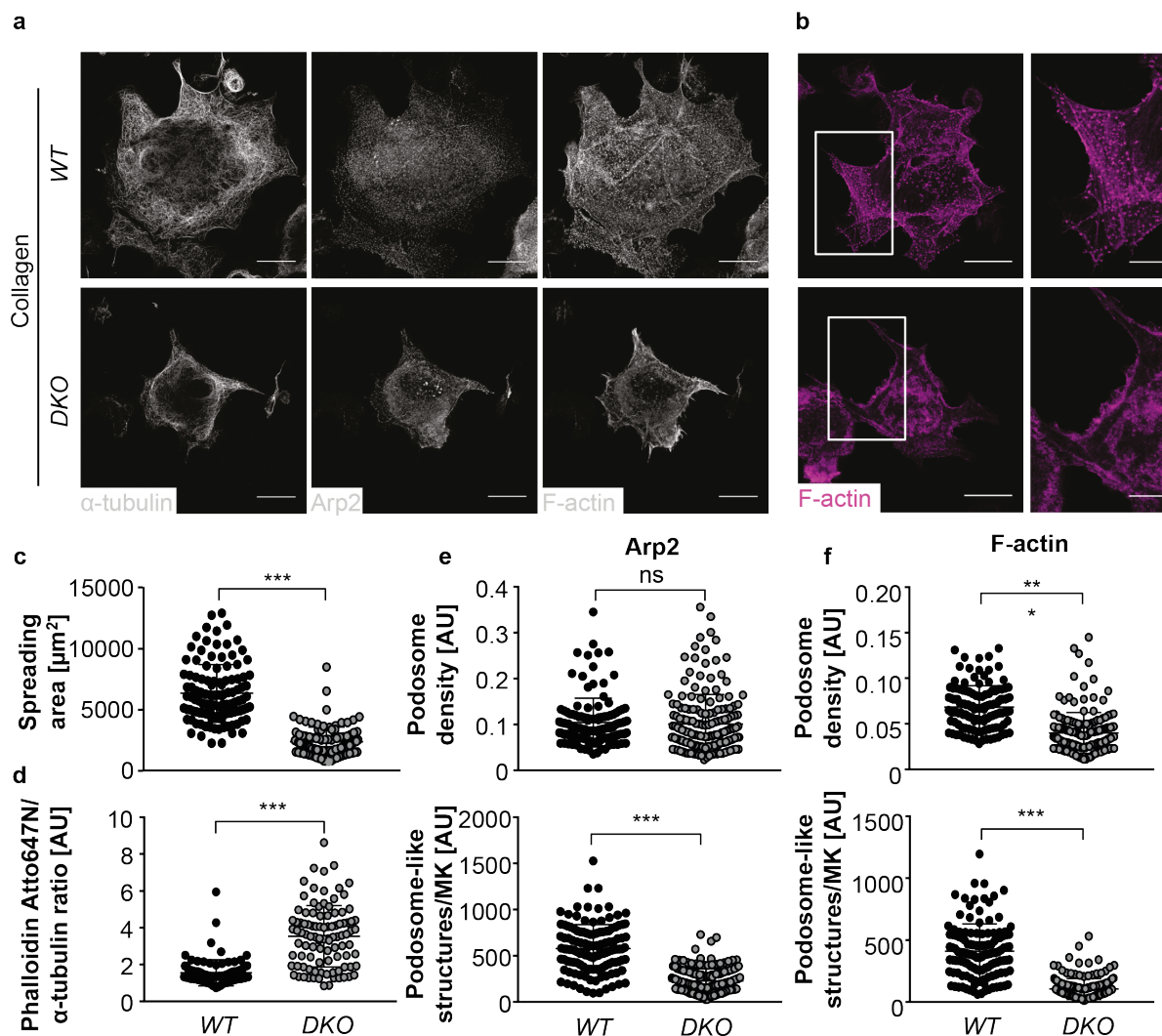
Figure 36. Aberrant spreading of *DKO* MKs on Horm collagen. (a, b) BM-derived *WT* and *DKO* MKs were spread on Horm collagen and analyzed by confocal microscopy (Leica TCS SP8, 40x objective). Representative lowest-plane images. Scale bars: 25 µm; insets: 10 µm. (**c**) Spreading area was quantified in at least 30 MKs per mouse using ImageJ Software. Values are mean ± SD (n = 3). (**d-f**) Analysis of F-actin cytoskeleton in *WT* and *DKO* MKs spread on Horm collagen. Quantification of phalloidin-Atto647N FI normalized to α-tubulin (**d**), podosome density (number per µm^2) as well as total numbers in the Arp2- (**e**) and F-actin- (**f**) channel in control and *DKO* MKs spread on Horm collagen. Quantification was done using ImageJ Software. Unpaired, two-tailed Student's t-test. ***P < 0.001. Becker, Scheller *et al*., **Blood Adv**, 2020.[219]

Similar observations of decreased spreading area (Figure 37a, b), increased F-actin content (Figure 37c) and reduced podosome density (Figure 37d) were made when spreading of double-deficient MKs on fibrinogen was investigated, suggesting a generally defective cytoskeletal functionality irrespective of the extracellular substrate. In agreement with this, double-deficient MKs analyzed by confocal microscopy in suspension also displayed an increased phalloidin fluorescence intensity (Figure 38a). In line with this increased F-actin content of *in vitro*-matured MKs, analysis of double-deficient MKs *in situ* also revealed aberrant F-actin accumulations in the periphery (Figure 38b, arrows).
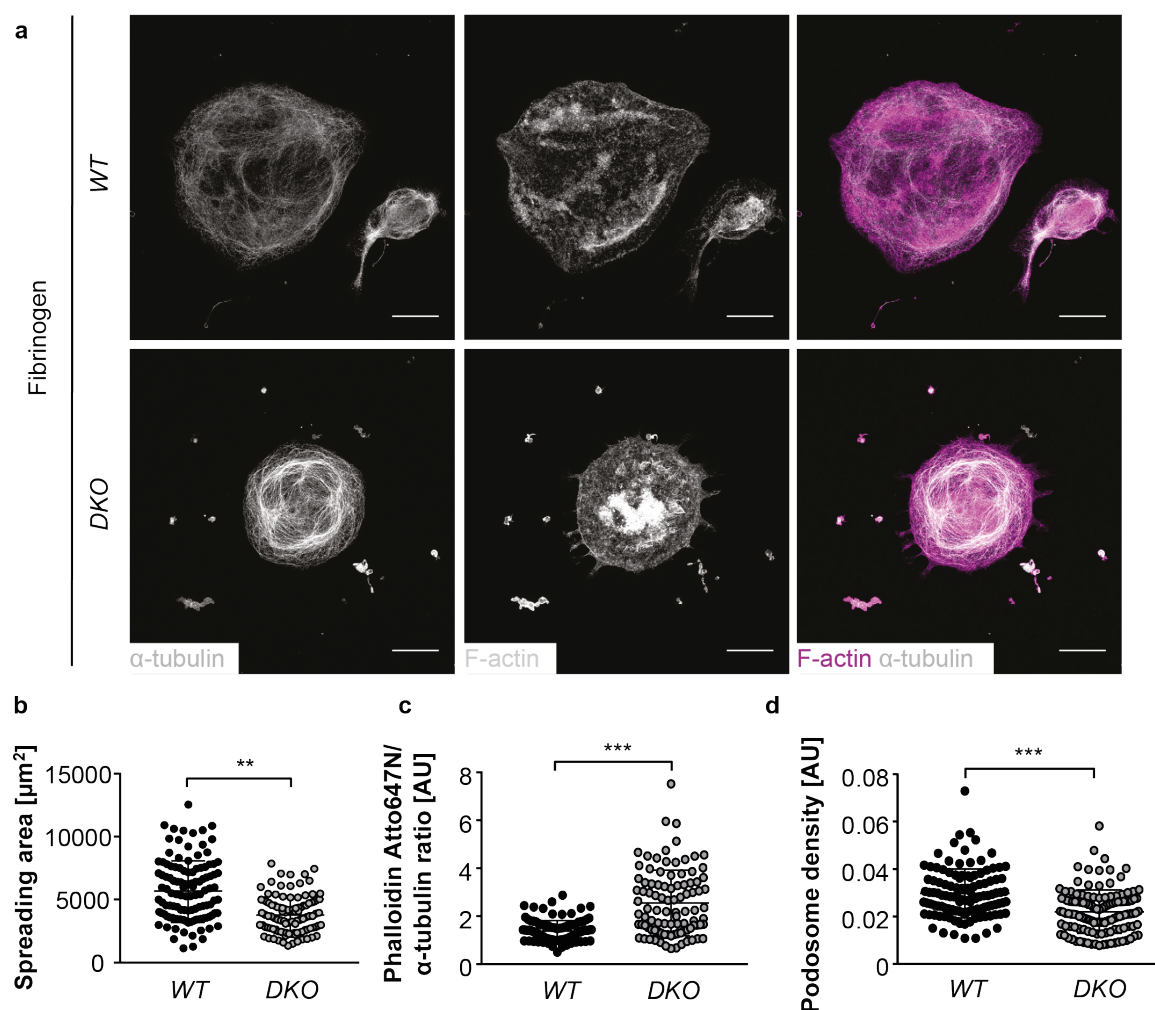
Figure 37. Impaired actin dynamics in *DKO* MKs spread on fibrinogen. Spreading area (**b**), phalloidin FI normalized to α-tubulin (**c**) and podosome density (**d**) of at least 30 BM-derived *WT* and *DKO* MKs per animal spread on fibrinogen were analyzed by confocal fluorescence microscopy (**a**) (Leica TCS SP8, 40x objective) and analyzed using ImageJ Software. Values are mean ± SD (n = 3). Unpaired, two-tailed Student's t-test. *P < 0.05; **P < 0.01; ***P < 0.001. Becker, Scheller *et al.*, **Blood Adv**, 2020.[219]

Of note, impaired spreading, increased F-actin content and a reduced density of podosome-like structures were to a much lesser extent also observed in *Cof1*^{-/-} MKs, whereas spreading

capacities were unaltered upon lack of Twf1 (Figure 39a-f). In summary, these findings imply critical overlapping functions of Twf1 and Cof1 in actin remodeling during MK spreading.
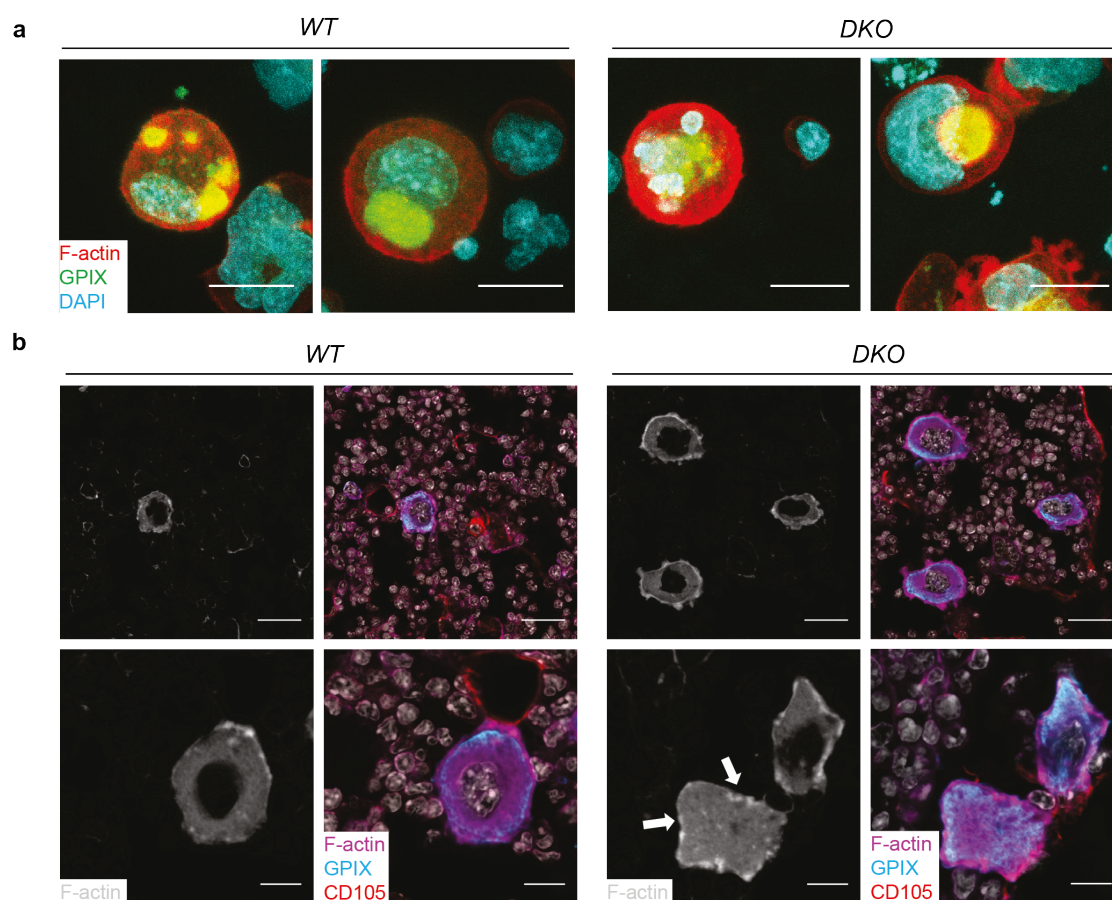
Figure 38. Aberrant F-actin accumulation in *DKO* BM MKs *in vitro* and *in situ*. (**a**) *WT* and *DKO* MKs stained for α-tubulin and F-actin were analyzed in suspension at a Leica TCS SP8 (40x objective). Scale bars: 20 μm. (**b**) Sinusoidal vessels (CD105), megakaryocytes (GPIX) and F-actin (phalloidin) were visualized in femoral cryosections of *WT* and *DKO* mice and imaged using a Leica TCS SP8 (40x objective). Arrows point to irregular F-actin accumulations in the MK periphery (n = 3). Scale bars: upper panel: 25 μm; lower panel: 10 μm. Becker, Scheller *et al*., **Blood Adv**, 2020.[219]

4.3.5 Altered microtubule modifications account for defective platelet generation in Twf1/Cof1-deficient mice

Since proplatelet elongation has been described to be mainly microtubule-driven we next investigated whether the impaired PPF from double-deficient MKs could be attributed to altered posttranslational modifications. Both acetylation and detyrosination have been associated with increased microtubule longevity,[127,221] which prompted us to assess levels of detyrosinated and acetylated microtubules in spread MKs. Interestingly, spread double-deficient MKs analyzed by confocal microscopy exhibited increased microtubule detyrosi-nation as well as acetylation, on both Horm collagen (Figure 40b) as well as fibrinogen (Figure 40d). Consistent with the altered posttranslational modifications, *WT* MKs treated

with the microtubule-disrupting toxin colchicine displayed marked spreading defects, while treatment of *Twf1*^{-/-}/*Cof1*^{-/-} MKs did not affect spreading area, as before irrespective of the used substrate (Figure 40c, e).
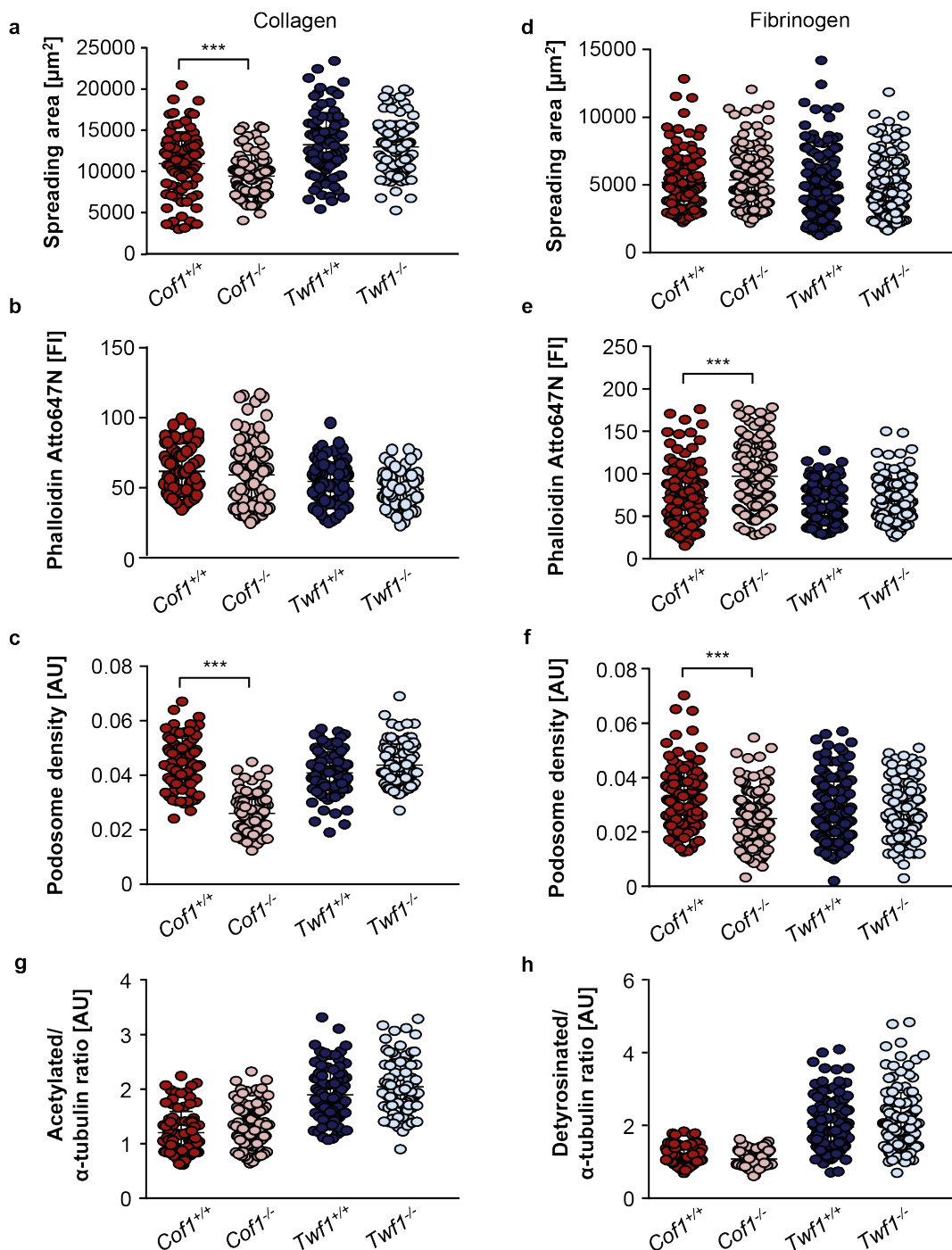
Figure 39. Mildly defective spreading and podosome formation of *Cof1*^{-/-}, but not *Twf1*^{-/-} MKs. BM MKs derived from *Twf1*^{-/-} or *Cof1*^{-/-} mice and the respective controls were spread on Horm collagen or fibrinogen. Spreading area (**a, d**), phalloidin FI (**b, e**) as well as podosome density (**c, f**) were analyzed by confocal microscopy (Leica TCS SP8, 40x objective) and quantified using ImageJ Software. Values are mean ± SD (n = 3). Unpaired, two-tailed Student's t-test. **P < 0.01, ***P < 0.001. (**g, h**) Analysis of microtubule acetylation and detyrosination in *Twf1*^{-/-} or *Cof1*^{-/-} BM MKs or the respective *WT* controls spread on Horm collagen and analyzed by ImageJ Software. Values are mean ± SD (n = 3). Becker, Scheller *et al*., **Blood Adv**, 2020.[219]
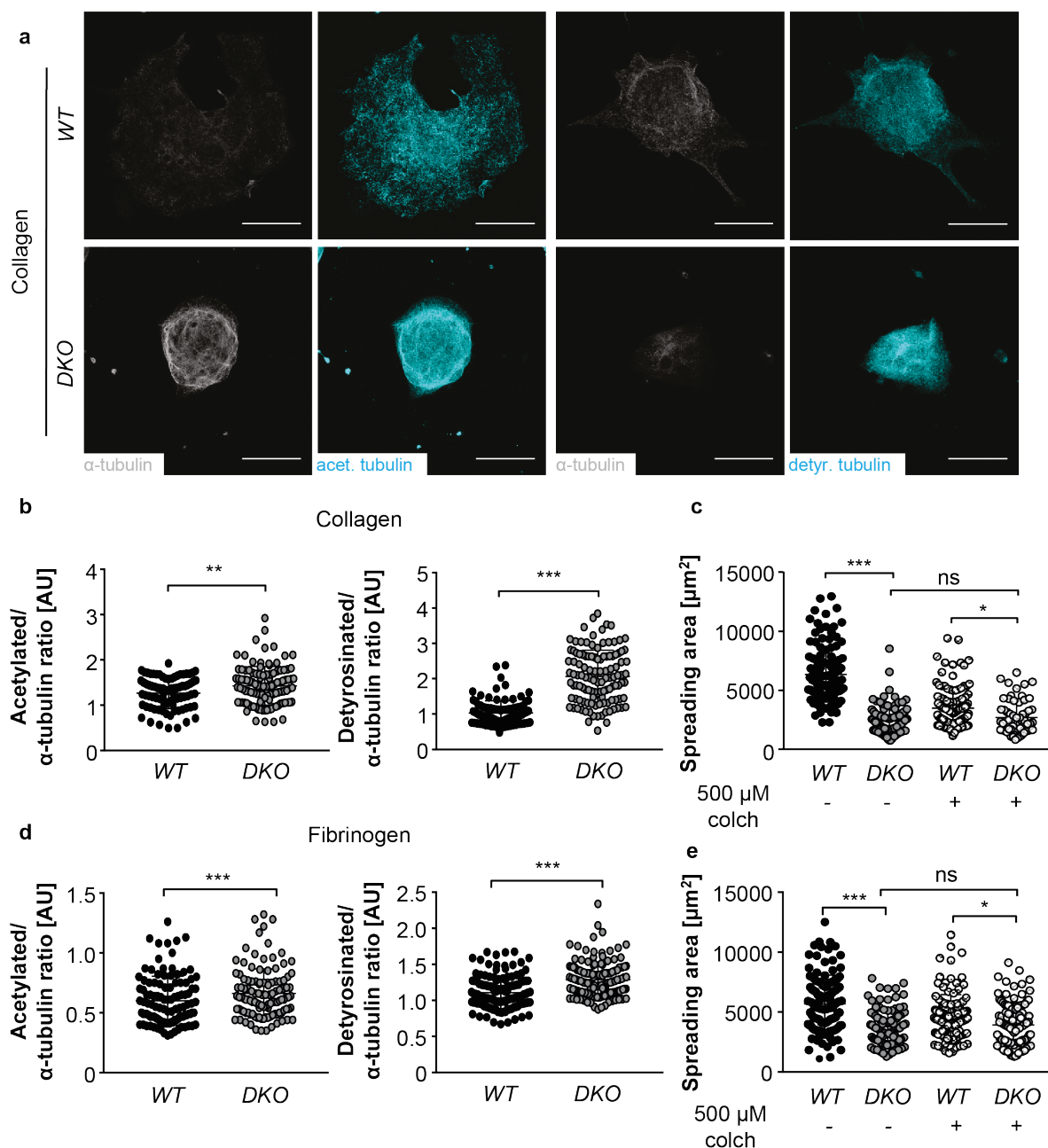
Figure 40. Altered microtubule stability in spread MKs upon concomitant loss of Twf1 and Cof1. BM-derived *WT* and *DKO* MKs MKs were spread on Horm collagen (**a, b, c**) or fibrinogen (**d, e**), stained for acetylated or detyrosinated microtubules and analyzed by confocal microscopy (Leica TCS SP8, 40x objective). Scale bars: 25 µm. (**b, d**) FI of acetylated or detyrosinated microtubules normalized to α-tubulin was assessed using ImageJ Software. Values are mean ± SD (n = 3). Unpaired, two-tailed Student's t-test. **P < 0.01; ***P < 0.001. (**c, e**) Spreading on both substrates was repeated upon preincubation of BM MKs with 500 µm colchicine for 30 min at 37°C. Values are mean ± SD (n = 3). One-way ANOVA with Sidak correction for multiple comparisons. *P < 0.05; ***P < 0.001. Becker, Scheller *et al.*, **Blood Adv**, 2020.[219]

In contrast to double-deficient MKs, microtubule modifications upon spreading of *Cof1^-/-* or *Twf1^-/-* MKs on Horm collagen were unaffected (Figure 39g, h). In line with spread MKs, levels of detyrosinated microtubules were significantly increased in proplatelet-forming *Twf1^-/-* /*Cof1^-/-* MKs analyzed by confocal microscopy (Figure 41a, b), while acetylation appeared to

be unaffected, suggesting that increased detyrosination accounts for the defective proplatelet release from double-deficient MKs *in vivo*. Of note, similarly increased levels of detyrosinated microtubules were also observed in thrombin-stimulated double-deficient platelets spread on fibrinogen (Figure 45d). Taken together, microtubule detyrosination appears to impair turnover, thus affecting PPF *in vivo*.
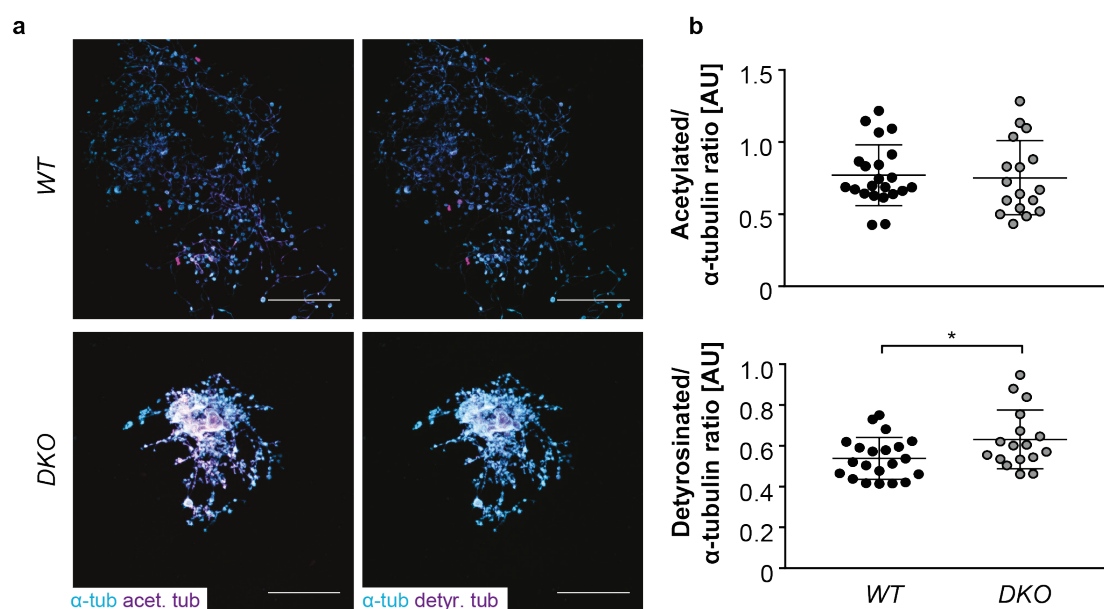
Figure 41. Enhanced microtubule detyrosination in proplatelet-forming *DKO* MKs. Confocal microscopic analysis (**a**) and quantification (**b**) of acetylated and detyrosinated microtubules in proplatelet-forming BM MKs derived from *WT* and *DKO* mice. Images were acquired at a confocal microscope (Leica TCS SP8, 40x objective). Scale bars: 25 µm. Values are mean ± SD (n = 3). Unpaired, two-tailed Student's t-test. *P < 0.05. Becker, Scheller *et al.*, **Blood Adv**, 2020.[219]

4.3.6 Altered equilibrium of cytoskeleton-regulatory proteins affects microtubule stability in double-deficient MKs but not platelets

In order to identify the underlying cause for the aberrant F-actin distribution and increased microtubule stability in *Twf1⁻/⁻/Cof1⁻/⁻* MKs, we analyzed mRNA and protein levels of known regulators of both actin and microtubule dynamics in MKs and platelets. Among these, the formin mDia1, EB1 and APC have been described to stabilize microtubules in migrating fibroblasts, while further affecting F-actin polymerization in MKs and platelets.[124,222,223] Indeed, we found mRNA levels of both *Diaph1* and *Apc* to be markedly reduced in *Twf1⁻/⁻/Cof1⁻/⁻* MKs (Figure 42a, b), which was reflected by a significantly decreased expression of both proteins as determined by immunoblotting (Figure 42c, d), while protein content was surprisingly unaffected in platelets derived from double-deficient mice. Levels of the known cytoskeletal regulator RhoA on the other hand were unaltered in double-deficient MKs. Of note and similarly to double-deficient MKs, mRNA levels of *Diaph1* and *Apc* were markedly

reduced in *Cof1^-/-* MKs (Figure 43a, b), while the reduced protein content of APC was restricted to *Twf1^-/-/Cof1^-/-* MKs suggesting that additional degradation of the protein might occur.
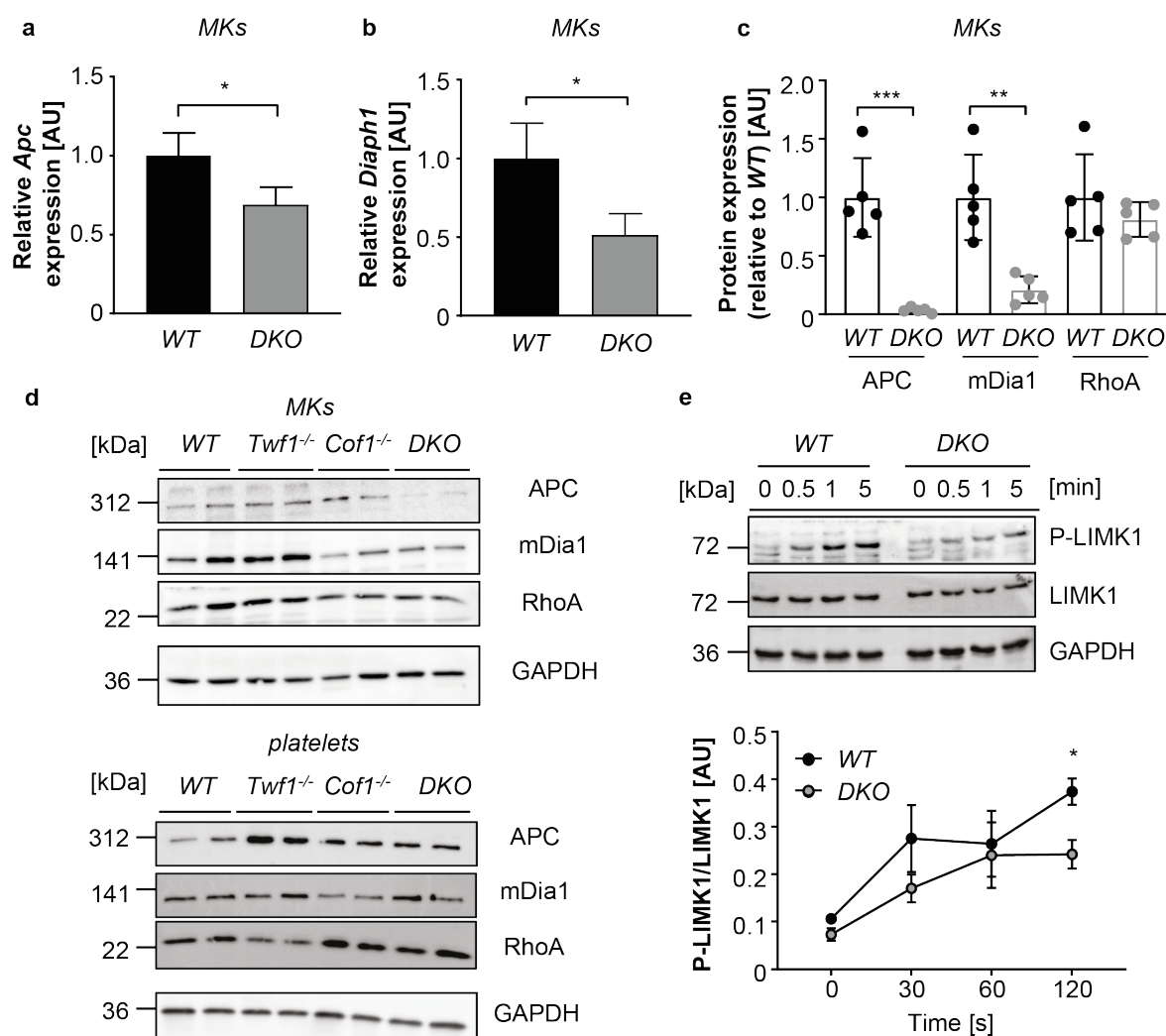
Figure 42. Diminished APC and mDia1 expression and altered LIM-Kinase phosphorylation in *DKO* MKs and platelets, respectively. mRNA levels of *Apc* (**a**) and *Diaph1* (**b**) in BM-derived MKs were determined by qPCR and normalized to *Sdha* and *Actb*. Values are mean ± SD (n = 3). Unpaired, two-tailed Student's t-test. *P < 0.05. (**c, d**) Immunoblots of *WT*, *Twf1^-/-*, *Cof1^-/-* or *DKO* MKs or washed platelets for the cytoskeletal regulatory proteins APC, mDia1 and RhoA. GAPDH served as a loading control. (**c**) Densitometric analysis was performed using ImageJ Software. Values were normalized to *WT* levels. Values are mean ± SD. Unpaired, two-tailed Student's t-test. **P < 0.01. (**e**) *WT* and *DKO* platelets were stimulated with 0.1 U mL^-1 thrombin for 5 min at lysed at the respective time points. Phosphorylation (T508) and total LIMK levels were analyzed by immunoblotting. Densitometry was performed using ImageJ Software. Unpaired, two-tailed Student's t-test. *P < 0.05. Becker, Scheller *et al.*, **Blood Adv**, 2020.[219]

In addition to altered levels of mDia1 and APC, we found phosphorylation of the Cof1-regulatory protein LIMK1, which has been linked to actin and microtubule dynamics as well, to be markedly impaired in *Twf1^-/-/Cof1^-/-* platelets (Figure 42e), suggesting a negative feedback loop to cause its impaired activation upon stimulation with thrombin.
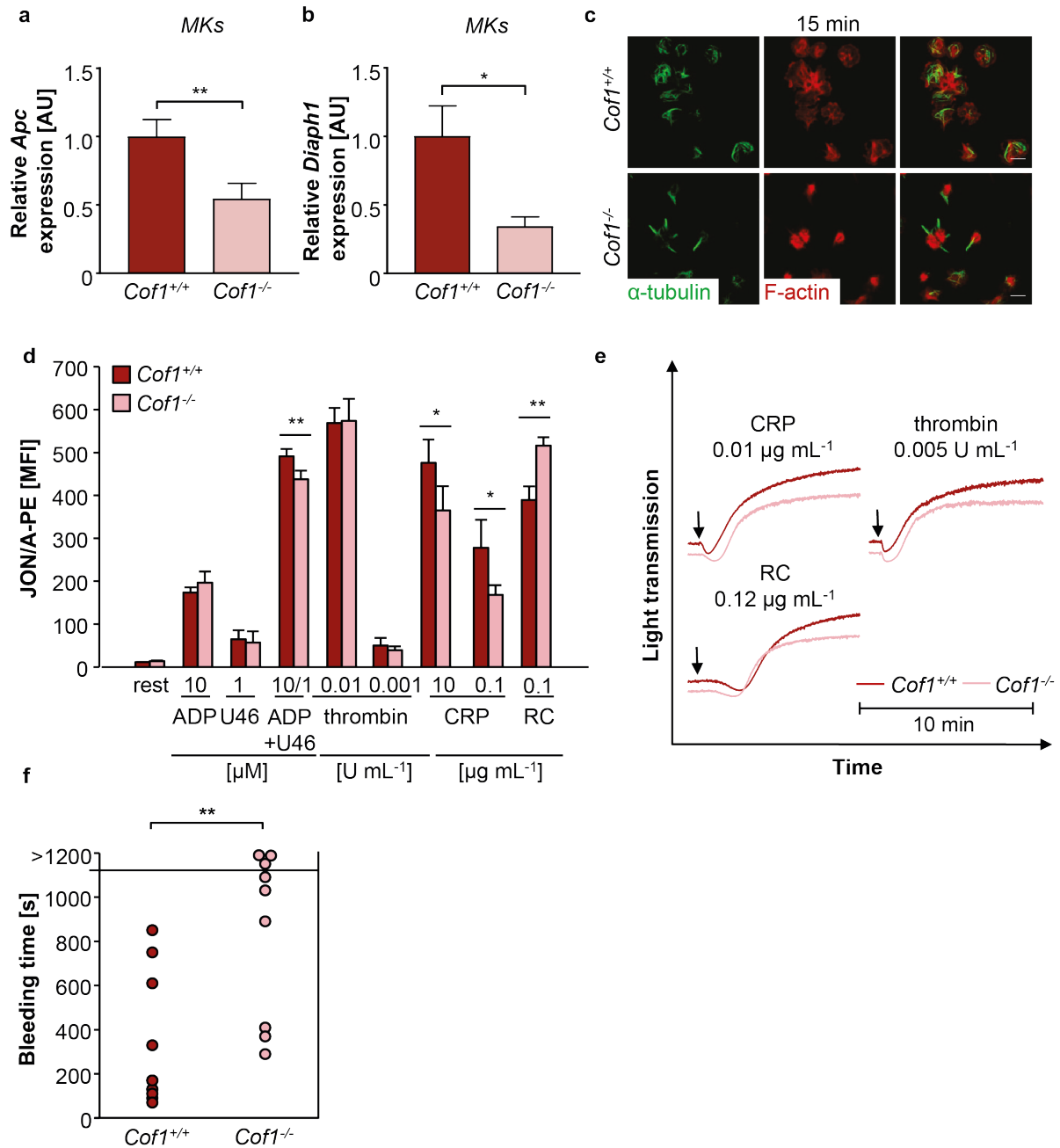
Figure 43. Analysis of MK and platelet function in *Cof1*-/- mice. mRNA content of *Apc* (**a**) and *Diaph1* (**b**) were quantified by RT-qPCR in *WT* and *Cof1*-/- MKs. Values are mean ± SD (n = 3). Unpaired, two-tailed Student's t-test. *P < 0.05. **P < 0.01. (**c**) Fibrinogen-spread *WT* and *Cof1*-/- platelets were stained for α-tubulin and F-actin (Phalloidin Atto647N) and analyzed by confocal microscopy (Leica TCS SP5, 100x objective). Values are mean ± SD. (**d**) JON/A-PE binding to activated αIIbβ3 integrins upon stimulation of platelets was assessed by flow cytometry. Values are mean ± SD (n = 5). Unpaired, two-tailed Student's t-test. *P < 0.05; **P < 0.01. (**e**) Light transmission in response to different platelet agonists was assessed at an aggregometer. Arrows indicate addition of the agonist (n = 5). (**f**) Determination of tail bleeding time on filter paper in *Cof1*-/- and control mice. Each dot represents one animal. Unpaired, two-tailed Student's t-test and Fisher's exact test. **P < 0.01. Becker, Scheller *et al*., **Blood Adv**, 2020.[219]

The unaltered protein content in double-deficient platelets prompted us to further assess platelet function *in vitro* and *in vivo*. Integrin activation and degranulation of *Twf1*-/-/*Cof1*-/-

platelets in response to stimulation with different agonists as assessed by flow cytometry was mildly impaired (Figure 44a, b), but did not exceed activation defects observed in *Cof1^{-/-}* platelets (Figure 43d). Similarly, reduced aggregation responses in double-deficient platelets were reminiscent of what has been described for *Cof1^{-/-}* platelets (Figure 43e, 44c) as was a marked prolongation of tail bleeding times (Figure 43f, 44d).
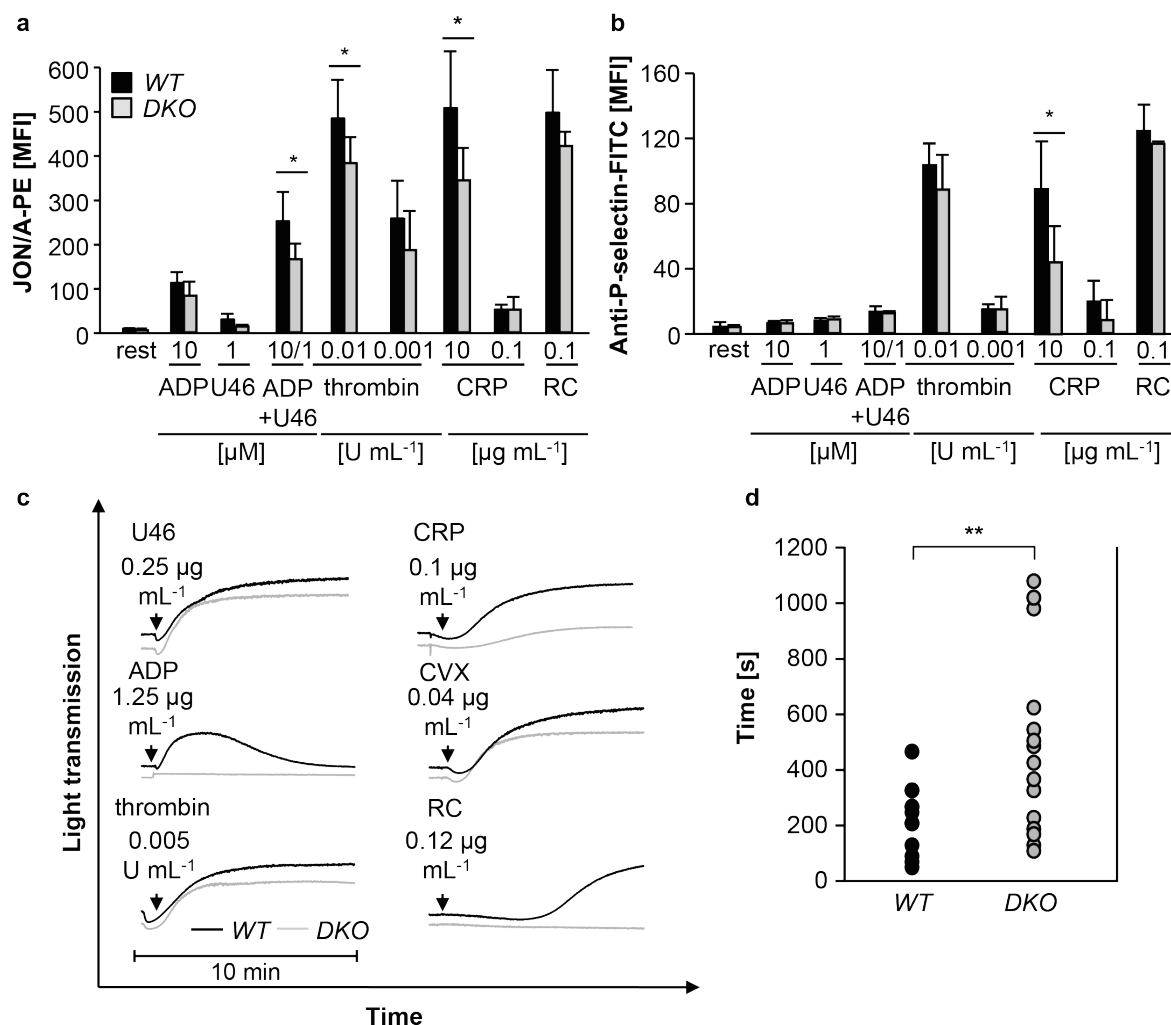
Figure 44. Slightly impaired platelet reactivity in Twf1/Cof1-deficient mice. Integrin αIIbβ3 activation (**a**) and degranulation (**b**) in response to platelet agonists were assessed by flow cytometry. Values are mean ± SD (n = 5). Unpaired, two-tailed Student's t-test. *P < 0.05. (**c**) Platelet aggregation was determined upon stimulation of PRP (ADP) or washed platelets with different platelet agonists. Addition of agonists are indicated with arrows (n = 5). (**d**) Hemostasis was investigated in a tail bleeding time assay on filter paper (n = 10). Unpaired, two-tailed Student's t-test and Fisher's exact test. **P < 0.01. Becker, Scheller *et al.*, **Blood Adv**, 2020.[219]

Ultimately and in line with our findings from double-deficient MKs, platelets derived from Twf1/Cof1-deficient exhibited an increased F-actin content (Figure 45a, b) as well as impaired and delayed spreading capacities, which could be normalized upon treatment with colchicine (Figure 45c). All in all, we were able to identify an altered equilibrium of

microtubule- and actin-regulatory proteins to account for the observed defects in MK cytoskeletal rearrangements resulting in impaired PPF and macrothrombocytopenia *in vivo*.
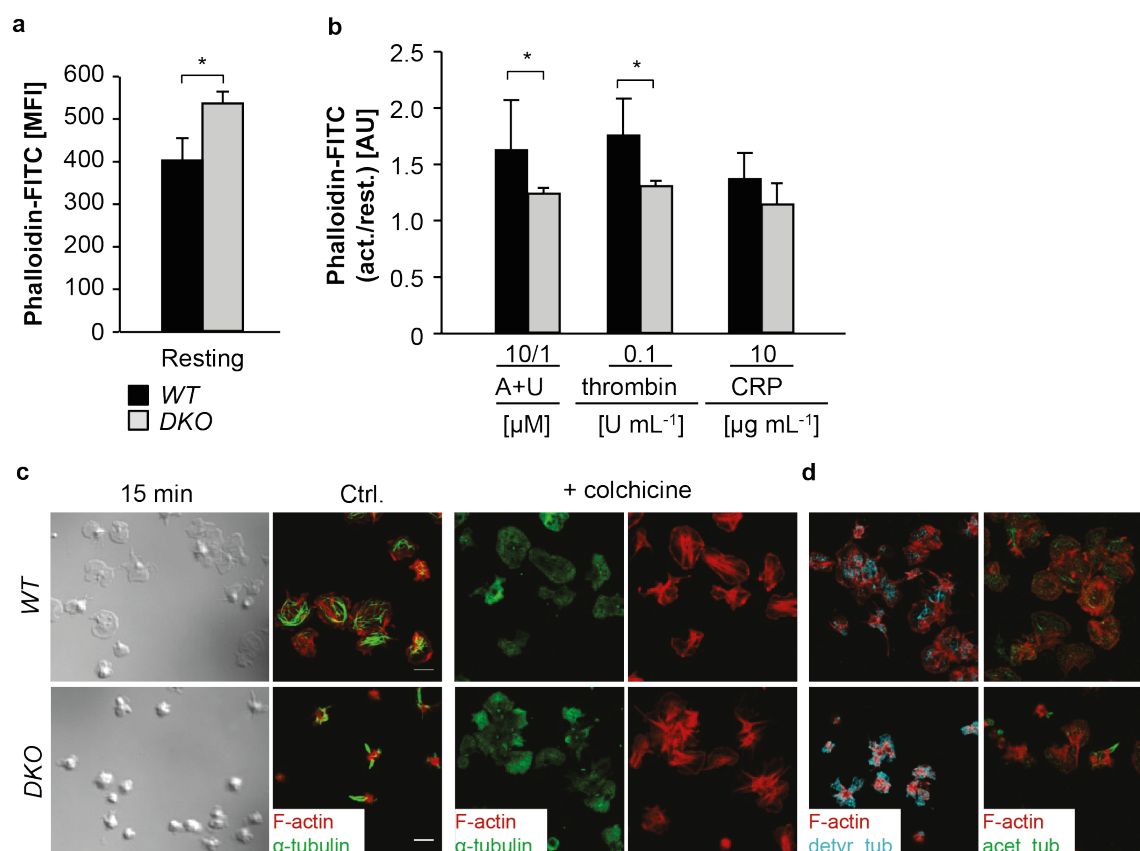
Figure 45. Altered cytoskeletal dynamics in *DKO* platelets. F-actin content in resting platelets (**a**) and upon stimulation with different agonists (**b**) were determined by flow cytometry after incubation with phalloidin-FITC. The ratio of activated and resting platelets ± SD is shown (n = 4). Unpaired, two-tailed Student's t-test. *P < 0.05. (**c**) Untreated or colchicine-treated washed platelets were spread on fibrinogen and analyzed by differential interference contrast or confocal microscopy (Leica TCS SP5, 100x objective). Scale bars: 3 μm. Values are mean ± SD (n = 6). (**d**) Washed platelets were spread on fibrinogen for 15 min, stained for detyrosinated and acetylated tubulin and analyzed by confocal microscopy (Leica TCS SP5, 100x objective) (n = 3). Experiments were performed by Dr. Inga Scheller. Becker, Scheller *et al.*, **Blood Adv**, 2020.[219]

4.4 G6b-B is a major regulator of MK maturation and BM homeostasis

G6b-B-deficient mice have been shown to develop severe macrothrombocytopenia and myelofibrosis.[155] Similar observations of significantly lowered platelet counts and concomitant focal BM fibrosis were made in patients with variants in *MPIG6B*.[154] The underlying mechanisms leading to impaired PPF and altered BM homeostasis, however, still remain elusive.

4.4.1 Spontaneous mutation within *Mpig6b* results in macrothrombocytopenia

Previous work from our group (Stritt, Heck *et al.,* unpublished) identified several mice in a C57Bl/6 mouse line with severely lowered platelet counts and a concomitant increase in

platelet size (Figure 46a, b), which was referred to as Orphan, since the underlying mutation was unknown.
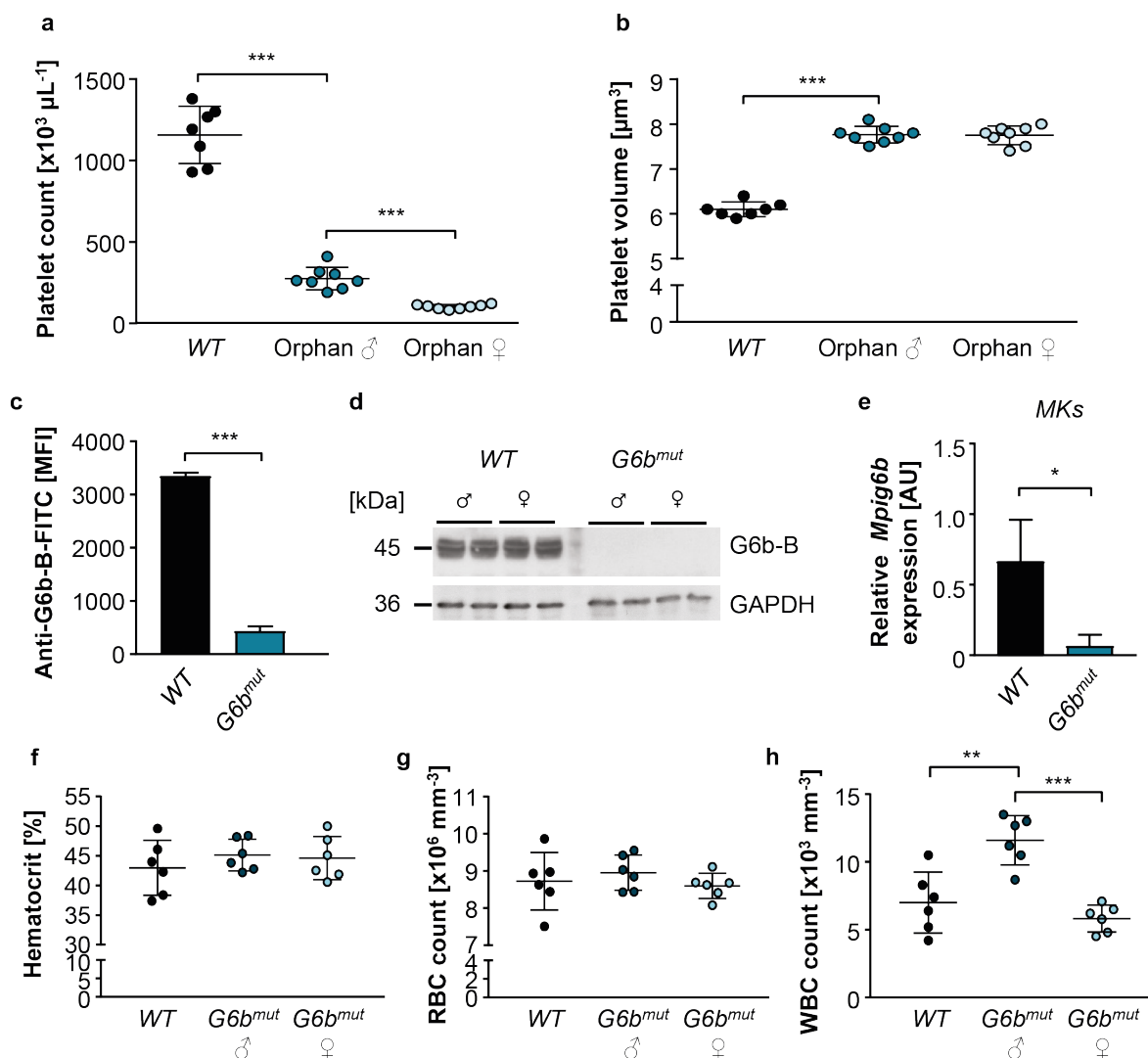
Figure 46. Identification of a spontaneous mutation within *Mpig6b* leading to macrothrombocytopenia in mice. Platelet count (**a**) and size (**b**) of 8-week-old Orphan mice were determined at an automated blood cell analyzer. Values are mean ± SD (n = 8). Unpaired, two-tailed student's t-test. ***P < 0.001. A splice acceptor site mutation within *Mpig6b* was detected by whole exome sequencing. Orphan mice are further referred to as *G6b^{mut}*. (**c-e**) Absence of G6b-B protein in platelets was verified by flow cytometry (**c**) and immunoblotting (**d**) as well as in MKs by RT-qPCR (**e**). Flow cytometry was performed by Dr. Timo Vögtle. qPCR was performed by Dr. Georgi Manukjan. Values are mean ± SD (n = 3). Unpaired, two-tailed student's t-test. *P < 0.05; ***P < 0.001. Hematocrit (**f**), RBC count (**g**) and WBC count (**h**) in 6-week-old mice were assessed at an automated blood cell analyzer. Values are mean ± SD (n = 6). One-way ANOVA with Tukey's correction for multiple comparisons. **P < 0.01; ***P < 0.001.

In order to unravel the cause for the recessively inherited macrothrombocytopenia, we performed whole exome sequencing with the help of Dr. Richa Barthi of the CoreUnit Systems Medicine Würzburg and identified an intronic missense mutation within *Mpig6b* (c.404-1G>A), encoding for the inhibitory platelet receptor G6b-B. Interestingly, lack of G6b-B has previously been associated with macrothrombocytopenia and myelofibrosis in mice.[155]

The Orphan mice are thus further referred to as *G6b^{mut}*. To investigate the impact of the mutation, we first investigated surface expression of G6b-B on *G6b^{mut}* platelets by flow cytometry and found G6b-B to be absent from the platelet surface (Figure 46c). Similarly, G6b-B protein was lacking in platelet lysates derived from male and female *G6b^{mut}* mice (Figure 46d). The detectable, albeit low levels of G6b-B mRNA still present in cultured murine MKs suggests nonsense-mediated decay to account for the degradation of remnant G6b-B mRNA (Figure 46e). In contrast to platelet counts, RBC counts and, consequently, hematocrit were unaltered in *G6b^{mut}* mice (Figure 46f, g), although WBC count was slightly elevated in male *G6b^{mut}* mice (Figure 46h). Taken together, we identified an intronic mutation within *Mpig6b* leading to loss of G6b-B expression in murine MKs and platelets.

4.4.2 Impaired function of *G6b^{mut}* platelets

	WT		*G6b^{mut}* ♂		*G6b^{mut}* ♀	
	mean	SD	mean	SD	mean	SD
α-GPIb	491,25	±68,3	410,25	±6,4	435,75	±27,37
α-GPIX	603,75	±57,14	638,25	±41,63	635,5	±61,26
α-GPV	351,25	±39,32	281	±4,32*	245,5	±14,2**
α-CD9	1213,25	±112,62	1004,25	±25,38*	987,5	±80,98*
α-GPVI	69	±8,49	36,25	±1,26**	36,75	±3,2**
α-α2bβ3	634,75	±43,02	760,75	±60,9*	625,5	±66,06
α-α2	71,25	±3,77	73,75	±1,26	71,5	±1,29
α-β3	328	±50,02	432,25	±22,88*	375	±15,45
α-CLEC-2	187	±37,6	160	±18,81	176,25	±21,78

Table 1. GP expression on *WT* and *G6b^{mut}* platelets. MFI of major GPs was assessed by flow cytometry. Values are mean ± SD (n = 5). Unpaired, two-tailed student's t-test. *P < 0.05; **P < 0.01.

Analysis of surface expression of major platelet glycoproteins on *G6b^{mut}* platelets revealed a slight decrease in GPV (20-30%) and CD9 (20%) expression as well as a 50% reduction in GPVI surface abundance (Table 1), which is in line with previous observations from *G6b^{-/-}* platelets.[155] Moreover, activation of αIIbβ3 integrins as well as degranulation as assessed by P-selectin exposure upon stimulation with GPCR (thrombin, ADP, U46619) or (hem)ITAM agonists (CRP, RC) were markedly impaired in *G6b^{mut}* platelets with generally more severe defects seen in female mice (Figure 47a, b). In order to identify the cause of the thrombocytopenia, we next assessed platelet recovery upon GPIbα-mediated platelet depletion and found it to be markedly delayed in *G6b^{mut}* mice suggesting defective platelet generation in the absence of G6b-B (Figure 47c, d).

Strikingly, the impaired platelet reactivity *in vitro* further translated into highly defective hemostasis in *G6b^mut* mice *in vivo* as assessed in the filter paper tail bleeding assay (Figure 47e). In contrast, platelet spreading on fibrinogen upon stimulation with thrombin was indistinguishable between *WT* and *G6b^mut* platelets (Figure 48a, b), in line with an unaltered

Figure 47. Defective platelet activation and recovery in the absence of G6b-B. αIIbβ3 integrin activation (**a**) and P-selectin exposure (**b**) upon stimulation with different platelet agonists were determined by flow cytometry in washed blood. Values are mean ± SD (n = 5). Unpaired, two-tailed student's t-test. *P < 0.05; **P < 0.01; ***P < 0.001. (**c, d**) Recovery of platelet counts upon depletion was analyzed by flow cytometry over 10 consecutive days in male (**c**) and female (**d**) mice, respectively. Values were normalized to the values on day 0. Values are mean ± SD (n = 5). Unpaired, two-tailed student's t-test. **P < 0.01; ***P < 0.001. (**e**) Platelet function *in vivo* was assessed in a tail bleeding time assay on filter paper. Fisher's exact test (n = 10).

appearance of the platelet cytoskeleton analyzed by confocal fluorescence microscopy of F-actin and α-tubulin (Figure 48c). TEM confirmed the markedly increased size of *G6b^{mut}* platelets compared to the *WT* and further revealed an aberrant distribution of granules with some platelets being almost devoid of any (Figure 48d). These findings suggest that G6b-B is involved in the regulation of platelet reactivity as well as granule distribution *in vitro* and *in vivo*.
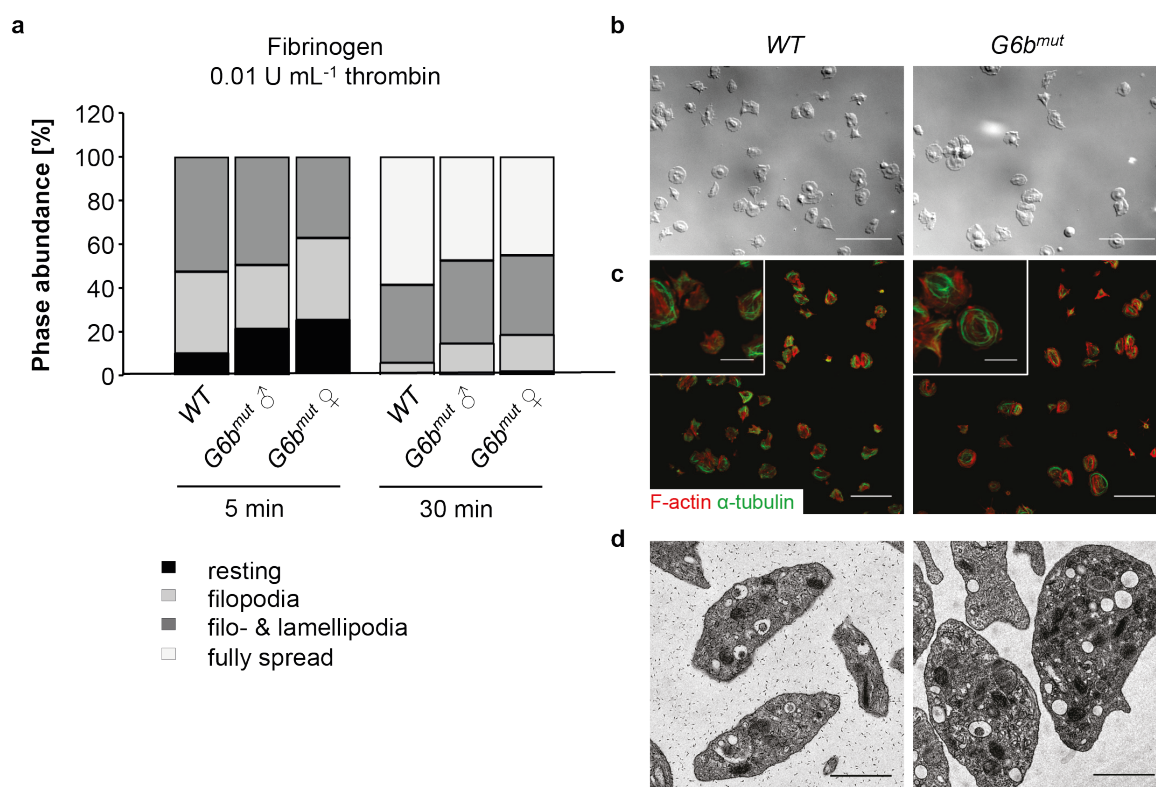
Figure 48. Unaltered spreading of *G6b^{mut}* platelets. (**a, b**) Washed platelets were stimulated with 0.01 U mL^{-1} thrombin and allowed to spread on fibrinogen. Resting, filopodia-forming, lamellipodia-forming and spread platelets were analyzed after 5 and 30 min by DIC microscopy (n = 3). Scale bars: 20 μm. (**c**) After 30 min of spreading, platelets were immunostained for F-actin and α-tubulin and analyzed by confocal microscopy at a Leica TCS SP5 (100x objective). Scale bars: 15 μm; insets: 5 μm. (**d**) Morphology of *WT* and *G6b^{mut}* platelets was assessed by TEM. Scale bars: 1 μm.

4.4.3 G6b-B-deficiency induces splenomegaly, myelofibrosis and sex-specific osteosclerosis

G6b^{mut} mice presented with a marked splenomegaly, suggesting extramedullary hemato-poiesis in these animals (Figure 49a). Of note, the increase in spleen size was generally more prominent in female *G6b^{mut}* mice. We performed immunofluorescence staining on spleen cryosections and indeed found MK numbers to be significantly increased in the spleens of both male and female *G6b^{mut}* mice compared to the respective *WT* controls (Figure 49b, c).
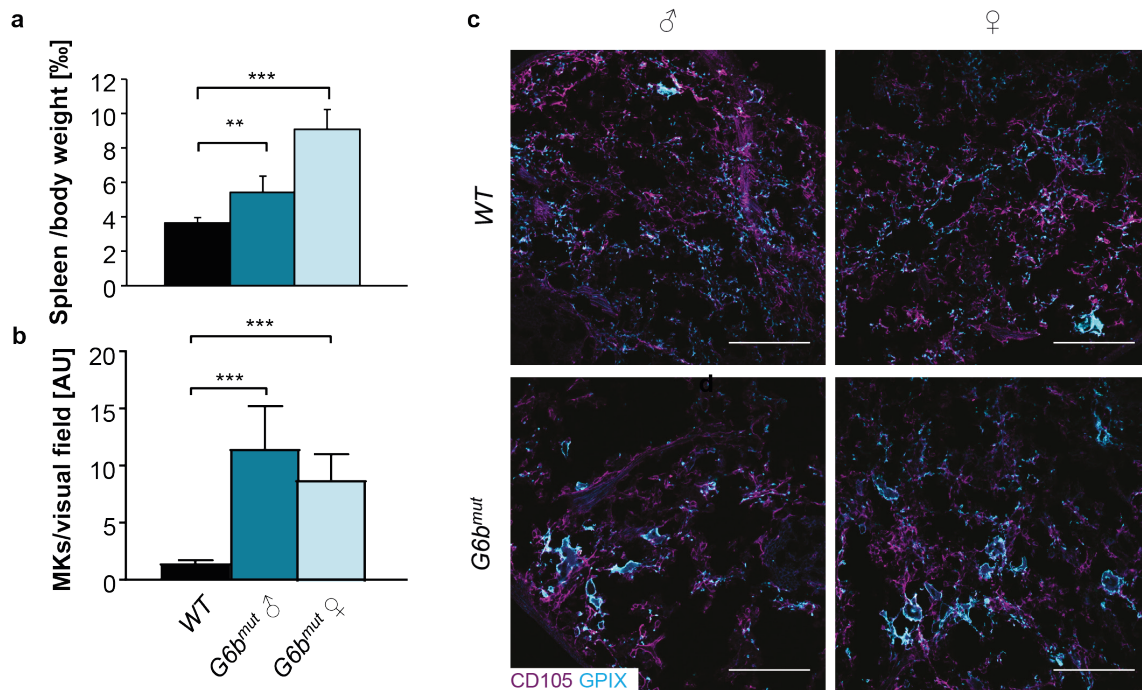
Figure 49. Splenomegaly and extramedullary hematopoiesis in *G6b^mut* mice. (**a**) Quantification of spleen to body weight assessed in 8-week-old *WT* and male and female *G6b^mut* mice. Values are mean ± SD (n = 8). One-way ANOVA with Tukey's correction for multiple comparisons. **P < 0.01; ***P < 0.001. (**b**) MK numbers were determined by manual counting of H&E-stained paraffin sections of *WT* and *G6b^mut* mice. Values are mean ± SD (n = 4). One-way ANOVA with Tukey's correction for multiple comparisons. ***P < 0.001. (**c**) Splenic cryosections were immunofluorescently stained for CD105 and GPIX and analyzed by confocal microscopy on a Leica TCS SP8 (25x objective). Scale bars: 100 μm.

The elevated number of MKs in the spleen prompted us to investigate the morphology of the BM as the main site of hematopoiesis, since G6b-B-deficiency has been associated with the development of myelofibrosis in mice and humans.[154,155] H&E stainings on BM paraffin sections of 3-week-old mice revealed a grossly unaltered BM morphology in male *G6b^mut* mice compared to the *WT*, although a beginning myelofibrosis and an increased vessel density was already evident in the BM of female *G6b^mut* mice (Figure 50a). Of note, platelet counts at this age were still comparable between male and female *G6b^mut* mice (Figure 50b). In contrast, male *G6b^mut* mice at 8 weeks of age exhibited dramatic myelofibrosis evident by increased deposition of collagen fibers within the BM, while female mutant mice presented with an osteosclerotic phenotype leading to loss of BM cell mass as well as an accumulation of adipocytes (Figure 50c). Interestingly, this reduction in BM cellularity was reflected by even lower platelet counts in female mice compared to their male littermates (Figure 50d), which was further correlated with the more severe splenomegaly detected in female mice (Figure 49a). In summary, these findings demonstrate an explicit role of G6b-B in the maintenance of BM homeostasis.
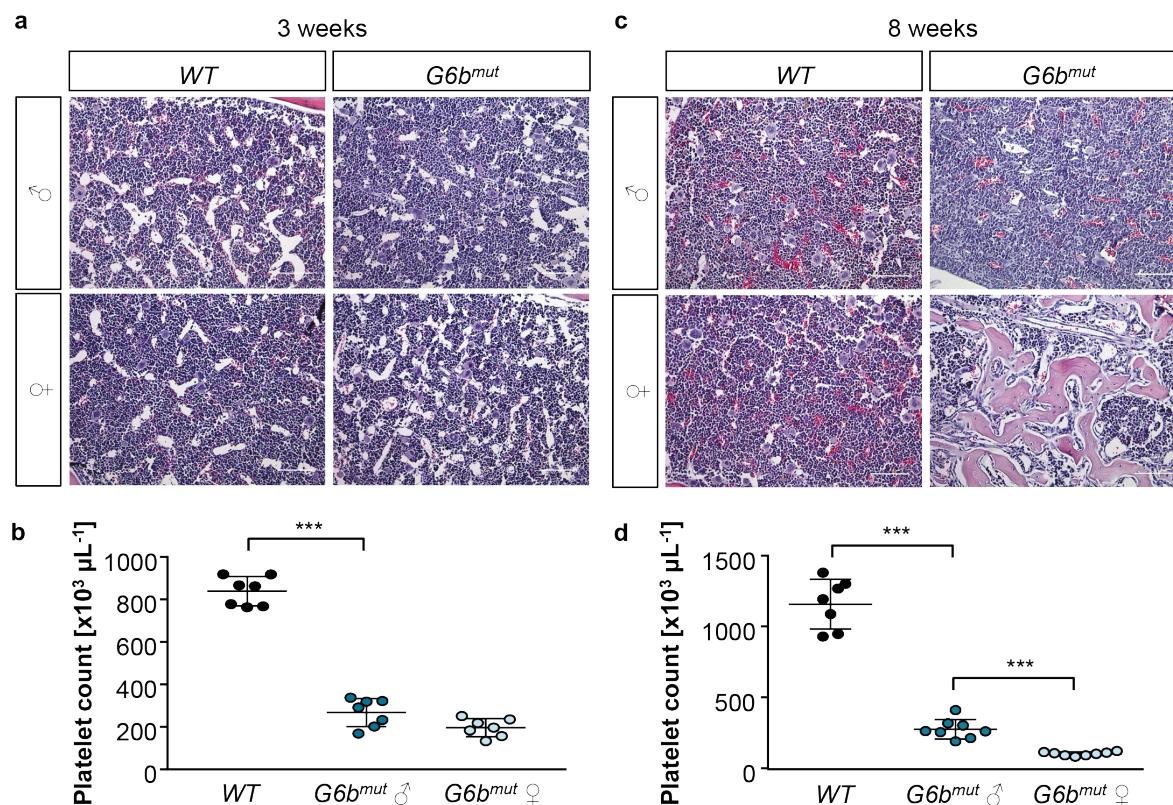
Figure 50. Progressing osteosclerosis in female *G6b^{mut}* mice. BM paraffin sections of 3- (**a**) and 8-week-old (**c**) female and male *WT* and *G6b^{mut}* mice were stained with H&E and analyzed by brightfield microscopy (20x objective). Scale bars: 100 µm. (**b, d**) Platelet counts of *WT* and *G6b^{mut}* mice at 3 (**b**) and 8 weeks (**d**) of age were assessed at an automated blood cell analyzer. Values are mean ± SD. Unpaired, two-tailed Student's t-test. ***P < 0.001.

4.4.4 Female-specific bone remodeling defects are sex hormone-related

In order to visualize the differences in bone resorption and growth, male and female *WT* and *G6b^{mut}* femoral bones were analyzed by µCTs at the Institute of Orthopaedic Research and Biomechanics, University of Ulm. As visible in Figure 51a, female mice at 10 weeks of age displayed a profound increase in bone mass in the cortical bone, while the number of trabeculae on the contrary appeared to be significantly reduced, suggesting an overall dysregulation of bone remodeling. This was reflected by quantification of *bone to tissue volume* (BV/TV) in cortical and trabecular bone, which mirrored the sex-specific differences and highlighted the osteosclerotic as well osteoporotic phenotype present in female mice (Figure 51a, c, d). In contrast to femoral bones, visualization of bone trabeculae in vertebrae of female *WT* and *G6b^{mut}* mice by von Kossa staining only revealed osteoporosis, suggesting that osteosclerosis was limited to cortical bones (Figure 51b). Of note, analysis of *Mpig6b* mRNA levels in *in vitro*-matured osteoblasts and osteoclasts confirmed its absence from both cell types (Figure 51e), thus highlighting that the effects on bone remodeling were due to altered MK behavior in *G6b^{mut}* mice.
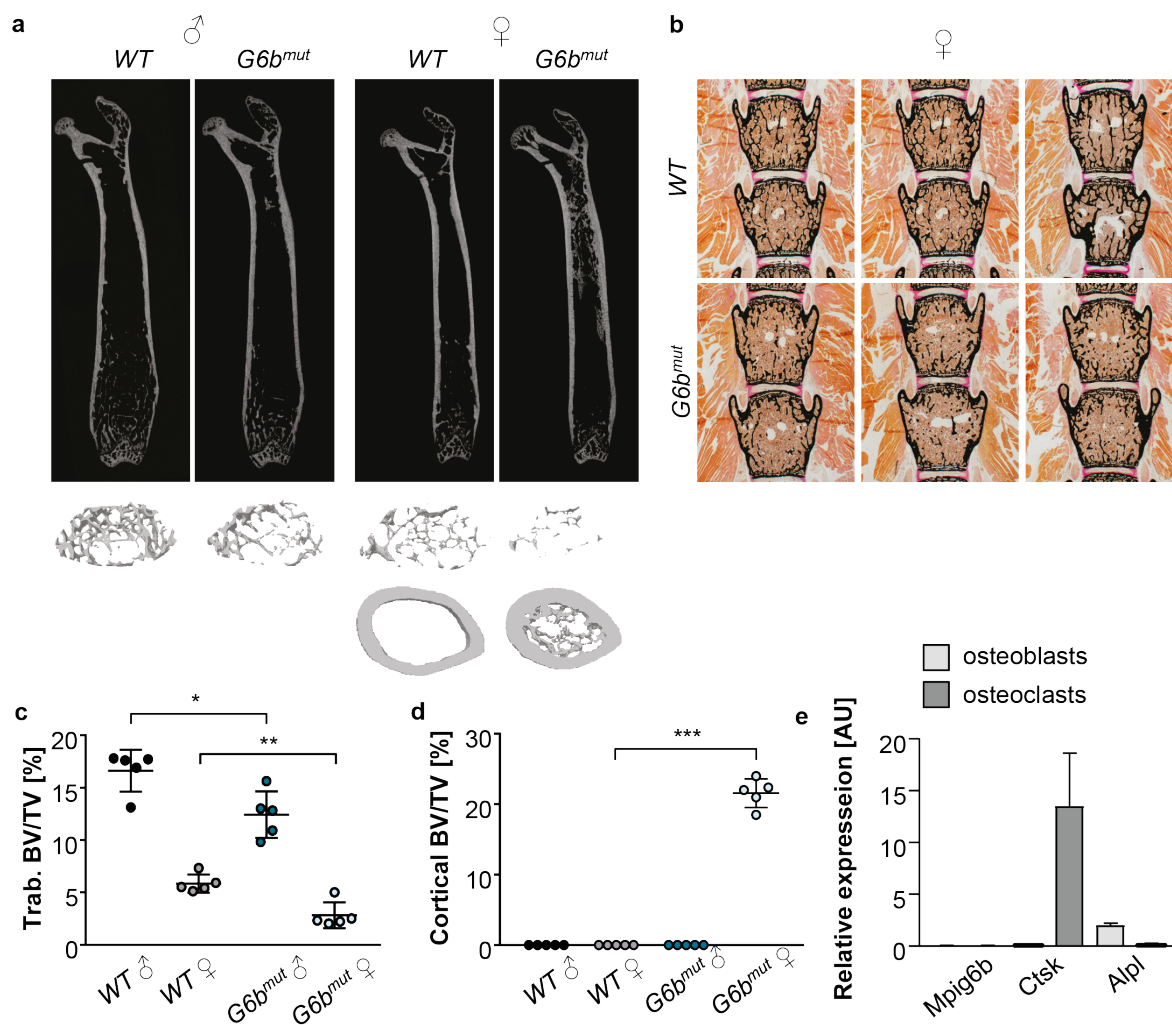
Figure 51. Osteoporosis and -sclerosis in female *G6b^mut* mice. (**a**) Femoral bones of male and female *WT* and *G6b^mut* mice were analyzed by µCTs. Cross-sections display cortical part of the bone. Analysis was performed by Dr. Melanie Haffner-Luntzer, University of Ulm. (**b**) Von Kossa staining of bone trabeculae in paraffin sections of vertebrae of female *WT* and *G6b^mut* mice. Stainings were performed by Anke Jeschke, University Hospital Hamburg. (**c, d**) Quantification of trabecular (**c**) and cortical (**d**) BV/TV in male and female mutant mice and the respective controls. Values are mean ± SD (n = 5). One-way ANOVA with Sidak correction for multiple comparisons. *P < 0.05; **P < 0.01; ***P < 0.001. (**e**) Relative expression values of *Mpig6b* (G6b-B), *Ctsk* (cathepsin K) and *Alpl* (alkaline phosphatase) in *in vitro*-matured osteoblast and osteoclasts. Values are mean ± SD (n = 3).

While femur length was indistinguishable between *WT* and *G6b^mut* mice (Figure 52a), further analyses of µCTs indicated a dramatic reduction of trabeculae (Figure 52b) as well as *bone mineral density* (BMD) (Figure 52c) in the trabeculae of female mice. In line with the osteosclerosis observed in cortical bone, endosteal diameter was markedly reduced (Figure 52d), while, consequently, cortical thickness was significantly increased in female bones (Figure 52e). Surprisingly, BMD as a measure of mineralization was similarly reduced in cortical bone as in trabecular bone (Figure 52f), thus implying a general decrease in bone mineralization in female mice lacking G6b-B.
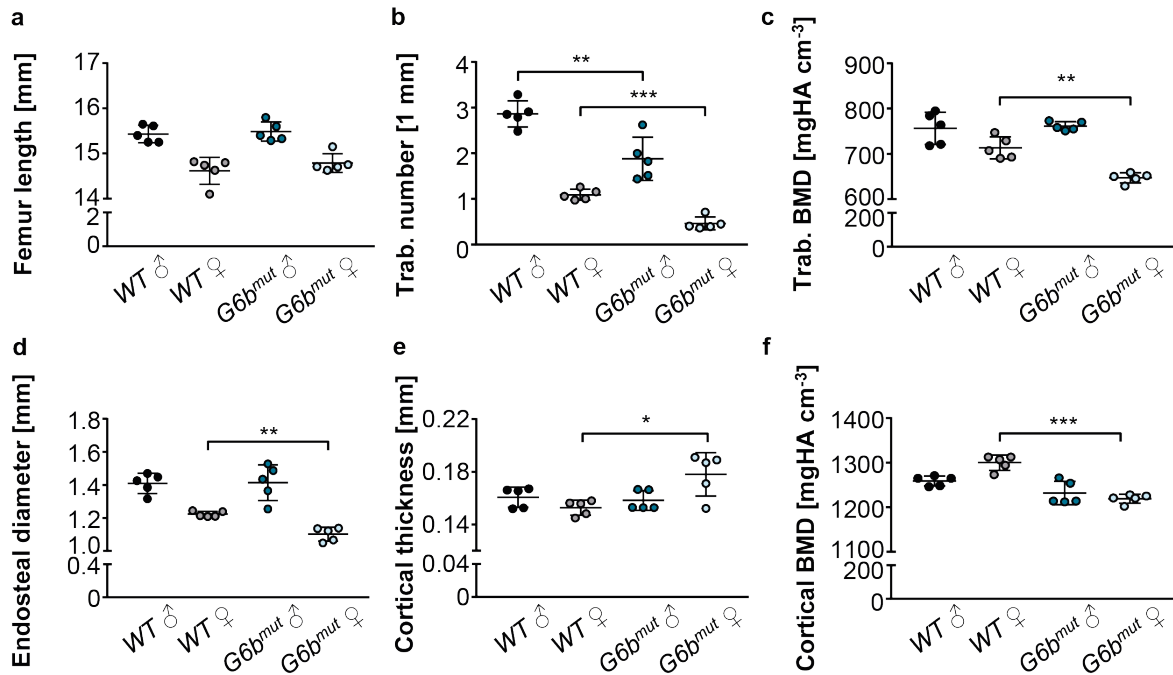
Figure 52. Altered bone parameters in female *G6b^mut* mice. Femur length (**a**), trabecular numbers (**b**), BMD (**c, f**), endosteal diameter (**d**) and cortical thickness of femora were assessed in µCTs. Analysis was performed by Dr. Melanie Haffner-Luntzer, University of Ulm. Values are mean ± SD (n = 5). One-way ANOVA with Sidak correction for multiple comparisons. *P < 0.05; **P < 0.01; ***P < 0.001.
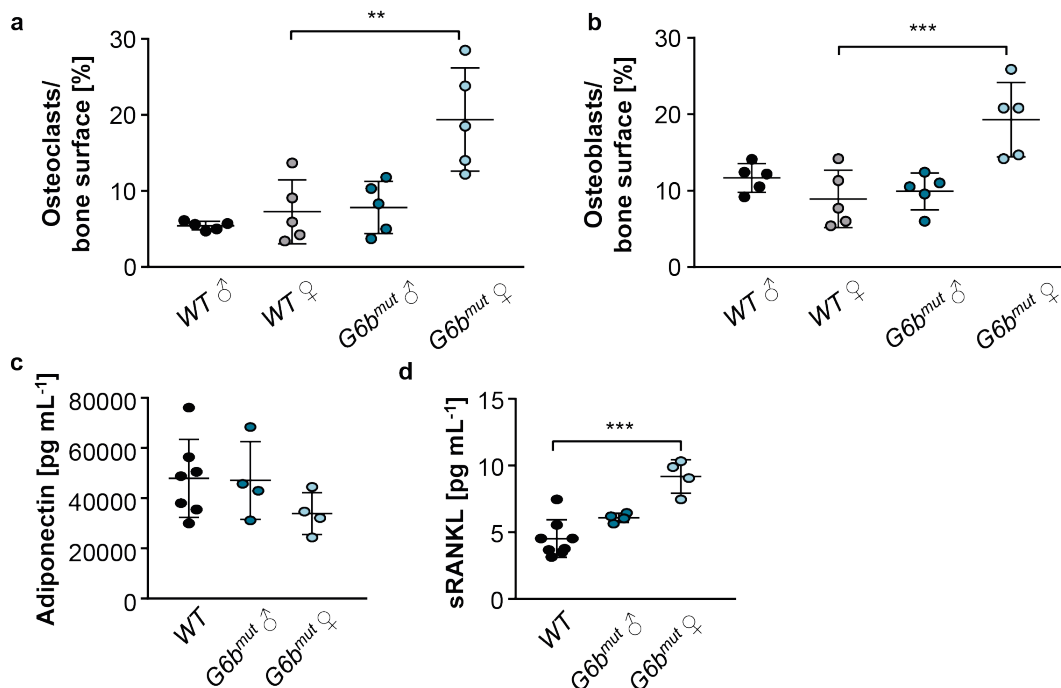
Figure 53. Female *G6b^mut* mice exhibit a high turnover osteoporosis. The number of osteoclasts (**a**) and osteoblasts (**b**) per bone surface were analyzed by staining for TRAP using an HRP-coupled antibody or using Toluidin Blue, respectively. Analysis was performed by Dr. Melanie Haffner-Luntzer, University of Ulm. Values are mean ± SD (n = 5). One-way ANOVA with Sidak correction for multiple comparisons. **P < 0.01; ***P < 0.001. (**c, d**) BM plasma levels of sRANKL and adiponectin were assessed using a Multiplex cytokine assay. Values are mean ± SD (n = 5). One-way ANOVA with Sidak correction for multiple comparisons. **P < 0.01; ***P < 0.001.

Quantification of osteoclast and osteoblast numbers in paraffin sections surprisingly revealed an increased abundance of both cell types in trabecular bone (Figure 53a, b), a phenotype referred to as high turnover osteoporosis.[224]
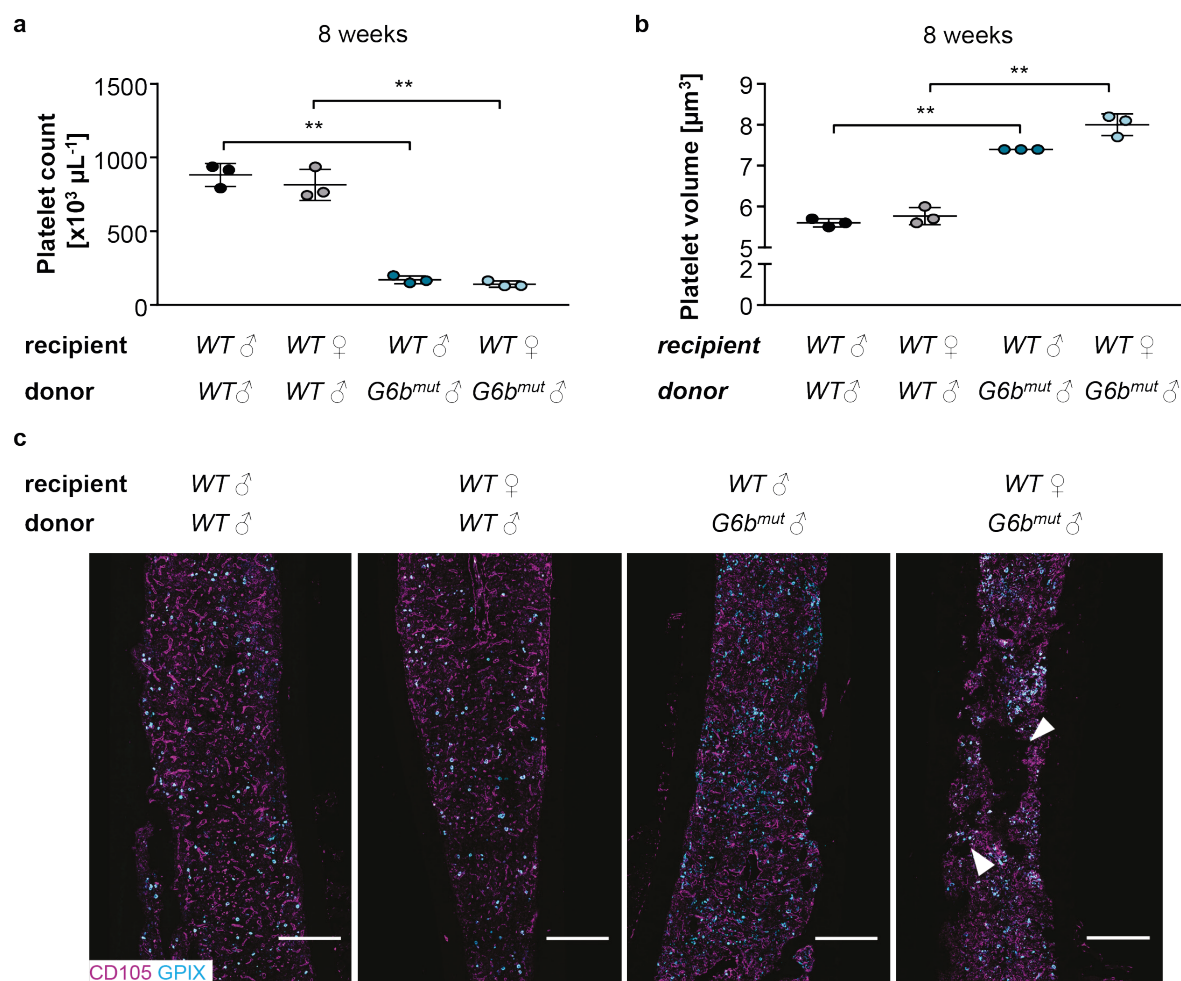
Figure 54. Beginning osteosclerosis in female BM-transplanted *G6b^mut* mice. Female and male *WT* mice were lethally irradiated and injected with BM derived from male *WT* or G6b^mut mice. Platelet count (**a**) and size (**b**) 8 weeks after transplantation were determined by automated blood cell analysis. Values are mean ± SD (n = 3). One-way ANOVA with Sidak correction for multiple comparisons. **P < 0.01. (**c**) Immunofluorescently stained cryosections of BM-chimeric *WT* and *G6b^mut* mice were analyzed by confocal microscopy (Leica TCS SP8, 25x objective). Arrowheads highlight areas with reduced BM cellularity. Scale bars: 500 μm.

While levels of adiponectin secreted by adipocytes in the BM were unaltered in the BM plasma of female mutant mice (Figure 53c), the increase in osteoclast numbers was reflected by elevated levels of sRANKL (Figure 53d). In order to identify whether the observed differences were sex hormone-related, 6-week-old male and female *WT* mice were lethally irradiated and transplanted with BM derived from either male *WT* or *G6b^mut* mice. Platelet count and size as well as well BM architecture were analyzed using an automated blood cell analyzer and confocal microscopy, respectively. Surprisingly, we did not observe differences in platelet count or size between female and male chimeric *G6b^mut* mice (Figure 54a, b).
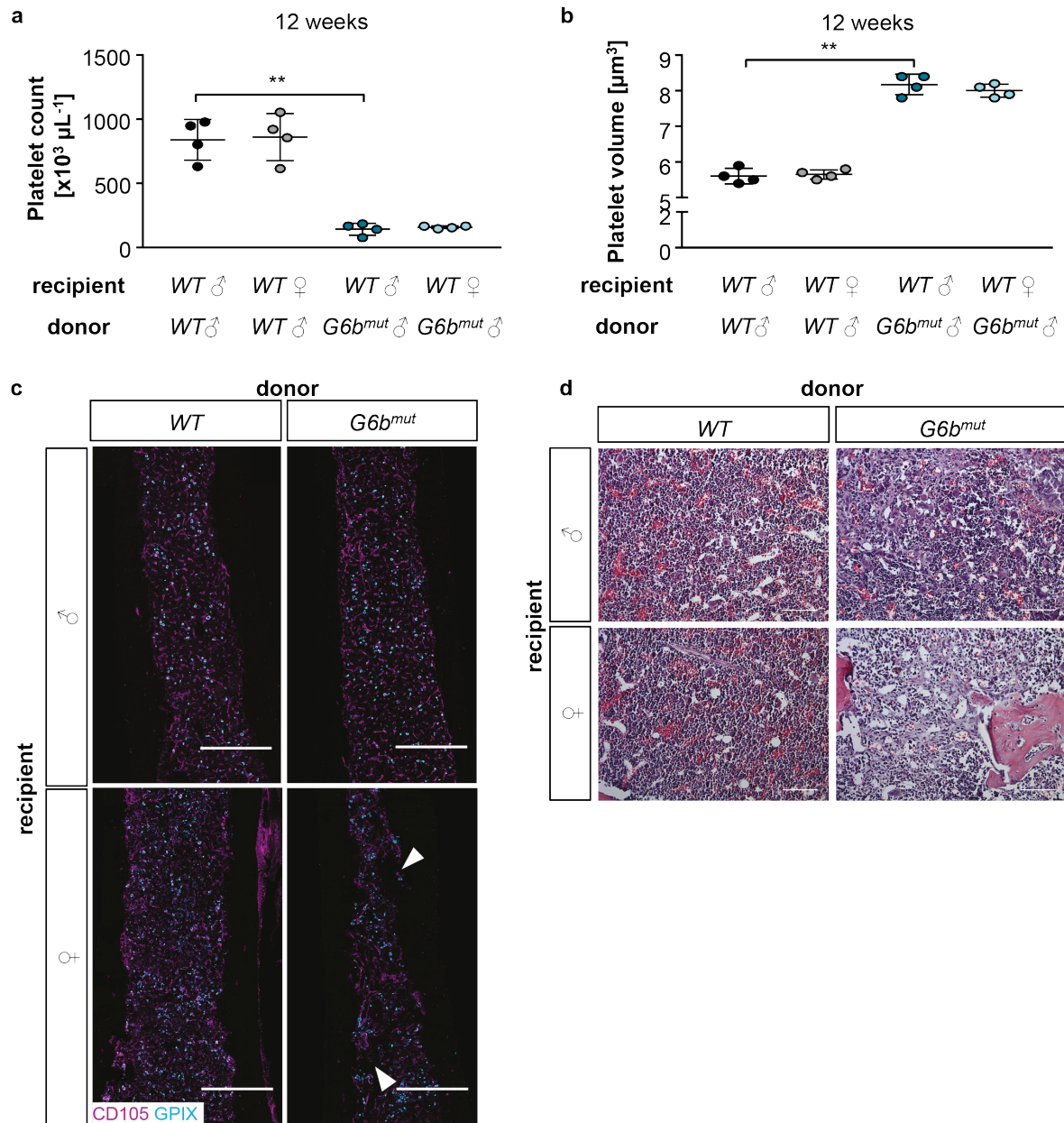
Figure 55. Sex-specific osteosclerosis albeit indistinguishable platelet counts in BM-chimeric *G6b^{mut}* mice. (**a, b**) Platelet parameters were assessed at an automated blood cell analyzer. Values are mean ± SD (n = 4). One-way ANOVA with Sidak correction for multiple comparisons. **P < 0.01. BM architecture was analyzed by confocal microscopy (Leica TCS SP8, 25x objective) (**c**) and by H&E stainings on paraffin sections (**d**). (**c**) Arrowheads highlight osteosclerotic areas. Scale bars: 500 µm.

Analysis of the BM in cryosections stained for CD105 and GPIX on the other hand revealed a beginning osteosclerosis specifically in female mice, suggesting the phenotype to be induced by differences in hormone levels or altered paracrine signaling mechanisms (Figure 54c). While platelet counts were still undistinguishable in 12-week-old BM-transplanted *G6b^{mut}* mice (Figure 55a, b), osteosclerosis was evident in femoral bones of female mice as assessed by immunofluorescence stainings on cryosections (Figure 55c) as well as H&E

stainings on paraffin sections (Figure 55d). Moreover, BM myelofibrosis in male chimeric *G6b^mut^* mice was strikingly more severe compared to untransplanted mice, suggesting that the increased deposition of collagen and reticulin fibers leads to substitution of BM cells and thus results in reduced platelet counts in male mice as well.

4.4.5 Myelofibrosis in *G6b^mut^* mice is due to altered cytokine release

A progressive myelofibrotic phenotype has been described in *G6b^-/-^* mice,[155] but the underlying mechanisms leading to collagen and reticulin deposition are still incompletely understood. To further decipher how altered MK reactivity can affect BM homeostasis, we first determined abundance of BM MKs in whole femora cryosections by confocal microscopy (Figure 56a, b) and found the number of intact MKs to be markedly increased in *G6b^mut^* mice.
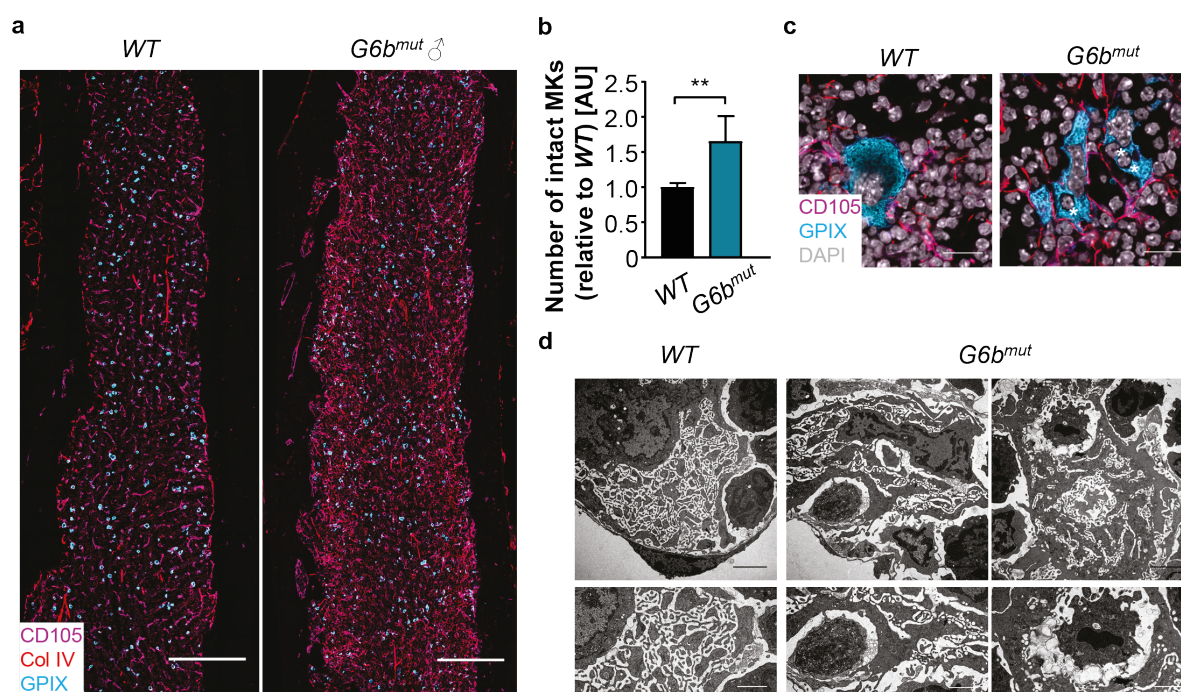
Figure 56. Increased fibrosis, MK abundance and emperipolesis in the BM of *G6b^mut^* mice. (**a**) Whole femora cryosections of *WT* and *G6b^mut^* mice were immunofluorescently stained for collagen IV, GPIX and CD105 and analyzed by confocal microscopy (Leica TCS SP8, 25x objective). Scale bars: 500 μm. (**b**) Intact GPIX-positive MKs were manually counted in whole femora cryosections of *WT* and *G6b^mut^* mice. Values were normalized to the control. Values are mean ± SD (n = 4). Unpaired, two-tailed student's t-test. **P < 0.01. (**c**) Emperipolesis of neutrophils into BM MKs was visualized in femoral cryosections stained for GPIX, collagen I and CD105. Asterisks highlight intracellular neutrophilic nuclei. Images were acquired at a Leica TCS SP8 (40x objective). Scale bars: 15 μm. (**d**) TEM of BM MKs displaying emperipolesis of neutrophils into *G6b^mut^* MKs. Scale bars: 3 μm; insets: 1.5 μm.

Of note, we detected a high level of MK fragmentation within the BM in the absence of G6b-B, which impeded an exact determination of MK numbers. Staining with the sinusoid marker collagen IV further revealed aberrant and dilated vessel structures in the BM of *G6b^mut^* mice. In addition, *G6b^mut^* mice exhibited an increased amount of neutrophil emperipolesis into MKs, a finding that has been linked to myelofibrosis in previous studies (Figure 56c, d).[141]

It is well established that an elevated release of TGFβ1 promotes collagen and reticulin deposition due to increased collagen synthesis on the one hand and inhibited metalloproteinase activity on the other hand.[225,226] Immunosorbent assays indeed revealed increased TGFβ1 concentrations in BM plasma of *G6b^{mut}* mice, while blood plasma levels were unaffected (Figure 57a, c). Since we observed an aberrant vessel morphology in the BM of *G6b^{mut}* mice we also assessed levels of VEGFA in BM and blood plasma, but were unable to detect differences (Figure 57b, d), thus suggesting that the observed alterations were not caused by altered vascularization and vessel growth, but are rather due to VEGF-independent vessel remodeling. Of note and in addition to altered TGFβ1 levels, enhanced concentrations of the proinflammatory cytokine IL-6 were also observed in BM and blood plasma of male G6b-B-mutant mice, thus implying its involvement in the promotion of myelo-fibrosis (Figure 57e, f).
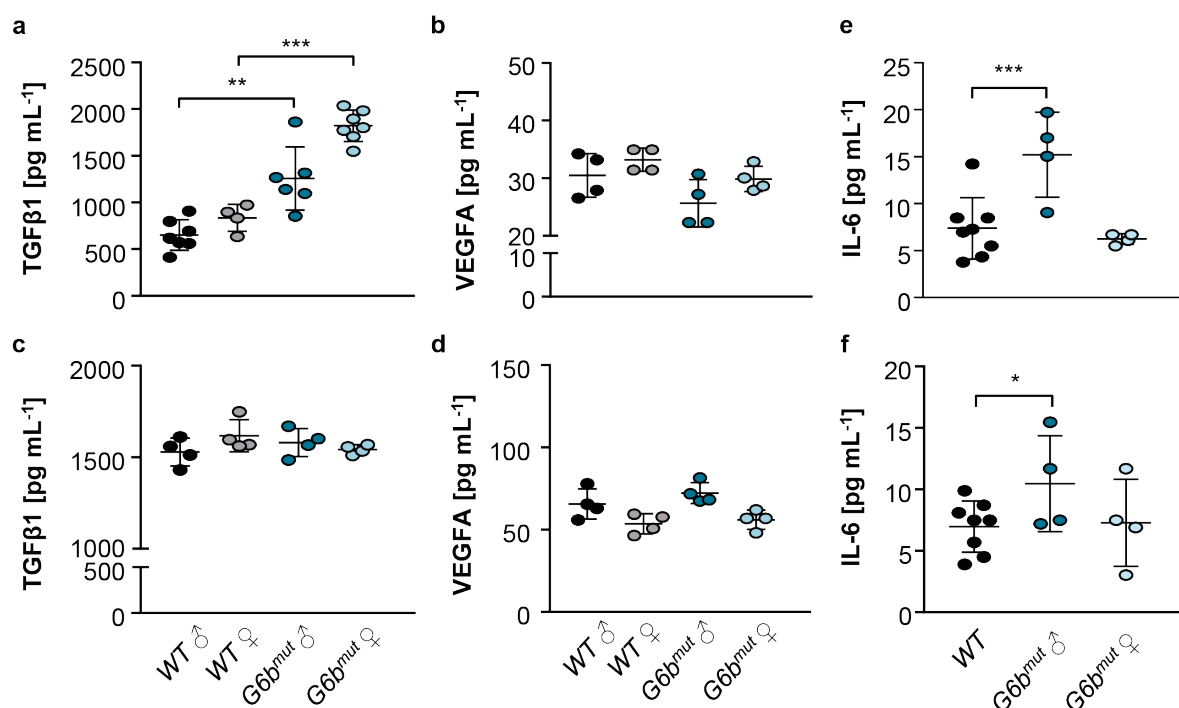
Figure 57. Increased TGFβ1 levels in BM but not blood plasma of *G6b^{mut}* mice. Levels of TGFβ1 and VEGFA were analyzed in BM (**a, b**) and blood plasma (**c, d**) of *WT* and *G6b^{mut}* mice using purchased enzyme-linked immunosorbent assays. Levels of IL-6 in BM (**e**) and blood plasma (**f**) of *WT* and *G6b^{mut}* mice were assessed using a customized Multiplex cytokine assay. Values are mean ± SD. One-way ANOVA with Sidak correction for multiple comparisons. **P < 0.05; **P < 0.01; ***P < 0.001.

4.4.6 Impaired maturation and reduced PPF of *G6b^{mut}* MKs *in vitro*

Due to the abnormal MK morphology in *G6b^{mut}* mice observed in whole femora cryosections, we next investigated the appearance of *G6b^{mut}* MKs *in situ* by performing TEM. In contrast to *WT* MKs with a clearly developed DMS surrounded by a peripheral zone as well as normally

distributed granules, the DMS in *G6b^{mut}* MKs was markedly underdeveloped and appeared dilated (Figure 58a). Quantification of DMS and nuclear area in *G6b^{mut}* MKs revealed a distinct decrease in DMS fraction, while the nuclear area was comparable to the *WT* (Figure 58b). These findings imply an intrinsic maturation defect to account for the observed alterations in MK functionality, since several previous publications suggested an accumulation of immature MKs to be responsible for an increased secretion of TGFβ1.[146]
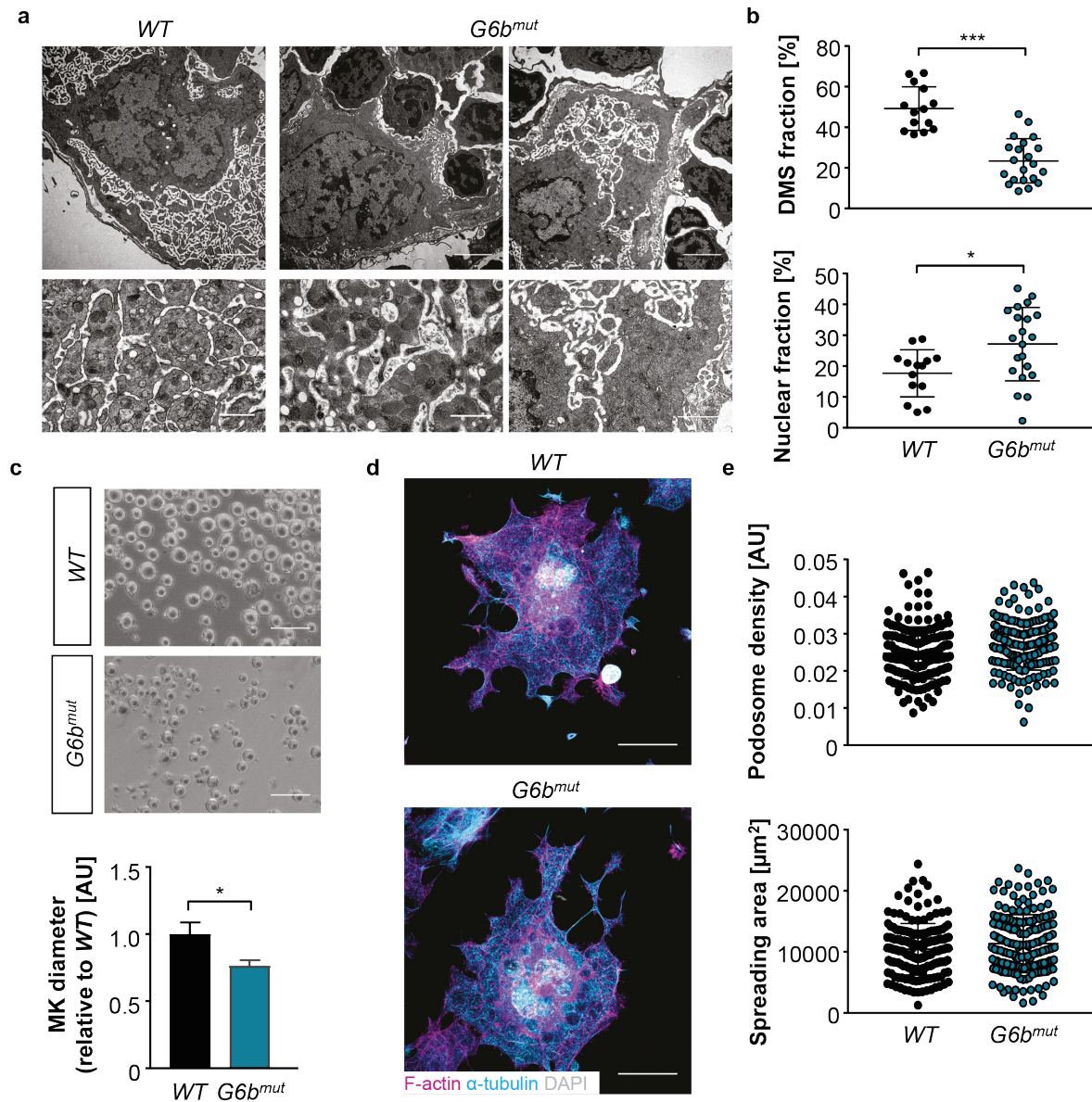
Figure 58. Defective maturation of *G6b^{mut}* MKs *in vitro* and *in situ*. a) MK morphology and DMS distribution *in situ* were analyzed by TEM. Scale bars: 3 μm; insets: 1 μm. (**b**) Percentage of DMS and nuclear fraction were manually quantified using ImageJ Software. Values are mean ± SD (n = 3). Unpaired, two-tailed student's t-test. *P < 0.05; ***P < 0.001. (**c**) TPO-matured MKs were imaged on a brightfield microscope (20x objective). MK diameter was determined using ImageJ Software. Scale bars: 100 μm. Values are mean ± SD (n = 3). Unpaired, two-tailed student's t-test. *P < 0.05. Visualization (**d**) and quantification of spreading area and podosome numbers (**e**) in *WT* and *G6b^{mut}* MKs spread on Horm collagen. Cytoskeleton was visualized by confocal microscopy (Leica TCS SP8, 40x objective). Nuclei were counterstained using DAPI. Scale bars: 40 μm. Analysis was done using ImageJ Software. Values are mean ± SD (n = 3).

To assess MK maturation *in vitro*, MK precursors were isolated from whole BM and cultured in the presence of TPO.
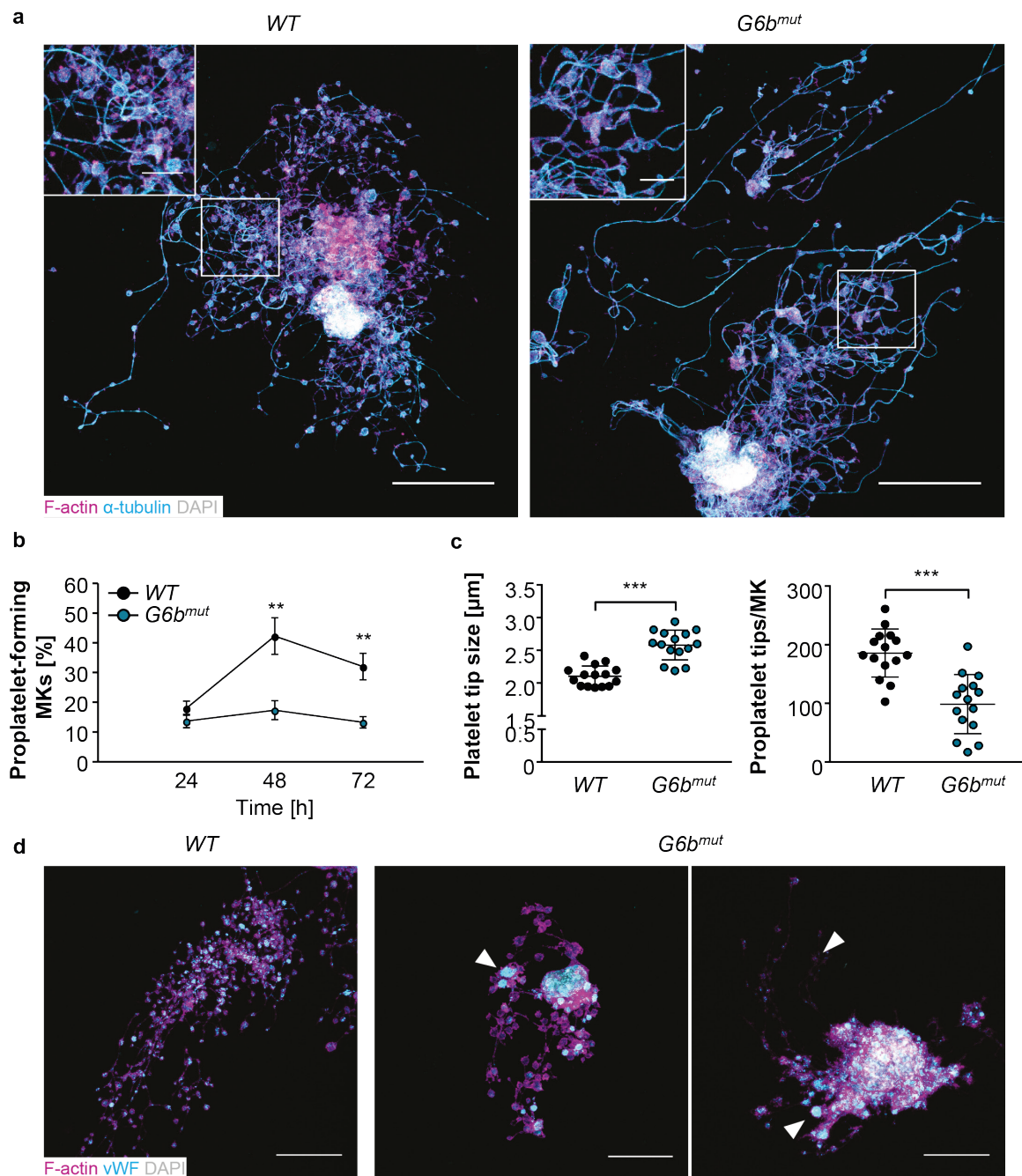
Figure 59. Impaired PPF of *G6b^mut* MKs. (**a**) Proplatelet-forming MKs were stained for F-actin and α-tubulin and visualized by confocal microscopy (Leica TCS SP8, 40x objective). Nuclei were visualized using DAPI. Scale bars: 40 μm; insets: 10 μm. (**b**) Percentage of proplatelet-forming MKs was counted manually. An average of five visual fields per well is shown. Values are mean ± SD (n = 3). Unpaired, two-tailed student's t-test. **P < 0.01. (**c**) Proplatelet tip size and number of platelets per MK were assessed manually using ImageJ Software. Values are mean ± SD (n = 3). Unpaired, two-tailed student's t-test. ***P < 0.001. (**d**) Distribution of α-granules in *WT* and *G6b^mut* MKs was analyzed by confocal microscopy (Leica TCS SP8, 40x objective). Arrowheads point to irregularly distributed vWF. Scale bars: 30 μm.

Determination of MK diameter in enriched MK cultures revealed a marked decrease in the mean size of *G6b^mut* MKs (Figure 58b) suggesting impaired TPO-induced maturation. Surprisingly, spreading of *G6b^mut* MKs on Horm collagen was unaltered as manifested by a comparable spreading area and podosome formation compared to the *WT*. In contrast to previous studies,[155] these findings indicate that cytoskeletal rearrangements may be unaffected in the absence of G6b-B (Figure 59c, d). The severe macrothrombocytopenia as well as delayed platelet recovery observed in *G6b^mut* mice encouraged us to investigate PPF in *WT* and *G6b^mut* MKs *in vitro*. Confocal microscopy of proplatelet-forming *WT* and *G6b^mut* MKs revealed a grossly normal cytoskeleton in the mutant cells with a similar distribution of F-actin and α-tubulin within proplatelet shafts and tips (Figure 59a). In contrast, the total number of proplatelet-forming MKs was markedly reduced compared to *WT* controls (Figure 59b). Moreover, the proplatelet diameter was significantly increased, while the number of proplatelet tips was reduced in the mutant MKs (Figure 59c), which became further evident by visualization of the microtubule cytoskeleton using confocal microscopy (Figure 59a; insets). Since granule distribution *in situ* appeared to be affected by loss of G6b-B, we also analyzed α-granule transport within proplatelet-forming MKs by staining for vWF. While *WT* MKs displayed a well-organized distribution of granules into proplatelet tips, granule transport in *G6b^mut* MKs appeared irregular with occasional proplatelets being highly vWF-positive and some being devoid of any α-granules (Figure 59d; arrowheads), thus implying defective granule generation and/or distribution. In summary, these findings suggest that impaired MK maturation accounts for suppressed PPF in the absence of functional G6b-B *in vitro* and *in vivo*.

4.4.7 Altered progenitor and MK precursor distribution within the BM of *G6b^mut* mice

The immature morphology of BM MKs *in situ* in addition to the highly impaired PPF of *in vitro*-cultured *G6b^mut* MKs prompted us to investigate whether MK precursors in the BM were also altered in numbers. To this end, we first determined the abundance of c-kit$^+$Sca$^-$ cells by flow cytometry and found it to be decreased in *G6b^mut* mice. At the same time, the number of CD34$^-$CD16/32$^-$ MEPs was reduced, while we did not observe any differences in the amount of CMPs or GMPs, respectively (Figure 60a, b). Analysis of the mean size of BM MKs by flow cytometry revealed an increased abundance of small- and medium-sized MKs, while the number of big MKs was markedly reduced (Figure 60c). Most importantly, granular MKs were almost absent from the BM of *G6b^mut* mice suggesting a distinct maturation defect leading to the accumulation of small, immature MKs.
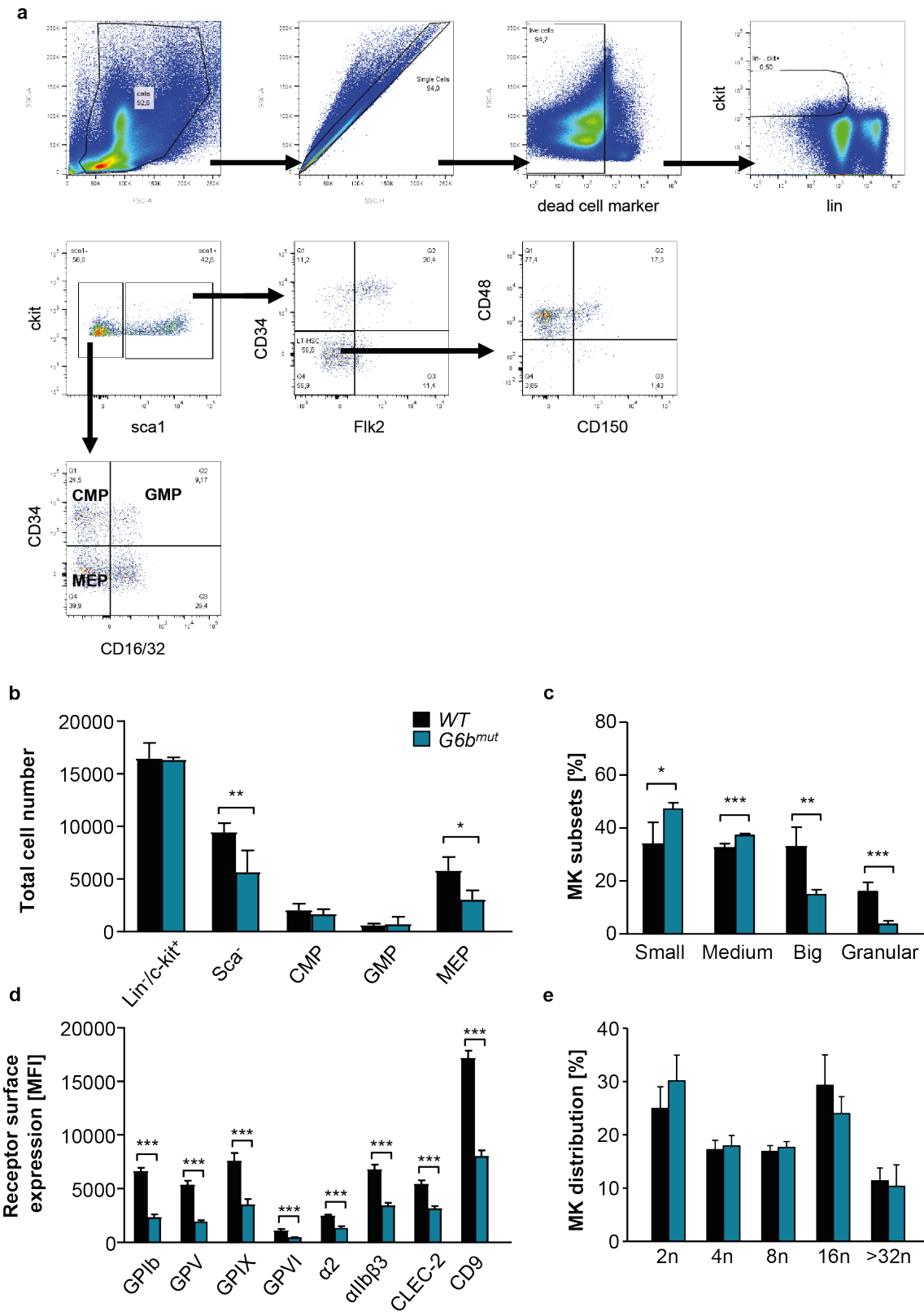
Figure 60. Altered progenitor distribution and reduced MK GP expression in _G6b^mut_ mice. Flow cytometric gating strategy (**a**) and analysis (**b**) of hematopoietic progenitors in whole BM of _WT_ and _G6b^mut_ mice. Experiment was performed by Carina Gross. Values are mean ± SD (n = 4). Unpaired, two-tailed student's t-test. *P < 0.05; **P < 0.01. Average MK size distribution (**c**), FI of major MK glycoproteins (**d**) and MK ploidy (**e**) were determined by flow cytometry in whole BM of _WT_ and _G6b^mut_ mice. Analysis was done using FlowJo Software. Values are mean ± SD (n = 4). Unpaired, two-tailed student's t-test. *P < 0.05; **P < 0.01; ***P < 0.001.

In order to assess whether this defect in cytoplasmic maturation coincided with impaired polyploidization of *G6b^mut* MKs, we analyzed ploidy of native BM MKs by flow cytometry. Interestingly, we did not observe any differences in ploidy levels between *WT* and *G6b^mut* MKs, highlighting that endomitosis was largely unaffected in the absence of G6b-B (Figure 60e), which is in line with a grossly normal nuclear MK fraction observed by TEM (Figure 58a, b) and previous studies.[155] To further decipher the maturation state of *G6b^mut* MKs, we investigated the surface expression levels of major MK GPs by flow cytometry. Strikingly, expression levels of all tested GPs were significantly reduced on *G6b^mut* MKs (Figure 60d), thus further confirming an MK maturation defect *in vivo*.

4.4.8 Altered mRNA profile in native *G6b^mut* MKs
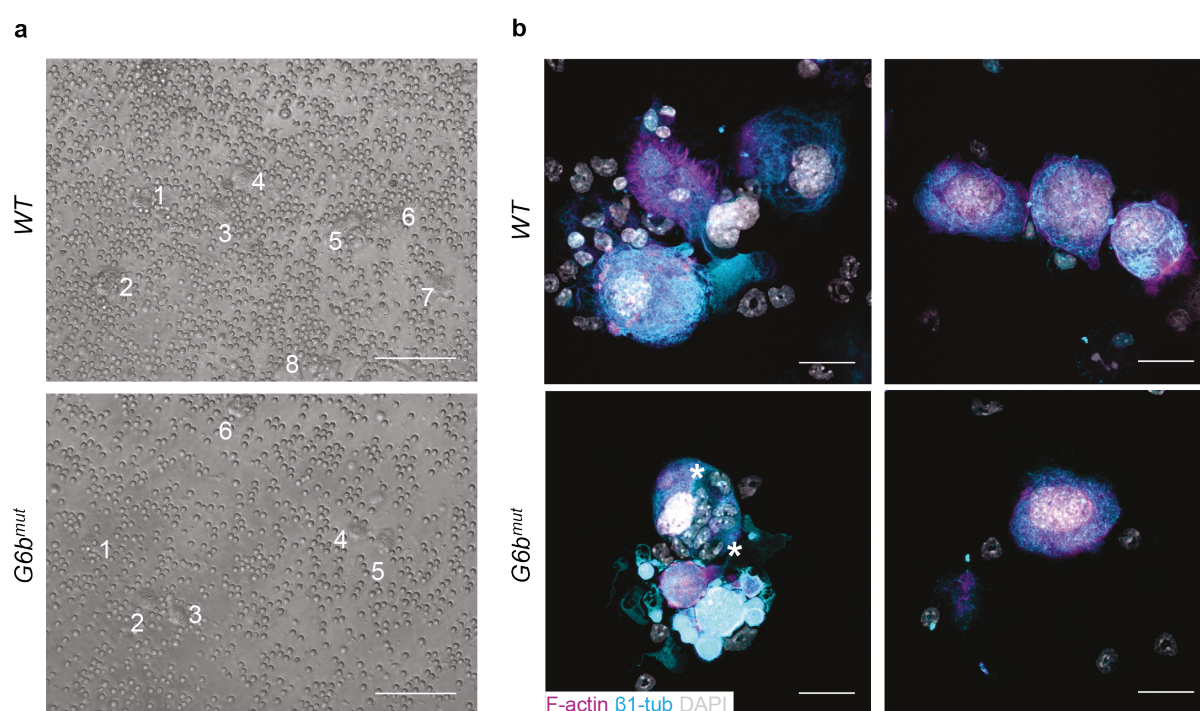
Figure 61. Novel protocol for the isolation of native MKs from the BM. (**a**) Native MKs were isolated from whole BM using a magnetically labeled anti-CD61 antibody. Images display cell population after positive selection. Numbers are indicative for MK enrichment. Scale bars: 100 µm. (**b**) CD61+ cells were subjected to a density gradient enrichment and analyzed by confocal microscopy at a Leica TCS SP8 (40x objective) upon staining for β1-tubulin and F-actin. Nuclei were counterstained using DAPI. Scale bars: 25 µm.

The impaired maturation of *G6b^mut* BM MKs *in vitro* and *in vivo* indicated an altered transcription of MK-specific genes in the mutant cells. In order to identify possible expression profile differences compared to *WT* MKs, we first established a protocol for high-purity isolation of native BM MKs using magnetic beads directed against integrin β3, which is highly expressed on platelets and MKs. The presence of MKs was verified by brightfield microscopy (Figure 61a).
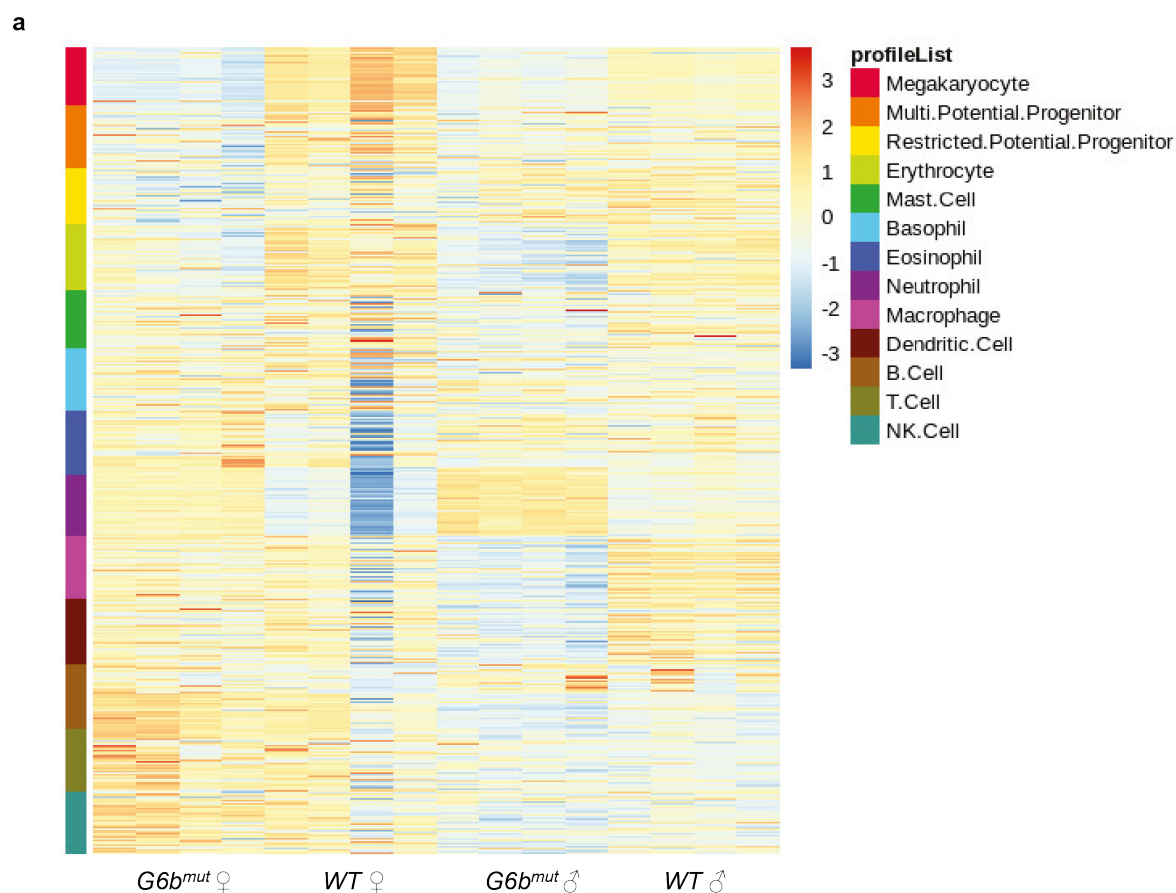
Figure 62. Altered mRNA profile in _G6b^mut_ MKs. (**a**) mRNA was isolated from positively selected MKs after gradient enrichment using Trizol and mRNA profile was analyzed by RNA sequencing. Overview heatmap displays up- and downregulated genes of different hematopoietic cell subsets in female and male _WT_ and _G6b^mut_ MKs (n = 4). RNA isolation was carried out by Dr. Georgi Manukjan. Analysis was performed by Dr. Sascha Dietrich, CoreUnit Systems Medicine, University of Würzburg.

Subsequently, MKs were immediately enriched on a density gradient. Immunofluorescence stainings for β1-tubulin and F-actin verified the presence of MKs in the isolated fraction (Figure 61b). Of note, we detected an increased incidence of neutrophil emperipolesis into _G6b^mut_ BM MKs under these experimental settings as well (Figure 61b; asterisk). Enriched MKs were immediately Trizol-lysed and RNA sequencing on female and male _WT_ and _G6b^mut_ MKs was performed by Dr. Sascha Dietrich at the CoreUnit Systems Medicine Würzburg. As visible in Figure 62a, mRNA profiles between _WT_ and _G6b^mut_ MKs were markedly different. These alterations were most evident upon analysis of neutrophil- and MK-specific genes. In contrast to low levels of neutrophil-specific mRNAs in MKs derived from male or female _WT_ mice, these genes were markedly upregulated in _G6b^mut_ MKs (Figure 63a), most likely due to the aforementioned emperipolesis. MK-specific gene profiles on the other hand were virtually not induced in _G6b^mut_ MKs from both male and female mice (Figure 63b).

Figure 63. Reduced MK-specific mRNA profile in *G6b^mut* MKs. (a, b) Heatmaps for the expression of neutrophil- (**a**) and MK-specific genes (**b**) in female and male *WT* and *G6b^mut* MKs. Genes were chosen according to Haeomsphere database. (**c**) MK differentiation pathway plot comparing MK-specific gene expression in female and male *WT* and *G6b^mut* MKs (n = 4). Enrichment maps were performed using Clusterprofiler. Analysis was performed by Dr. Sascha Dietrich, CoreUnit Systems Medicine, University of Würzburg.

In-depth analysis of the MK differentiation profile using pathway plots highlighted the significant downregulation of MK-specific genes (Figure 63c), among them the most prominent MK- and platelet glycoproteins as well as several transcription factors involved in the induction of the MK lineage such as GATA-1. In summary, analysis of the RNA profile of *G6b^mut* MKs revealed a markedly reduced expression of MK-specific genes, which might account for the observed maturation impairments *in vitro* and *in vivo*.

4.4.9 Impaired TPO signaling and reduced GATA-1 expression in *G6b^mut* MKs

TPO signaling has previously been linked to the induction of GATA-1 protein expression.[146] The reduced MK-specific mRNA profile together with the impaired maturation upon TPO-stimulation *in vitro* suggested alterations in TPO responsiveness upon loss of G6b-B. Stimulation of *WT* MKs with 50 ng mL⁻¹ TPO induced a robust phosphorylation of the TPO-linked signaling molecules JAK2 and STAT5 (Figure 64a-d). In contrast, phosphorylation as well as total protein levels of c-Mpl, JAK2 and STAT5 appeared to be significantly reduced in *G6b^mut* MKs. JAK2 signaling has further been described to induce Shp2 phosphorylation,

although it is controversially discussed, whether Shp2 stimulates or inhibits JAK2 signaling.[93] As apparent in Figure 64a, TPO signaling induced Shp2 phosphorylation in *WT* and *G6b^mut* MKs, but phosphorylation as well as total protein levels of the phosphatase were significantly lower in *G6b^mut* MKs (Figure 64b).
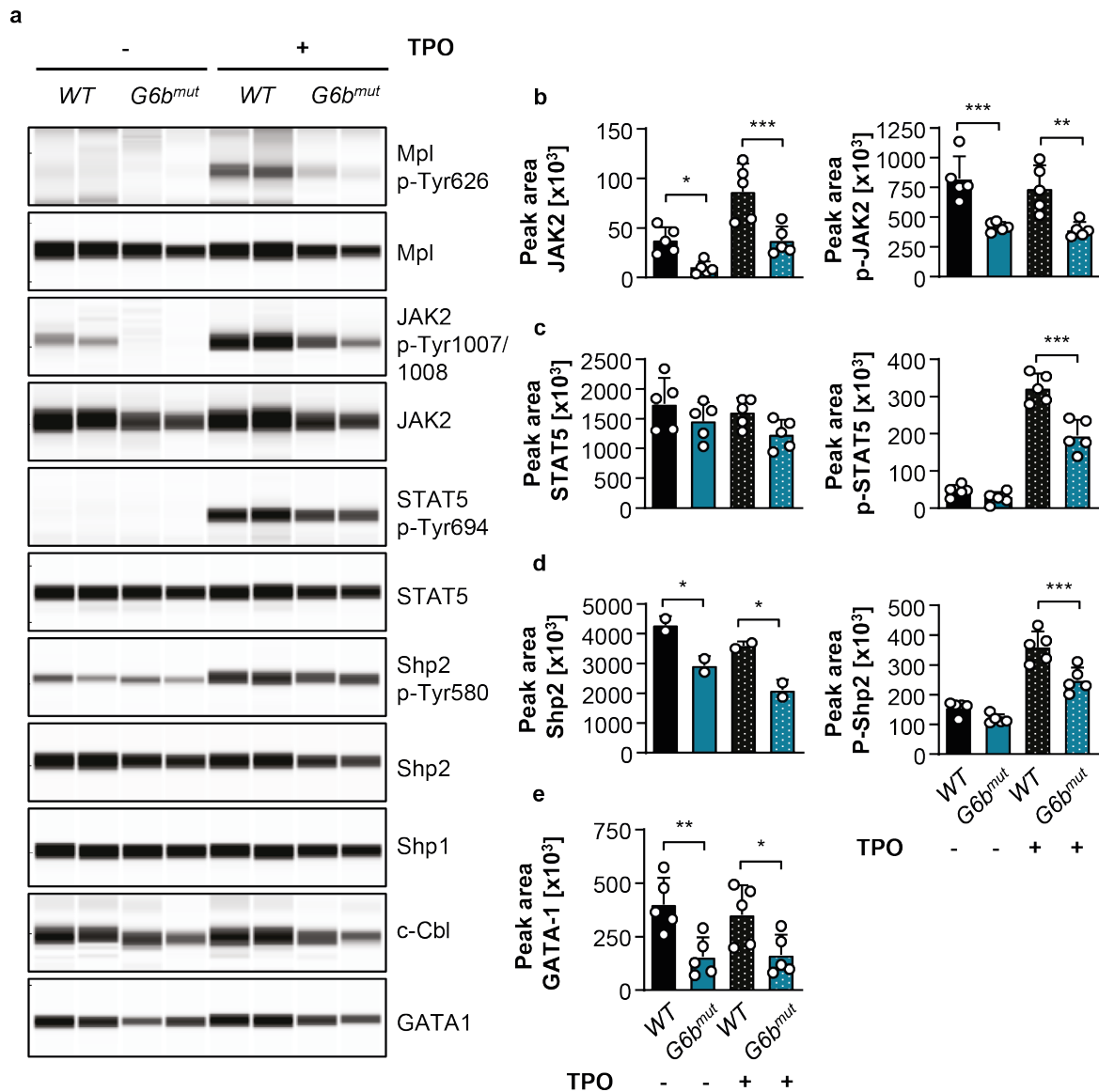
Figure 64. Reduced Shp2 phosphorylation and GATA-1 expression in *G6b^mut* MKs. Phosphorylation and total expression levels of TPO-related signaling molecules and GATA-1 in TPO-stimulated *WT* and *G6b^mut* MKs were visualized (**a**) and quantified (**b, c**) by quantitative capillary-based gel electrophoresis analysis. Immuno-blotting was performed by Dr. Zoltan Nagy. Values are mean ± SD (n = 5). One-way ANOVA with Sidak correction for multiple comparisons. *P < 0.05; **P < 0.01; ***P < 0.001

On the opposite, Shp1 expression was indistinguishable between *WT* and *G6b^mut* MKs. Moreover and in addition to decreased c-Mpl expression and phosphorylation, the expression of the E3 ubiquitin-ligase c-Cbl, which has previously been associated with c-Mpl degradation, was also reduced in *G6b^mut* MKs. In order to assess whether these impairments

in TPO signaling affected transcriptional activation, we analyzed GATA-1 protein levels and found its expression to be significantly decreased in *G6b^{mut}* MKs. Whether reduced GATA-1 levels are causative for or a result of reduced c-Mpl levels and impaired TPO signaling still needs to be addressed, since GATA-1 is induced by c-Mpl signaling on the one hand, but is in turn also able to increase c-Mpl expression.[227]

5 DISCUSSION

5.1 The role of soluble GPV in vascular and lymphatic development

The contribution of ITAM receptors to the maintenance of vascular integrity, in particular the role of CLEC-2 during lymphatic vessel development, is long established, although the underlying signaling mechanisms are still incompletely understood. The only known endogenous ligand of CLEC-2 - podoplanin - is expressed on LECs, but absent from the blood vasculature. Several studies implicated the presence of an intravascular ligand of CLEC-2, above all due to its contribution to hemostasis, but so far its existence is still controversially discussed.[22] Several studies suggested CLEC-2 to support thrombus formation at the junction between cardinal vein and primary lymph sac or at the lymphovenous junction in adults by interaction with its endogenous ligand podoplanin on LECs.[17] However, these findings are challenged, since animals lacking the αIIbβ3 adapter molecules talin-1 or kindlin-3 do not display blood-lymphatic misconnections, thus contradicting the hypothesis of thrombus formation to contribute to vessel separation.

GPV was first identified as the only membrane GP being cleaved upon thrombin-mediated platelet activation.[228] Subsequent studies were able to show that loss of *Gp5* was not associated with a Bernard-Soulier-like phenotype and that thrombin-stimulated platelet activation was grossly normal upon GPV-deficiency.[174] Moreover, a collagen-binding site within GPV was supposedly involved in collagen-dependent platelet adhesion and activation.[229] Nevertheless, the exact function of GPV as part of the GPIb-V-IX complex on the platelet surface still remains elusive. Our group was now able to identify a significant contribution of GPV to hemostasis and thrombosis *in vivo*, since its deficiency was able to compensate for lack of the (hem)ITAM receptors GPVI and CLEC-2 (Beck *et al*., unpublished). Moreover, the results identified sGPV to account for the observed compensation, since transgenic mice, in which thrombin-mediated GPV cleavage was rendered impossible, recapitulated the key findings made in GPV-deficient mice. These results prompted us to investigate, whether GPV deficiency or loss of its thrombin-cleaved form might also substitute for lack of CLEC-2 during lymphatic and vascular development. In contrast to our expectations, lack of thrombin-cleaved GPV aggravated blood-lymphatic misconnections resulting in a dramatic leakage of blood into the peritoneal cavity due to impaired tight junction density in mesenteric vessels during embryogenesis as well as in adult animals. Accordingly, sGPV appears to not only be indispensable to safeguard hemostasis upon vessel injury, but might also be involved in regulating vascular and lymphatic integrity in cooperation with CLEC-2.
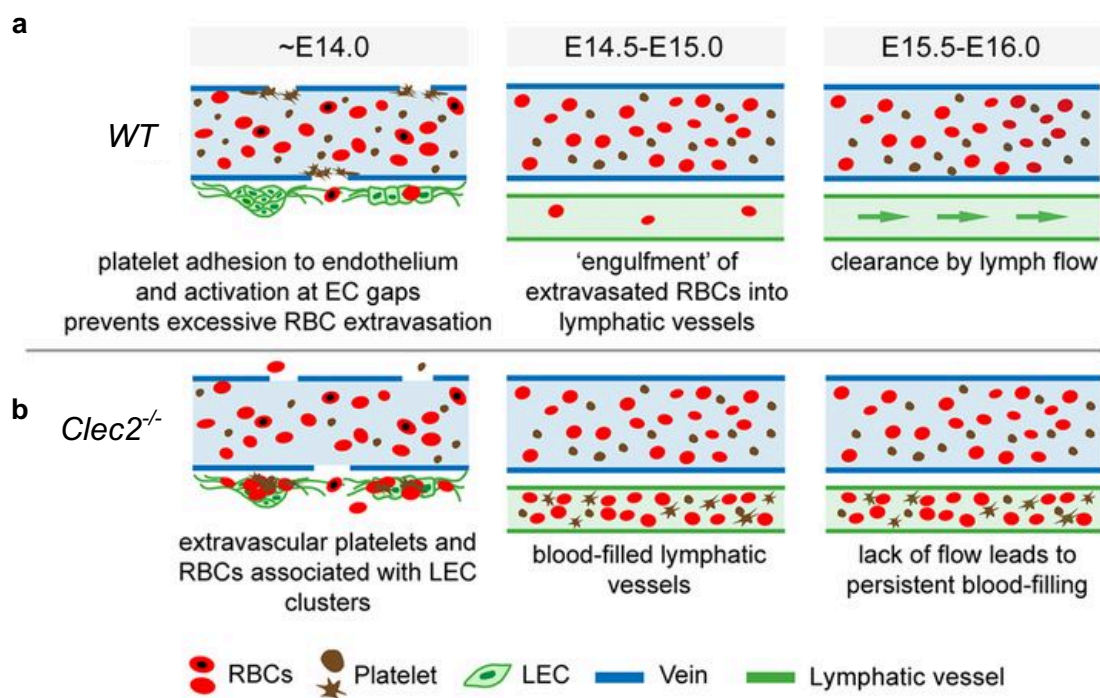
Figure 65. Platelet-dependent maintenance of venous integrity in embryonic mesenteries. (**a**) RBC extravasation through holes in the venous vasculature in embryonic mesenteries of *WT* mice is prevented by platelet interactions with ECs or surrounding cells. Leaked RBCs are engulfed by LECs and cleared by lymph flow. (**b**) Increased RBC leakage in *Clec2*^{-/-} embryos due to loss of platelet-dependent sealing of venous holes. Accumulation of RBC within lymph vessels caused by ineffective lymph flow-mediated vessel maturation aggravates the blood-filling of lymph vessels. Modified from: Zhang *et al.*, **Development**, 2018.[196]

That CLEC-2 might not only be important for lymphatic development, but is further required for venous maturation was strongly implied in a recent study by Zhang *et al.*. The group was able to identify a transient loss in mesenteric venous integrity in *WT* mice during embryogenesis leading to the egress of RBCs into the interstitial space.[196] There, RBCs are engulfed by developing lymphatic vessel precursors and cleared via lymphatic flow. *Clec2*^{-/-} animals on the other hand displayed a significant increase in RBC extravasation even prior to the development of the first LECs, suggesting that CLEC-2 is essential for preventing RBC release from venules. These findings contradict previous studies that proposed CLEC-2-podoplanin interactions on LECs to account for the prevention of blood-lymphatic mixing during embryogenesis.[21,230] Strikingly, podoplanin was found to be expressed on mesothelial cells as well as venule-associated fibroblasts suggesting platelet CLEC-2 to be able to interact with these vessel-surrounding cells instead of the developing LECs. This hypothesis, however, is contradicted, since platelets were exclusively located outside the vasculature in embryos of *Clec2*^{-/-} mice, whereas no platelet extravasation was observed in *WT* mesenteries, which challenges the idea of a platelet-mesothelial cell interaction, but rather implies the presence of an intravascular ligand. As illustrated in Figure 65, platelet adhesion

might therefore be essential to seal EC gaps, thus preventing the excessive extravasation of RBCs. This notion is further supported by several studies identifying a role of CLEC-2 in hemostasis in thrombosis, which relies on the presence of its extracellular domain rather than on intracellular signaling transduction, thus supporting the idea of a potential intravascular ligand.[22,184]

The findings of the present study further support this hypothesis and imply sGPV to be markedly involved in the maintenance of venous integrity during development. While a mild RBC leakage into the interstitial space was observed in the absence of CLEC-2 alone, RBCs dramatically accumulated in lymphatic vessels of $Clec2^{-/-}/Gp5^{KIN}$ mesenteries leading to aberrant vessel maturation and dilation (Figure 13, 19). According to the current model (Figure 65), sGPV might therefore be a backup mechanism to prevent RBC extravasation upon lack of CLEC-2 by directly stimulating endothelial cell maturation, since we identified a reduced ZO-1 expression in embryonic mesenteries by confocal microscopy in both blood as well as lymphatic ECs (Figure 20). As published previously, lack of CLEC-2 impairs lymphatic vessel maturation including valve development due to insufficient lymph flow, which is necessary to induce LEC-specific transcriptional activation.[194] These impairments in addition to the deteriorated mesenteric architecture development in double-transgenic embryos might then translate into increased mesenteric and intestinal endothelial permeability leading to blood leakage into the peritoneal cavity in adults (Figure 18), primarily also due to decreased ZO-1 expression in intestinal tissue (Figure 20). In this context, the decrease in platelet lifespan detected in $Clec2^{-/-}/Gp5^{KIN}$ mice might not be caused by increased platelet clearance, but is more likely induced by a severe blood leakage into the peritoneal cavity, which might also explain the marked anemia and the concomitant decrease in hematocrit values.

A recent publication identified an increased proportion of CLEC-2-positive *extracellular vesicles* (EV) within blood and lymph of mice subjected to rheumatoid arthritis.[231] EVs are constantly released by platelets, but their numbers are highly increased upon platelet activation. Interestingly, CLEC-2-positive EVs were able to interact with LECs in *WT* mice suggesting their contribution to LEC modulation, thus pointing to a so far unknown role of EVs within the lymph vasculature.[231] The contribution of EVs to lymphatic development has not been investigated, but their release might enable the interaction of CLEC-2 with its ligand podoplanin. According to this hypothesis, CLEC-2-deficiency alone might therefore impair EV-mediated LEC maturation. Moreover, since thrombin-cleaved GPV appears to be important for platelet activation through interfering with the coagulation cascade, its absence might further reduce platelet EV release, thus additionally preventing EV-LEC interactions.

This is, however, only speculation at present and will require further studies which are planned for the upcoming months.

Unfortunately, we were so far unable to identify a ligand of sGPV. However, this study suggests its presence within the circulation or on ECs, where it could directly modulate EC behavior. This notion is further supported by the delayed angiogenesis observed in the retina in the absence of (s)GPV as well as an altered vessel appearance in the skin (Figure 11, 12, 16). In addition to this possible direct modulation of ECs by thrombin-cleaved sGPV, the observed differences in EC behavior might also result from an altered coagulation response, which we were able to identify in both GPV-deficient as well as -transgenic mice. The finding of accelerated fibrin generation in $Gp5^{-/-}$ and $Gp5^{KIN}$ mice implies an enhanced coagulation response therein. The coagulation pathway is markedly regulated by a plethora of proteins that are either activated or directly secreted by ECs. An altered communication between ECs and the coagulation cascade might therefore also affect EC behavior and lead to altered vascular integrity. Further studies are required to explore the EC-regulatory role of sGPV, which might also play a role during inflammatory challenges, in which CLEC-2 has been shown to control vascular integrity.

5.2 GPVI-triggered granule release in the resolution of retinopathy

ROP is a severe and possibly blinding disease occurring in preterm infants born before gestational week 28, often receiving additional ventilation to assist in lung inflation. Disease onset is characterized by a relative increase in oxygen saturation, which induces an arrest in normal retinal vascularization and instead promotes an initial vasoobliteration and a subsequent overshooting vessel growth leading to aberrant vascular tuft formation.[32] Since retinal development in mice is induced after birth in contrast to an exclusively fetal vascularization in humans, ROP can be experimentally investigated upon exposure of mice to 75% oxygen between P7 and P12. Subsequent analysis of retinal development at P17 by immunofluorescence and confocal microscopy enables a visualization of abnormal vessel maturation.

Interestingly, thrombocytopenia has previously been associated with more severe cases of ROP.[39] A recent study now verified these findings and further identified platelet granules to account for an improved resolution of experimental OIR in mice.[40] The authors were able to show that platelet depletion aggravated ROP by increasing the formation of neovascular tufts due to enhanced VEGFA expression and/or release in the retina. Accordingly, platelet trans-fusions into mice suffering from retinopathy significantly ameliorated the resolution of neovascularization albeit unaffected vasoobliteration. To further distinguish whether platelet granules were essential for the resolution of ROP, the authors injected granule-depleted

platelets into OIR mice and found neovascularization to be worsened to a similar degree as upon platelet depletion and thus concluded the release of platelet-derived antiangiogenic molecules to ameliorate ROP progression.

In the present study, we were aiming to further elucidate if and how platelet granule release might influence the progression of experimental retinopathy in mice by taking advantage of a variety of transgenic mouse lines lacking platelet GP receptors that have previously been associated with the regulation of vascular integrity. First and foremost, we were able to confirm the previously proposed role of platelets during ROP by inducing thrombocytopenia upon injection of anti-GPIbα antibodies (R300). While physiological vascularization was unaffected by platelet depletion, retinopathy was severely deteriorated, as revealed by enhanced vaso-obliteration as well as increased vascular tuft formation (Figure 21). In contrast to the afore-mentioned study, we observed an enlarged avascular area in platelet-depleted OIR mice as well, most likely due to differences in the experimental setup. However, we similarly obser-ved reduced platelet counts in OIR mice compared to controls at P17, thus demonstrating that platelet counts are affected upon induction of retinopathy (Figure 21).

Since the experimental setup of *in vitro*-degranulated platelets was challenged by our own observations, we next assessed, whether α-granules indeed participated in ROP progression by analyzing *Nbeal2*^{-/-} mice, which lack functional platelet α-granules.[99] Strikingly, we found disease progression to be significantly affected as shown by increased vasoobliteration as well as neovascularization (Figure 22). Of note, previous publications identified platelet secretion to be of importance in the prevention of hemorrhagic bleeding upon ischemic stroke, while it appeared to be dispensable for the maintenance of vascular integrity upon skin or lung inflammation.[232] The present findings might therefore recapitulate pathological mechanisms found upon ischemic stroke, since the pathogenesis of both ROP as well as stroke is tightly coupled to the underlying neuronal network.

Several platelet GPs have been identified to essentially contribute to the maintenance of vascular integrity under (thrombo-)inflammatory conditions, most importantly GPIbα as well as the (hem)ITAM receptors GPVI and CLEC-2. GPIbα-deficiency in the transgenic *GPIb-IL4R-tg* mice was associated with increased bleeding upon *lipopolysaccharide* (LPS)-induced lung inflammation, while blockade of the receptor on the other hand was shown to be beneficial in an experimental model of ischemic stroke in mice.[218,233] Strikingly, we were unable to detect differences in OIR outcome between *GPIb-IL4R-tg* and *WT* mice mice or upon antibody-mediated GPIbα blockade on P15/16 (Figure 23). Some experiments even revealed reduced vasoobliteration upon GPIbα-blockade, which is again in line with findings from the ischemic brain, where receptor blockade was also shown to improve disease

outcome. Furthermore, it supports the above-mentioned observation of impaired ROP resolution in mice lacking α-granules, which were also shown to contribute to cerebral hemostasis in the setting of experimental ischemic stroke. Taken together, the here presented data indicate that related mechanisms account for the resolution of ROP and the maintenance of vascular integrity in ischemic stroke, although further experiments need to address this hypothesis in the future.

In addition to GPIbα, the (hem)ITAM receptors GPVI and CLEC-2 have been shown to markedly contribute to vascular integrity during development as well as in the setting of inflammation. As described in 5.1, CLEC-2 is critically involved in lymphatic and venous development, although it was recently suggested that its expression might be dispensable for lymphatic integrity during adulthood.[198] Moreover, several publications identified its role in the maintenance of vascular integrity in the course of lung inflammation - either alone or in cooperation with GPVI, which is, however, still controversially discussed.[190,218] Functional redundancies between both proteins are also proposed to maintain hemostasis in the absence of either GPVI or CLEC-2.[207] Strikingly, we could detect increased vasoobliteration in conditional $Clec2^{-/-}$ mice, thus implying a contribution of platelet CLEC-2 to the resolution of ROP (Figure 24). This role is independent of CLEC-2-LEC interactions, since the retina is devoid of any lymphatic vessels, suggesting that the CLEC-2 ligand podoplanin might either be upregulated in the vasculature or its vicinity or that a so far unknown ligand mediates vessel growth in the presence of CLEC-2. These findings are partly in line with previous observations from the ischemic brain, in which antibody-mediated blockade of CLEC-2 did not affect inflammatory hemostasis, suggesting that the receptor might play a minor role in regulating vascularization processes (as observed in ROP), but is dispensable for the maintenance of vascular integrity in the brain (May *et al*., unpublished).

GPVI-mediated platelet recruitment to sites of inflammation has been assessed in a plethora of models, in which GPVI was mainly shown to prevent inflammatory bleeding.[234] Two independent studies showed that GPVI-blockade can induce hemorrhage in inflamed tissue, namely in a model of myocardial infarction and in growing primary tumors.[193,235] Strikingly, vascularization and subsequent tumor growth were significantly attenuated in hetero- and orthotopic tumor models upon treatment with GPVI-blocking F(ab)$_2$ fragments to a similar extent as upon platelet depletion, thus suggesting GPVI to be essential for the maintenance of vascular integrity and angiogenesis therein. A comparable dysfunction in tumor vascularization leading to intratumoral hemorrhage was observed in GPVI-deficient mice, albeit to a lesser extent than upon GPVI-blockade. To identify whether platelet secretion and the subsequent decrease in VEGFA levels upon induction of experimental retinopathy might

also be triggered by GPVI activation, we analyzed disease progression in *Gp6*^{-/-} animals and found it to be dramatically deteriorated in relation to the respective *WT* (Figure 25). These findings strongly suggest that GPVI mediates platelet activation and subsequent granule release during ROP, which in turn ameliorates the resolution of neovascularization. Of note, we did not observe altered vascularization at P17 in untreated *Gp6*^{-/-} mice, thus excluding a generally defective angiogenesis to account for the observed defects. In contrast to the here presented results in ROP, GPVI-depletion did not cause hemorrhagic bleeding during ischemic stroke in mice, which was in line with an unaffected neurological outcome.[236]

Surprisingly, and in contrast to what has been described in solid tumors, antibody-mediated GPVI-blockade on P15/16 did not affect ROP scores. In sharp contrast, GPVI-depletion on P6 on the other hand markedly deteriorated OIR resulting in significantly increased vasoobliteration and enhanced neovascularization (Figure 26). These findings, although unexpected, might be due to two different mechanisms: first and foremost, JAQ1 F(ab)$_2$ is thought to specifically block the collagen-binding site within GPVI. Collagen, however, is not the only ligand of GPVI, which has recently been shown to also bind to fibrinogen and polymerized fibrin, although the physiological relevance of both is still controversially discussed.[237] Interestingly, fibrinogen has previously been described to be upregulated in the retinal layer upon OIR, thus strongly implying its role in ROP progression.[238] The here presented findings might therefore indicate that either fibrinogen or another ligand could induce GPVI activation in the setting of OIR. Secondly, GPVI might play a role during earlier phases of disease progression. GPVI-blockade was induced on P15/16, while GPVI-depletion was already initiated on P6 prior to the induction of ROP, thus implicating a role of GPVI already during disease onset. To further unravel the temporal importance of GPVI during ROP, blockade of the receptor consistently from P6 to P17 in future studies will facilitate our understanding of how GPVI contributes to ROP. Of note, injection of JAQ1 IgG into mice induces a transient thrombocytopenia for up to 72h, which might interfere with disease progression in these animals as well.[179] Future studies will aim to address, whether platelet depletion during the initial, hyperoxic stages of ROP (P6 – P12) affect disease onset.

Previous studies suggested platelet transfusions to ameliorate ROP resolution or prevent its progression, which was supported by a positive correlation between the degree of thrombocytopenia and disease severity.[40] The present findings suggest that a GPVI- and partly CLEC-2-triggered platelet granule release promotes the resolution of experimental retinopathy in mice, which might help to understand the exact role of platelets in ROP progression and to improve disease outcome.

5.3   PPF regulation by Twf1 and Cof1

A tight regulation of the MK cytoskeleton is essential to enable the guided release of proplatelets into the bloodstream, thus maintaining physiological platelet counts. The microtubule cytoskeleton has previously been shown to be indispensable for PPF by enabling elongation of the proplatelet shaft through microtubule polymerization and sliding.[132] Microtubule turnover is regulated by microtubule-interacting proteins such as EBs on the one hand as well as posttranslational modifications on the other hand. Posttranslational detyrosination and acetylation of microtubules have been associated with increased filament longevity thus suggesting impaired microtubule dynamics.[127,130,221] On the contrary, F-actin nucleation is necessary for proplatelet branching thus increasing the number of available platelet tips, while further being required for the degradation of the basement membrane, which is necessary to enable PPF into BM sinusoids.[85,121] F-actin dynamics are mainly regulated by different actin-binding proteins. While Pfn1 and Tβ4 sequester G-actin, ADF and Cof1 have been identified as actin-severing proteins, which weaken longitudinal and lateral binding of F-actin filaments.[101] Two Twf isoforms, Twf1 and 2a, have been identified in murine MKs and platelets, but so far only the function of Twf2a as a negative regulator of platelet reactivity was investigated in more detail, while the function of Twf1 remained elusive.[116]

We could now show that both Twf isoforms are non-redundantly expressed in MKs and platelets, since no additional defects in platelet reactivity or MK functionality were detected in *Twf1^-/-^/Twf2a^-/-^* mice mice (Figure 27). Interestingly, Twf1 was proposed to act in concert with Cof1, since combined deficiency in both resulted in synthetic lethality in yeast.[113] Similarly to Cof1, Twf1 was identified to induce actin severing and depolymerization, which prompted us to investigate how deficiency of both proteins might affect cytoskeletal rearrangements in MKs and platelets. Strikingly, Twf1/Cof1 double-deficient mice exhibited a marked macrothrombocytopenia due to impaired PPF, which was based on defective podosome formation on the one hand and decreased microtubule turnover on the other hand. F-actin dynamics were significantly attenuated leading to an accumulation of F-actin filaments in *DKO* MKs *in vitro* and *in situ* as well as an increased F-actin content in platelets, which impeded spreading irrespective of the ECM substrate (Figure 36, 37). Most importantly, altered F-actin rearrangements in double-deficient MKs impaired the formation of podosomes, actin-rich structures linking the cytoskeleton to integrins in the plasma membrane, thus enabling an increased interaction with the respective matrix protein. Podosomes have strongly been implicated in enabling the initial formation of proplatelet pseudopods by degrading matrix and basement membrane proteins.[121] Lack of functional podosome assembly might thus prevent efficient ECM degradation, which is supported by

findings from *Cof1⁻/⁻* MKs that also exhibited aberrant F-actin structures and thrombocytopenia despite unaltered PPF *in vitro*. This discrepancy between *in vitro* and *in vivo* findings strongly implies that reduced ECM degradation in *Cof1⁻/⁻* MKs might account for the reduced PPF *in vivo*.
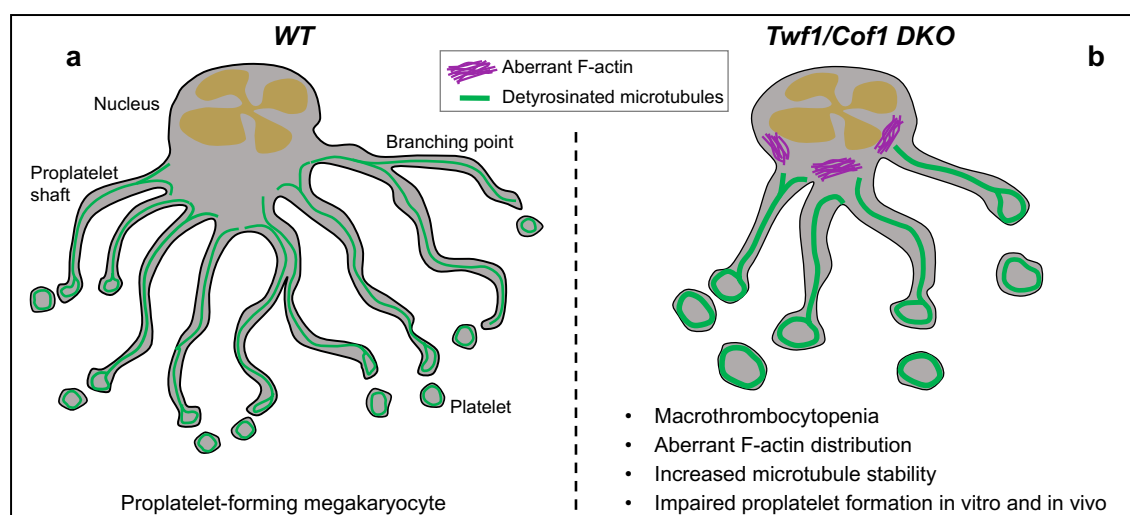
Figure 66. PPF in *WT* and Twf1/Cof1-deficient mice. (**a**) *WT* MKs are able to release proplatelets from elongated shafts in a rapid, shear-dependent process. (**b**) PPF from double-deficient MKs is severely impaired due to aberrant F-actin structures leading to defective podosome formation as well increased detyrosination of microtubules resulting in thickening of proplatelet shafts. Becker, Scheller *et al*., **Blood Adv**., 2020.[219]

In addition to aberrant F-actin accumulations, microtubule dynamics were significantly affected in the absence of both Twf1 and Cof1 leading to a thickening and shortening of proplatelet protrusions *in vitro* and *in vivo* as assessed by confocal and two-photon intravital microscopy, respectively (Figure 33, 34). Several proteins have been associated with the regulation of both actin and microtubule dynamics, most importantly the formin mDia1 as well as APC, which both promote actin nucleation, but have further been described to be involved in microtubule stabilization upon interaction with EBs.[124,239] Surprisingly, we were here able to identify decreased mRNA and protein levels of mDia1 and APC in *DKO* MKs (Figure 42), which strikingly were also shown to negatively regulate PPF in mice and humans before, while EB levels appeared to be increased.[222,240] The here presented findings suggest that a tight regulation of the whole protein complex comprising EBs, formins and APC is essential for the orchestration of PPF *in vitro* and *in vivo*. Moreover, we identified a feedback loop, linking Cof1 to LIMK1 activation, which appeared to be decreased in the absence of Cof1 and Twf1 (Figure 42). Similarly to the aforementioned reduction in mDia1 and APC levels, impaired LIMK1 phosphorylation might not only impair downstream regulators of the F-actin cytoskeleton, but might further affect microtubule stability, which has been shown to be

altered upon LIMK1 phosphorylation *in vitro*.[241] Reduced LIMK1 activation might therefore result in microtubule stabilization, which is in line with the thickening of proplatelet shafts observed in *DKO* mice *in vivo*.

Moreover, Twf1/Cof1-deficient MKs exhibited an increased detyrosination and acetylation of microtubules. While it is controversially discussed whether posttranslational modifications affect microtubule stability, it is well described that both modifications are associated with increased microtubule longevity, thus implying decreased filament turnover. Since proplatelet generation requires both filament assembly as well as sliding, the enhanced detyrosination of microtubules detected in proplatelet-forming *DKO* MKs might affect tubule elongation (Figure 66). The differences further translated into an altered microtubule constitution in double-deficient platelets, but evidently did not interfere with platelet function since *DKO* platelets merely recapitulated the phenotype of *Cof1*^{-/-} platelets. This is further supported by the observation of unaltered mDia1 and APC protein levels in *DKO* platelets, suggesting that the remaining protein pool in MKs was evenly distributed to the fewer platelets. In line with this, we found granule numbers in platelets (Figure 28) as well as granule transport in proplatelet-forming MKs (Figure 34) to be unaffected in the absence of Twf1 and Cof1. The grossly unaffected platelet reactivity of Twf1/Cof1 double-deficient platelets further suggests that both proteins are less critical in maintaining the hemostatic function of the cells, while being essential for the guided formation of proplatelets into vessel sinusoids. The more dramatic defects observed in *Cof1*^{-/-} compared to *Twf1*^{-/-} mice might at least partly be explained by the high expression of Cof1 on protein level, which ranks among the most abundantly expressed proteins in platelets.[242]

Altered cytoskeletal dynamics and subsequent thrombocytopenia have been associated with a plethora of variants in actin- or microtubule-regulatory genes including *ACT1, DIAPH1* and *FLNA*, thus highlighting the importance of a functional cytoskeletal crosstalk during PPF in humans.[223,243,244] Although no mutations in *TWF1* or *COF1* have been identified so far, several thrombocytopenic mice such as *Pfn1*^{-/-}, *Twf2a*^{-/-} or *Cdc42*^{-/-} mice presented with highly disturbed Cof1 phosphorylation patterns.[105,116,118] Moreover, altered Cof1 activity was associated with thrombocytopenia in a murine model of *von Willebrand disease* (VWD) type 2B. Strikingly, mutated MKs exhibited thickened proplatelet extensions, which could be rescued upon reactivation of LIMK/Cof1 signaling.[245] These findings are in line with a recent publication describing severely impaired PPF of MKs derived from VWD-type 2B patients.[246] Strikingly, we observed a similar thickening of proplatelet shafts in *DKO* MKs *in vitro* and *in vivo*, suggesting a comparable dysregulation of actin and microtubule cytoskeleton to account for the observed alterations (Figure 66). Taken together, the here presented findings

support the hypothesis of a LIMK1/Cof1/Twf1-mediated regulation of PPF and further identify Twf1 to share functions with Cof1 rather than with its homologue Twf2a.

5.4 G6b-B-dependent MK maturation

The MK- and platelet-specific receptor G6b-B consists of a single variable-type Ig domain and contains an ITIM as well as an ITSM consensus sequence.[186] G6b-deficiency in mice results in a dramatic macrothrombocytopenia due to impaired PPF from BM MKs and a concomitant progressive myelofibrosis and splenomegaly.[155] A similarly severe thrombo-cytopenia and concomitant myelofibrosis was also observed upon disruption of G6b-B signaling in transgenic mice with mutated ITIM and ITSM.[188]

In the last part of this thesis the spontaneous macrothrombocytopenia and myelofibrosis in a *WT* mouse line previously identified and described (Heck, Stritt *et al.*, unpublished) was identified by whole exome sequencing to be caused by a splice acceptor site mutation within *Mpig6b*. The mutation resulted in loss of protein expression in MKs and platelets, most likely due to nonsense-mediated decay, since transcription was not fully abolished as shown by remnant amounts of *Mpig6b* mRNA in cultured MKs (Figure 46). G6b-B was identified to be essential for MK maturation, since native and cultured *G6b^{mut}* MKs presented with defective cytoplasmic maturation, which might at least in part be explained by reduced c-Mpl exposure leading to impaired TPO signaling and ineffective GATA-1 expression. Together, these defects culminated in an overall reduced expression of MK-specific genes and thus prevented MK maturation leading to the accumulation of immature MKs in the BM of the mutant mice, which promoted the progression of myelofibrosis (Figure 56).

The distinct impairment in cytoplasmic MK maturation in *G6b^{mut}* mice could be attributed to a marked decrease in MK-related protein expression. mRNA levels of all tested platelet-specific glycoproteins, the platelet- and MK-specific β1-tubulin as well as the TF GATA-1 were significantly reduced in *G6b^{mut}* MKs, thus hampering MK maturation *in vitro* and *in vivo*. MK maturation strongly relies on GATA-1-dependent gene transcription, which was shown in a mouse model with reduced GATA-1 protein expression levels. These *Gata1^{low}* mice exhibit anemia, thrombocytopenia and myelofibrosis due to enhanced c-Mpl signaling and impaired ribosomal protein functions, which was in line with other mouse models of myelofibrosis exhibiting ribosomal defects.[247,248] In contrast to *G6b^{mut}* MKs, TPO signaling in *Gata1^{low}* mice was enhanced, similarly to what has been described for PMF patients. This discrepancy might be due to the rather late upregulation of G6b-B during MK maturation and its absence from HSCs and subsequent progenitor cells.[155] While GATA-1 levels in *Gata1^{low}* mice are reduced throughout maturation from HSCs to MKs, the defects described in *G6b^{mut}* MKs only become evident at the stage at which G6b-B would normally be upregulated to exert its

function. The unaltered ploidy distribution observed in *G6b^mut* MK populations therefore strongly demonstrates polyploidization to occur prior to or independent of G6b-B signaling. The resulting immature MKs are polyploid, but exhibit a highly underdeveloped DMS, are significantly smaller in size and are therefore almost unable to form proplatelets, resulting in the severe thrombocytopenia observed in *G6b^mut* mice.

As previously described, lack of c-Mpl specifically in MKs and platelets, while being dispensable for thrombopoiesis, surprisingly promotes the maturation of precursors into MKs, thus culminating in a dramatic megakaryo- and thrombocytosis.[153] The reduced expression level of c-Mpl detected on G6b-B-mutant MKs might therefore similarly drive the maturation of precursor cells towards the MK lineage, which is in line with a decreased amount of MEPs in the BM of *G6b^mut* mice (Figure 60). In contrast to conditional c-Mpl-deficient mice, however, G6b-deficiency additionally prevented cytoplasmic MK maturation, thus resulting in the accumulation of immature, small MKs with defective granule synthesis and, presumably, aberrant cytokine release. These findings are supported by an irregular granule distribution in proplatelet-forming MKs (Figure 59) as well as in platelets (Figure 48). *G6b^mut* MKs further exhibited decreased Shp2 expression levels, while Shp1 levels were rather unaffected (Figure 64). Previous studies identified a Shp2-RUNX1-axis to affect MK maturation *in vivo* as verified by a reduced MK size *in situ* as well as reduced ploidy levels upon lack of Shp2 in MKs.[187,249] The role of Shp2 within the JAK-STAT signaling cascade is still controversially discussed, since Shp2-deficiency on the one hand delayed STAT5 dephosphorylation *in vitro* suggesting STAT5 to be deactivated by Shp2. On the other hand, Shp2-mutant cells displayed impaired JAK2 phosphorylation, which was in line with reduced STAT5 activity in the mammary gland of *Shp2^-/-* mice, thus rather implying Shp2 to positively regulate JAK/STAT activity thereby affecting MK maturation.[93] On another note, a recent publication identified a dramatic megakaryopoiesis in mice overexpressing heparanase, an endo-glucoronidase responsible for the cleavage of heparan sulfate proteoglycans such as perlecan, the newly identified ligand of G6b-B.[189,250] Consequently, the striking megakaryocytosis in the BM of *G6b^mut* mice, in which perlecan-dependent G6b-B signaling is lacking, might be caused by restricted G6b-B activity, thus resulting in enhanced MK proliferation.

Increased levels of TGFβ1 have previously been identified to drive the deposition of collagen and reticulin fibers in a plethora of murine models of BM fibrosis and have also been observed in human subjects suffering from PMF or IMF.[147,148,226] As mentioned above, *G6b^mut* mice exhibited a reduced expression of the TF GATA-1, which has been shown to be indispensable for MK maturation. Interestingly, *Gata1^low* mice display an accumulation of immature

MKs in the BM reminiscent of the phenotype observed in G6b-B-mutant mice, which is accompanied by an increased release of TGFβ1, enhanced emperipolesis of neutrophils into defective MKs as well as impaired granule synthesis.[145,150] In contrast, polyploidization was also markedly impaired in *Gata1*^{low} mice, whereas it was unaffected in G6b-B-mutant MKs, thus suggesting that the mouse models are not fully comparable. Nonetheless, similarly increased TGFβ1 levels were present in the BM of G6b-B-mutant mice (Figure 57) in line with impaired granule distribution (Figure 59) and an enhanced neutrophil uptake, which was further reflected by an upregulation of neutrophil-specific genes in *G6b*[mut] MKs as assessed by RNA sequencing (Figure 56, 63). These findings strongly imply an elevated TGFβ1 release from immature MKs to account for the observed progression of myelofibrosis. In addition to TGFβ1, male *G6b*[mut] mice also displayed increased levels of IL-6 in BM and blood plasma (Figure 57). Although IL-6 is a cytokine generally associated with inflammation, it has been shown to be significantly upregulated in patients suffering from PMF as well as in a murine model of myelofibrosis, e.g. through fibronectin-*toll-like-receptor* (TLR) 4-mediated secretion from BM MKs.[251,252] The sex-specific increase in IL-6 levels is in line with enhanced WBC counts exclusively in male mice, thus suggesting that the overall inflammatory response is increased in these animals, reminiscent of the dramatic myelofibrosis present in the BM of these animals. Since female mice develop a progressive osteosclerosis associated with loss of BM cellularity, these sex-specific differences in IL-6 release might be due to increased extramedullary hematopoiesis in female mice underlined by a more severe spleno-megaly in these animals (Figure 49).

Similar to G6b-B-deficient mice, our *G6b*[mut] mice displayed defective platelet activation and recovery, which translated into a dramatically impaired hemostatic response. Interestingly, however, *G6b*[mut] mice presented with sex-specific differences in platelet counts and reactivity as well as the degree of splenomegaly. Analysis of the BM architecture in female mice revealed a dramatic osteosclerosis of the cortical bone beginning at 6-8 weeks of age and leading to decreased BM cellularity in addition to the dramatic myelofibrosis that was also present in the BM of male mice (Figure 50). The alterations were associated with increased cytokine release, above all in sRANKL and TGFβ1, which likely impacted osteoclast and osteoblast numbers in female BM and further appeared to be dependent on estrogen levels, since BM transplantation of *G6b*[mut] BM into female *WT* mice induced osteosclerosis as well. Interestingly, osteosclerosis was also previously described to develop in *Gata1*^{low} mice, suggesting the phenotype to at least partly derive from impaired GATA-1 signaling and a subsequent increased secretion of osteogenic cytokines from immature MKs.[160] Similarly, conditional MK and platelet-specific c-Mpl-deficient mice exhibited progressive osteosclerosis specifically in female mice, which is in line with the enhanced bone formation detected in

female $G6b^{mut}$ mice, thus implying that the reduced c-Mpl protein expression in $G6b^{mut}$ MKs might also affect osteoblast proliferation.[158] Strikingly, female mice did not only exhibit osteosclerotic lesions in the cortical bone, but further displayed osteoporosis in their trabecular bone associated with osteoblast and osteoclast accumulations, a phenotype referred to as high turnover osteoporosis. These contradicting results suggest bone remodeling to generally be affected upon lack of G6b-B. As mentioned above, $G6b^{mut}$ mice exhibited an increased release of TGFβ1 into the BM, which was associated with a progressive myelofibrosis. Elevated TGFβ1 levels, however, have also been associated with bone remodeling disorders. Interestingly, the cytokine is able to act in a dual role on both osteoclasts and osteoblasts, depending on the locally prevailing estrogen levels. MK-derived TGFβ1 exerts a pro-proliferative effect on osteoblasts, thus inducing increased bone formation,[58,162] which is in line with enhanced osteoblast numbers and cortical osteosclerosis in female mice. Elevated estrogen concentrations in female mice further induce TGFβ1-secretion from osteoblasts thus stimulating osteoclast apoptosis,[165] which in turn would reduce bone degradation and additionally promote osteosclerosis in female $G6b^{mut}$ mice. Strikingly, however, female $G6b^{mut}$ mice also exhibited elevated sRANKL levels in BM plasma, which in turn has been shown to be essential for osteoclastogenesis and -function and might therefore contribute to the osteoporotic phenotype present in the trabecular bone of female $G6b^{mut}$ mice. It still remains elusive why the cytokines exert their functions differently in cortical and trabecular bone, which suggests an altered BM environment or differences in MK-osteoclast-osteoblast crosstalk to account for the observed ambivalently defective bone remodeling in female $G6b^{mut}$ mice.

Recently, several *MPIG6B* variants have been identified in humans, which were associated with macrothrombocytopenia and concomitant focal myelofibrosis.[154,253] While a single nucleotide exchange in $G6b^{mut}$ mice was detected in a splice acceptor site within intron 2 of *Mpig6b* (c.404-1G>A), two of the described families presented with a base pair duplication in a splice donor site (c.61_61+1dup), one family had a frameshift mutation (c.149dup; p.Ala52GlyfsX128) and one family had a homozygous missense mutation (c.469G>A; p.Gly157Arg). Although the mutations are not similar between the species, the here introduced mouse model might be a valuable tool to better understand the aberrant MK behavior leading to myelofibrosis and thrombocytopenia in human subjects. In addition, several publications reported increased G6b-B expression in patients suffering from PMF or related myeloproliferative disorders.[156,254] While these studies suggested G6b-B to serve as a biomarker for the prediction of disease severity, its upregulation might also imply a distinct function in counter-regulating disease progression. The dramatic myelofibrosis observed upon G6b-deficiency might therefore also be directly caused by lack of G6b-B signaling,

which, under physiological circumstances, partly prevents aberrant MK evolvement. However, this hypothesis needs to be validated in future studies in order to identify the exact function of G6b-B in MKs and its mechanistic link to the induction of myelofibrosis.

In summary, our data identifies G6b-B as a major regulator of gene expression during MK maturation and further unravels its role in the progression of myelofibrosis. Overall, the present study provides new insights into the mechanisms orchestrating MK maturation, PPF and platelet function *in vivo*.

5.5 Concluding remarks

In the here presented thesis, the role of platelet receptors in the maintenance of vascular integrity was analyzed under different inflammatory and disease settings. On the one hand, sGPV - in cooperation with CLEC-2 - was identified as a novel regulator of vascular and lymphatic development. In order to further understand the exact mechanism through which sGPV supports vessel integrity during development, it will be essential to identify possible ligands mediating its effects on endothelial cells or platelets, respectively. In addition, it will be indispensable to address whether the observed defects in venous integrity upon lack of CLEC-2 and sGPV might also play a role in other experimental settings assessing vascular integrity, since the function of sGPV might not be restricted to CLEC-2-mediated signaling.

In the second part of the thesis, the (hem)ITAM receptors GPVI and CLEC-2 were identified to mediate platelet activation upon experimentally induced ROP in mice, thus supporting disease resolution due to enhanced granule release. So far the contribution of $\alpha IIb\beta 3$ integrins to ROP progression and outcome have not been investigated, which will definitely be of value to interpret the present data. Since the present findings suggest GPVI-mediated platelet activation to occur independently of collagen binding, it will now be important to test whether this activation is alternatively induced via fibrin, fibrinogen or a so far unidentified GPVI ligand. Furthermore, it will be essential to determine, which granule-specific proteins might mediate the decrease in VEGFA levels. Several publications suggest the presence of distinct α-granule subpopulations, which are differentially released upon activation.[255] A selective secretion of antiangiogenic proteins such as endostatin (e.g. observed upon TxA$_2$ stimulation of platelets)[256] might thus contribute to an enhanced resolution of ROP, which would improve disease outcome in affected preterm-born infants.

Analysis of the distinct functions of actin-binding proteins in murine MKs and platelets revealed a so far undescribed redundancy between Twf1 and Cof1. In contrast to their role in the regulation of actin/microtubule crosstalk during PPF, the Twf1 homologue Twf2a was dispensable for PPF but essentially involved in the regulation of platelet reactivity. Further

studies are aiming at unraveling the exact signaling pathway important for cytoskeletal rearrangements during PPF. A specific focus therein will be on elucidating the role of the Rho GTPases RhoA, Cdc42 and RhoB, which have been shown to exert functions upstream of Cof1.

Finally, G6b-B was identified to be critically involved in maintaining MK maturation by directly affecting c-Mpl expression and TPO signaling. Since it was previously proposed that a Shp2-RUNX1-axis might affect MK maturation, currently ongoing experiments are aiming at identifying differences in RUNX1 activity by immunoprecipitation and subsequent -blotting. Moreover, current investigations suggest differences in TPO signaling capacities between $G6b^{mut}$ and $G6b^{-/-}$ mice. In order to decipher these alterations, we are now assessing, whether G6b-B protein remnants in $G6b^{mut}$ MKs might affect the phenotypic outcome. Moreover, we here identified the cytokine TGFβ1 to markedly affect both the progression of myelofibrosis as well as the sex-specific osteosclerosis. To induce a reversion of the phenotype, $G6b^{mut}$ mice are currently being intercrossed with conditional MK- and platelet-specific $Tgfb1^{-/-}$ mice. This will not only reveal, whether the myelofibrosis is strictly TGFβ1-diven, but it will further assist in deciphering, whether the female-specific osteosclerosis is also induced by osteoblast-secreted TGFβ1.

REFERENCES

1.   Garcia MD, Larina IV. Vascular development and hemodynamic force in the mouse yolk sac. *Front Physiol*. 2014;5:308.

2.   Poole TJ, Coffin JD. Vasculogenesis and angiogenesis: two distinct morphogenetic mechanisms establish embryonic vascular pattern. *J Exp Zool*. 1989;251(2):224-231.

3.   Shalaby F, Rossant J, Yamaguchi TP, et al. Failure of blood-island formation and vasculogenesis in Flk-1-deficient mice. *Nature*. 1995;376(6535):62-66.

4.   Yamashita J, Itoh H, Hirashima M, et al. Flk1-positive cells derived from embryonic stem cells serve as vascular progenitors. *Nature*. 2000;408(6808):92-96.

5.   Flamme I, Frolich T, Risau W. Molecular mechanisms of vasculogenesis and embryonic angiogenesis. *J Cell Physiol*. 1997;173(2):206-210.

6.   Risau W. Mechanisms of angiogenesis. *Nature*. 1997;386(6626):671-674.

7.   Carmeliet P, Ferreira V, Breier G, et al. Abnormal blood vessel development and lethality in embryos lacking a single VEGF allele. *Nature*. 1996;380(6573):435-439.

8.   Sumanas S, Lin S. Ets1-related protein is a key regulator of vasculogenesis in zebrafish. *PLoS Biol*. 2006;4(1):e10.

9.   Suri C, Jones PF, Patan S, et al. Requisite role of angiopoietin-1, a ligand for the TIE2 receptor, during embryonic angiogenesis. *Cell*. 1996;87(7):1171-1180.

10.   Hellstrom M, Phng LK, Hofmann JJ, et al. Dll4 signalling through Notch1 regulates formation of tip cells during angiogenesis. *Nature*. 2007;445(7129):776-780.

11.   Lobov IB, Renard RA, Papadopoulos N, et al. Delta-like ligand 4 (Dll4) is induced by VEGF as a negative regulator of angiogenic sprouting. *Proc Natl Acad Sci U S A*. 2007;104(9):3219-3224.

12.   Wang HU, Chen ZF, Anderson DJ. Molecular distinction and angiogenic interaction between embryonic arteries and veins revealed by ephrin-B2 and its receptor Eph-B4. *Cell*. 1998;93(5):741-753.

13.   le Noble F, Moyon D, Pardanaud L, et al. Flow regulates arterial-venous differentiation in the chick embryo yolk sac. *Development*. 2004;131(2):361-375.

14.   Wigle JT, Oliver G. Prox1 function is required for the development of the murine lymphatic system. *Cell*. 1999;98(6):769-778.

15.   Marcelo KL, Goldie LC, Hirschi KK. Regulation of endothelial cell differentiation and specification. *Circ Res*. 2013;112(9):1272-1287.

16.   Karkkainen MJ, Haiko P, Sainio K, et al. Vascular endothelial growth factor C is required for sprouting of the first lymphatic vessels from embryonic veins. *Nat Immunol*. 2004;5(1):74-80.

17.   Suzuki-Inoue K, Osada M, Ozaki Y. Physiologic and pathophysiologic roles of interaction between C-type lectin-like receptor 2 and podoplanin: partners from in utero to adulthood. *J Thromb Haemost*. 2017;15(2):219-229.

18.   Finney BA, Schweighoffer E, Navarro-Nunez L, et al. CLEC-2 and Syk in the megakaryocytic/platelet lineage are essential for development. *Blood*. 2012;119(7):1747-1756.

19.   Suzuki-Inoue K, Inoue O, Ding G, et al. Essential in vivo roles of the C-type lectin receptor CLEC-2: embryonic/neonatal lethality of CLEC-2-deficient mice by blood/lymphatic misconnections and impaired thrombus formation of CLEC-2-deficient platelets. *J Biol Chem*. 2010;285(32):24494-24507.

20.   Osada M, Inoue O, Ding G, et al. Platelet activation receptor CLEC-2 regulates blood/lymphatic vessel separation by inhibiting proliferation, migration, and tube formation of lymphatic endothelial cells. *J Biol Chem*. 2012;287(26):22241-22252.

21.   Bertozzi CC, Schmaier AA, Mericko P, et al. Platelets regulate lymphatic vascular development through CLEC-2-SLP-76 signaling. *Blood*. 2010;116(4):661-670.

22.   Haining EJ, Cherpokova D, Wolf K, et al. CLEC-2 contributes to hemostasis independently of classical hemITAM signaling in mice. *Blood*. 2017;130(20):2224-2228.

23.   Potente M, Makinen T. Vascular heterogeneity and specialization in development and disease. *Nat Rev Mol Cell Biol*. 2017;18(8):477-494.

24.   Stacker SA, Williams SP, Karnezis T, Shayan R, Fox SB, Achen MG. Lymphangiogenesis and lymphatic vessel remodelling in cancer. *Nat Rev Cancer*. 2014;14(3):159-172.

25.   Stanczuk L, Martinez-Corral I, Ulvmar MH, et al. cKit Lineage Hemogenic Endothelium-Derived Cells Contribute to Mesenteric Lymphatic Vessels. *Cell Rep*. 2015;10(10):1708-1721.

26.   Gariano RF, Gardner TW. Retinal angiogenesis in development and disease. *Nature*. 2005;438(7070):960-966.

27. Ozaki H, Seo MS, Ozaki K, et al. Blockade of vascular endothelial cell growth factor receptor signaling is sufficient to completely prevent retinal neovascularization. *Am J Pathol*. 2000;156(2):697-707.
28. Stalmans I, Ng YS, Rohan R, et al. Arteriolar and venular patterning in retinas of mice selectively expressing VEGF isoforms. *J Clin Invest*. 2002;109(3):327-336.
29. Feeney SA, Simpson DA, Gardiner TA, Boyle C, Jamison P, Stitt AW. Role of vascular endothelial growth factor and placental growth factors during retinal vascular development and hyaloid regression. *Invest Ophthalmol Vis Sci*. 2003;44(2):839-847.
30. Saint-Geniez M, D'Amore PA. Development and pathology of the hyaloid, choroidal and retinal vasculature. *Int J Dev Biol*. 2004;48(8-9):1045-1058.
31. Alvarez Y, Cederlund ML, Cottell DC, et al. Genetic determinants of hyaloid and retinal vasculature in zebrafish. *BMC Dev Biol*. 2007;7:114.
32. Hellstrom A, Smith LE, Dammann O. Retinopathy of prematurity. *Lancet*. 2013;382(9902):1445-1457.
33. Chen J, Smith LE. Retinopathy of prematurity. *Angiogenesis*. 2007;10(2):133-140.
34. Plate KH, Breier G, Weich HA, Risau W. Vascular endothelial growth factor is a potential tumour angiogenesis factor in human gliomas in vivo. *Nature*. 1992;359(6398):845-848.
35. Dorrell MI, Aguilar E, Friedlander M. Retinal vascular development is mediated by endothelial filopodia, a preexisting astrocytic template and specific R-cadherin adhesion. *Invest Ophthalmol Vis Sci*. 2002;43(11):3500-3510.
36. Alon T, Hemo I, Itin A, Pe'er J, Stone J, Keshet E. Vascular endothelial growth factor acts as a survival factor for newly formed retinal vessels and has implications for retinopathy of prematurity. *Nat Med*. 1995;1(10):1024-1028.
37. Pierce EA, Avery RL, Foley ED, Aiello LP, Smith LE. Vascular endothelial growth factor/vascular permeability factor expression in a mouse model of retinal neovascularization. *Proc Natl Acad Sci U S A*. 1995;92(3):905-909.
38. Liu CH, Wang Z, Sun Y, SanGiovanni JP, Chen J. Retinal expression of small non-coding RNAs in a murine model of proliferative retinopathy. *Sci Rep*. 2016;6:33947.
39. Jensen AK, Ying GS, Huang J, Quinn GE, Binenbaum G. Longitudinal study of the association between thrombocytopenia and retinopathy of prematurity. *J AAPOS*. 2018;22(2):119-123.
40. Cakir B, Liegl R, Hellgren G, et al. Thrombocytopenia is associated with severe retinopathy of prematurity. *JCI Insight*. 2018;3(19).
41. Boyce BF, Hughes DE, Wright KR, Xing L, Dai A. Recent advances in bone biology provide insight into the pathogenesis of bone diseases. *Lab Invest*. 1999;79(2):83-94.
42. Tondravi MM, McKercher SR, Anderson K, et al. Osteopetrosis in mice lacking haematopoietic transcription factor PU.1. *Nature*. 1997;386(6620):81-84.
43. Matsumoto M, Kogawa M, Wada S, et al. Essential role of p38 mitogen-activated protein kinase in cathepsin K gene expression during osteoclastogenesis through association of NFATc1 and PU.1. *J Biol Chem*. 2004;279(44):45969-45979.
44. Luchin A, Purdom G, Murphy K, et al. The microphthalmia transcription factor regulates expression of the tartrate-resistant acid phosphatase gene during terminal differentiation of osteoclasts. *J Bone Miner Res*. 2000;15(3):451-460.
45. Raggatt LJ, Partridge NC. Cellular and molecular mechanisms of bone remodeling. *J Biol Chem*. 2010;285(33):25103-25108.
46. Simonet WS, Lacey DL, Dunstan CR, et al. Osteoprotegerin: a novel secreted protein involved in the regulation of bone density. *Cell*. 1997;89(2):309-319.
47. Chabadel A, Banon-Rodriguez I, Cluet D, et al. CD44 and beta3 integrin organize two functionally distinct actin-based domains in osteoclasts. *Mol Biol Cell*. 2007;18(12):4899-4910.
48. Li YP, Chen W, Liang Y, Li E, Stashenko P. Atp6i-deficient mice exhibit severe osteopetrosis due to loss of osteoclast-mediated extracellular acidification. *Nat Genet*. 1999;23(4):447-451.
49. Boyle WJ, Simonet WS, Lacey DL. Osteoclast differentiation and activation. *Nature*. 2003;423(6937):337-342.
50. Komori T, Yagi H, Nomura S, et al. Targeted disruption of Cbfa1 results in a complete lack of bone formation owing to maturational arrest of osteoblasts. *Cell*. 1997;89(5):755-764.
51. Florencio-Silva R, Sasso GR, Sasso-Cerri E, Simoes MJ, Cerri PS. Biology of Bone Tissue: Structure, Function, and Factors That Influence Bone Cells. *Biomed Res Int*. 2015;2015:421746.
52. Schoppet M, Preissner KT, Hofbauer LC. RANK ligand and osteoprotegerin: paracrine regulators of bone metabolism and vascular function. *Arterioscler Thromb Vasc Biol*. 2002;22(4):549-553.

53.   Nakashima T, Hayashi M, Fukunaga T, et al. Evidence for osteocyte regulation of bone homeostasis through RANKL expression. *Nat Med*. 2011;17(10):1231-1234.

54.   Nakamura T, Imai Y, Matsumoto T, et al. Estrogen prevents bone loss via estrogen receptor alpha and induction of Fas ligand in osteoclasts. *Cell*. 2007;130(5):811-823.

55.   Hofbauer LC, Khosla S, Dunstan CR, Lacey DL, Spelsberg TC, Riggs BL. Estrogen stimulates gene expression and protein production of osteoprotegerin in human osteoblastic cells. *Endocrinology*. 1999;140(9):4367-4370.

56.   Eghbali-Fatourechi G, Khosla S, Sanyal A, Boyle WJ, Lacey DL, Riggs BL. Role of RANK ligand in mediating increased bone resorption in early postmenopausal women. *J Clin Invest*. 2003;111(8):1221-1230.

57.   Crane JL, Cao X. Bone marrow mesenchymal stem cells and TGF-beta signaling in bone remodeling. *J Clin Invest*. 2014;124(2):466-472.

58.   Tang Y, Wu X, Lei W, et al. TGF-beta1-induced migration of bone mesenchymal stem cells couples bone resorption with formation. *Nat Med*. 2009;15(7):757-765.

59.   Neptune ER, Frischmeyer PA, Arking DE, et al. Dysregulation of TGF-beta activation contributes to pathogenesis in Marfan syndrome. *Nat Genet*. 2003;33(3):407-411.

60.   Okada S, Nakauchi H, Nagayoshi K, Nishikawa S, Miura Y, Suda T. In vivo and in vitro stem cell function of c-kit- and Sca-1-positive murine hematopoietic cells. *Blood*. 1992;80(12):3044-3050.

61.   Kiel MJ, Yilmaz OH, Iwashita T, Yilmaz OH, Terhorst C, Morrison SJ. SLAM family receptors distinguish hematopoietic stem and progenitor cells and reveal endothelial niches for stem cells. *Cell*. 2005;121(7):1109-1121.

62.   Doulatov S, Notta F, Eppert K, Nguyen LT, Ohashi PS, Dick JE. Revised map of the human progenitor hierarchy shows the origin of macrophages and dendritic cells in early lymphoid development. *Nat Immunol*. 2010;11(7):585-593.

63.   Yang L, Bryder D, Adolfsson J, et al. Identification of Lin(-)Sca1(+)kit(+)CD34(+)Flt3- short-term hematopoietic stem cells capable of rapidly reconstituting and rescuing myeloablated transplant recipients. *Blood*. 2005;105(7):2717-2723.

64.   Seita J, Weissman IL. Hematopoietic stem cell: self-renewal versus differentiation. *Wiley Interdiscip Rev Syst Biol Med*. 2010;2(6):640-653.

65.   Cheng H, Zheng Z, Cheng T. New paradigms on hematopoietic stem cell differentiation. *Protein Cell*. 2020;11(1):34-44.

66.   Zhu J, Emerson SG. Hematopoietic cytokines, transcription factors and lineage commitment. *Oncogene*. 2002;21(21):3295-3313.

67.   Xavier-Ferrucio J, Krause DS. Concise Review: Bipotent Megakaryocytic-Erythroid Progenitors: Concepts and Controversies. *Stem Cells*. 2018;36(8):1138-1145.

68.   Lu R, Neff NF, Quake SR, Weissman IL. Tracking single hematopoietic stem cells in vivo using high-throughput sequencing in conjunction with viral genetic barcoding. *Nat Biotechnol*. 2011;29(10):928-933.

69.   Yamamoto R, Morita Y, Ooehara J, et al. Clonal analysis unveils self-renewing lineage-restricted progenitors generated directly from hematopoietic stem cells. *Cell*. 2013;154(5):1112-1126.

70.   Jacobsen SEW, Nerlov C. Haematopoiesis in the era of advanced single-cell technologies. *Nat Cell Biol*. 2019;21(1):2-8.

71.   Sanjuan-Pla A, Macaulay IC, Jensen CT, et al. Platelet-biased stem cells reside at the apex of the haematopoietic stem-cell hierarchy. *Nature*. 2013;502(7470):232-236.

72.   Nishikii H, Kanazawa Y, Umemoto T, et al. Unipotent Megakaryopoietic Pathway Bridging Hematopoietic Stem Cells and Mature Megakaryocytes. *Stem Cells*. 2015;33(7):2196-2207.

73.   Haas S, Hansson J, Klimmeck D, et al. Inflammation-Induced Emergency Megakaryopoiesis Driven by Hematopoietic Stem Cell-like Megakaryocyte Progenitors. *Cell Stem Cell*. 2015;17(4):422-434.

74.   Woolthuis CM, Park CY. Hematopoietic stem/progenitor cell commitment to the megakaryocyte lineage. *Blood*. 2016;127(10):1242-1248.

75.   Akashi K, Traver D, Miyamoto T, Weissman IL. A clonogenic common myeloid progenitor that gives rise to all myeloid lineages. *Nature*. 2000;404(6774):193-197.

76.   Pronk CJ, Rossi DJ, Mansson R, et al. Elucidation of the phenotypic, functional, and molecular topography of a myeloerythroid progenitor cell hierarchy. *Cell Stem Cell*. 2007;1(4):428-442.

77.   Tsang AP, Visvader JE, Turner CA, et al. FOG, a multitype zinc finger protein, acts as a cofactor for transcription factor GATA-1 in erythroid and megakaryocytic differentiation. *Cell*. 1997;90(1):109-119.

78.   Bresnick EH, Lee HY, Fujiwara T, Johnson KD, Keles S. GATA switches as developmental drivers. *J Biol Chem*. 2010;285(41):31087-31093.

79.   Grass JA, Boyer ME, Pal S, Wu J, Weiss MJ, Bresnick EH. GATA-1-dependent transcriptional repression of GATA-2 via disruption of positive autoregulation and domain-wide chromatin remodeling. *Proc Natl Acad Sci U S A*. 2003;100(15):8811-8816.

80.   Ikonomi P, Rivera CE, Riordan M, Washington G, Schechter AN, Noguchi CT. Overexpression of GATA-2 inhibits erythroid and promotes megakaryocyte differentiation. *Exp Hematol*. 2000;28(12):1423-1431.

81.   Martin F, Prandini MH, Thevenon D, Marguerie G, Uzan G. The transcription factor GATA-1 regulates the promoter activity of the platelet glycoprotein IIb gene. *J Biol Chem*. 1993;268(29):21606-21612.

82.   Kuvardina ON, Herglotz J, Kolodziej S, et al. RUNX1 represses the erythroid gene expression program during megakaryocytic differentiation. *Blood*. 2015;125(23):3570-3579.

83.   Lordier L, Bluteau D, Jalil A, et al. RUNX1-induced silencing of non-muscle myosin heavy chain IIB contributes to megakaryocyte polyploidization. *Nat Commun*. 2012;3:717.

84.   Noetzli LJ, French SL, Machlus KR. New Insights Into the Differentiation of Megakaryocytes From Hematopoietic Progenitors. *Arterioscler Thromb Vasc Biol*. 2019;39(7):1288-1300.

85.   Machlus KR, Thon JN, Italiano JE, Jr. Interpreting the developmental dance of the megakaryocyte: a review of the cellular and molecular processes mediating platelet formation. *Br J Haematol*. 2014;165(2):227-236.

86.   Bartley TD, Bogenberger J, Hunt P, et al. Identification and cloning of a megakaryocyte growth and development factor that is a ligand for the cytokine receptor Mpl. *Cell*. 1994;77(7):1117-1124.

87.   de Sauvage FJ, Hass PE, Spencer SD, et al. Stimulation of megakaryocytopoiesis and thrombopoiesis by the c-Mpl ligand. *Nature*. 1994;369(6481):533-538.

88.   Murone M, Carpenter DA, de Sauvage FJ. Hematopoietic deficiencies in c-mpl and TPO knockout mice. *Stem Cells*. 1998;16(1):1-6.

89.   Kaushansky K. Determinants of platelet number and regulation of thrombopoiesis. *Hematology Am Soc Hematol Educ Program*. 2009:147-152.

90.   Kuter DJ, Beeler DL, Rosenberg RD. The purification of megapoietin: a physiological regulator of megakaryocyte growth and platelet production. *Proc Natl Acad Sci U S A*. 1994;91(23):11104-11108.

91.   Harrison DA. The Jak/STAT pathway. *Cold Spring Harb Perspect Biol*. 2012;4(3).

92.   Miyakawa Y, Rojnuckarin P, Habib T, Kaushansky K. Thrombopoietin induces phosphoinositol 3-kinase activation through SHP2, Gab, and insulin receptor substrate proteins in BAF3 cells and primary murine megakaryocytes. *J Biol Chem*. 2001;276(4):2494-2502.

93.   Xu D, Qu CK. Protein tyrosine phosphatases in the JAK/STAT pathway. *Front Biosci*. 2008;13:4925-4932.

94.   Lordier L, Jalil A, Aurade F, et al. Megakaryocyte endomitosis is a failure of late cytokinesis related to defects in the contractile ring and Rho/Rock signaling. *Blood*. 2008;112(8):3164-3174.

95.   Breton-Gorius J, Reyes F. Ultrastructure of human bone marrow cell maturation. *Int Rev Cytol*. 1976;46:251-321.

96.   Eckly A, Heijnen H, Pertuy F, et al. Biogenesis of the demarcation membrane system (DMS) in megakaryocytes. *Blood*. 2014;123(6):921-930.

97.   Schulze H, Korpal M, Hurov J, et al. Characterization of the megakaryocyte demarcation membrane system and its role in thrombopoiesis. *Blood*. 2006;107(10):3868-3875.

98.   Albers CA, Cvejic A, Favier R, et al. Exome sequencing identifies NBEAL2 as the causative gene for gray platelet syndrome. *Nat Genet*. 2011;43(8):735-737.

99.   Deppermann C, Cherpokova D, Nurden P, et al. Gray platelet syndrome and defective thrombo-inflammation in Nbeal2-deficient mice. *J Clin Invest*. 2013.

100.   Italiano JE, Jr., Lecine P, Shivdasani RA, Hartwig JH. Blood platelets are assembled principally at the ends of proplatelet processes produced by differentiated megakaryocytes. *J Cell Biol*. 1999;147(6):1299-1312.

101.   Pollard TD. Actin and Actin-Binding Proteins. *Cold Spring Harb Perspect Biol*. 2016;8(8).

102.   Ghalloussi D, Dhenge A, Bergmeier W. New insights into cytoskeletal remodeling during platelet production. *J Thromb Haemost*. 2019;17(9):1430-1439.

103.   Courtemanche N, Pollard TD. Interaction of profilin with the barbed end of actin filaments. *Biochemistry*. 2013;52(37):6456-6466.

104. Xue B, Leyrat C, Grimes JM, Robinson RC. Structural basis of thymosin-beta4/profilin exchange leading to actin filament polymerization. *Proc Natl Acad Sci U S A*. 2014;111(43):E4596-4605.

105. Bender M, Stritt S, Nurden P, et al. Megakaryocyte-specific Profilin1-deficiency alters microtubule stability and causes a Wiskott-Aldrich syndrome-like platelet defect. *Nat Commun*. 2014;5:4746.

106. Paul AS, Pollard TD. Review of the mechanism of processive actin filament elongation by formins. *Cell Motil Cytoskeleton*. 2009;66(8):606-617.

107. Chen Z, Borek D, Padrick SB, et al. Structure and control of the actin regulatory WAVE complex. *Nature*. 2010;468(7323):533-538.

108. Carlier MF, Laurent V, Santolini J, et al. Actin depolymerizing factor (ADF/cofilin) enhances the rate of filament turnover: implication in actin-based motility. *J Cell Biol*. 1997;136(6):1307-1322.

109. McCullough BR, Grintsevich EE, Chen CK, et al. Cofilin-linked changes in actin filament flexibility promote severing. *Biophys J*. 2011;101(1):151-159.

110. Bender M, Eckly A, Hartwig JH, et al. ADF/n-cofilin-dependent actin turnover determines platelet formation and sizing. *Blood*. 2010;116(10):1767-1775.

111. Johnston AB, Collins A, Goode BL. High-speed depolymerization at actin filament ends jointly catalysed by Twinfilin and Srv2/CAP. *Nat Cell Biol*. 2015;17(11):1504-1511.

112. Paavilainen VO, Oksanen E, Goldman A, Lappalainen P. Structure of the actin-depolymerizing factor homology domain in complex with actin. *J Cell Biol*. 2008;182(1):51-59.

113. Goode BL, Drubin DG, Lappalainen P. Regulation of the cortical actin cytoskeleton in budding yeast by twinfilin, a ubiquitous actin monomer-sequestering protein. *J Cell Biol*. 1998;142(3):723-733.

114. Moseley JB, Okada K, Balcer HI, Kovar DR, Pollard TD, Goode BL. Twinfilin is an actin-filament-severing protein and promotes rapid turnover of actin structures in vivo. *J Cell Sci*. 2006;119(Pt 8):1547-1557.

115. Nevalainen EM, Braun A, Vartiainen MK, et al. Twinfilin-2a is dispensable for mouse development. *PLoS One*. 2011;6(8):e22894.

116. Stritt S, Beck S, Becker IC, et al. Twinfilin 2a regulates platelet reactivity and turnover in mice. *Blood*. 2017;130(15):1746-1756.

117. Pleines I, Hagedorn I, Gupta S, et al. Megakaryocyte-specific RhoA deficiency causes macrothrombocytopenia and defective platelet activation in hemostasis and thrombosis. *Blood*. 2012;119(4):1054-1063.

118. Pleines I, Dutting S, Cherpokova D, et al. Defective tubulin organization and proplatelet formation in murine megakaryocytes lacking Rac1 and Cdc42. *Blood*. 2013;122(18):3178-3187.

119. Antkowiak A, Viaud J, Severin S, et al. Cdc42-dependent F-actin dynamics drive structuration of the demarcation membrane system in megakaryocytes. *J Thromb Haemost*. 2016;14(6):1268-1284.

120. Dutting S, Gaits-Iacovoni F, Stegner D, et al. A Cdc42/RhoA regulatory circuit downstream of glycoprotein Ib guides transendothelial platelet biogenesis. *Nat Commun*. 2017;8:15838.

121. Schachtner H, Calaminus SD, Sinclair A, et al. Megakaryocytes assemble podosomes that degrade matrix and protrude through basement membrane. *Blood*. 2013;121(13):2542-2552.

122. Spindler M, van Eeuwijk JMM, Schurr Y, et al. ADAP deficiency impairs megakaryocyte polarization with ectopic proplatelet release and causes microthrombocytopenia. *Blood*. 2018;132(6):635-646.

123. Walker RA, O'Brien ET, Pryer NK, et al. Dynamic instability of individual microtubules analyzed by video light microscopy: rate constants and transition frequencies. *J Cell Biol*. 1988;107(4):1437-1448.

124. Wen Y, Eng CH, Schmoranzer J, et al. EB1 and APC bind to mDia to stabilize microtubules downstream of Rho and promote cell migration. *Nat Cell Biol*. 2004;6(9):820-830.

125. Coles CH, Bradke F. Coordinating neuronal actin-microtubule dynamics. *Curr Biol*. 2015;25(15):R677-691.

126. Aillaud C, Bosc C, Peris L, et al. Vasohibins/SVBP are tubulin carboxypeptidases (TCPs) that regulate neuron differentiation. *Science*. 2017;358(6369):1448-1453.

127. Kreis TE. Microtubules containing detyrosinated tubulin are less dynamic. *EMBO J*. 1987;6(9):2597-2606.

128. Bieling P, Kandels-Lewis S, Telley IA, van Dijk J, Janke C, Surrey T. CLIP-170 tracks growing microtubule ends by dynamically recognizing composite EB1/tubulin-binding sites. *J Cell Biol*. 2008;183(7):1223-1233.

129. Webster DR, Wehland J, Weber K, Borisy GG. Detyrosination of alpha tubulin does not stabilize microtubules in vivo. *J Cell Biol*. 1990;111(1):113-122.

130.	Wloga D, Gaertig J. Post-translational modifications of microtubules. *J Cell Sci*. 2010;123(Pt 20):3447-3455.
131.	Tablin F, Castro M, Leven RM. Blood platelet formation in vitro. The role of the cytoskeleton in megakaryocyte fragmentation. *J Cell Sci*. 1990;97 (Pt 1):59-70.
132.	Patel SR, Richardson JL, Schulze H, et al. Differential roles of microtubule assembly and sliding in proplatelet formation by megakaryocytes. *Blood*. 2005;106(13):4076-4085.
133.	Bender M, Thon JN, Ehrlicher AJ, et al. Microtubule sliding drives proplatelet elongation and is dependent on cytoplasmic dynein. *Blood*. 2015;125(5):860-868.
134.	Patel SR, Hartwig JH, Italiano JE, Jr. The biogenesis of platelets from megakaryocyte proplatelets. *J Clin Invest*. 2005;115(12):3348-3354.
135.	Richardson JL, Shivdasani RA, Boers C, Hartwig JH, Italiano JE, Jr. Mechanisms of organelle transport and capture along proplatelets during platelet production. *Blood*. 2005;106(13):4066-4075.
136.	Schieber M, Crispino JD, Stein B. Myelofibrosis in 2019: moving beyond JAK2 inhibition. *Blood Cancer J*. 2019;9(9):74.
137.	Harrison C, Kiladjian JJ, Al-Ali HK, et al. JAK inhibition with ruxolitinib versus best available therapy for myelofibrosis. *N Engl J Med*. 2012;366(9):787-798.
138.	Cervantes F, Dupriez B, Pereira A, et al. New prognostic scoring system for primary myelofibrosis based on a study of the International Working Group for Myelofibrosis Research and Treatment. *Blood*. 2009;113(13):2895-2901.
139.	Xing S, Wanting TH, Zhao W, et al. Transgenic expression of JAK2V617F causes myeloproliferative disorders in mice. *Blood*. 2008;111(10):5109-5117.
140.	Bruns I, Lucas D, Pinho S, et al. Megakaryocytes regulate hematopoietic stem cell quiescence through CXCL4 secretion. *Nat Med*. 2014;20(11):1315-1320.
141.	Schmitt A, Jouault H, Guichard J, Wendling F, Drouin A, Cramer EM. Pathologic interaction between megakaryocytes and polymorphonuclear leukocytes in myelofibrosis. *Blood*. 2000;96(4):1342-1347.
142.	Malara A, Abbonante V, Zingariello M, Migliaccio A, Balduini A. Megakaryocyte Contribution to Bone Marrow Fibrosis: many Arrows in the Quiver. *Mediterr J Hematol Infect Dis*. 2018;10(1):e2018068.
143.	Leask A, Abraham DJ. TGF-beta signaling and the fibrotic response. *FASEB J*. 2004;18(7):816-827.
144.	Le Bousse-Kerdiles MC, Martyre MC. Dual implication of fibrogenic cytokines in the pathogenesis of fibrosis and myeloproliferation in myeloid metaplasia with myelofibrosis. *Ann Hematol*. 1999;78(10):437-444.
145.	Vannucchi AM, Bianchi L, Cellai C, et al. Development of myelofibrosis in mice genetically impaired for GATA-1 expression (GATA-1(low) mice). *Blood*. 2002;100(4):1123-1132.
146.	Vannucchi AM, Bianchi L, Paoletti F, et al. A pathobiologic pathway linking thrombopoietin, GATA-1, and TGF-beta1 in the development of myelofibrosis. *Blood*. 2005;105(9):3493-3501.
147.	Chagraoui H, Komura E, Tulliez M, Giraudier S, Vainchenker W, Wendling F. Prominent role of TGF-beta 1 in thrombopoietin-induced myelofibrosis in mice. *Blood*. 2002;100(10):3495-3503.
148.	Martyre MC, Magdelenat H, Bryckaert MC, Laine-Bidron C, Calvo F. Increased intraplatelet levels of platelet-derived growth factor and transforming growth factor-beta in patients with myelofibrosis with myeloid metaplasia. *Br J Haematol*. 1991;77(1):80-86.
149.	Ling T, Crispino JD, Zingariello M, Martelli F, Migliaccio AR. GATA1 insufficiencies in primary myelofibrosis and other hematopoietic disorders: consequences for therapy. *Expert Rev Hematol*. 2018;11(3):169-184.
150.	Centurione L, Di Baldassarre A, Zingariello M, et al. Increased and pathologic emperipolesis of neutrophils within megakaryocytes associated with marrow fibrosis in GATA-1(low) mice. *Blood*. 2004;104(12):3573-3580.
151.	Grosse J, Braun A, Varga-Szabo D, et al. An EF hand mutation in Stim1 causes premature platelet activation and bleeding in mice. *J Clin Invest*. 2007;117(11):3540-3550.
152.	Guerrero JA, Bennett C, van der Weyden L, et al. Gray platelet syndrome: proinflammatory megakaryocytes and alpha-granule loss cause myelofibrosis and confer metastasis resistance in mice. *Blood*. 2014;124(24):3624-3635.
153.	Ng AP, Kauppi M, Metcalf D, et al. Mpl expression on megakaryocytes and platelets is dispensable for thrombopoiesis but essential to prevent myeloproliferation. *Proc Natl Acad Sci U S A*. 2014;111(16):5884-5889.

154. Hofmann I, Geer MJ, Vogtle T, et al. Congenital macrothrombocytopenia with focal myelofibrosis due to mutations in human G6b-B is rescued in humanized mice. *Blood*. 2018;132(13):1399-1412.

155. Mazharian A, Wang YJ, Mori J, et al. Mice lacking the ITIM-containing receptor G6b-B exhibit macrothrombocytopenia and aberrant platelet function. *Sci Signal*. 2012;5(248):ra78.

156. Psaila B, Wang G, Rodriguez-Meira A, et al. Single-Cell Analyses Reveal Megakaryocyte-Biased Hematopoiesis in Myelofibrosis and Identify Mutant Clone-Specific Targets. *Mol Cell*. 2020;78(3):477-492 e478.

157. Bock O, Loch G, Schade U, et al. Osteosclerosis in advanced chronic idiopathic myelofibrosis is associated with endothelial overexpression of osteoprotegerin. *Br J Haematol*. 2005;130(1):76-82.

158. Alvarez MB, Xu L, Childress PJ, et al. Megakaryocyte and Osteoblast Interactions Modulate Bone Mass and Hematopoiesis. *Stem Cells Dev*. 2018;27(10):671-682.

159. Bord S, Vedi S, Beavan SR, Horner A, Compston JE. Megakaryocyte population in human bone marrow increases with estrogen treatment: a role in bone remodeling? *Bone*. 2000;27(3):397-401.

160. Kacena MA, Shivdasani RA, Wilson K, et al. Megakaryocyte-osteoblast interaction revealed in mice deficient in transcription factors GATA-1 and NF-E2. *J Bone Miner Res*. 2004;19(4):652-660.

161. Lee YS, Kwak MK, Moon SA, et al. Regulation of bone metabolism by megakaryocytes in a paracrine manner. *Sci Rep*. 2020;10(1):2277.

162. Tang Y, Hu M, Xu Y, et al. Megakaryocytes promote bone formation through coupling osteogenesis with angiogenesis by secreting TGF-beta1. *Theranostics*. 2020;10(5):2229-2242.

163. Lee K, Jessop H, Suswillo R, Zaman G, Lanyon L. Endocrinology: bone adaptation requires oestrogen receptor-alpha. *Nature*. 2003;424(6947):389.

164. Raisz LG. Pathogenesis of osteoporosis: concepts, conflicts, and prospects. *J Clin Invest*. 2005;115(12):3318-3325.

165. Hughes DE, Dai A, Tiffee JC, Li HH, Mundy GR, Boyce BF. Estrogen promotes apoptosis of murine osteoclasts mediated by TGF-beta. *Nat Med*. 1996;2(10):1132-1136.

166. Chung HW, Seo JS, Hur SE, et al. Association of interleukin-6 promoter variant with bone mineral density in pre-menopausal women. *J Hum Genet*. 2003;48(5):243-248.

167. Du C, Xu Y, Yang K, et al. Estrogen promotes megakaryocyte polyploidization via estrogen receptor beta-mediated transcription of GATA1. *Leukemia*. 2017;31(4):945-956.

168. Nagata Y, Yoshikawa J, Hashimoto A, Yamamoto M, Payne AH, Todokoro K. Proplatelet formation of megakaryocytes is triggered by autocrine-synthesized estradiol. *Genes Dev*. 2003;17(23):2864-2869.

169. Deppermann C, Kratofil RM, Peiseler M, et al. Macrophage galactose lectin is critical for Kupffer cells to clear aged platelets. *J Exp Med*. 2020;217(4).

170. Mehta A, Mahtta D, Gulati M, Sperling LS, Blumenthal RS, Virani SS. Cardiovascular Disease Prevention in Focus: Highlights from the 2019 American Heart Association Scientific Sessions. *Curr Atheroscler Rep*. 2020;22(1):3.

171. Sharda A, Flaumenhaft R. The life cycle of platelet granules. *F1000Res*. 2018;7:236.

172. Nurden AT, Didry D, Rosa JP. Molecular defects of platelets in Bernard-Soulier syndrome. *Blood Cells*. 1983;9(2):333-358.

173. Ware J, Russell S, Ruggeri ZM. Generation and rescue of a murine model of platelet dysfunction: the Bernard-Soulier syndrome. *Proc Natl Acad Sci U S A*. 2000;97(6):2803-2808.

174. Kahn ML, Diacovo TG, Bainton DF, Lanza F, Trejo J, Coughlin SR. Glycoprotein V-deficient platelets have undiminished thrombin responsiveness and Do not exhibit a Bernard-Soulier phenotype. *Blood*. 1999;94(12):4112-4121.

175. Massberg S, Gawaz M, Gruner S, et al. A crucial role of glycoprotein VI for platelet recruitment to the injured arterial wall in vivo. *J Exp Med*. 2003;197(1):41-49.

176. Bergmeier W, Piffath CL, Goerge T, et al. The role of platelet adhesion receptor GPIbalpha far exceeds that of its main ligand, von Willebrand factor, in arterial thrombosis. *Proc Natl Acad Sci U S A*. 2006;103(45):16900-16905.

177. Mori J, Pearce AC, Spalton JC, et al. G6b-B inhibits constitutive and agonist-induced signaling by glycoprotein VI and CLEC-2. *J Biol Chem*. 2008;283(51):35419-35427.

178. Kato K, Kanaji T, Russell S, et al. The contribution of glycoprotein VI to stable platelet adhesion and thrombus formation illustrated by targeted gene deletion. *Blood*. 2003;102(5):1701-1707.

179. Nieswandt B, Schulte V, Bergmeier W, et al. Long-term antithrombotic protection by in vivo depletion of platelet glycoprotein VI in mice. *J Exp Med*. 2001;193(4):459-469.

180.   Nieswandt B, Pleines I, Bender M. Platelet adhesion and activation mechanisms in arterial thrombosis and ischaemic stroke. *J Thromb Haemost*. 2011;9 Suppl 1:92-104.
181.   Ginsberg MH, Partridge A, Shattil SJ. Integrin regulation. *Curr Opin Cell Biol*. 2005;17(5):509-516.
182.   Severin S, Pollitt AY, Navarro-Nunez L, et al. Syk-dependent phosphorylation of CLEC-2: a novel mechanism of hem-immunoreceptor tyrosine-based activation motif signaling. *J Biol Chem*. 2011;286(6):4107-4116.
183.   Suzuki-Inoue K, Inoue O, Ozaki Y. Novel platelet activation receptor CLEC-2: from discovery to prospects. *J Thromb Haemost*. 2011;9 Suppl 1:44-55.
184.   May F, Hagedorn I, Pleines I, et al. CLEC-2 is an essential platelet-activating receptor in hemostasis and thrombosis. *Blood*. 2009;114(16):3464-3472.
185.   Michelsen ADC, M.; Frelinger, A.; Newman, P. Platelets. 4th edition.; 2019.
186.   Coxon CH, Geer MJ, Senis YA. ITIM receptors: more than just inhibitors of platelet activation. *Blood*. 2017;129(26):3407-3418.
187.   Mazharian A, Mori J, Wang YJ, et al. Megakaryocyte-specific deletion of the protein-tyrosine phosphatases Shp1 and Shp2 causes abnormal megakaryocyte development, platelet production, and function. *Blood*. 2013;121(20):4205-4220.
188.   Geer MJ, van Geffen JP, Gopalasingam P, et al. Uncoupling ITIM receptor G6b-B from tyrosine phosphatases Shp1 and Shp2 disrupts murine platelet homeostasis. *Blood*. 2018;132(13):1413-1425.
189.   Vogtle T, Sharma S, Mori J, et al. Heparan sulfates are critical regulators of the inhibitory megakaryocyte-platelet receptor G6b-B. *Elife*. 2019;8.
190.   Boulaftali Y, Hess PR, Getz TM, et al. Platelet ITAM signaling is critical for vascular integrity in inflammation. *J Clin Invest*. 2013;123(2):908-916.
191.   Bultmann A, Li Z, Wagner S, et al. Impact of glycoprotein VI and platelet adhesion on atherosclerosis--a possible role of fibronectin. *J Mol Cell Cardiol*. 2010;49(3):532-542.
192.   Boilard E, Nigrovic PA, Larabee K, et al. Platelets amplify inflammation in arthritis via collagen-dependent microparticle production. *Science*. 2010;327(5965):580-583.
193.   Volz J, Mammadova-Bach E, Gil-Pulido J, et al. Inhibition of platelet GPVI induces intratumor hemorrhage and increases efficacy of chemotherapy in mice. *Blood*. 2019;133(25):2696-2706.
194.   Sweet DT, Jimenez JM, Chang J, et al. Lymph flow regulates collecting lymphatic vessel maturation in vivo. *J Clin Invest*. 2015;125(8):2995-3007.
195.   Hess PR, Rawnsley DR, Jakus Z, et al. Platelets mediate lymphovenous hemostasis to maintain blood-lymphatic separation throughout life. *J Clin Invest*. 2014;124(1):273-284.
196.   Zhang Y, Daubel N, Stritt S, Makinen T. Transient loss of venous integrity during developmental vascular remodeling leads to red blood cell extravasation and clearance by lymphatic vessels. *Development*. 2018;145(3).
197.   Abtahian F, Guerriero A, Sebzda E, et al. Regulation of blood and lymphatic vascular separation by signaling proteins SLP-76 and Syk. *Science*. 2003;299(5604):247-251.
198.   Haining EJ, Lowe KL, Wichaiyo S, et al. Lymphatic blood filling in CLEC-2-deficient mouse models. *Platelets*. 2020:1-16.
199.   Nieswandt B, Bergmeier W, Rackebrandt K, Gessner JE, Zirngibl H. Identification of critical antigen-specific mechanisms in the development of immune thrombocytopenic purpura in mice. *Blood*. 2000;96(7):2520-2527.
200.   Nieswandt B, Bergmeier W, Schulte V, Rackebrandt K, Gessner JE, Zirngibl H. Expression and function of the mouse collagen receptor glycoprotein VI is strictly dependent on its association with the FcRgamma chain. *J Biol Chem*. 2000;275(31):23998-24002.
201.   Bergmeier W, Rackebrandt K, Schroder W, Zirngibl H, Nieswandt B. Structural and functional characterization of the mouse von Willebrand factor receptor GPIb-IX with novel monoclonal antibodies. *Blood*. 2000;95(3):886-893.
202.   Bergmeier W, Schulte V, Brockhoff G, Bier U, Zirngibl H, Nieswandt B. Flow cytometric detection of activated mouse integrin alphaIIbbeta3 with a novel monoclonal antibody. *Cytometry*. 2002;48(2):80-86.
203.   Schulte V, Rabie T, Prostredna M, Aktas B, Gruner S, Nieswandt B. Targeting of the collagen-binding site on glycoprotein VI is not essential for in vivo depletion of the receptor. *Blood*. 2003;101(10):3948-3952.
204.   Unkeless JC. Characterization of a monoclonal antibody directed against mouse macrophage and lymphocyte Fc receptors. *J Exp Med*. 1979;150(3):580-596.

205.   Tiedt R, Schomber T, Hao-Shen H, Skoda RC. Pf4-Cre transgenic mice allow the generation of lineage-restricted gene knockouts for studying megakaryocyte and platelet function in vivo. *Blood*. 2007;109(4):1503-1506.

206.   Kanaji T, Russell S, Ware J. Amelioration of the macrothrombocytopenia associated with the murine Bernard-Soulier syndrome. *Blood*. 2002;100(6):2102-2107.

207.   Bender M, May F, Lorenz V, et al. Combined in vivo depletion of glycoprotein VI and C-type lectin-like receptor 2 severely compromises hemostasis and abrogates arterial thrombosis in mice. *Arterioscler Thromb Vasc Biol*. 2013;33(5):926-934.

208.   Ward CM, To TH, Pederson SM. ngsReports: a Bioconductor package for managing FastQC reports and other NGS related log files. *Bioinformatics*. 2020;36(8):2587-2588.

209.   Harrow J, Frankish A, Gonzalez JM, et al. GENCODE: the reference human genome annotation for The ENCODE Project. *Genome Res*. 2012;22(9):1760-1774.

210.   Aurbach K, Spindler M, Haining EJ, Bender M, Pleines I. Blood collection, platelet isolation and measurement of platelet count and size in mice-a practical guide. *Platelets*. 2019;30(6):698-707.

211.   Dobin A, Davis CA, Schlesinger F, et al. STAR: ultrafast universal RNA-seq aligner. *Bioinformatics*. 2013;29(1):15-21.

212.   Yu G, Wang LG, Han Y, He QY. clusterProfiler: an R package for comparing biological themes among gene clusters. *OMICS*. 2012;16(5):284-287.

213.   Kawamoto T, Shimizu M. A method for preparing 2- to 50-micron-thick fresh-frozen sections of large samples and undecalcified hard tissues. *Histochem Cell Biol*. 2000;113(5):331-339.

214.   Haffner-Luntzer M, Kemmler J, Heidler V, et al. Inhibition of Midkine Augments Osteoporotic Fracture Healing. *PLoS One*. 2016;11(7):e0159278.

215.   Tual-Chalot S, Allinson KR, Fruttiger M, Arthur HM. Whole mount immunofluorescent staining of the neonatal mouse retina to investigate angiogenesis in vivo. *J Vis Exp*. 2013(77):e50546.

216.   Watson SP, Herbert JM, Pollitt AY. GPVI and CLEC-2 in hemostasis and vascular integrity. *J Thromb Haemost*. 2010;8(7):1456-1467.

217.   Suzuki-Inoue K. Essential in vivo roles of the platelet activation receptor CLEC-2 in tumour metastasis, lymphangiogenesis and thrombus formation. *J Biochem*. 2011;150(2):127-132.

218.   Rayes J, Jadoui S, Lax S, et al. The contribution of platelet glycoprotein receptors to inflammatory bleeding prevention is stimulus and organ dependent. *Haematologica*. 2018;103(6):e256-e258.

219.   Becker IC, Scheller I, Wackerbarth LM, et al. Actin/microtubule crosstalk during platelet biogenesis in mice is critically regulated by Twinfilin1 and Cofilin1. *Blood Adv*. 2020;4(10):2124-2134.

220.   Bender M, Giannini S, Grozovsky R, et al. Dynamin 2-dependent endocytosis is required for normal megakaryocyte development in mice. *Blood*. 2015;125(6):1014-1024.

221.   Webster DR, Borisy GG. Microtubules are acetylated in domains that turn over slowly. *J Cell Sci*. 1989;92 (Pt 1):57-65.

222.   Pan J, Lordier L, Meyran D, et al. The formin DIAPH1 (mDia1) regulates megakaryocyte proplatelet formation by remodeling the actin and microtubule cytoskeletons. *Blood*. 2014;124(26):3967-3977.

223.   Stritt S, Nurden P, Turro E, et al. A gain-of-function variant in DIAPH1 causes dominant macrothrombocytopenia and hearing loss. *Blood*. 2016;127(23):2903-2914.

224.   Avioli LV. Heterogeneity of osteoporotic syndromes and the response to calcitonin therapy. *Calcif Tissue Int*. 1991;49 Suppl 2:S16-19.

225.   Badalucco S, Di Buduo CA, Campanelli R, et al. Involvement of TGFbeta1 in autocrine regulation of proplatelet formation in healthy subjects and patients with primary myelofibrosis. *Haematologica*. 2013;98(4):514-517.

226.   Ciurea SO, Merchant D, Mahmud N, et al. Pivotal contributions of megakaryocytes to the biology of idiopathic myelofibrosis. *Blood*. 2007;110(3):986-993.

227.   Yamaguchi Y, Zon LI, Ackerman SJ, Yamamoto M, Suda T. Forced GATA-1 expression in the murine myeloid cell line M1: induction of c-Mpl expression and megakaryocytic/erythroid differentiation. *Blood*. 1998;91(2):450-457.

228.   Berndt MC, Phillips DR. Purification and preliminary physicochemical characterization of human platelet membrane glycoprotein V. *J Biol Chem*. 1981;256(1):59-65.

229.   Moog S, Mangin P, Lenain N, et al. Platelet glycoprotein V binds to collagen and participates in platelet adhesion and aggregation. *Blood*. 2001;98(4):1038-1046.

230.   Uhrin P, Zaujec J, Breuss JM, et al. Novel function for blood platelets and podoplanin in developmental separation of blood and lymphatic circulation. *Blood*. 2010;115(19):3997-4005.

231. Tessandier N, Melki I, Cloutier N, et al. Platelets Disseminate Extracellular Vesicles in Lymph in Rheumatoid Arthritis. *Arterioscler Thromb Vasc Biol*. 2020;40(4):929-942.

232. Deppermann C, Kraft P, Volz J, et al. Platelet secretion is crucial to prevent bleeding in the ischemic brain but not in the inflamed skin or lung in mice. *Blood*. 2017;129(12):1702-1706.

233. Schuhmann MK, Guthmann J, Stoll G, Nieswandt B, Kraft P, Kleinschnitz C. Blocking of platelet glycoprotein receptor Ib reduces "thrombo-inflammation" in mice with acute ischemic stroke. *J Neuroinflammation*. 2017;14(1):18.

234. Boulaftali Y, Mawhin MA, Jandrot-Perrus M, Ho-Tin-Noe B. Glycoprotein VI in securing vascular integrity in inflamed vessels. *Res Pract Thromb Haemost*. 2018;2(2):228-239.

235. Pachel C, Mathes D, Arias-Loza AP, et al. Inhibition of Platelet GPVI Protects Against Myocardial Ischemia-Reperfusion Injury. *Arterioscler Thromb Vasc Biol*. 2016;36(4):629-635.

236. Kleinschnitz C, Pozgajova M, Pham M, Bendszus M, Nieswandt B, Stoll G. Targeting platelets in acute experimental stroke: impact of glycoprotein Ib, VI, and IIb/IIIa blockade on infarct size, functional outcome, and intracranial bleeding. *Circulation*. 2007;115(17):2323-2330.

237. Gawaz M. Novel Ligands for Platelet Glycoprotein VI. *Thromb Haemost*. 2018;118(3):435-436.

238. Lajko M, Cardona HJ, Taylor JM, Shah RS, Farrow KN, Fawzi AA. Hyperoxia-Induced Proliferative Retinopathy: Early Interruption of Retinal Vascular Development with Severe and Irreversible Neurovascular Disruption. *PLoS One*. 2016;11(11):e0166886.

239. Zuidscherwoude M, Green HLH, Thomas SG. Formin proteins in megakaryocytes and platelets: regulation of actin and microtubule dynamics. *Platelets*. 2019;30(1):23-30.

240. Strassel C, Moog S, Mallo L, et al. Microtubule plus-end tracking Adenopolyposis Coli negatively regulates proplatelet formation. *Sci Rep*. 2018;8(1):15808.

241. Gorovoy M, Niu J, Bernard O, et al. LIM kinase 1 coordinates microtubule stability and actin polymerization in human endothelial cells. *J Biol Chem*. 2005;280(28):26533-26542.

242. Zeiler M, Moser M, Mann M. Copy number analysis of the murine platelet proteome spanning the complete abundance range. *Mol Cell Proteomics*. 2014;13(12):3435-3445.

243. Kunishima S, Okuno Y, Yoshida K, et al. ACTN1 mutations cause congenital macrothrombocytopenia. *Am J Hum Genet*. 2013;92(3):431-438.

244. Nurden P, Debili N, Coupry I, et al. Thrombocytopenia resulting from mutations in filamin A can be expressed as an isolated syndrome. *Blood*. 2011;118(22):5928-5937.

245. Kauskot A, Poirault-Chassac S, Adam F, et al. LIM kinase/cofilin dysregulation promotes macrothrombocytopenia in severe von Willebrand disease-type 2B. *JCI Insight*. 2016;1(16):e88643.

246. Bury L, Malara A, Momi S, Petito E, Balduini A, Gresele P. Mechanisms of thrombocytopenia in platelet-type von Willebrand disease. *Haematologica*. 2019;104(7):1473-1481.

247. Gilles L, Arslan AD, Marinaccio C, et al. Downregulation of GATA1 drives impaired hematopoiesis in primary myelofibrosis. *J Clin Invest*. 2017;127(4):1316-1320.

248. Zingariello M, Sancillo L, Martelli F, et al. The thrombopoietin/MPL axis is activated in the Gata1(low) mouse model of myelofibrosis and is associated with a defective RPS14 signature. *Blood Cancer J*. 2017;7(6):e572.

249. Huang H, Woo AJ, Waldon Z, et al. A Src family kinase-Shp2 axis controls RUNX1 activity in megakaryocyte and T-lymphocyte differentiation. *Genes Dev*. 2012;26(14):1587-1601.

250. Tan YX, Cui H, Wan LM, et al. Overexpression of heparanase in mice promoted megakaryopoiesis. *Glycobiology*. 2018;28(5):269-275.

251. Malara A, Gruppi C, Abbonante V, et al. EDA fibronectin-TLR4 axis sustains megakaryocyte expansion and inflammation in bone marrow fibrosis. *J Exp Med*. 2019;216(3):587-604.

252. Panteli KE, Hatzimichael EC, Bouranta PK, et al. Serum interleukin (IL)-1, IL-2, sIL-2Ra, IL-6 and thrombopoietin levels in patients with chronic myeloproliferative diseases. *Br J Haematol*. 2005;130(5):709-715.

253. Melhem M, Abu-Farha M, Antony D, et al. Novel G6B gene variant causes familial autosomal recessive thrombocytopenia and anemia. *Eur J Haematol*. 2017;98(3):218-227.

254. Cardin S, Bilodeau M, Roussy M, et al. Human models of NUP98-KDM5A megakaryocytic leukemia in mice contribute to uncovering new biomarkers and therapeutic vulnerabilities. *Blood Adv*. 2019;3(21):3307-3321.

255. Italiano JE, Jr., Battinelli EM. Selective sorting of alpha-granule proteins. *J Thromb Haemost*. 2009;7 Suppl 1:173-176.

256. Battinelli EM, Markens BA, Italiano JE, Jr. Release of angiogenesis regulatory proteins from platelet alpha granules: modulation of physiologic and pathologic angiogenesis. *Blood*. 2011;118(5):1359-1369.

6 APPENDIX

6.1 Abbreviations

ACD	Acid citrate dextrose
ADAM	A disintegrin and metalloproteinase
ADAP	Adhesion and degranulation-promoting adaptor protein
ADF	Actin depolymerizing factor
ADF-H	ADF-homology domain
ADP	Adenosine diphosphate
APC	Adenomatous polyposis coli
APS	Ammonium persulfate
Arp2/3	Actin-related proteins 2/3
ATP	Adenosine triphosphate
Atpi6	ATPase, H^+ transporting, [vacuolar proton pump] member I
AU	Arbitrary unit
BM	Bone marrow
BMD	Bone mineral density
BSA	Bovine serum albumin
BV/TV	Bone volume to tissue volume
Ca^{2+}	Calcium cation
cAMP	Cyclic adenosine monophosphate
CAP	Cyclase-associated protein
CD	Cluster of differentiation
Cdc42	Cell division control protein 42 homolog
CLEC-2	C-type lectin-like receptor 2
CLIP	Cytoplasmic linker protein
CLP	Common lymphoid progenitors
CMP	Common myeloid progenitor
c-Mpl	Myeloproliferative leukemia protein
Cof1	Cofilin1
Colch	Colchicine
Col	Collagen
CRP	Collagen-related peptide
CP	Capping protein
CT	Computed tomography
CVX	Convulxin

CXCL	Chemokine (C-X-C Motif) ligand
DAG	Diacylglycerol
DAPI	4'-6-Diamidino-2-phenylindole
°C	Degree Celsius
Dll4	Delta-like-4
Diaph1	Mammalian Diaphanous
DIC	Differential interference contrast
Dlx5	Distal-less homeobox 5
DNA	Deoxyribonucleic acid
dNTP	Deoxynucleotide triphosphates
DMEM	Dulbecco's modified eagle medium
DMS	Demarcation membrane system
DMSO	Dimethylsulfoxide
DPBS	Dulbecco's phosphate buffered saline
E	Embryonic day
EB	End binding protein
EC	Endothelial cell
ECL	Enhanced chemiluminescence
ECM	Extracellular matrix
EDTA	Ethylenediaminetetraacetic acid
e.g.	Exempli gratia
EGTA	Ethylene glycol tetraacetic acid
ELISA	Enzyme-linked immunosorbent assay
Eph	Ephrin
ER	Estrogen receptor
ERK	Extracellular signal-regulated kinases
et al.	et alii
Etv2	ETS variant 2
EV	Extracellular vesicle
Fab	Fragment antigen-binding
F-actin	Filamentous actin
FCS	Fetal calf serum
FcR	Fc receptor
FGF	Fibroblast-derived growth factor
FITC	Fluorescein-isothiocyanate
Fli	Friend leukemia integration

Flk	Fetal liver kinase
Flt	Fms-related receptor kinase
FOG1	Friend of GATA1
FSC	Forward scatter
G-actin	Globular actin
GAPDH	Glycerinaldehyd-3-phosphate-dehydrogenase
GATA	GATA-binding factor
GEF	Guanine nucleotide exchange factor
GP	Glycoprotein
GPCR	G-protein-coupled receptor
GPS	Gray platelet syndrome
Grb2	Growth factor receptor-bound protein 2
GTP	Guanine triphosphate
h	Hour
HCl	Hydrogen chloride
H&E	Hematoxylin-Eosin
HEK	Human embryonic kidney
HEPES	N-2-Hydroxyethylpiperazine-N'-2-ethanesulfonic acid
HRP	Horseradish peroxidase
HSC	Hematopoietic stem cell
Ig	Immunoglobulin
IHC	Immunohistochemistry
IL	Interleukin
IMF	Chronic idiopathic myelofibrosis
IP	Immunoprecipitation
i.p.	Intraperitoneally
ITAM	Immunoreceptor tyrosine-based activation motif
ITIM	Immunoreceptor tyrosine-based inhibition motif
ITSM	Immunoreceptor tyrosine-based switch motif
i.v.	Intravenously
IVM	Intravital microscopy
JAK	Janus kinase
kb	Kilo base pairs
kDa	Kilo Dalton
Klf1	Krueppel-like factor 1
LAT	Linker of activated T cells

LIMK	LIM kinase
LEC	Lymphatic endothelial cells
LSK	$Lin^+/Sca-1^+/c-Kit^+$
LT	Long-term
LYVE	Lymphatic vessel endothelial receptor
MAC1	Macrophage antigen 1
MAPK	Mitogen-activated protein kinase
M-CSF	Macrophage colony-stimulating factor
µCT	Micro-computed tomography
mDia	Mammalian Diaphanous
MEP	Megakaryocyte-erythroid progenitor
MFI	Mean fluorescence intensity
min	Minute
MK	Megakaryocyte
MLC	Myosin light chain
MMP	Matrix metalloproteinase
Mpig6b	Megakaryocyte and platelet inhibitory receptor G6b
MPP	Multipotent progenitors
mRNA	Messenger RNA
MYH	Non-muscle myosin heavy chain
N	Number of chromosome sets
NaCl	Sodium chloride
NaOH	Sodium hydroxide
NBEAL2	Neurobeachin-like 2
NIH	National Institute for Health Research
NP-40	Nonidet P-40
Nrp	Neuropilin
n.s.	Non-significant
OCS	Open canalicular system
OD	Optical density
OIR	Oxygen-induced retinopathy
Orai1	Ca^{2+} release-activated calcium channel protein 1
P	Phosphorylation/postnatal day
PAGE	Polyacrylamide gel electrophoresis
PAR	Protease-activated receptors
PBMC	Peripheral blood mononuclear cells

PCR	Polymerase chain reaction
PDGF	Platelet-derived growth factor
PE	Phycoerythrin
PECAM	Platelet endothelial cell adhesion molecule
Pf4	Platelet factor 4
PFA	Paraformaldehyd
Pfn	Profilin
PGI_2	Prostacycline
PI	Propidium iodide
PI3K	Phosphoinositide 3-kinase
PIP_2	Phosphatidylinositol-4,5-biphosphate
PIP_3	Phosphatidylinositol-3.4,5-triiphosphate
PIPES	Piperazine-N,N'-bis(2-ethanesulfonic acid)
PK	Protein kinase
PL	Phospholipase
PMF	Primary myelofibrosis
PPF	Proplatelet formation
Prox1	Prospero homeodomain transcription factor
PRP	Platelet-rich plasma
PTH	Parathyroid hormone
PTPN	Protein-tyrosine phosphatase non-receptor type
PVDF	Polyvinylidene difluoride
PS	Phosphatidylserine
Rac1	Ras-related C3 botulinum toxin substrate 1
RANK	Receptor activator of NF-κB
RBC	Red blood cell
RC	Rhodocytin
Rest	Resting
RhoA	Ras homologue family member A
RNA	Ribonucleic acid
ROCK	Rho kinase
ROP	Retinopathy of prematurity
rpm	Rotation per minute
RT	Room temperature
RT-PCR	Reverse transcription polymerase chain reaction
RUNX	Runt-related transcription factor

s	Soluble
S1P	Sphingosine-1-phosphate
Sca1	Stem cell antigen 1
SCF	Stem cell factor
SD	Standard deviation
SDS	Sodium dodecyl sulfate
SFK	Src family kinase
SH2	Src homology 2
Shp	SH2-domain-containing protein tyrosine phosphatase
SLP-76	SH2 domain-containing leukocyte protein of 76 kDa
SMC	Smooth muscle cells
SOCE	Store-operated Ca^{2+} entry
SSC	Side scatter
ST	Short-term
STAT	Signal transducer and activator of transcription
STIM	Stromal interaction molecule
Syk	Spleen tyrosine kinase
Tβ4	Thymosin β4
TEM	Transmission electron microscopy
TEMED	Tetramethylethylenediamine
TF	Transcription factor
TGF	Transforming growth factor
Thr	Thrombin
TIMP	Tissue inhibitors of metalloproteinase
TLT-1	Trem-like transcript 1
TLR	Toll-like receptor
TNF	Tumor necrosis factor
TP	Thromboxane receptor
TPO	Thrombopoietin
TRAP	Tartrate-resistant acid phosphatase
Twf	Twinfilin
TxA_2	Thrombxane A_2
U46	U46619
VEGF	Vascular endothelial growth factor
VWD	Von Willebrand disease
vWF	Von Willebrand factor

WAS	Wiskott-Aldrich syndrome
WBC	White blood cell
WT	Wildtype
ZO	Zonula occludens

6.2 Acknowledgements

The animal caretakers, without whom our work would not be possible. Thank you for taking such good care of our animals.

The Graduate School of Life Sciences for allowing us to participate in numerous transferable skill courses and for the coordination of the PhD program.

The German Excellence Initiative and the Graduate School of Life Sciences for granting my fellowship, which enabled my attendance at several international conferences and allowed me to be financially independent.

Katja Aurbach: I know that I would not be writing this without you. Thank you for always having my back.

Lou Wackerbarth: Thank you for deciding to do your bachelor thesis in our lab. My life would not be the same without you in it. Thank you for proofreading this thesis, for your unlimited support and help and for being one of the best friends I could have asked for.

Sarah Beck for her loyalty and support even throughout the most difficult times.

All members of Office 3: Katja, Lou, Tobi, Stefano, Bodo, Andreas, Julia, Charly. Thank you! I cannot imagine how lab life would have been without you.

All other members of the Nieswandt lab, who made my time in the group unforgettable and with whom I happily spent countless hours laughing (in the lab and outside).

Sarah, Lou, Tobi, Zoltan and Georgi for carefully proofreading this thesis, useful discussions and their helpful ideas.

And most importantly I would like to thank my friends and family:

Janina, Ella, Marie, Lou, Hannah, Valentina, Katja, Tin, Fabi, Kathrin, Saskia, Michi, Marie, Metti – I cannot thank you enough. You made every day bearable and stood by me in every situation. I am in awe of how lucky I was to get to be your friend. Thank you, always and forever!

My parents, my brother, my grandma and my aunt: I cannot imagine life without your unlimited love and strength. I am eternally grateful for having you.

6.3 Publications

6.3.1 Articles

Becker IC, Nieswandt B. *et al*. **GPVI-triggered α-granule release narrows the progression of experimental ROP.** In preparation, 2020

Becker IC, Nieswandt B. *et al*. **G6b-B is a central regulator of megakaryocyte maturation and bone marrow homeostasis.** In preparation, 2020

Becker IC*, Scheller I*, Wackerbarth LM, Beck S, Heib T, Aurbach K, Manukjan G, Gross C, Spindler M, Nagy Z, Stritt S, Witke W, Lappalainen P, Bender M, Schulze H, Pleines I, Nieswandt B. **Actin/microtubule crosstalk during platelet biogenesis in mice is critically regulated by Twinfilin1 and Cofilin1.** Blood Adv. 2020 May 26;4(10):2124-2134. doi: 10.1182/bloodadvances.2019001303

Gotru SK, Gil-Pulido J, Beyersdorf N, Diefenbach A, Becker IC, Vögtle T, Remer K, Chubanov V, Gudermann T, Hermanns HM, Nieswandt B, Kerkau T, Zernecke A, Braun A. **Cutting Edge: Imbalanced Cation Homeostasis in MAGT1-Deficient B Cells Dysregulates B Cell Development and Signaling in Mice.** J Immunol. 2018 Apr 15;200(8):2529-2534. doi: 10.4049/jimmunol.1701467

Gotru SK, Chen W, Kraft P, Becker IC, Wolf K, Stritt S, Zierler S, Hermanns HM, Rao D, Perraud AL, Schmitz C, Zahedi RP, Noy PJ, Tomlinson MG, Dandekar T, Matsushita M, Chubanov V, Gudermann T, Stoll G, Nieswandt B, Braun A. **TRPM7 Kinase Controls Calcium Responses in Arterial Thrombosis and Stroke in Mice.** Arterioscler Thromb Vasc Biol. 2018 Feb;38(2):344-352. doi: 10.1161/ATVBAHA.117.310391

Haining EJ, Cherpokova D, Wolf K, Becker IC, Beck S, Eble JA, Stegner D, Watson SP, Nieswandt B. **CLEC-2 contributes to hemostasis independently of classical hemITAM signaling in mice.** Blood. 2017 Nov 16;130(20):2224-2228. doi: 10.1182/blood-2017-03-771907

Stritt S, Beck S, Becker IC, Vögtle T, Hakala M, Heinze KG, Du X, Bender M, Braun A, Lappalainen P, Nieswandt B. **Twinfilin 2a regulates platelet reactivity and turnover in mice.** Blood. 2017 Oct 12;130(15):1746-1756. doi: 10.1182/blood-2017-02-770768

6.3.2 Oral presentations

XXVIIth Congress of the International Society on Thrombosis and Haemostasis, Melbourne, Australia, 2019 (ISTH 2019 Early Career Award)
'*Unexpected redundant function of Twf1 and Cof1 is essential for platelet biogenesis'*

10th Platelets Meeting 2018, Ramat Gan, Israel
'*CLEC-2 contributes to hemostasis independently of classical hemITAM signaling in mice'*

XXVIth Congress of the International Society on Thrombosis and Haemostasis, Berlin, Germany, 2017 (ISTH 2017 Young Investigator Award)
'*Twinfilin 2a regulates platelet reactivity and turnover in mice'*

6.3.3 Poster presentations

International Symposium of the Graduate School of Life Science: EUREKA!, Würzburg, Germany, October 2019. "Myelofibrosis and osteosclerosis in mice carrying a novel mutation in *Mpig6b*"

International Symposium of the Graduate School of Life Science: EUREKA!, Würzburg, Germany, October 2018. "Soluble Glycoprotein V is involved in the maintenance of the mesenteric vascular integrity"

International Symposium of the Graduate School of Life Science: EUREKA!, Würzburg, Germany, October 2017. "Cooperative regulation of lymphatic development through the platelet glycoproteins CLEC-2 and GPV"

Joint Symposium of the Collaborative Research Center 688 and the Comprehensive Heart Failure Center Würzburg, Germany, October 2016. "Analysis of cellular regulation of platelet adhesion receptors in thrombosis and hemostasis"

International Symposium of the Graduate School of Life Science: EUREKA!, Würzburg, Germany, October 2016. "Glycoprotein V is a novel modulator of vascular integrity"

6.4   Affidavit

I hereby confirm that my thesis entitled "The role of megakaryocytes and platelets in vascular and osteogenic development" is the result of my own work. I did not receive any help or support from commercial consultants. All sources and/or materials applied are listed and specified in the thesis.

Furthermore, I confirm that this thesis has not yet been submitted as part of another examination process neither in identical nor in similar form.

Würzburg, May 2020   _____

Isabelle Carlotta Becker

6.5   Eidesstattliche Erklärung

Hiermit erkläre ich an Eides statt, die Dissertation „Die Rolle von Megakaryozyten und Thrombozyten in vaskulärer und ostegener Entwicklung " eigenständig, d.h. insbesondere selbstständig und ohne Hilfe eines kommerziellen Promotionsberaters, angefertigt und keine anderen als die von mir angegebenen Quellen und Hilfsmittel verwendet zu haben.

Ich erkläre außerdem, dass die Dissertation weder in gleicher noch in ähnlicher Form bereits in einem anderen Prüfungsverfahren vorgelegen hat.

Würzburg, Mai 2020   _____

Isabelle Carlotta Becker